GEOMETRICALLY NONLINEAR VIBRATION ANALYSIS OF FUNCTIONALLY GRADED POROUS PLATES AND SHELLS

Thesis

Submitted in partial fulfilment of the requirements for the degree of

DOCTOR OF PHILOSOPHY

by

NAVEEN KUMAR H S

DEPARTMENT OF MECHANICAL ENGINEERING

NATIONAL INSTITUTE OF TECHNOLOGY KARNATAKA,

SURATHKAL, MANGALORE – 575025

SEPTEMBER - 2022

DECLARATION

I hereby declare that the Research Thesis entitled **"Geometrically nonlinear vibration analysis of functionally graded porous plates and shells"** which is being submitted to the **National Institute of Technology Karnataka, Surathkal** in partial fulfillment of the requirements for the award of the degree of **Doctor of Philosophy** in **Mechanical Engineering** is a *bonafide report of the research work carried out by me*. The material contained in this Research Thesis has not been submitted to any other Universities or Institutes for the award of any degree.

Register Number	:	**197078ME012**
Name of the Research Scholar	:	**NAVEEN KUMAR H S**
Signature of the Research Scholar	:	30/09/2022.

Department of Mechanical Engineering

Place: NITK, Surathkal

Date: 30/09/2022.

CERTIFICATE

This is to certify that the Research Thesis entitled " **Geometrically nonlinear vibration analysis of functionally graded porous plates and shells** " submitted by **Mr. NAVEEN KUMAR H S (Register Number: 197078ME012)** as the record of the research work carried out by him, *is accepted as the Research Thesis submission* in partial fulfilment of the requirements for the award of the Degree of **Doctor of Philosophy.**

Research Guide

30/09/2022

Dr. Subhaschandra Kattimani

Associate Professor

Department of Mechanical Engineering

NITK, Surathkal

राष्ट्रीय प्रौद्योगिकी संस्थान, कर्नाटक
यांत्रिकी अभियांत्रिकी विभाग
Dept. of Mechanical Engineering
National Institute of Technology Karnataka

Chairman-DRPC

Department of Mechanical Engineering

Date: 30/09/2022

ACKNOWLEDGEMENT

It provides immense pleasure to acknowledge all the people who have helped, encouraged, and supported me throughout my dissertation. It is my humble appreciation towards everyone who has sacrificed their comfort in some form or other for completing my doctoral studies.

First of all, I would like to express my sincere gratitude and heartiest thanks to my supervisor ***Dr. Subhaschandra Kattimani***, Associate Professor, Department of Mechanical Engineering, National Institute of Technology Karnataka (NITK), Surathkal, for considering me worthy of working under his esteemed guidance. This research outcome results from his excellent guidance and support throughout the work. This thesis could not have attained its present form in content and presentation without his active interest, timely support, direction, and valuable guidance. My professional ethics, problem-solving skills, and knowledge level have received a professional boost through all those days I spent in his proximity. His vast knowledge and insight into the area of advanced composite structures have helped me to overcome the hurdles throughout my dissertation. The words are insufficient to express my deep feeling and heartfelt thanks to my supervisor for his unhesitating guidance throughout my doctoral work. For all this, I will remain grateful to him throughout my career.

I take this opportunity to thank ***Dr. Ravikiran Kadoli***., Professor and Head of the Department of Mechanical Engineering, for his continuous and timely support.

I would like to express my most profound appreciation to the research progress assessment committee members, ***Dr. Poornesh Kumar K*** and ***Dr. Arun Kumar Thalla***, for their valuable remarks, suggestions, and technical advice during my research.

I express my sincere gratitude to all the faculty members of the Department of Mechanical Engineering of NITK Surathkal for their unbiased appreciation and support throughout this research work.

I thank my fellow mates in the Mechanical engineering department NITK: **Esayas L Shirko**, ***Vinayak, Bhakshi, Chethan, Rakesh Patil, Atul, Sai Kumar, Shreyas, Ashok Kumar K, Phani***, and ***Sanjay***, for all the technical discussions and fun we have had in

the last three years. Also, I thank my friends outside the research domain: ***Jagadish***, ***Prasad***, ***Babu***, ***Vinay***, ***Navin***, ***Nagaraju***, ***Praveen Kumar P***, and ***Atul Vasanth Sawale,*** for their constant motivation and support.

I take this opportunity to thank all my colleagues at ***Government Polytechnic Hiriyur*** who have supported me directly or indirectly to expedite towards my goal. I am grateful to ***Udayachanda Govekar***, ***Vasudeva N***, ***Veeranna V***, ***Chandrakala H***, ***Seenappa M P***, ***Shashidhara K N***,, ***Manjunatha***, ***Prasad Kumar C M***, ***Ramesh T R***, ***Umesh E***, and ***Srinivasa G A*** who stood by me during my difficult days and supported me by being a source of my courage. In addition, I take this opportunity to thank the ***Department of Collegiate and Technical Education, Bangalore, Government of Karnataka***, for deputing me to pursue my Ph.D.

I would like to take this opportunity to express my gratitude to my family. Words cannot express how grateful I am to my father, Mr. ***Shivaramaiah***, and mother, Mrs. ***Shanthamma***, for their blessings, love, and all the sacrifices they have made on my behalf. It gives me immense pleasure to thank my sisters, Mrs. ***Hemavathi H S*** and Mrs. ***Lakshmi H S***, brothers-in-law, Mr. ***Suresh C K***, Mr. ***Madan Kumar H N***, and Mr. ***Ramu H R***, father-in-law, Mr. ***Ramesh H R*** and mother-in-law, Mrs. ***Radhamma*** for their constant support.

It gives me immense pleasure to express my sincere gratitude to my wife, Smt. ***Sowmya H R*** and my son Master ***Eshan Surya N*** for their unmatchable sacrifice, love, and support towards me.

Above all, I am highly indebted to the almighty ***Lord Shiva,*** who always blessed me to overcome every hurdle of my life and accomplish my goals with ease.

NAVEEN KUMAR H S.

National Institute of Technology Karnataka, Surathkal

Date: 30/09/2022.

ABSTRACT

Functionally graded materials (FGM) are typically a mixture of two or more distinguished materials with a smooth and continuous variation of constituent material properties in one or more directions. FGM shows a heterogeneous characteristic that permits the structures to avoid and eliminate the stress concentration and delamination phenomena commonly observed in laminated composites. However, FGM is susceptible to developing pores due to manufacturing constraints which decreases the strength of FGM. Also, vibrations caused in functionally graded (FG) structures exhibit large amplitudes due to the structures' flexibility. Therefore, it is crucial to investigate the effect of porosities on the geometrically nonlinear behavior of porous FG plates and shells. In this dissertation, the effect of porosities and their distributions on porous FG plates and shells subjected to different geometrical non-uniformities, temperature, two-directional gradation, and saturated porosities are considered for the analysis.

The effects of nonlinear temperature distribution and geometrical non-uniformities such as different types of variable thickness and skew angle are considered for the analysis. A nonlinear finite element model is developed by employing the first-order shear deformation theory in conjunction with von Kármán's geometric nonlinearity relations. The governing equations are derived using Hamilton's principle. Then, the direct iterative approach and Newmark's time integration method are utilized to extract the numerical results. Effective material characteristics of the porous FG plate constantly change in the thickness direction. The influence of porosity and its distributions on the nonlinear vibration and dynamic behavior of the geometrically non-uniform porous FG plates are investigated.

Generally, FGM has been limited to altering material properties in a single direction. However, this approach may be ineffective for designing components frequently subjected to considerable temperature changes in different directions. Therefore, the numerical evaluation is extended to analyze two-directional functionally graded porous (TDFGP) plates and shells with four different materials. The influence of porosities and two-directional gradation profiles for four distinct materials with longitudinal and transverse gradation are considered for the analysis. The vibration and dynamic

responses of TDFGP plates and shells are evaluated for various shell forms such as spherical, hyperboloid, ellipsoid, and cylindrical shells.

It is inevitable to produce flawless FGM devoid of the entrapment of fluids in pores using contemporary production procedures, which drastically vary the performance of FGM. Thus, the influence of fluid-filled pores on the nonlinear vibration and supersonic flutter analysis of FG saturated porous materials (FGSPM) plates in the thermal environment has been studied. The effects of pore fluid pressure and temperature-dependent elastic stiffness coefficients on the nonlinear flutter behavior of FGSPM plates are evaluated using poroelasticity theory and Piston theory.

The results reveal that the porosity nature and its distributions significantly affect the nonlinear behavior of the geometrically non-uniform FG porous plates under thermal load. In addition, the nonlinear behaviors can be changed and controlled considerably by altering the volume fraction gradation profiles in the required direction for each material with an appropriate combination of materials. The FGSPM plates exhibit enhanced stiffness without increasing weight compared to the FG plates with void porosity. It is believed that the research work presented in this dissertation may considerably help in the usability of porous FG plates and shells in the advanced engineering domains of aerospace, bio-medical, electronics, nuclear energy, and smart structures.

KEYWORDS: Functionally graded materials; Porosity; Two-directional gradation; Saturated porosities; von Kármán's geometric nonlinearity; Flutter bounds.

TABLE OF CONTENTS

ACKNOWLEDGEMENT v

ABSTRACT vii

LIST OF TABLES xvii

LIST OF FIGURES xxiii

NOMENCLATURE xxviii

CHAPTER 1 1

INTRODUCTION AND LITERATURE REVIEW 1

1.1. ADVANCED COMPOSITE MATERIALS 1

1.2. MATERIAL HOMOGENIZATION OF FGM 4

1.3. APPLICATIONS OF THE FGM 7

1.4. ANALYSIS OF FGM STRUCTURES 9

1.4.1. Nonlinear vibration and dynamic responses of the FGM structures 9

1.4.2. Influence of geometrical non-uniformities on FGM structures 12

1.4.3. Porosity influence on FGM structures 15

1.4.4. Analysis of bi / multi-directional gradation of FGM structures ... 17

1.4.5. Analysis of FG saturated porous material structures 19

1.4.6. Analysis of vibration and flutter characteristics of supersonic FGM structures 20

1.5. SCOPE AND OBJECTIVE OF THE DISSERTATION 21

1.6. CONTRIBUTIONS FROM THE DISSERTATION 24

1.7. OVERVIEW OF THE DISSERTATION BY CHAPTER 24

CHAPTER 2 29

INFLUENCE OF POROSITY DISTRIBUTION ON NONLINEAR FREE VIBRATION AND TRANSIENT RESPONSES OF POROUS FUNCTIONALLY GRADED SKEW PLATES 29

2.1. INTRODUCTION 29

2.2. PROBLEM DESCRIPTION AND GOVERNING EQUATION 30

2.2.1. Materials and Methods 30

2.2.2. Kinematics of deformations 34

2.2.3. Nonlinear finite element modeling of PFGS plate 37

2.2.4. Skew Boundary Transformation 41

2.3. Solution methodology 42

2.3.1. Nonlinear frequency parameter analysis 42

2.3.2. Nonlinear transient analysis 43

2.4. RESULTS AND DISCUSSIONS 44

2.5. Convergence and validation 45

2.6. Parametric Studies 48

2.7. Nonlinear frequency analysis 48

2.7.1. Effect of volume fraction grading index (m) 48

2.7.2. Effect of skew angle on porosity distributions 52

2.7.3. Effect of thickness and aspect ratio 55

2.7.4. Effect of porosity volume index (e_p) 58

2.7.5. Effect of boundary conditions 59

2.8. Nonlinear transient deflection analysis 60

2.8.1. Effect of porosity volume index 61

2.8.2. Effect of volume fraction grading index 63

2.9. CONCLUSIONS 64

CHAPTER 3 67

EFFECT OF DIFFERENT GEOMETRICAL NON-UNIFORMITIES ON NONLINEAR VIBRATION OF POROUS FUNCTIONALLY GRADED SKEW PLATES.....67

3.1. INTRODUCTION.....67

3.2. PROBLEM DESCRIPTION AND GOVERNING EQUATION.....68

3.2.1. TPFGS plate geometry.....68

3.2.2. Variable thickness.....69

3.3. RESULTS AND DISCUSSIONS.....70

3.3.1. Convergence and validation.....71

3.3.2. Numerical results.....72

3.3.3. Effect of volume fraction grading index and taper ratio.....72

3.3.4. Effect of porosity volume index.....76

3.3.5. Effect of thickness and aspect ratio.....77

3.3.6. Effect of porosity volume index on the NLFP with different boundary conditions.....80

3.4. CONCLUSIONS.....87

CHAPTER 4.....89

GEOMETRICALLY NONLINEAR VIBRATION AND TRANSIENT RESPONSES OF POROUS FG SKEW PLATE SUBJECTED TO THERMAL LOADS.....89

4.1. INTRODUCTION.....89

4.2. PROBLEM DESCRIPTION AND GOVERNING EQUATION.....90

4.2.1. Temperature-dependent effective material properties.....90

4.2.2. Constitutive equations.....93

4.2.3. Strain-displacement relations.....94

4.2.4. Nonlinear strain displacement equations.....95

4.2.5. Nonlinear finite element formulation.....96

4.3. RESULTS AND DISCUSSIONS 97
4.4. Convergence and validation 98
4.5. Nonlinear frequency analysis of the PFGS plate 103
4.5.1. Effect of temperature rise on the NLFR 103
4.5.2. Effect of skew angle 104
4.5.3. Effect of porosity volume index 105
4.5.4. Effect of thickness and aspect ratio 109
4.5.5. Effect of boundary conditions 112
4.6. Geometrically nonlinear transient response analysis 113
4.6.1. Effect of porosity volume index and skew angle 113
4.6.2. Effect of volume fraction grading index 116
4.7. CONCLUSIONS 118
CHAPTER 5 120
NONLINEAR ANALYSIS OF TWO-DIRECTIONAL FUNCTIONALLY GRADED DOUBLY CURVED PANELS WITH POROSITIES 120
5.1. INTRODUCTION 120
5.2. PROBLEM DESCRIPTION AND GOVERNING EQUATION 121
5.2.1. TDFGM shell geometry 121
5.2.2. Effective material properties 123
5.2.3. Nonlinear strain displacement equations 124
5.2.4. Constitutive equations 125
5.3. RESULTS AND DISCUSSIONS 125
5.3.1. Convergence and comparison study 126
5.3.2. Effect of TDFGM volume fractions 129
5.3.3. Effect of porosity volume index 133
5.3.4. Effect of thickness and aspect ratios 135

5.3.5. Effect of curvature ratio 136
5.3.6. Effect of boundary conditions 137
5.4. CONCLUSIONS 140
CHAPTER 6 142
GEOMETRICALLY NONLINEAR BEHAVIOR OF TWO-DIRECTIONAL FUNCTIONALLY GRADED POROUS PLATES WITH FOUR DIFFERENT MATERIALS 142
6.1. INTRODUCTION 142
6.2. PROBLEM DESCRIPTION AND GOVERNING EQUATION 143
6.2.1. The geometry of the TDFGPP 143
6.2.2. Nonlinear FE formulation and governing equations of motion 143
6.3. RESULTS AND DISCUSSIONS 144
6.3.1. Effect of TDFGPP volume fractions 144
6.3.2. Effect of porosity volume index (PVI) 149
6.3.3. Effect of thickness and aspect ratios 150
6.3.4. Effect of boundary conditions 151
6.4. CONCLUSIONS 152
CHAPTER 7 155
GEOMETRICALLY NONLINEAR ANALYSIS OF FUNCTIONALLY GRADED SATURATED POROUS PLATES 155
7.1. INTRODUCTION 155
7.2. PROBLEM DESCRIPTION AND GOVERNING EQUATION 156
7.2.1. The geometry of functionally graded saturated porous material plates 156
7.2.2. Constitutive relations 157
7.3. RESULTS AND DISCUSSIONS 158

7.3.1. Convergence and comparison study 159

7.3.2. Effect of Skempton coefficient (B) and volume fraction grading index (m) 159

7.3.3. Influence of porosity volume index (e_p) for various Skempton coefficients 165

7.3.4. Effect of thickness and aspect ratios 168

7.3.5. Effect of different support conditions 171

7.4. CONCLUSIONS 172

CHAPTER 8 173

SUPERSONIC FLUTTER CHARACTERISTICS OF FUNCTIONALLY GRADED SATURATED POROUS PLATES UNDER THERMAL LOADING 173

8.1. INTRODUCTION 173

8.2. PROBLEM DESCRIPTION AND GOVERNING EQUATION 175

8.2.1. Constitutive relations 175

8.2.2. Aerodynamic loading using first-order piston theory 176

8.2.3. The total potential energy principle 176

8.3. RESULTS AND DISCUSSIONS 178

8.3.1. Convergence and comparison study 178

8.3.2. Effect of VFGI with different temperature gradients 181

8.3.3. Effect of fluid-free porosity and its porosity distributions 181

8.3.4. Effect of Skempton coefficient (saturated-fluid pressure) 185

8.3.5. Effect of thickness ratio and aspect ratio 187

8.3.6. Effect of yawed flow angles 191

8.3.7. Effect of boundary conditions 195

8.4. CONCLUSIONS 195

CHAPTER 9.....197

CONCLUSIONS AND FUTURE SCOPE.....197

9.1. MAJOR FINDINGS.....197

9.2. SCOPE FOR THE FUTURE RESEARCH 199

APPENDIX - I 201

APPENDIX - II.....203

REFERENCES.....205

LIST OF TABLES

Table 2.1: The Properties of isotropic materials (Huang and Shen 2004). 44
Table 2.2: Comparing the fundamental natural frequency parameter for Si_3N_4 / SUS304 FGM square plate (a = 0.2; b = 0.2; h = 0.025, SSSS). 45
Table 2.3: Comparison of fundamental frequency for an isotropic skew plate (a/b = 1, SSSS). 45
Table 2.4: Comparison of fundamental natural frequency for different porosity volume index for simply supported square Al_2O_3 / Al porous FGM plate. 46
Table 2.5: Comparison of nonlinear frequency ratio (NLFR) (ω_{NL}/ω) with different values of amplitude ratios for Si_3N_4 / SUS304 FGM square plate (a/h = 10, m = 1, and SSSS). 47
Table 2.6: Effect of volume fraction grading index for different porosity distributions on the NLFR (ω_{NL}/ω) of Si_3N_4 / SUS304 PFGS plate (a/b = 1, a/h = 50, e_p = 0.10, Φ = 0°, and SSSS). 49
Table 2.7: Influence of Skew angle for different porosity distributions on the NLFR (ω_{NL}/ω) of Si_3N_4 / SUS304 PFGS plate. (a/b = 1, a/h = 50, e_p = 0.10, m = 2, and SSSS). 52
Table 2.8: Effect of thickness ratio for various skew angles on the fundamental NLFR (ω_{NL}/ω) for different porosity distributions of Si3N4 / SUS304 PFGS plate (a/b = 1, m = 2, e_p = 0.10, W_{max}/h = 1.0, and SSSS). 53
Table 2.9: Effect of aspect ratio for various skew angles on the fundamental NLFR (ω_{NL}/ω) for different porosity distributions of Si_3N_4 / SUS304 PFGS plate. (a/h = 50, m = 2, e_p = 0.10, W_{max}/h = 1.0, and SSSS). 56
Table 2.10: Effect of porosity volume index for various skew angles on the NLFR (ω_{NL}/ω) for different porosity distributions of simply supported Si_3N_4 / SUS304 PFGS plate. (a/h = 20, a/b = 1, m = 1, and W_{max}/h = 1.0). 59
Table 3.1: Comparison of the square isotropic tapered plate with various boundary conditions. 71
Table 3.2: Effect of volume fraction grading index on the NLFR (ω_{NL}/ω) of linearly variable thickness Si_3N_4 / SUS304 TPFGS plate for the different taper ratio (β). (a/b = 1, h_0 = 1/10, e_p = 0.1, Φ = 0°, χ = 0, and SSSS). 73

Table 3.3: Effect of volume fraction index on the NLFR (ω_{NL}/ω) of bi-linearly variable thickness Si_3N_4 / SUS304 TPFGS plate for the different taper ratio ($\beta = \chi$). ($a/b = 1$, $h_0 = 1/10$, $e_p = 0.1$, $\Phi = 0°$, and SSSS). 74
Table 3.4: Effect of volume fraction index on the NLFR (ω_{NL}/ω) of exponentially variable thickness Si_3N_4 / SUS304 TPFGS plate for the different taper ratio (β). ($a/b = 1$, $h_0 = 1/10$, $e_p = 0.1$, $\Phi = 0°$, $\chi = 0$, and SSSS)..... 75
Table 3.5: Effect of porosity volume index on the NLFR (ω_{NL}/ω) of linearly variable thickness Si_3N_4 / SUS304 TPFGS plate for the different taper ratio (β) and skew angle (Φ). ($a/b = 1$, $h_0 = 1/10$, $m = 2$, $W_{max}/h = 1.0$, $\chi = 0$, and SSSS)..... 76
Table 3.6: Effect of porosity parameter index on the NLFR (ω_{NL}/ω) of bi-linearly variable thickness Si_3N_4 / SUS304 TPFGS plate for the different taper ratio ($\beta = \chi$) and skew angle (Φ). ($a/b = 1$, $h_0 = 1/10$, $m = 2$, $W_{max}/h = 1.0$, and SSSS). 77
Table 3.7: Effect of porosity parameter index on the NLFR (ω_{NL}/ω) of exponentially variable thickness Si_3N_4 / SUS304 TPFGS plate for the different taper ratio (β) and skew angle (Φ). ($a/b = 1$, $h_0 = 1/10$, $m = 2$, $W_{max}/h = 1.0$, $\chi = 0$, and SSSS). 78
Table 3.8: Effect of thickness-to-length ratio (a/h_0) on the NLFR (ω_{NL}/ω) of linearly variable thickness Si_3N_4 / SUS304 TPFGS plate for the different taper ratio (β) and skew angle (Φ). ($a/b = 1$, $m = 2$, $e_p = 0.1$, $W_{max}/h = 1.0$, $\chi = 0$, and SSSS). 79
Table 3.9: Effect of thickness-to-length ratio (a/h_0) on the NLFR (ω_{NL}/ω) of bi-linearly variable thickness Si_3N_4 / SUS304 TPFGS plate for the different taper ratio ($\beta = \chi$) and skew angle (Φ). ($a/b = 1$, $m = 2$, $e_p = 0.1$, $W_{max}/h = 1.0$, and SSSS). 79
Table 3.10: Effect of thickness-to-length ratio (a/h_0) on the NLFR (ω_{NL}/ω) of exponentially variable thickness Si_3N_4 / SUS304 TPFGS plate for the different taper ratio (β) and skew angle (Φ). ($a/b = 1$, $m = 2$, $e_p = 0.1$, $W_{max}/h = 1.0$, $\chi = 0$, and SSSS). 80
Table 3.11: Effect of aspect ratio (a/b) on the NLFR (ω_{NL}/ω) of linearly variable thickness Si_3N_4 / SUS304 TPFGS plate for the different taper ratio (β) and skew angle (Φ). ($h_0 = 1/10$, $m = 2$, $e_p = 0.1$, $W_{max}/h = 1.0$, $\chi = 0$, and SSSS)..... 81
Table 3.12: Effect of aspect ratio (a/b) on the NLFR (ω_{NL}/ω) of bi-linearly variable thickness Si_3N_4 / SUS304 TPFGS plate for the different taper ratio ($\beta = \chi$) and skew angle (Φ). ($h_0 = 1/10$, $m = 2$, $e_p = 0.1$, $W_{max}/h = 1.0$, and SSSS). 82

Table 3.13: Effect of aspect ratio (a/b) on the NFR (ω_{NL}/ω) of exponentially variable thickness Si_3N_4 / SUS304 TPFGS plate for the different taper ratio (β) and skew angle (Φ). ($h_0 = 1/10$, $m = 2$, $e_p = 0.1$, $W_{max}/h = 1.0$, $\chi = 0$, and SSSS).....83
Table 4.1: Coefficients of the temperature-dependent constituent materials Si_3N_4 and SUS304: Young's modulus E (Pa) and the coefficient of thermal expansion α (1/K) (Reddy and Chin 1998).....98
Table 4.2: Comparison of the fundamental natural frequency of simply supported Al/Al_2O_3 FG square plates.....100
Table 4.3: Comparison of fundamental natural frequency for simply supported Si_3N_4 / SUS304 square FG plate under thermal loading. ($a = b = 0.2$, $a/h = 8$).....101
Table 4.4: The dimensionless natural frequency comparison for an isotropic skew plate ($a/b = 1$, SSSS).....101
Table 4.5: Natural frequency comparison for SSSS Al_2O_3/Al porous FG plate with various porosity volume indexes.....103
Table 4.6: Influence of various skew angles on the NLFR for the porosity distributions P_e and P_c ($a/b = 1$, $a/h = 10$, $e_p = 0.1$, $m = 2$, $W_{max}/h = 1.0$, and SSSS).....105
Table 4.7: Influence of porosity volume index on NLFR for different thermal loadings ($a/b = 1$, $a/h = 10$, $m = 2$, $W_{max}/h = 1.0$, and SSSS).....106
Table 4.8: Effect of thickness ratio on NLFR under different thermal loadings (a/b=1, $m = 2$, $e_p = 0.1$, $W_{max}/h = 1.0$, and SSSS).....110
Table 4.9: Effect of aspect ratio on NLFR under thermal loading (a/h =10, $m = 2$, $e_p = 0.1$, $W_{max}/h = 1.0$, and SSSS).....111
Table 5.1: Material properties of the doubly curved TDFGM shells (Ebrahimi and Dabbagh 2021; Zhao et al. 2009).....127
Table 5.2: Comparison of fundamental frequency of in-plane FG plate for different m_x (a/h =100, a/b = 1, $R/a = \infty$).....127
Table 5.3: Comparison of fundamental frequency of SSSS square porous FG spherical shell panels composed of Al_2O_3/SUS304 for different e_p and m_z (a/h =100, $a/b = 1$, $R/a = 1$, $m_x = 0$, P_e, and SSSS).....128
Table 5.4: Comparison of NLFR square FG shell panels composed of ZrO_2/Al (a/h =100, $m_z = 2$, $m_x = 0$, $R/a = 50$, and SSSS).....128

Table 5.5: NLFR (ω_{NL} /ω) of square TDFGM porous cylindrical shell panels for different volume fraction grading index (a/h =20, R/a = 20, e_p = 0, and SSSS). 130
Table 5.6: NLFR (ω_{NL} /ω) of square TDFGM porous spherical shell panels for different volume fraction grading index (a/h =20, R/a = 20, e_p = 0, and SSSS). 131
Table 5.7: NLFR (ω_{NL} /ω) of square TDFGM porous hyperboloid shell panels for different volume fraction grading index (a/h =20, R/a = 20, e_p = 0, and SSSS). 132
Table 5.8: NLFR (ω_{NL} /ω) of square TDFGM porous ellipsoid shell panels for different volume fraction grading index (a/h =20, R/a = 20, e_p = 0, and SSSS). 133
Table 5.9: NLFR (ω_{NL} /ω) of square TDFGM porous shell panels for different porosity volume index (a/h =20, R/a = 20, $m_x = m_z = 2$, W_{max}/h = 1.5, and SSSS).....134
Table 5.10: NLFR (ω_{NL} /ω) of square TDFGM porous shell panels with different thickness ratios (R/a = 20, e_p = 0.1, $m_x = m_z = 2$, W_{max}/h = 1.5, and SSSS).....136
Table 5.11: NLFR (ω_{NL} /ω) of TDFGM porous shell panels with different aspect ratios (a/h = 20, R/a = 50, e_p = 0.1, $m_x = m_z = 2$, W_{max}/h = 1.5, and SSSS). 137
Table 5.12: NLFR (ω_{NL} /ω) of square TDFGM porous shell panels with different curvature ratios (a/h =20, e_p = 0.1, $m_x = m_z = 2$, W_{max}/h = 1.5, and SSSS).....138
Table 6.1: NLFR (ω_{NL} /ω) of the TDFGPP for different VFGI (a/h =100, a/b = 1, e_p = 0, and SSSS).....145
Table 6.2: NLFR (ω_{NL} /ω) of the square TDFGPP for different PVI (e_p) (a/h =100, $m_x = m_z = 2$, and SSSS). 147
Table 6.3: NLFR (ω_{NL} /ω) of the square TDFGPP for different thickness ratios (e_p = 0.1, $m_x = m_z = 2$, W_{max}/h = 1.5, and SSSS).....150
Table 6.4: NLFR (ω_{NL} /ω) of the TDFGPP for different aspect ratios (a/h = 100, e_p = 0.1, $m_x = m_z = 2$, W_{max}/h = 1.5, and SSSS).....151
Table 7.1: Dimensionless fundamental frequency of FG porous square plates (e_p = 0) (a/b =1). 161
Table 7.2: Dimensionless deflection of FG porous square plates (e_p = 0) (a/b =1)..161
Table 7.3: Effect of Skempton coefficient (B) and VFGI on the NLFR (ω_{NL}/ω) of Si_3N_4/SUS304 FGSPM square plate. (a/h =10, e_p = 0.1, $P_d = P_e$, & SSSS). 162
Table 7.4: Effect of Skempton coefficient (B) and VFGI on the NLFR (ω_{NL}/ω) of Si_3N_4/SUS304 FGSPM square plate. (a/h =10, e_p = 0.1, $P_d = P_c$, & SSSS). 163

Table 7.5: Influence of thickness ratio on the NLFR (ω_{NL}/ω) of Si_3N_4/SUS304 FGSPM plate for different Skempton coefficient (B). (a/b = 1, m = 2, W_{max}/h = 1.0, e_p = 0.1). 169
Table 7.6: Influence of aspect ratio on the NLFR (ω_{NL}/ω) of Si_3N_4/SUS304 FGSPM plate for different Skempton coefficient (B). (a/h = 10, m = 2, W_{max}/h = 1.0, e_p = 0.1). 170
Table 8.1: Comparison of the flutter bounds of the square FG plate with different temperature gradients. 179
Table 8.2: A comparison of the critical aerodynamic pressure of the simply supported square FG plate with different VFGI (m). (T_c = 300 K). [Ref: Zhou et al. (2018)]...180
Table 8.3: Comparison of the critical aerodynamic pressure of the square FG plate with different porosity distributions. (m = 1). [Ref: Zhou et al. (2018)]. 180

LIST OF FIGURES

Figure 1.1: Variation of properties in traditional composites and FGM. 3
Figure 1.2: FGM with ceramic and metal as material constituents. 3
Figure 1.3: Variation of the volume fractions of the ceramic material (V_c) along with the non-dimensional thickness (z/h)..... 5
Figure 1.4: The variation of effective Young's modulus for the different VFGI of the FGM along with the non-dimensional thickness (z/h). 6
Figure 1.5: Practical applications of FGM..... 8
Figure 2.1: The geometry of the PFGS plate. 31
Figure 2.2: Porosity distribution in PFGS plate (a) P_e (b) P_c, and (c) P_{tb}. 32
Figure 2.3: Variation of effective Young's modulus of FGP plate made of Si_3N_4 / SUS304 for different porosity distributions and VFGI (m). 34
Figure 2.4: Comparison of dimensionless nonlinear transient deflection of the simply supported orthotropic plate. 47
Figure 2.5: Effect of different volume fraction grading indices on NLFP of ZrO_2 / Ti-6Al-4V PFGS plate for various porosity distributions and boundary conditions. 51
Figure 2.6: Effect of skew angle on NLFP of ZrO_2 / Ti-6Al-4V PFGS plate for various porosity distributions and boundary conditions. (a/b = 1, a/h = 80, m = 2, e_p = 0.3).. 54
Figure 2.7: Effect of porosity volume index for different skew angles on the NLFR of ZrO_2 / Ti-6Al-4V PFGS plates with various porosity distributions and boundary conditions. 57
Figure 2.8: Influence of porosity distributions on the NLFR for various boundary conditions for ZrO_2 / Ti-6Al-4V PFGS plate. 60
Figure 2.9: Effect of porosity volume index on central deflection (w_c / h) for various skew angles and porosity distributions on simply supported Si_3N_4 / SUS304 PFGS plate. 62
Figure 2.10: Effect of volume fraction grading index on central deflection (w_c / h) for different porosity distribution on the simply supported Si_3N_4 / SUS304 PFGS plate. 64
Figure 3.1: The geometry of the TPFGS plate. (a) Bi-linearly variable thickness, (b) Linearly variable thickness, and (c) Exponentially variable thickness. 68

Figure 3.2: Effect of taper ratio and porosity volume index on the NLFP for the Linearly variable thickness of the TPFGS plate. (a) P_d=P_e and SSSS, (b) P_d=P_c and SSSS, (c) P_d=P_e and SCSC, (d) P_d=P_c and SCSC, (e) P_d=P_e and SCSC, and (f) P_d=P_c and SCSC. 84
Figure 3.3: Effect of taper ratio and porosity parameter index on the NLFP for the Bi-linearly Variable thickness of the TPFGS plate. (a) P_d=P_e and SSSS, (b) P_d=P_c and SSSS, (c) P_d=P_e and SCSC, (d) P_d=P_c and SCSC, (e) P_d=P_e and SCSC, and (f) P_d=P_c and SCSC. 85
Figure 3.4: Effect of taper ratio and porosity parameter index on the NLFP for the exponentially Variable thickness of the TPFGS plate. (a) P_d=P_e and SSSS, (b) P_d=P_c and SSSS, (c) P_d=P_e and SCSC, (d) P_d=P_c and SCSC, (e) P_d=P_e and SCSC, and (f) P_d=P_c and SCSC. 86
Figure 4.1: Young modulus as a function of temperature for Si_3N_4 / SUS304 FG porous plate with different VFGI. (a) P_e, (b) P_c, and (c) Perfect FG plate. 93
Figure 4.2: Nonlinear frequency ratio (NLFR) comparison of a SSSS Si_3N_4 / SUS304 FG plate in under thermal loading ($a = b = 1$, $a/h = 10$, and $m = 2$). 102
Figure 4.3: Comparison of dimensionless nonlinear transient deflection of the simply supported orthotropic plate. 102
Figure 4.4: Effects of temperature rise on NLFR for the porosity distributions P_e and P_c ($a/b = 1$, $a/h = 10$, $e_p = 0.1$, $\Phi = 0°$, $m = 2$, and SSSS). 104
Figure 4.5: Influence of various porosity volume indices for different temperatures on NLFP ($a/b = 1$, $a/h = 10$, $m = 2$, and $W_{max}/h = 1.0$). 109
Figure 4.6: Influence of various boundary conditions for the porosity distributions P_e and P_c on NLFR. ($a/b = 1$, $a/h = 10$, $m = 2$, $e_p = 0.1$, $\Phi = 30°$, and $\Delta T = 300$). 112
Figure 4.7: Influence of porosity volume index on transient deflections of the PFGS plate with different skew angles and temperature rise ($a/b = 1$, $a/h = 30$, $m = 2$, and SSSS). 115
Figure 4.8: Influence of volume fraction grading index (m) on transient deflections of the PFGS plate with different skew angles and temperature rise ($a/b = 1$, $a/h = 30$, $e_p = 0.15$, and SSSS) 117
Figure 5.1: TDFGM doubly curved porous shell geometry. 122

Figure 5.2: The TDFGM doubly curved porous shells schematic diagram (a) Cylindrical, (b) Spherical, (c) Hyperboloid, and (d) Ellipsoid. 122
Figure 5.3: The geometry of the porosity distributions in the TDFGM porous shell (a) Evenly distributed porosity (P_e) and (b) Centrally distributed porosity (P_c). 123
Figure 5.4: Comparison of nonlinear central deflection (w_c/h) of FGM plate..... 129
Figure 5.5: Nonlinear central deflection of square TDFGM porous panels for different volume fraction grading index and porosity distributions (a/h = 20, e_p = 0.1, and R/a = 20). 132
Figure 5.6: Nonlinear central deflection of square TDFGM porous panels for different porosity distributions and porosity volume index (a/h = 20, $m_x = m_z$ = 2, R/a = 20). 139
Figure 5.7: NLFR (ω_{NL} /ω) of square TDFGM porous panels for different porosity distributions and support conditions (a/h =40, R/a = 50, e_p = 0.1, and $m_x = m_z$ = 2). 140
Figure 6.1: TDFGPP geometry is composed of Si_3N_4/SUS304 and Al/Aluminium oxide..... 143
Figure 6.2: Nonlinear central deflections of square TDFGM porous plate for different VFGI (m_x and m_z) (a/h = 100, and e_p = 0.1)..... 146
Figure 6.3: Nonlinear transient deflections of square TDFGPP for different VFGI (a/h = 100, e_p = 0.1). (a) EDP (P_e), and (b) CDP (P_c). 147
Figure 6.4: Nonlinear central deflections of TDFGPP for different porosity distributions and PVI (e_p) (a/h = 100, and $m_x = m_z$ = 2). 148
Figure 6.5: Nonlinear transient deflections of the TDFGPP with CDP (P_c) for different PVI (e_p) (a/h = 100, a/b = 1, and $m_x = m_z$ = 2). (a) EDP (P_e), and (b) CDP (P_c). 149
Figure 6.6: Nonlinear central deflections of TDFGPP for different support conditions (a/h = 100, a/b = 1, $m_x = m_z$ = 2, and e_p = 0.1). 151
Figure 6.7: Nonlinear transient deflections of the TDFGPP for different support conditions and porosity distributions (a/h = 100, a/b = 1, $m_x = m_z$ = 2, and e_p = 0.1). 152
Figure 7.1: Cross-section of the FGSPM plate showing the porosity distributions in an undrained state. (a) Evenly distributed porosity (P_e) and (b) Centrally distributed porosity (P_c). 157

Figure 7.2: Effect of VFGI on the central deflection (w_c/h) of Si_3N_4/SUS304 FGSPM square plate for different porosity distributions. (a/h =10, B = 0.5, e_p = 0.1, & SSSS). 164
Figure 7.3: Effect of Skempton coefficient (B) on the central deflection (w_c/h) of Si_3N_4/SUS304 FGSPM square plate for different porosity distributions. (a/h =10, e_p = 0.1, m = 2, & SSSS). 164
Figure 7.4: Influence of Skempton coefficient (B) on the linear frequency and NLFR (ω_{NL}/ω) of Si_3N_4/SUS304 FGSPM square plate for different porosity volume index. (a/h =10, m = 2, W_{max}/h = 1,). (a) P_e, & SSSS, (b) P_e, & CCCC, (c) P_c, & SSSS, and (d) P_c, & CCCC. 167
Figure 7.5: Influence of porosity volume index on the central deflection (w_c/h) of Si_3N_4/SUS304 FGSPM square plate for different porosity distributions. (a/h =10, B = 0.5, m = 2, & SSSS). 168
Figure 7.6: Influence of Skempton coefficient (B) on the central deflection (w_c/h) of Si_3N_4/SUS304 FGSPM square plate for various boundary conditions. (a/h =10, B = 0.5, e_p = 0.1, & m = 2).....171
Figure 8.1: The variations of the λ_{cr} for various amplitude ratios (W_{max}/h) of the simply supported FGSPM plate having different VFGI and temperature gradients (a/b = 1, a/h = 20, e_p = 0, and B = 0). 181
Figure 8.2: The variations of the λ_{cr} for various amplitude ratios (W_{max}/h) of the simply supported square FGSPM plate with different thermal loads and porosity distributions (a/h = 20, m = 1, and B = 0). (a) P_e, and (b) P_c. 183
Figure 8.3: The variations of the nonlinear frequencies for various porosity distributions of the simply supported square FGSPM plate having different thermal loads with aerodynamic pressure (λ) (a/h = 20, m = 1, W_{max}/h = 1, and B = 0). (a) P_e, and (b) P_c. 184
Figure 8.4: The variations of the λ_{cr} for various Skempton coefficients (B) of the simply supported square FGSPM plate with different porosity distributions and thermal loads (a/h = 20, m = 1, and e_p = 0.2). (a) T_c = 300 K , (b) T_c = 400 K, and (c) T_c = 600 K. 186
Figure 8.5: The variations of the nonlinear frequencies for various Skempton coefficients (B) of the simply supported square FGSPM plate having different thermal

loads and porosity distributions with aerodynamic pressure (λ) (a/h = 20, m = 1, and W_{max}/h = 1). 188
Figure 8.6: Effect of thickness ratio on the critical aerodynamic pressure for different Skempton coefficients (B) of simply supported FGSPM plate having different porosity distributions and thermal loads (a/b = 1, W_{max}/h = 1, m = 1, and e_p = 0.2). 190
Figure 8.7: Effect of aspect ratio on the critical aerodynamic pressure for different Skempton coefficients (B) of simply supported FGSPM plate having different porosity distributions and thermal loads (a/h = 20, W_{max}/h = 1, m = 1, and e_p = 0.2). 191
Figure 8.8: The variations of the critical aerodynamic pressure (λ_{cr}) of the square FGSPM plate having different VFGI, porosity volume index (e_p), and thermal loadings with yawed flow angles (a/h = 20, W_{max}/h = 1, and B = 0). 192
Figure 8.9: The variations of the critical aerodynamic pressure (λ_{cr}) of the square FGSPM plate having different Skempton coefficient (B), porosity distributions, and thermal loadings with yawed flow angles (a/h = 20, W_{max}/h = 1, m = 1, and e_p = 0.2). 193
Figure 8.10: The variations of the λ_{cr} with amplitude ratio (W_{max}/h) of the square FGSPM plate having different yawed flow angles, porosity distributions, and thermal loadings with boundary conditions (a/h = 20, m = 1, B = 0.2, and e_p = 0.2). 194

NOMENCLATURE

BDFGM	Bi-directional functionally graded materials
CDP (P_c)	Centrally distributed porosities (P_c)
CPT	Classical plate theory
EDP (P_e)	Evenly distributed porosities (P_e)
FE	Finite element
FGM	Functionally graded materials
FG	Functionally graded
FGP	Functionally graded porous
FGS	Functionally graded skew
FGSPM	Functionally graded saturated porous material
FSDT	First-order shear deformation theory
HSDT	Higher-order shear deformation theory
NLFR	Nonlinear frequency ratio (ω_{NL}/ω)
NLFP	Nonlinear frequency parameter (ω_{NL})
PFGS	Porous functionally graded skew
TDFGP	Two-directional functionally graded porous
TPFGS	Tapered porous functionally graded skew
TSDT	Third-order shear deformation theory
PFGS	Porous functionally graded skew
VFGI (m)	Volume fraction grading index
e_p	Porosity volume index
P_d	Type of porosity distributions
P_{tb}	High porosity distribution near the top and bottom surface while narrow at the middle
B	Skempton coefficient
λ	Aerodynamic pressure loading
λ_{cr}	Critical aerodynamic pressure loading
ω	Linear frequency
ω_{NL}	Nonlinear frequency

P	Load parameter
w_c/h	Nonlinear central deflections
q_0	Uniformly distributed load
W_{max}/ h	Amplitude Ratio

CHAPTER 1

INTRODUCTION AND LITERATURE REVIEW

This chapter presents a brief introduction and a comprehensive literature survey on advanced composite materials. In particular, functionally graded materials (FGM) are unveiled. Significant contributions by many researchers with respect to FGM and its broad spectrum of applications have been discussed. The literature on basic structural characteristics such as linear and nonlinear free vibration, dynamic responses, and flutter bounds with various configurations is briefly discussed. In addition, the porosity influence on the structural characteristics of porous FGM is presented comprehensively. From the extensive literature survey, the prominent research gaps have been identified and incorporated as the research objectives of this dissertation. In the end, the organization of the thesis chapters has been delineated.

1.1. ADVANCED COMPOSITE MATERIALS

Composite materials are a class of advanced materials produced by a solid-state combination of one or more materials having specific chemical and physical properties. These composite materials offer superior properties and are more lightweight than their parent materials. Besides, composite materials with microstructures are tailored to achieve the desired characteristics. For laminated composite plates, customizations are accomplished generally by varying the stacking sequence, ply thickness, and ply material. However, traditional composites have several disadvantages that cannot be mitigated, such as interfaces, generation of residual stresses, stress concentration, delamination, thermal stresses, and the occurrence of cracks. Besides, in engineering, metals have been utilized for decades due to their superior strength and toughness. Similar to traditional composites, the metal's strength declines at elevated temperatures. The ceramic materials have strong heat resistance properties. However, the low toughness of ceramics typically limits their applicability.

Hence, a new class of composite material has emerged to overcome the drawbacks of traditional composite and isotropic materials, known as functionally graded materials (FGM). FGM is not new to humankind; bone, teeth, human skin, and bamboo trees are all nature-built FGM forms (Saleh et al. 2020). The idea of FGM was first proposed by material scientists from Japan in 1984 (Koizumi 1997). The concept of developing the new functionally graded (FG) material was to enhance the adhesion and reduce the thermal stresses in ceramic-metal composites developed for reusable rocket engines. Meanwhile, FGM principles have stimulated worldwide research and have been applied to ceramics, metals, and organic composites to create enhanced materials with superior physical properties. Hence, in recent years, great attention has been focused on FGM because of its excellent performance and widespread applications in thermal, structural, biomedical, electronics, and optoelectronics.

FGM is an inhomogeneous or heterogeneous composite material in which the composition and material properties vary smoothly and constantly in a preferred direction, as shown in Figure 1.1. Different microstructural phases within FGM have distinct functions, and the gradation of their properties confers multi-structural status on FGM as a whole. For example, a functionally graded (FG) plate is used as a thermal barrier/structural application in which the gradation is through the thickness. The top and bottom surfaces have isotropic constituent materials of ceramic and metal, respectively. The portion between the top and bottom surfaces has a varying composition of two constituent materials. Thus, in a single FG material, one can obtain the properties of two different materials with the variable volume fractions of each constituent material in a chosen direction, as shown in Figure 1.2. Due to the ceramic material's low thermal conductivity, the FG material's ceramic portion provides high-temperature resistance. On the other hand, the FG's ductile metal portion prevents fracture due to high-temperature gradient stresses in a short period. Thus, FGM does not have well-defined boundaries or interfaces between their regions compared to traditional composite materials. Hence, FGM can easily avoid the drawbacks of composites.

FGM is typically composed of two constituent materials: metal and ceramic, and is manufactured using various techniques, including deposition, solid-state, and liquid-

state procedures (Naebe and Shirvanimoghaddam 2016; Saleh et al. 2020). Thin FGM is utilized in microscale coating applications. These are manufactured through deposition-based processes like vapor deposition, thermal spray, and electrophoretic deposition. Constructing a continuous or discontinuous graded layer and FGMs with gradient properties in one, two, or three orientations is feasible using these techniques. Furthermore, powder metallurgy, additive manufacturing, and friction stir additive manufacturing are the most promising solid-state FGM production techniques. Even though these techniques produce a discontinuous gradient, the gradation may be regulated to a higher degree, making them suitable for numerous industrial applications.

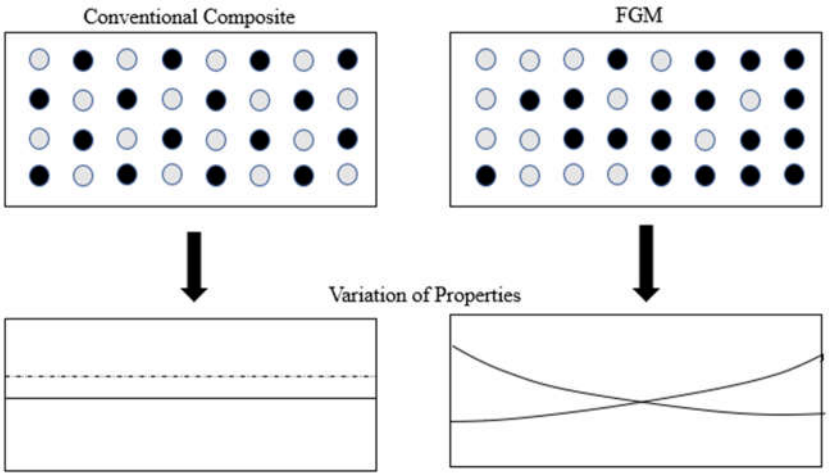

Figure 1.1: Variation of properties in traditional composites and FGM.

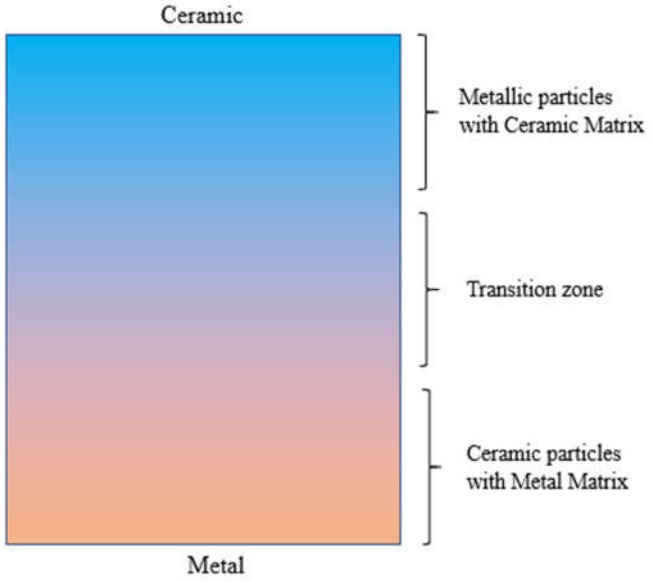

Figure 1.2: FGM with ceramic and metal as material constituents.

Additionally, numerous techniques, such as centrifugal force methods, slip casting, tape casting, and infiltration, fall within the liquid state principle when manufacturing FGM with gradient properties. These technologies may generate graded materials with continuous properties, most of which are less expensive than other processes. In addition to the difficulties associated with molten metal, it is challenging to manage the gradation and wettability between materials using these techniques.

1.2. MATERIAL HOMOGENIZATION OF FGM

FGM is microscopically inhomogeneous. The volume fraction of the two or more material constituents is varied smoothly and continuously as a continuous function of the material position in one or more directions in the structure. The mechanics of a material's primary task is to predict the material behavior, which requires the determination of the FG composition's effective material properties, termed homogenization. Homogenization is employed when precise information about the phases' size, shape, and distribution is unavailable. The graded microstructure's effective material properties are evaluated based on the volume fraction distribution of the dispersed phase. Hence, FGM is classified into three categories such as continuously, discretely, and multiphase graded microstructures. The continuously graded microstructure is the commonly used method for analyzing FGM structures. Further, the continuously graded microstructure uses several mathematical models to predict the effective material properties of FGM. The power-law model, exponential law model, sigmoid law model, rule of mixtures, Mori-Tanaka scheme, and self-consistent estimation model are some of the most widely used mathematical models. However, the power-law model is the most common and accepted model to predict the effective material properties.

The FGM with a continuously graded microstructure along the thickness direction comprises two isotropic and homogeneous materials: metal and ceramic. Besides, if the top surface of the FGM is solely ceramic $(z = h/2)$ and the bottom surface is exclusively metal $(z = -h/2)$. An expression for the variation of the volume fractions of the ceramic material along the thickness direction for FGM can be written as follows:

$$V_C = \left(\frac{1}{2} + \frac{z}{h}\right)^m \tag{1.1}$$

where V_c represents the volume fractions of the ceramic material, h is the thickness of the FGM structure, z is the distance from the mid-plane of the FGM $(h/2 \le z \le -h/2)$, and m $(0 \le m \le \infty)$ is a volume fraction grading index (VFGI). VFGI (m) indicates the material variation profile through the FGM thickness. Then, changing the value of VFGI produces an infinite number of composition distributions of both the constituent materials in the thickness direction. i.e., the z-axis as depicted in Figure 1.3.

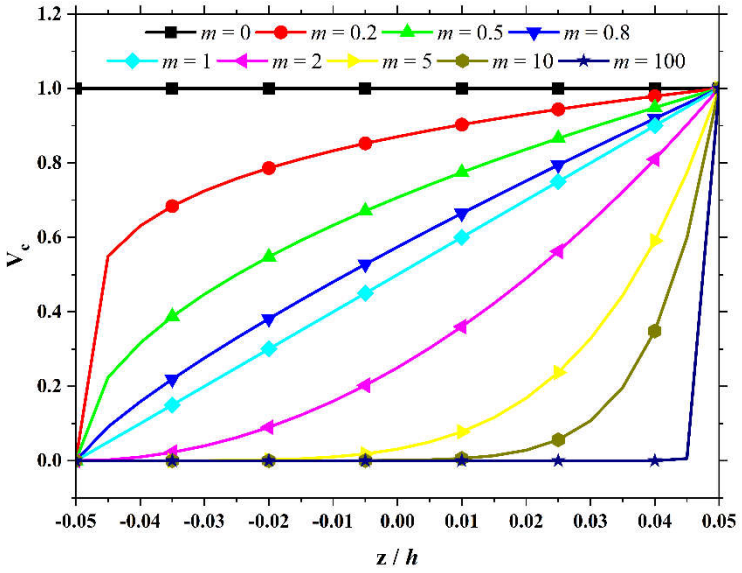

Figure 1.3: Variation of the volume fractions of the ceramic material (V_c) along with the non-dimensional thickness (z/h).

Furthermore, the properties depend on the position to accurately represent the effective material properties of FGM. Hence, the power-law series is used to obtain the effective material properties of the FGM. The position-dependent effective material properties of the FGM $(\mathrm{P_{fg}}(z))$, such as Young's modulus $(E_{fg}(z))$, density $(\rho_{fg}(z))$, and Poisson's ratio $(\vartheta_{fg}(z))$, can be written as follows:

$$\mathrm{P_{fg}}(z) = \sum_{j=1} P_j \left(V_f\right)_j \tag{1.2}$$

where $\mathrm{P_{fg}}$ (z) is the effective material properties of the FGM along the thickness direction. The material properties and volume fractions of the constituent material j are

denoted by P_j and $(V_f)_j$. In addition, the sum of volume fractions of the constituent materials of FGM is always unity and forms the equation as follows:

$$\sum_{j=1}\left(V_f\right)_j = 1 \tag{1.3}$$

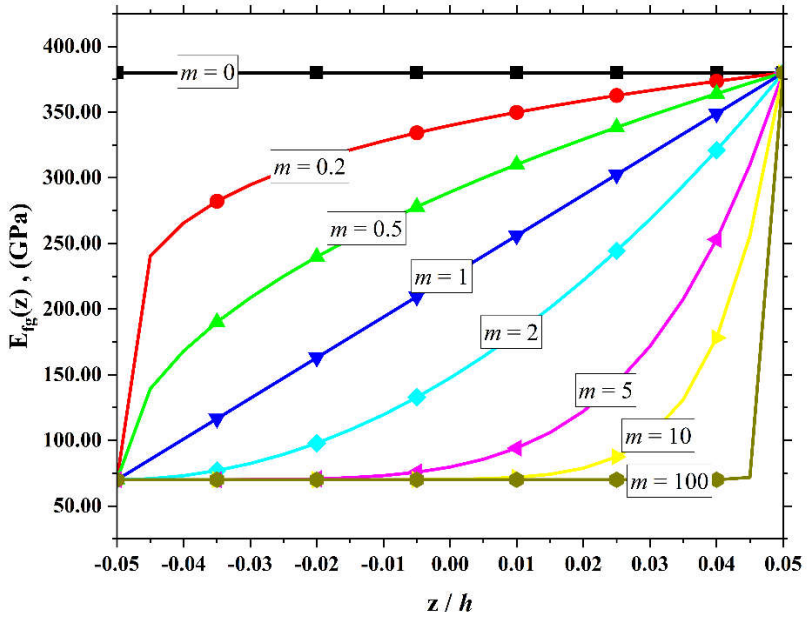

Figure 1.4: The variation of effective Young's modulus for the different VFGI of the FGM along with the non-dimensional thickness (z/h).

The position-dependent effective material properties such as Young's modulus $(E_{fg}(z))$, density $(\rho_{fg}(z))$, and Poisson's ratio $(\vartheta_{fg}(z))$ of the FGM can be obtained from Eqs. (1.1) - (1.3) and are as follows:

$$E_{\mathrm{fg}}\left(z\right) = (E_t - E_b)\left(\frac{1}{2} + \frac{z}{h}\right)^m + E_b \tag{1.4a}$$

$$\rho_{\mathrm{fg}}\left(z\right) = (\rho_t - \rho_b)\left(\frac{1}{2} + \frac{z}{h}\right)^m + \rho_b \tag{1.4b}$$

$$\vartheta_{\mathrm{fg}}\left(z\right) = (\vartheta_t - \vartheta_b)\left(\frac{1}{2} + \frac{z}{h}\right)^m + \vartheta_b \tag{1.4c}$$

where E, ρ, and ϑ are Young's modulus, density, and Poisson's ratio of each constituent material. The subscripts t and b represent the ceramic and metallic constituent materials, respectively, of the FGM.

Eqs. (1.4) illustrates that the FGM structure becomes a fully ceramic isotropic material for $m = 0$, while the structure becomes a fully metal isotropic material for the greater values of m (say 100). Further, employing the effective Young's modulus of FGM obtained from Eq. (1.4a), the variation of effective Young's modulus $(E_{fg}(z))$ for the different compositions of the FGM along with the non-dimensional thickness (z/h) is depicted in Figure 1.4.

1.3. APPLICATIONS OF THE FGM

The FGM is the perfect solution for the increasing demand for applications necessitating differing properties from the same constituent materials. Sometimes, these components require high hardness on one side versus high ductility on the other. Also, it requires wear, heat, mechanical shock, hardness with toughness, and corrosion resistance properties. Attaining these combinations of various properties in a single material without losing the constituent materials' actual properties is possible with FGM. However, it is also equally important to note that processed FGM properties depend on constituent material properties and various processing techniques to attain desired properties. Therefore, FGM with gradient properties has potential applications in aerospace, energy, automotive, machine parts, cutting tools, optoelectronics, semiconductors bio-systems, and building (Saleh et al. 2020), as shown in Figure 1.5.

Aerospace applications: FGM can withstand a high thermal gradient or extreme degradation. Hence, FGM is suitable for rocket engines, spacecraft gear structures, heat exchange plates, and structural applications such as reflectors, solar panels, camera bunks, turbine wheels, turbine blade coating, nose covers, and space shuttles.

Automobile applications: FGM with gradient properties must withstand thermal, pressure, and stresses. Hence, the components that use FGM in automotive include diesel pistons, cylinder liners, combustion chambers, racing car brakes, drive shafts, flywheels, leaf springs, and CNG storage cylinders.

Machinery and equipment applications: FGM is widely used in the manufacturing sector to improve the corrosion resistance, hardness, strength, surface wear, thermal and wear resistance of cutting tools, forming molds, machine engine blocks, grinding, milling cutters, and turning tools.

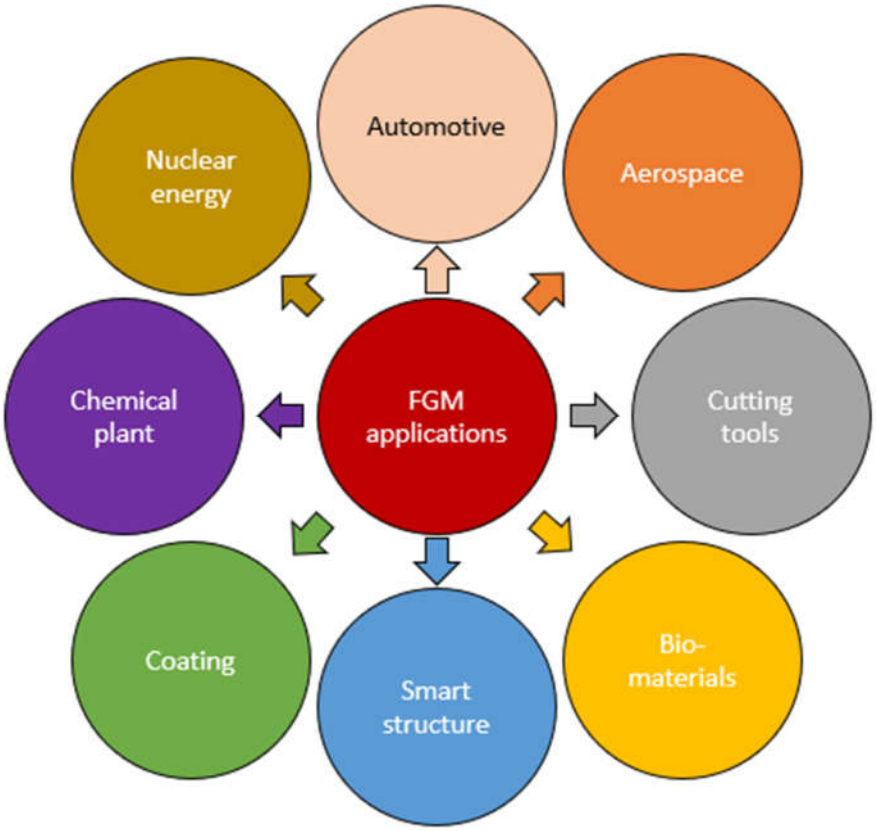

Figure 1.5: Practical applications of FGM.

Bio-medical applications: The biocompatibility of medical components whose bonding strength, corrosion, and abrasion resistance cannot be obtained through a homogeneous structure. Therefore, FGM is widely used in prosthetic devices, artificial teeth, and bone components.

Defense applications: The essential characteristics of FGM are the ability to reduce the weight of vehicles and inhibit crack propagation. This property makes it useful in defense applications as a penetration-resistant material for armor plates and bullet-proof vests. The other defense components that use FGM are the guide rods, precision rollers, shafts, tubes, latches, axle housings, and firing pins.

Energy and electronics application: The FGM with a thermal grade is used in various energy systems rather than running a single material at very high or low temperatures, as in thermal power generators, solar power components, energy conversion devices, capacitors, sensors, and electrodes. Further, FGM can also be used in batteries,

semiconductors (transistors, diodes, and optoelectronic devices), piezoelectric devices, and integrated circuits for electronics applications.

1.4. ANALYSIS OF FGM STRUCTURES

1.4.1. Nonlinear vibration and dynamic responses of the FGM structures

Mechanical systems tend to vibrate during their operations; this leads to resonant amplitudes of the system. Identifying the system's resonant amplitude and frequency is essential to avoid system failure. The nonlinear free vibration analysis of the structures provides the necessary information on the system's resonant values. Numerous investigations carried out on the nonlinear free vibration analysis of FGM plates are encapsulated in this section. The researchers have presented many computational techniques, such as the analytical approach, approximate method, semi-analytical approach, state-space approach, finite element (FE) approach etc., to evaluate the FGM structure's nonlinear frequency. Among them, the most important articles are discussed here in detail.

Praveen et al. (1998) presented the finite element formulation to study the static and dynamic thermoelastic responses of FG plates subjected to pressure and thermal loading. For the formalism of equations of motion, the first-order shear deformation theory (FSDT) was combined with von Kármán strain displacement relations. Reddy (2000) continued the same work to construct an analytical and nonlinear finite element formulation based on third-order shear deformation theory (TSDT) and the FSDT. The thermomechanical coupling, time dependence, and von Kármán nonlinearity were considered for the analysis. The gradation of properties through the thickness of the plate was based on power-law distribution. The stresses and deflection are computed for FG plates with different ceramic and metal mixture phases. It can be observed that the gradation was vital in determining the responses of the FG plates. Yang and Shen (2002) investigate the free and forced vibration of initially stressed FG plates in the thermal environment. A semi-analytical approach was developed using Reddy's TSDT and von Kármán's geometric nonlinearity. The material properties depend on the nonlinear functions of the temperature and gradation through the plate's thickness according to the power-law distribution. The FG plate was initially subjected to in-plane loads and had both immovable boundary conditions. The authors found that the

intermediate material properties of the FGM do not necessarily have the intermediate properties of the constituent materials for the dynamic response of the plate under thermal loadings.

Huang and Shen (2004) developed the analytical solution to study the nonlinear free vibration and dynamic response of FG plates under the thermal environment. The temperature-dependent material properties are graded along the thickness direction according to power-law distribution in terms of the volume fraction of the material's constituents. The authors assumed that the temperature is constant along the plate's surface. The formalism is based on the higher-order shear deformation theory (HSDT) in conjunction with von Kármán's assumptions about thermal loading. The perturbation techniques are adopted to extract the nonlinear frequencies and dynamic responses of FG plates. Besides, Huang and Shen (2006) continued the same work by applying piezoelectric actuators in thermal environments. The piezoelectric layer's material properties are assumed to be independent of thermal loadings and electric fields. A semi-analytical approach was developed along with transverse and in-plane loads in the framework of classical laminate plate theory (CLPT) with the elastic foundation to investigate the large deflection and post-buckling response of FG rectangular plates by Yanga and Shen (2003). According to the power-law distribution method, the material properties are temperature-dependent and graded along the thickness direction in terms of the constituent material's volume fractions.

The nonlinear transient response of the geometrically imperfect FG plates subjected to uniform thermal loading on the plate surfaces was investigated by Yang and Huang (2007). The authors utilized the HSDT with von Kármán sense for the analytical formulation. The geometric imperfections considered are sine, global, and local types. Yang et al. (2010) presented work on nonlinear vibration and nonlinear transient analysis of FG plates having a surface crack exited by transverse force. The material properties of the FGM were distributed exponentially across the plate's thickness. The formulation relied on TSDT, von Kármán-type assumptions, and the rotational spring model. Their results show that cracked FGM plates have lower natural frequencies, lower nonlinear to linear frequency ratios, and higher dynamic deflections than perfect FGM plates. Wang and Zu et al. (2017b) developed an analytical formulation by

considering the effects of both material and geometrical nonlinearities for the large amplitude motions. The authors investigated the FG rectangular plate's dynamic behavior moving with longitudinal velocity under thermoelastic loadings. The change in velocity of the plate has a significant effect on the resonance amplitude of the plate. Further, the authors (Wang and Zu 2017d) continued investigating the geometrically nonlinear oscillations of FG plates moving with longitudinal speed without thermal loading. The material property gradation is through the thickness direction and obeys the sigmoid law. The frequency response characteristics of FG plates with longitudinal speed were affected by the excitation amplitude, moving speed, and the in-plane pretension force.

Chen et al. (2005; 2006) derived an analytical formulation for the nonlinear equations of motion for arbitrary initial stresses on FG plates based on CLPT to investigate the linear and nonlinear frequencies. The initial stress considered for the problem is a combination of pure bending stress and extensional stress. Galerkin's approximate and Runge-Kutta methods are adopted to solve the analytical formulation. The simple power-law distribution was used to obtain effective material properties. They concluded that the nonlinear frequency parameter increases with an increase in the vibration amplitude and volume fraction grading index due to initial tensile stresses. Woo et al. (2006) presented an analytical solution to obtain nonlinear free vibration of FG plates. The governing equations were obtained using von Kármán's assumptions for large transverse deflections and mixed Fourier series analysis under thermal loading. It can be seen that the natural frequency increases with an increase in the amplitude of vibration.

Talha et al. (2011) investigated the nonlinear free vibration of FG plates by using nonlinear FE equations based on HSDT associated with Green-Lagrange's nonlinear relations considered for large deflections of the plate. The material property gradation occurs along the thickness direction, utilizing the power-law distribution. It can be observed from the results that the nonlinear frequency ratio decreases with an increase in the volume fraction grading index. In contrast, it increases with the rise in amplitude ratio. Alijani et al. (2011) presented an analytical solution for the nonlinear free vibration of FG rectangular plates coupled with thermal effects by adopting a multi-

modal energy method, pseudo-arc-length, and collocation methods. The formulation was based on the FSDT and the von Kármán assumptions. Malekzadeh et al. (2015) proposed in-plane material gradation effects and found the nonlinear vibration of FG plates for different boundary conditions by considering the differential quadrature method. The formulation was based on the classical plate theory (CPT). Green's strain tensor and von Kármán assumptions were used to model the FG plate's geometrical nonlinearity. The effective material properties were graded along with the in-plane directions of the plate. Parida et al. (2018) studied the nonlinear vibration behavior of the FG plate, which rests on an elastic foundation in the thermal environment. The mathematical formulation is based on the HSDT using the Green-Lagrange type of geometric nonlinearity. The material properties depend on the temperature and are graded along the plate's thickness direction using the power-law distribution. The direct iterative technique is adopted to extract the nonlinear frequency of the system.

1.4.2. Influence of geometrical non-uniformities on FGM structures

The literature reveals that the vibration and dynamic response analyses of the FGM porous structures focused on geometrically uniform beams and plates. However, geometrically nonuniform functionally graded structures are found to have minimal space, even though it facilitates an engineer to have various alignment opportunities in case of obstacles. The skewness and variable thicknesses in the geometry of the FG structures significantly affect the variation of the stiffness. Hence, geometrical non-uniformities considerably affect the nonlinear frequency and dynamic responses of the FG plates. Sundararajan et al. (2005) developed nonlinear FE governing equations by adopting von Kármán assumptions to examine the nonlinear free vibration characteristics of FG rectangular and skew plates under the thermal environment. The temperature distribution along the thickness direction was obtained by solving a one-dimensional steady-state heat conduction equation. The material properties were graded according to the Mori-Tanak method. A FE method coupled with the direct iterative technique was adopted to solve the nonlinear governing equation obtained from Lagrange's equations of motion. The results show that the skewness in the FG plate increases the frequency ratio compared to the rectangular plate. Prakash et al. (2008) investigated FG skew plate's post-buckling behavior in a thermal environment. The

formulation was developed based on the shear deformable FE approach. The Mori-Tanaka method was used to determine the effective material properties of the FG skew plates from the temperature-dependent material constituents. The nonlinear governing equations developed using von Kármán nonlinearity are solved by the Newton-Raphson method to examine the FG skew plate's nonlinear behavior under thermal load. The bifurcation type buckling of the FG skew plate was studied by considering the skew angles, temperature rise, volume fraction grading index, and geometrical parameters.

Upadhyay and Shukla (2013) presented nonlinear static analysis and nonlinear dynamic responses of FG skew plates. The analytical solutions were derived using the HSDT in conjunction with von Kármán's nonlinear kinematics, and equations of motion were derived using Hamilton's principle. The skewness of the FG plate was described with the skew angle to the *x*-axis. The authors concluded that the material's functionally grading has significant efficacy for cases of high or moderate skew angles (less skewed plates). Zhang et al. (2015) investigated the large deflection analyses of the FG skew plates reinforced with carbon nanotubes (CNT) resting on the Pasternal elastic foundation using an element-free IMLS-Ritz method. The formulation for the moderately thick skew plate considered for the study was developed based on the FSDT with von Kármán assumptions. Besides, Lei et al. (2015) adopted the same approach for the buckling analysis of FG skew plates reinforced with carbon nanotube composites resting on the Pasternak foundation. The effect of CNT distributions, CNT ratios, elastic foundation, and geometrical parameters under various boundary conditions was studied on the FG-CNT plates' buckling behavior. Parida et al. (2017) presented the nonlinear free vibration behavior of FG skew plates under thermal environments. The nonlinear FE model developed was based on the HSDT and Green Lagrange's geometric nonlinearity subjected to thermal loading. The material properties are temperature-dependent and vary according to the power-law distribution method. The governing equations were developed using Hamilton's principle and solved using a direct iterative technique. Tomar and Talha (2019) developed the nonlinear FE model to investigate the FG laminated skew plate's nonlinear vibration behavior under a thermal environment. The gradation occurs in the thickness direction, and material properties were considered temperature-dependent. The nonlinear FE equations were

obtained from the HSDT in conjunction with von Kármán kinematics. The governing equation was derived using the variational principle and extracted the nonlinear response using the direct iterative technique.

Xu and Zhou (2009) studied the stresses and displacement distributions of the FG plates with varying thicknesses. The material's properties were obtained according to the exponential law. The analytical formulations were developed based on the three-dimensional elasticity theory, and the Fourier series was used to solve the unknown expressions. Bouguenina et al. (2015) investigated the simply supported FG plate's buckling under thermal loading with linearly variable thickness. The numerical formulation was developed using the finite difference method in the framework of FSDT. The uniform temperature distribution is assumed to occur along the thickness direction. Sigmoid and power-law distribution methods obtain the FG plate's material properties variation. Thang et al. (2016) proposed an analytical approach to investigate the effects of the variable thickness on buckling and post-buckling behaviors of the imperfect FG plates resting on the elastic foundation. The effective material properties were governed by the sigmoid law and graded through the FG plate's thickness. The formulation was developed based on the CPT in conjunction with von Kármán nonlinearity and solved using the Galerkin method and Airy's stress function. The results show that the variable thickness considerably affects the FG plate's nonlinear behavior. Lieu et al. (2018a) presented the flexural and free vibrational analysis of the in-plane bi-directional FG plates with variable thickness. The numerical formulation was based on iso-geometric analysis in which a non-uniform rational B-spline (NURBS) surface represents the volume fraction grading index and the plate's varying thickness. Power law distribution method for symmetrical and asymmetrical models were used to characterize the inhomogeneity of in-plane material.

Minh et al. (2019) examined the FG plate's stability with an exponentially variable thickness with a central crack. A FE formulation was developed based on the TSDT, and phase-field theory was used to model the defects. The properties were assumed to vary along the thickness direction according to the simple power-law distribution method. The effects of exponential variable thickness, crack angle, length, and volume fraction index of the FG plate on critical buckling values in the plate's instability were

investigated. Chen et al. (2020) presented a mathematical model and analyzed the three-dimensional vibration behaviors of the variable thickness parallelogram plates with in-plane porous FGM. The geometrical models were established in the framework of the isogeometric approach and the three-dimensional theory. The porosities are assumed to be distributed along the in-plane direction of FG plates by considering symmetrical, non-symmetrical, and uniform distributions. Kumar et al. (2021) performed the free vibration analysis of the porous FG plates resting on an elastic foundation with variable thickness. The analytical formulation was based on the FSDT, and Hamilton's principle was used to solve the governing equation. A simple customized power, exponential, and sigmoid law were used to obtain the porous FG's material properties in the thickness direction.

1.4.3. Porosity influence on FGM structures

Plates, beams, and shells made of FG porous structures are commonly used in structural design problems. The porosity generation in the FG structures is due to the difference in solidification temperature of each constituent material and the fabrication limitations that arise during FGM manufacturing. Many authors researched the nonlinear vibration analysis and dynamic responses of FG porous structures. Wang et al. (2017c) presented the nonlinear vibration of porous FG rectangular plates moving in a thermal environment. The material properties of imperfect FG plates were formulated according to the modified power-law distribution method, incorporating the porosities along the thickness direction. The equations of motion developed were based on D'Alembert's principle with von Kármán's nonlinearity. Galerkin's approach and the harmonic balance method were used to discretize and solve differential equations. Furthermore, the authors (Wang and Zu 2017a) continued their work investigating the nonlinear vibration of the thin porous FG plates. According to the sigmoid law, the effective material properties of the plate vary continuously in the thickness direction. Besides, the authors extended their work on porous FG with piezoelectric smart materials plates. The results show that the material's electric potential, volume fraction grading index, and porosity volume index affect the porous FG plates' resonant response and resonance region. Besides, Wang et al. (2017a) presented the nonlinear vibration of porous FG rectangular plates, and the solution was obtained by adopting a

harmonic balance method. It was found that the different porosity distribution affects the vibration characteristics of the FG plates.

Gupta and Talha (2018) investigated the flexural response and nonlinear vibration of FG plates with porosities under a thermal environment. A finite element formulation was developed using HSDT with four unknowns. The temperature-dependent material properties of the porous FG plates constantly change in the thickness direction in terms of the modified rule of mixtures method. The temperature models used in the study are uniform, linear, nonlinear, exponential, and sinusoidal temperature rise. It can be observed that the effect of porosity has a significant impact on the metal and diminishes as ceramic content increases in the porous FG plates. Furthermore, the authors (Gupta and Talha 2017) continued their work on the initial geometrically imperfect FG plates. Two mathematical models, the Mori-Tanaka and Voigt models, were used to obtain the FG plate's material properties. They concluded that imperfect FG plates significantly affect the plate's nonlinear flexural and vibrational responses. Huang et al. (2019) focused on finding the nonlinear natural frequency and dynamic responses of FG porous plates with nonlinear elastic foundations. Evenly distributed and unevenly distributed porosities across the FG porous plate’s thickness were considered for the study. The material properties varied in the thickness direction according to the sigmoid distribution law. Based on the HSDT in conjunction with von Kármán nonlinearity, an analytical formulation for the equations of motion with the effects of nonlinear elastic foundations was developed.

Phung-Van et al. (2017) investigated the porous FG nanoplate's geometrically size-dependent nonlinear transient responses. The formulation was developed using the iso-geometric FE method based on the HSDT using the von Kármán assumptions and the Newmark integration technique. The gradation was through the plate's thickness, and the material properties were based on the Mori-Tanaka model and the rule of mixtures. The non-local approach to the FG nanoplates' behaviors for different volume fraction grading indexes was studied. Further, the authors (Phung-Van et al. 2019) continued the same work and demonstrated that the geometrically nonlinear transient responses are affected by various geometrical and material parameters. The results revealed that the porous FG nanoplate's porosity distributions reduce the plate's stiffness. Besides,

the authors (Phung-Van et al. 2020) extended their work to investigate the nonlinear transient responses of the porous FG plates under hygro-thermo-mechanical loadings. The TSDT with von Kármán assumptions was used to formulate the governing equations in the iso-geometric approach. The effects of moisture concentration, change in temperature, porosity volume index, and geometrical parameters on porous FG plates were studied. It was found that nonlinear transient responses are significantly affected by the porosity volume index, moisture concentration, and changes in temperature gradient and dynamic load characteristics. Xie et al. (2020) investigated the nonlinear free vibration of rectangular porous FG plates based on the energy balance approach with local concordant deformation assumption. The formulation was developed using the von Kármán assumptions and Lagrange's equations to obtain the governing equations of the FG plates. They found that the linear frequency is more sensitive to the porosity volume index than the nonlinear frequency ratio.

1.4.4. Analysis of bi / multi-directional gradation of FGM structures

Conventional FGM has been restricted to altering the material characteristics in only one direction (Boggarapu et al. 2021; Jha et al. 2013; Swaminathan and Sangeetha 2017). However, this approach may be ineffective when developing components for propulsion systems and space applications, which are frequently subjected to considerable temperature variations in various directions (Nemat-Alla 2003, 2009; Nemat-Alla et al. 2009). As a result, bi-directional FGM (BDFGM) was developed by adding another material into the traditional FGM to withstand the induced extreme thermal stresses in advanced engineering applications such as spacecraft and space shuttles. The BDFGM has inherited the advantages of the higher capability to reduce the thermal, mechanical, and residual stresses and contributes to a more flexible design than the traditional FGM by varying volume fractions of the constituent materials in two or more directions (Asemi et al. 2011; Van Do et al. 2017a; Nemat-Alla 2009; Nie and Zhong 2007; Shariyat and Alipour 2011; Sobhani Aragh and Hedayati 2012). As a result, the best understanding of the porous BDFGM structure is a critical challenge owing to the wide range of applications.

Recently, a series of investigations were performed to study the linear vibration and dynamic analysis of the BDFGM hollow cylinder and cylindrical shells in the

framework of three-dimensional elasticity equations (Asgari and Akhlaghi 2011), analytical methods (Ebrahimi and Najafizadeh 2014; Gao et al. 2019; Lü et al. 2009), finite element methods (Asgari et al. 2009), and an iso-geometric approach (Chen et al. 2020). Besides, a third-order shear deformation theory (TSDT) was used to analyze the buckling behavior of BDFGM thick cylindrical shells strengthened by axial stiffeners (Satouri et al. 2015). In addition, the meshfree radial point interpolation method (RPIM) was employed to extract the natural frequency of BDFGM thick cylindrical shells (Pilafkan et al. 2013).

Furthermore, several investigations were carried out to analyze the BDFGM plate structures in the framework of three-dimensional elasticity equations, analytical methods, finite element methods, and an iso-geometric approach, along with several shear deformation theories (Adineh and Kadkhodayan 2017; Alinaghizadeh and Shariati 2016; Do et al. 2020; Van Do et al. 2017a; Ghatage et al. 2020; Lü et al. 2009; Tang et al. 2019; Truong et al. 2019). Many studies on BDFGM plates have been carried out to examine the flexural (Adineh and Kadkhodayan 2017; Behravan Rad 2018; Esmaeilzadeh and Kadkhodayan 2019; Nemat-Alla 2009; Nemat-Alla et al. 2009; Nie and Zhong 2007; Rad and Shariyat 2013; Shariyat and Mohammadjani 2014; Zafarmand and Kadkhodayan 2015), vibrational (Alipour et al. 2010; Chen et al. 2021; Hong 2020; Katiyar and Gupta 2021; Kermani et al. 2012; Lieu et al. 2018b; Nie and Zhong 2010; Ramteke and Panda 2021), and stability (Ahlawat and Lal 2016; Van Do et al. 2017b; Lal and Ahlawat 2017; Rad and Shariyat 2013) behavior.

Additionally, investigations on BDFGM Euler Bernoulli/Timoshenko, along with nanobeams, have been carried out to examine the vibration behavior (Barati et al. 2020; Karamanlı 2018; Nejad and Hadi 2016; Nguyen et al. 2017; Tang and Ding 2019), nonlinear bending (Li et al. 2018), and buckling analysis (Nejad et al. 2016; Şimşek 2016). Besides, Lezgy- Nazargah (2015) employed the NURBS-dependent iso-geometric FE approach to examine the thermo-mechanical behavior of BDFGM beams. Furthermore several investigations into the bi-directional FG plates have been carried out to study the free vibrations and bending analysis based on the FE and iso-geometric approaches (Van Do et al. 2017a; Lieu et al. 2018a, 2019). The authors reported that extracting results for bi-directional FG plates is more complicated than for

unidirectional FG plates due to the gradation in two different directions. Besides, Allahkarami et al. (2020b; a) studied the dynamic buckling of bi-directional FG porous cylindrical and truncated conical shells. They concluded that porosity distributions could significantly affect the dynamic instability region in the FG structures.

1.4.5. Analysis of FG saturated porous material structures

Fabricating the perfect FGM without the entrapment of fluids in the pores is inevitable using modern-day manufacturing techniques. Hence, more research has been attributed to designing and analyzing the FG saturated porous material (FGSPM). Furthermore, Biot (DETOURNAY and CHENG 1993) was the first to develop the idea of saturated porosities in solid materials.

However, most researchers overlooked the fluid phase's effect and concentrated on the impact of porosity and porosity distributions on the mechanical properties of FG porous structures under drained conditions. Recently, Soleimani-Javid et al. (2021) investigated the vibrational behavior of saturated porous cylindrical micro-shells made of FGM coupled with nano-composite coverings in a viscoelastic medium. Based on classical plate theory, Arshid and Khorshidvand (2018) investigated free vibration response analysis utilizing a differential quadrature approach for the saturated FG porous circular plate. Arshid et al. (2021) studied the vibrational analysis of sandwich curved microbeams mounted on an elastic base in a high-temperature environment. In addition, Arshid et al. (2019) studied the FG saturated porous circular plates relying on the visco-Pasternak elastic foundation for various shear deformations. In the modified coupled stress theory paradigm, Amir et al. (2019) investigated the free vibration behavior of a saturated FG circular sandwich plate exposed to multi-physical stresses. Panah et al. (2019) numerically investigated a saturated porous FG circular plate's post-buckling and nonlinear bending behavior under a thermal environment. Feyzi and Khorshidvand (2017) examined the axisymmetric post-buckling response of a saturated porous FG circular plate under uniform radial compressive force. The results were compared to those obtained using CPT and solved by the shooting method on a homogeneous isotropic plate. Jabbari et al. (2014b; a; 2016) examined the mechanical buckling of a saturated porous FG circular plate. They derived the closed-form solution of critical buckling loads using the CPT and HSDT. Babaei et al. (2021; 2020) used the

two-dimensional axisymmetric elasticity theory to analyze the static and dynamic behavior of the FG saturated porous rotating truncated cone.

Additionally, the authors extended the work on the annular and elliptical sector saturated plates in the framework of 3D elasticity theory (Babaei et al. 2020c; a). The free vibration behavior of the cylindrical sandwich panel with FG saturated porous core was studied by Akbari et al. (2020). The formulation was based on linear Biot's theory in conjunction with the HSDT. The large amplitude deflection analysis of the FG saturated porous plate exposed to the transverse load was explored by Alhaifi et al. (2021). Ebrahimi and Habib (2016) investigated the natural frequencies and lateral deflections of rectangular plates with transverse variances in porosity with saturated fluid in pores. From the literature mentioned above, it can be accomplished that the fluid-saturated pores significantly affect the linear and geometrically nonlinear behavior of the FGSPM structures.

1.4.6. Analysis of vibration and flutter characteristics of supersonic FGM structures

Flutter is a type of dynamic instability that occurs while aircraft are in flight. It is a self-excited oscillation of the outer skin of an aircraft when subjected to supersonic airflow along its surface (Ibrahim et al. 2007a; Marzocca et al. 2011). The concept of flutter analysis of thin structures was first developed by Dowell (1966, 1970). Therefore, thin plates made of FGM are a common structural component due to their enhanced strength when subjected to thermal loads owing to aerodynamic or solar radiation heating.

In recent decades, various authors have investigated the flutter characteristics of the supersonic FG structures. An application of analytical and numerical methods such as the Rayleigh-Ritz method, Galerkin method, differential quadrature method, and FE method has been used to obtain the solutions for the flutter behavior of the FG structures at high speeds (Grover et al. 2016; Ibrahim et al. 2009; Li and Song 2014; Marques et al. 2017; Navazi and Haddadpour 2011; Prakash and Ganapathi 2006; Torabi and Afshari 2019; Yazdi 2019; Zhou et al. 2018). Moreover, numerous researchers have investigated the temperature effects on the analysis of flutter behavior of the FG

structures, where thermal effects have significant influences on the static and dynamic behavior of the flights in cruise at supersonic and hypersonic regimes (Barati and Shahverdi 2017; Chen et al. 2020; Ibrahim et al. 2009; Khorshidi and Karimi 2019; Navazi and Haddadpour 2007; Prakash and Ganapathi 2006; Sohn and Kim 2009, 2008; Su et al. 2019). Hence, aero-thermo-elastic analysis of FG structures for various geometrical non-uniformities has been investigated by various authors. Further, the nonlinear flutter behavior of the supersonic and hypersonic FG panels has been investigated by several authors (Farsadi et al. 2021; Ibrahim et al. 2007b, 2008; Navazi and Haddadpour 2011; Prakash et al. 2012; Sohn and Kim 2009; Yu et al. 2016). The results reveal that the aerodynamic pressure depends on the large amplitude deflections of FG structures, and piston theory is the most commonly applied methodology for analyzing the flutter characteristics. Besides, the authors concluded that the structure is more stable for higher critical aerodynamic pressure. Additionally, a few researchers have investigated the FG porous structures' linear vibration and flutter behavior at higher speeds with yawed angles (Bahaadini et al. 2019; Barati and Shahverdi 2017; Khalafi and Fazilati 2022; Muc and Flis 2021; Zhou et al. 2018). The authors revealed that the porosity distributions significantly affect the flutter bounds of the FG porous structures.

1.5. SCOPE AND OBJECTIVE OF THE DISSERTATION

The exhaustive literature review emphasizes the growing attention of researchers and the significance of geometrical nonlinearities in designing and analyzing FGM structures. Besides, the literature concerning the porosities in the FGM structures suggests that porosity distributions and their volume significantly affect the plate's structural behavior. Further, the literature in section 1.4.2 suggests that the different geometrical non-uniformities substantially influence the FG's structural behavior. Hence, several approaches, including analytical, semi-analytical, state-space, and FE models, are used to examine the structural behavior of FG plates. However, FE modeling is widely recognized for its simplicity, versatility, and efficacy. Consequently, FE modeling is appropriate for investigating FGM structures.

The evaluation of the structural behavior of FGM plates through nonlinear free vibration and dynamic analysis has been extensively investigated. The literature on the

nonlinear analysis of the geometrically non-uniform FG plate with and without being subjected to thermal loads is limited. However, the open literature contains a few investigations on FG plates with geometrical non-uniformities, although the most prevalent uses of FG structures are in these hostile environments. Further, during the manufacturing of FGM plates, a generation of porosities cannot be avoided due to the limitations of fabricating techniques. It is difficult to completely infiltrate the first and second constituent materials into the middle of the FG plate without leaving any pores. However, the materials can be easily infiltrated with fewer porosities at the top and bottom portions of the plate. In addition, porosities may generate due to the difference in the solidification temperature of each constituent material (Wattanasakulpong et al. 2012; Zhu et al. 2001). Consequently, the existence of porosities can weaken the strength of FGM. Therefore, it is essential to investigate the effect of porosities on the nonlinear vibration characteristics of FGM plates with geometrical non-uniformities.

A literature review reveals that traditional FGM can only alter material characteristics in a single direction. However, this paradigm may be ineffective when developing components for advanced engineering applications, which are frequently subjected to considerable temperature changes in several directions (Nemat-Alla 2003, 2009; Nemat-Alla et al. 2009). Hence, there is enormous scope for studying bi/Multi-directional FGM structures by adding another material into the traditional FGM to withstand the induced extreme thermal stresses that occur in multiple directions. The influence of the porosity distributions on the FG structures with different materials is primarily unknown and offers numerous opportunities for future research. This motivated the present research to explore the nonlinear analysis of the multi-directional FG porous structures (plates and shells).

The literature shows that it is unavoidable to produce flawless FGM devoid of fluid trapped in the pores. Consequently, increasing research has been devoted to designing and analyzing FGSPM. However, most research ignored the effect of the fluid phase, and researchers focused on the influence of porosity and porosity distributions on the analysis of the FG porous structures under drained conditions. However, the quantum of research related to the nonlinear analysis of FGSPM structures using the finite element method is scarce. Further, dynamic instability such as flutter occurs while the

aircraft is on a supersonic cruise. It oscillates an aircraft's outer skin when subjected to supersonic airflow along its surface.

Further, thin FG plates are a common structural component of aircraft and spacecraft due to their enhanced strength when subjected to thermal loads. Consequently, it is an important and challenging issue to consider the influence of saturated porosity distributions on the nonlinear analysis of FG plates under thermal loads for accurate design. This acts as a driving force to develop an FE formulation and evaluate the influence of fluid saturated porosities on the nonlinear analysis of FGSPM plates.

The prominent aim of this dissertation is to develop a nonlinear FE formulation to investigate the influence of porosity distributions on the nonlinear behavior of FG plates and shells under different geometrical non-uniformities and thermal loads. Further, the evaluation is expanded to analyze two-directional FG plates and shells with porosities. In addition, the effect of saturated fluids on the nonlinear vibration analysis of the FG saturated porous plates with different external loads, such as thermal and aerodynamic loads, needs to be analyzed. In this regard, the following analyses have been carried out:

- To develop a finite element formulation based on shear deformation theory for functionally graded porous plates and shells.
- To investigate the influence of porosity distributions on the nonlinear behavior of functionally graded porous plates with geometrical non-uniformities.
- To analyze the effects of nonlinear temperature variation on the nonlinear vibration and dynamic behavior of functionally graded porous skew plates.
- To evaluate the influence of porosity and its distributions on the nonlinear analysis of two-directional FG porous plates and shells.
- To study the effects of fluid saturated porosities on the nonlinear behavior of functionally graded saturated porous plates.
- To perform the flutter characteristics of fluid saturated porosities on the nonlinear behavior of functionally graded saturated porous plates subjected to thermal loads.

1.6. CONTRIBUTIONS FROM THE DISSERTATION

The following contributions have been made in the area of FG porous structures towards the preparation of the dissertation:

- The nonlinear FE model is developed successfully based on the shear deformation theory in conjunction with von Kármán's strain-displacement relations to study the nonlinear vibration, dynamic, and flutter behavior of porous functionally graded plates and shells.
- A detailed geometrically nonlinear analysis of FG porous plates is presented by considering the different porosity distributions and geometrical non-uniformities.
- A special emphasis has been placed on investigating the influence of temperature distribution across the thickness on the nonlinear behavior of the FG porous skew plates for various porosity distributions.
- The influence of two-directional gradation in FG porous plates and shells comprised of four distinct materials and different porosity distributions is studied.
- The influence of saturated porosities and their distributions on the nonlinear analysis of the FG saturated porous plates is investigated.
- Special attention has been paid to investigating the effect of saturated porosities on the nonlinear vibration and flutter behavior of supersonic FG saturated porous plates subjected to thermal loads.

1.7. OVERVIEW OF THE DISSERTATION BY CHAPTER

The present dissertation investigates the influence of porosity distributions on nonlinear free vibration and dynamic responses of the FG porous plates and shells using nonlinear FE formulation. The effects of temperature, geometrical non-uniformities, two-directional gradation with four different materials, saturated porosities, and aerodynamic loading are thoroughly studied. In this regard, the total potential energy principle and thermo-poro-elastic constitutive equations of FG porous material have been used to derive the governing equations of motion. An emphasis has been placed on evaluating the effects of different porosity distributions, porosity volume index,

volume fraction grading index, thermal loads, skew angle, variable thickness, aerodynamic loading, Skempton coefficient, and geometrical parameters (thickness ratio, aspect ratio, boundary conditions), etc.

This thesis comprises nine chapters. The first chapter presents a brief introduction and a comprehensive literature review on FG porous structures, bi-directional FG structures, FG saturated porous structures with geometrical non-uniformities, and temperature. Subsequently, the scope and objectives of the current research are stated based on the research gaps discovered during the literature review.

In chapter 2, a detailed nonlinear FE formulation based on the FSDT and von Kármán's geometric nonlinearity is presented to study the nonlinear responses of the FG porous skew plates. The position-dependent functional variation of effective material properties is determined using modified power-law series. The influence of the various porosity distributions, porosity volume index, volume fraction grading index, skew angle, thickness ratio, and aspect ratio on the nonlinear free vibration and transient responses of the FG porous skew plate is investigated.

Chapter 3 is concerned with evaluating the influence of porosity distributions on the nonlinear free vibration analysis of the FG porous plates with different geometrical non-uniformities. The different geometrical non-uniformities considered for the analysis are skewness and variable thickness, such as linearly, bi-linearly, and exponentially. This chapter extends the nonlinear FE formulation for FG porous plates analogous to the FG porous skew plates discussed in Chapter 2. The influence of porosity volume index, volume fraction grading index, taper ratio, skew angle, boundary conditions, thickness, and aspect ratio have also been evaluated.

The effect of temperature distribution across the thickness on the nonlinear responses of the FG porous skew plate for different porosity distributions has been discussed in Chapter 4. The nonlinear FE formulation derived in Chapter 2 is extended to include the effect of thermal loading. The temperature-dependent elastic coefficients are considered for the analysis. The influence of geometrical non-uniformity such as skew angle, porosity volume index, volume fraction grading index, thermal loads, aspect and thickness ratio on the structural behavior of the FG porous skew plate is assessed.

The influence of two-directional gradation of the FG porous shells with four different materials on the nonlinear free vibration and central deflection has been discussed in Chapter 5. The plate's volume fraction gradation profiles are considered in thickness and longitudinal directions. The nonlinear FE formulation derived in Chapter 2 has been extended to present the nonlinear central deflection and consider the influence of two-directional gradation with porosities. The effect of volume fraction grading profiles in different directions, porosity distributions, and porosity volume index for various geometrical parameters and shell geometries has been evaluated in detail.

Chapter 6 encapsulates the comprehensive investigation of the influence of two-directional gradation of the FG porous plates with four different materials on the nonlinear free vibration and central and transient deflection. The formulation derived in Chapter 5 has also been extended to FG porous plates. The effects of volume fraction grading profiles in different directions, porosity distributions, and porosity volume index for various geometrical parameters have been evaluated in detail.

In Chapter 7, the predominant influence of the pore fluid pressure on the nonlinear vibration and dynamic responses of the supersonic FGSPM plates has been assessed. The formulation of nonlinear FE obtained in Chapter 2 is expanded to include the saturated-fluid effects in the constitutive equations. The influence of the various saturated porosity distributions, Skempton coefficient, porosity volume index, volume fraction grading index, thickness ratio, and aspect ratio on the nonlinear free vibration and dynamic responses of the supersonic FGSPM plate is investigated.

The influence of fluid-saturated pores on the nonlinear vibration and flutter bounds of the supersonic FGSPM plate under thermal load has been encapsulated in Chapter 8. The formulation of nonlinear FE from Chapter 7 is enriched to include the effects of temperature and aerodynamic loading. The influence of the various saturated porosity distributions, aerodynamic loading, Skempton coefficient, porosity volume index, volume fraction grading index, thickness ratio, and aspect ratio on the nonlinear free vibration and flutter bounds of the supersonic FGSPM plate is evaluated.

The dissertation's significant findings are finally summarised in Chapter 9. Future possible work to enhance the applicability of FG porous structures has also been described. The appendix and reference list appear after the dissertation.

CHAPTER 2

INFLUENCE OF POROSITY DISTRIBUTION ON NONLINEAR FREE VIBRATION AND TRANSIENT RESPONSES OF POROUS FUNCTIONALLY GRADED SKEW PLATES

This chapter investigates the effects of porosity distributions on the nonlinear free vibration and transient responses of porous functionally graded skew (PFGS) plates. The effective material properties of the PFGS plate are obtained from the modified power-law series in which gradation varies through the thickness of the PFGS plate. A nonlinear FE formulation for the overall PFGS plate is derived by adopting FSDT in conjunction with von Karman's nonlinear strain displacement relations and the principle of virtual work. The direct iterative method and Newmark's integration technique are espoused to solve nonlinear mathematical relations. Influences of the porosity distributions and porosity volume indices on the nonlinear frequency responses of the PFGS plate are studied for various geometrical parameters with plate skewness. The effects of volume fraction grading index and skew angle on the plate's nonlinear dynamic behavior for various porosity distributions are illustrated in detail. The results indicate that the nonlinear frequency ratio is less sensitive to the increase in porosity volume index. The porosities in the gradation region and an increase in the plate's skewness significantly impact the nonlinear frequencies. In contrast, central deflections are more susceptible to evenly distributed porosity.

2.1. INTRODUCTION

FG plate is the amalgamation of two constituent materials with a gradation of material properties that varies from ceramic phase to metallic phase smoothly and continuously in a thickness direction. For a plate, if the gradation is through the thickness, the top and bottom surfaces have isotropic constituents of ceramic and metal

materials, respectively. The portion between the top and bottom surfaces has a varying composition of two constituent materials. Further, geometrical non-uniformities in the FG plates are significant in many engineering applications, as geometric modifications to a rectangular plate with uniform thickness affect the response properties. Despite tremendous developments in manufacturing techniques, the generation of porosities during the fabrication of FG plates cannot be avoided due to the limitations of fabricating techniques. Consequently, the existence of porosities can weaken the strength of FGMs.

In this chapter, a nonlinear FE model based on the FSDT and concatenated with von Karman's assumptions to assess the nonlinear free vibration and transient responses of the PFGS plate is developed. The governing equations are derived using the principle of virtual work, and the nonlinear natural frequency of the PFGS plate is computed by using a direct iterative technique. Newmark's integration technique is employed to extract the dimensionless nonlinear transient results. The PFGS plate's effective material properties are derived from the modified power-law distribution in which gradation varies through the thickness of the plate in terms of the volume fraction of the material constituents. The predominant effects of porosity distributions and skewness on the PFGS plate on the large amplitude free vibration and nonlinear transient responses are thoroughly investigated.

2.2. PROBLEM DESCRIPTION AND GOVERNING EQUATION

2.2.1. Materials and Methods

The dimensional parameters of the PFGS plate are length *a*, width *b*, and thickness *h,* as shown in Figure 2.1. The plate's skewness is considered by rotating the *y*-axis at an angle Φ called the skew angle. The PFGS plate comprises two isotropic and homogeneous materials; metal and ceramic. The volume fractions of the material constituents of the PFGS plate change continuously in the thickness direction. i.e., *z*-axis. The top surface of the PFGS plate is ceramic $(z = h/2)$, and the bottom surface is metal $(z = -h/2)$, as depicted in Figure 2.1.

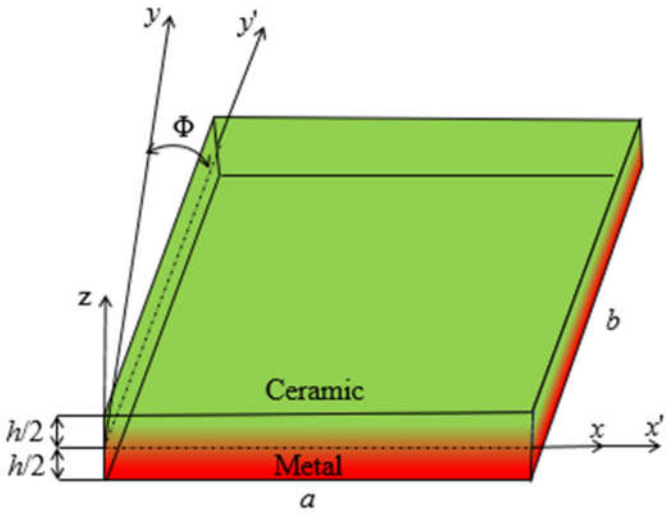

Figure 2.1: The geometry of the PFGS plate.

The effective material properties of the PFGS plate $(\mathrm{P}_{\mathrm{fg}}(z))$ are Young's modulus $(E_{fg}(z))$, the density $(\rho_{fg}(z))$, and the Poisson's ratio $(\vartheta_{fg}(z))$ at any point in the plate are determined by employing the modified power-law distribution method (Srividhya et al. 2018) by using Eq. (2.1).

$$\mathrm{P}_{\mathrm{fg}}(z) = P_t\left(V_c - \frac{e_p}{2}\right) + P_b\left(V_m - \frac{e_p}{2}\right) \tag{2.1}$$

where $\mathrm{P_{fg}(z)}$ is the effective material properties of the PFGS plate along the thickness direction. P_t and P_b are the ceramic and metal constituent material properties, respectively. V_c and V_m indicate volume fractions of the ceramic and metal, respectively. The ceramic material's volume fractions in the plate's thickness direction are represented identically to Eq. (1.1). e_p ($e_p << 1$) is the porosity volume index and $e_p = 0$ for a perfect (without porosity) FG skew plate. The sum of the volume fractions of ceramic and metal is always unity and forms the equations as follows:

$$V_c + V_m = 1 \tag{2.2}$$

From Eqs. (1.1), (2.1), and (2.2), the generalized effective material properties of the PFGS plate (Kiran et al. 2018) can be written as

$$\mathrm{P}_{\mathrm{fg}}(z) = (P_t - P_b)V_c + P_b - \left(\frac{e_p}{2}\right)(P_t + P_b)P_d \tag{2.3}$$

where P_d is the generalized representation of types of porosity distributions (P_e, P_c, & P_{tb}). The schematic representation of the imperfect plate with different porosity distributions is shown in Figure 2.2.

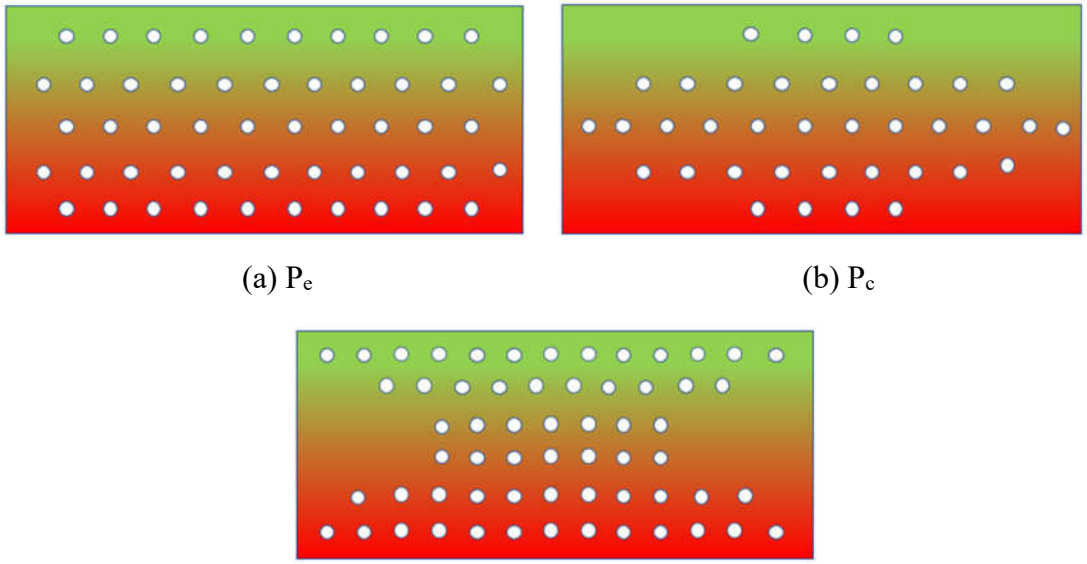

(a) P_e (b) P_c

(c) P_{tb}

Figure 2.2: Porosity distribution in PFGS plate (a) P_e (b) P_c, and (c) P_{tb}.

The different types of porosity distributions considered for the present analysis of the PFGS plate are given as follows:

a) *Evenly distributed porosity (EDP)* (P_e): The porosities are distributed evenly across the PFGS plate thickness, as shown in Figure 2.2(a). Further, the effective material properties incorporating the evenly distributed porosities are obtained by putting the value $P_d = 1$ in Eq. (2.3), and the modified equation becomes as follows:

$$P_{fg}(z) = (P_t - P_b)V_c + P_b - \left(\frac{e_p}{2}\right)(P_t + P_b) \tag{2.4}$$

b) *Centrally distributed porosity (CDP)* (P_c): The high density of porosities is distributed at the middle portion of the PFGS plate, as shown in Figure 2.2(b). The effective material properties for the centrally distributed porosities can be expressed as follows:

substituting $P_d = \left(1 - \frac{2|z|}{h}\right)$ in Eq. (2.3), as follows:

$$\mathrm{P}_{\mathrm{fg}}\left(z\right)=\left(P_t-P_b\right)V_c+P_b-\left(\frac{e_p}{2}\right)\left(P_t+P_b\right)\left(1-\frac{2|z|}{h}\right) \tag{2.5}$$

c) *High porosity distribution near the top and bottom surface while narrow at the middle* (P_{tb}): In this case, the high density of porosities is distributed nearer to the top and bottom surfaces while the low density of porosity distribution at the middle span of the PFGS plate as shown in Figure 2.2(c). The effective material properties for this type of porosity distribution, i.e., high porosity distribution closer to the top and the bottom surface while shallow at the middle span of the PFGS plate. The modified equation can be obtained as follows:

substituting $P_d=\left(\frac{2|z|}{h}\right)$ in Eq. (2.3), as follows:

$$\mathrm{P}_{\mathrm{fg}}\left(z\right)=\left(P_t-P_b\right)V_c+P_b-\left(\frac{e_p}{2}\right)\left(P_t+P_b\right)\left(\frac{2|z|}{h}\right) \tag{2.6}$$

The plate is assumed to have no pores in the ideal FG skew (FGS) plate. As a result, the weight and stiffness of the FGS plate remain constant. In the evenly distributed porosity (P_e), all the pores are presumed to be uniformly distributed across the PFGS plate thickness. Hence, the plate's weight and stiffness reduce abruptly, as shown in Figure 2.2 (a). Besides, in centrally distributed porosity (P_c), all the pores are assumed to be unevenly proportionally distributed across the plate's thickness. Therefore, the weight and stiffness reduce steadily, as shown in Figure 2.2 (b). Further, a reversed trend of P_c is followed for the case of P_{tb} type of porosity distributions, as shown in Figure 2.3 (c).

Additionally, the variation of Young's modulus as a function of different porosity distributions and VFGI of Si_3N_4 / SUS304 functionally graded porous (FGP) plates is shown in Figure 2.3. For the evenly distributed porosity (P_e) case, the variation profile of Young's modulus of P_e is the same as the ideal FG plate, but a decrease in amplitude can be observed. For the centrally distributed porosity (P_c) case, the amplitude matches the ideal FG plate at the top and bottom surfaces; meanwhile, it matches the P_e at the middle surface. It is because the porosity distribution is concentrated in the middle region and tends to zero at the top and bottom surfaces. In contrast, for the P_{tb} case, the amplitude matches with the ideal FG plate at the middle portion of the plate; meanwhile,

it matches with the P_e at the top and middle surface of the FGP plate. This is because the porosity distribution is concentrated at the top and bottom portion of the FGP plate and tends to zero at the middle surface.

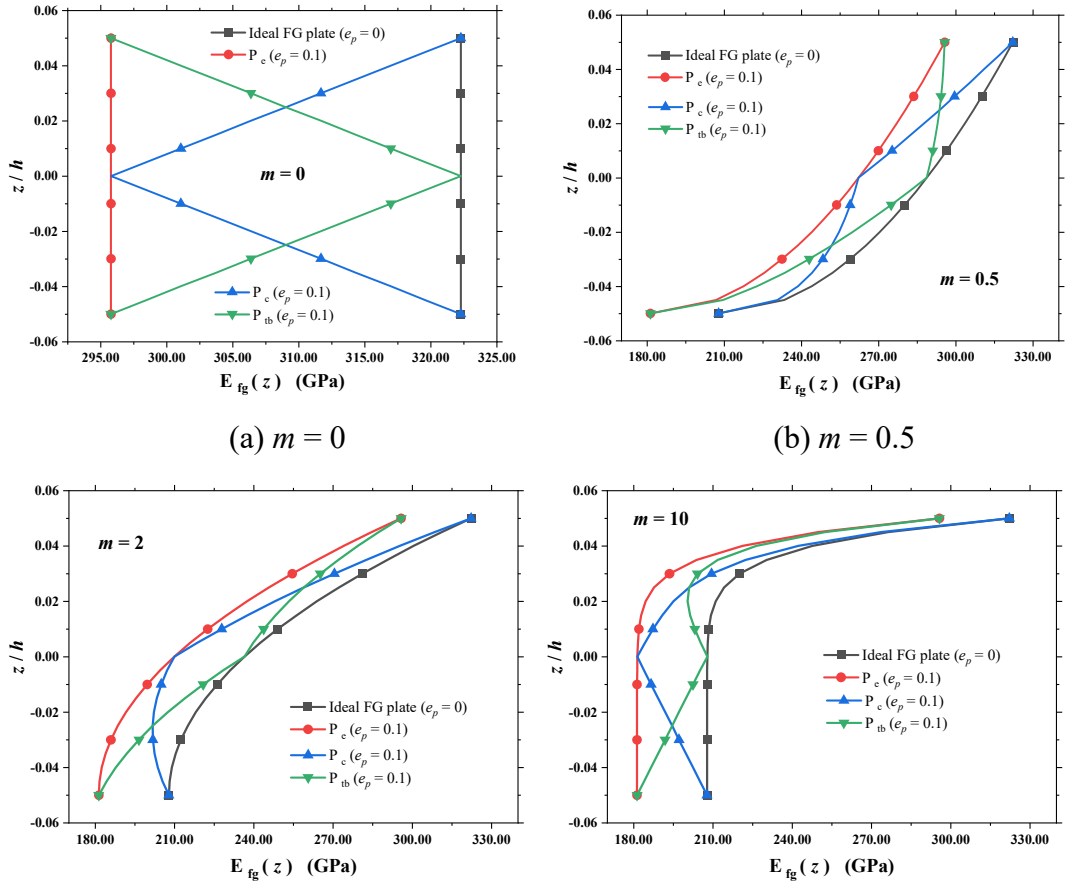

(a) $m = 0$ (b) $m = 0.5$

(c) $m = 2$ (d) $m = 10$

Figure 2.3: Variation of effective Young's modulus of FGP plate made of Si_3N_4 / SUS304 for different porosity distributions and VFGI (m).

2.2.2. Kinematics of deformations

The PFGS plate deformation's kinematics is based on the FSDT (Alimirzaei et al. 2019; Praveen and Reddy 1998; Tran et al. 2020). Accordingly, the displacements u_0, v_0, and w_0 at any point in the overall plate along x, y, and z-coordinate directions, respectively, are given by

$$u_0(x,y) = u_1(x,y) + z\,\theta_x(x,y)$$

$$v_0(x,y) = v_1(x,y) + z\,\theta_y(x,y)$$

$$w_0(x,y) = w_1(x,y) \tag{2.7}$$

where (u_1, v_1, and w_1) are the generalized displacements at a reference point (x, y) lying on the midplane (z = 0) of the PFGS plate in the direction of x, y, and z, respectively. θ_x and θ_y are the corresponding generalized rotations of a normal to the reference point at the reference plane about the y-axis and x-axis, respectively. For the simplicity of analysis, the generalized displacements are separated into variables of translational $\{d_t\}$ and rotational $\{d_r\}$ as follows:

$$\{d_t\} = [u_1\ v_1\ w_1]^T;\ \{d_r\} = [\theta_x\ \theta_y]^T \tag{2.8}$$

The state of strain at any given point in the overall PFGS plate can be expressed by the following strain vectors $\{\varepsilon_b\}$ and $\{\varepsilon_s\}$, where the $\{\varepsilon_b\}$ contains the in-plane and transverse normal strains and $\{\varepsilon_s\}$ contains the transverse shear strains.

$$\{\varepsilon_b\} = \{\varepsilon_{xx}\ \varepsilon_{yy}\ \gamma_{xy}\}^T;\ \{\varepsilon_s\} = \{\gamma_{xz}\ \gamma_{yz}\}^T \tag{2.9}$$

Employing von Karman's nonlinear strain-displacement relations, the geometric nonlinearity of the plate is presented for the strain-displacement relations in terms of middle plane deformations as,

$$\varepsilon_{xx} = \frac{\partial u_0}{\partial x} + \frac{1}{2}\left(\frac{\partial w_0}{\partial x}\right)^2;\ \varepsilon_{yy} = \frac{\partial v_0}{\partial y} + \frac{1}{2}\left(\frac{\partial w_0}{\partial y}\right)^2;\ \gamma_{xy} = \frac{\partial u_0}{\partial y} + \frac{\partial v_0}{\partial x} + \frac{\partial w_0}{\partial x}\frac{\partial w_0}{\partial y}$$

$$\gamma_{xz} = \frac{\partial u_0}{\partial z} + \frac{\partial w_0}{\partial x};\ \gamma_{yz} = \frac{\partial v_0}{\partial z} + \frac{\partial w_0}{\partial y} \tag{2.10}$$

Eq. (2.10) can be written as $\varepsilon = \varepsilon_L + \varepsilon_{NL}$ (2.11)

where the terms ε_L and ε_{NL} are the linear and nonlinear strains, respectively.

substituting Eq. (2.7) into Eq. (2.10) gives

$$\varepsilon_{xx} = \frac{\partial u_1}{\partial x} + z\frac{\partial \theta_x}{\partial x} + \frac{1}{2}\left(\frac{\partial w_1}{\partial x}\right)^2;\ \varepsilon_{yy} = \frac{\partial v_1}{\partial y} + z\frac{\partial \theta_y}{\partial y} + \frac{1}{2}\left(\frac{\partial w_1}{\partial y}\right)^2$$

$$\gamma_{xy} = \frac{\partial u_1}{\partial y} + \frac{\partial v_1}{\partial x} + z\left(\frac{\partial \theta_x}{\partial y} + \frac{\partial \theta_y}{\partial x}\right) + \frac{\partial w_1}{\partial x}\frac{\partial w_1}{\partial y};$$

$$\gamma_{xz} = \theta_x + \frac{\partial w_1}{\partial x};\ \gamma_{yz} = \theta_y + \frac{\partial w_1}{\partial y} \tag{2.12}$$

The in-plane strain vectors and the transverse shear strain vectors at any point in the plate can be expressed as

$$\{\varepsilon_b\} = \{\varepsilon_{tb}\} + z\{\varepsilon_{rb}\} + \{\varepsilon_{tbNL}\} \; ; \; \{\varepsilon_s\} = \{\varepsilon_{ts}\} + \{\varepsilon_{rs}\} \tag{2.13}$$

where the generalized strain vectors $\{\varepsilon_{tb}\}$, $\{\varepsilon_{rb}\}$, $\{\varepsilon_{tbNL}\}$, $\{\varepsilon_{ts}\}$ and $\{\varepsilon_{rs}\}$ appeared in Eq. (2.13) are given by

$$\{\varepsilon_{tb}\} = \left[\frac{\partial u_1}{\partial x} \;\; \frac{\partial v_1}{\partial y} \;\; \frac{\partial u_1}{\partial y} + \frac{\partial v_1}{\partial x}\right]^T ; \; \{\varepsilon_{tbNL}\} = \left[\frac{1}{2}\left(\frac{\partial w_1}{\partial x}\right)^2 \;\; \frac{1}{2}\left(\frac{\partial w_1}{\partial y}\right)^2 \;\; \frac{\partial w_1}{\partial x}\frac{\partial w_1}{\partial y}\right]^T$$

$$\{\varepsilon_{rb}\} = \left[\frac{\partial \theta_x}{\partial x} \;\; \frac{\partial \theta_y}{\partial y} \;\; \frac{\partial \theta_x}{\partial y} + \frac{\partial \theta_y}{\partial x}\right]^T ; \; \{\varepsilon_{ts}\} = \left[\frac{\partial w_1}{\partial x} \;\; \frac{\partial w_1}{\partial y}\right]^T ; \; \{\varepsilon_{rs}\} = \left[\theta_x \;\; \theta_y\right]^T \tag{2.14}$$

The state of stress and the corresponding state of strain at any point in the overall PFGS plate are described by

$$\{\sigma_b\} = \left[Q_b(z)\right]\{\varepsilon_b\} \; ; \; \{\sigma_s\} = \left[Q_s(z)\right]\{\varepsilon_s\} \tag{2.15}$$

where, $\{\sigma_b\} = \{\sigma_{xx} \;\; \sigma_{yy} \;\; \tau_{xy}\}^T \; ; \; \{\sigma_s\} = \{\tau_{xz} \;\; \tau_{yz}\}^T$ (2.16)

The terms appearing in Eq. (2.16) σ_{xx} and σ_{yy} are the normal stresses in the direction of the *x*-axis and *y*-axis, respectively. τ_{xy} is the in-plane shear stress, τ_{xz} and τ_{yz} are the transverse shear stresses. *T* indicates transpose, $\left[Q_b(z)\right]$ and $\left[Q_s(z)\right]$ are the elastic coefficient matrices and are the function of z- coordinate.

$$\left[Q_b(z)\right] = \begin{bmatrix} Q_{11} & Q_{12} & 0 \\ Q_{12} & Q_{22} & 0 \\ 0 & 0 & Q_{66} \end{bmatrix} ; \; \left[Q_s(z)\right] = k_s \begin{bmatrix} Q_{55} & 0 \\ 0 & Q_{44} \end{bmatrix} \tag{2.17}$$

where k_s is the shear correction coefficient. The value of the shear correction coefficient is considered as $\pi^2/12$. The elastic constants appearing in Eq. (2.17) can be expressed as

$$Q_{11} = Q_{22} = \frac{E_{fg}(Z)}{1-\left(\vartheta_{fg}(Z)\right)^2} \; ; \; Q_{12} = Q_{21} = \frac{\vartheta_{fg}(Z)E_{fg}(Z)}{1-\left(\vartheta_{fg}(Z)\right)^2}$$

$$Q_{44} = Q_{55} = Q_{66} = \frac{E_{fg}(Z)}{2\left(1+\vartheta_{fg}(Z)\right)} \tag{2.18}$$

The in-plane stress resultants, moment resultants, and transverse force resultants acting on the plate can be expressed as

$$N = \begin{Bmatrix} N_{xx} \\ N_{yy} \\ N_{xy} \end{Bmatrix} = \int_{-h/2}^{h/2} \begin{Bmatrix} \sigma_{xx} \\ \sigma_{yy} \\ \tau_{xy} \end{Bmatrix} dz \quad ; \quad M = \begin{Bmatrix} M_{xx} \\ M_{yy} \\ M_{xy} \end{Bmatrix} = \int_{-h/2}^{h/2} \begin{Bmatrix} \sigma_{xx} \\ \sigma_{yy} \\ \tau_{xy} \end{Bmatrix} z\, dz \quad ; \tag{2.19}$$

$$Q_s = \begin{Bmatrix} Q_y \\ Q_x \end{Bmatrix} = \int_{-h/2}^{h/2} \begin{Bmatrix} \sigma_{yz} \\ \sigma_{xz} \end{Bmatrix} dz \tag{2.20}$$

Then, the strain energy of the overall PFGS plate can be expressed as follows:

$$U = \frac{1}{2} \int_0^a \int_0^b \int_{-h/2}^{h/2} \left(\sigma_{xx}\, \varepsilon_{xx} + \sigma_{yy}\, \varepsilon_{yy} + \tau_{xy}\, \gamma_{xy} + \tau_{xz}\, \gamma_{xz} + \tau_{yz}\, \gamma_{yz} \right) dz\, dy\, dx \tag{2.21}$$

Substituting Eqs. (2.13) and (2.17) into Eq. (2.21), and by employing the principle of virtual work (Kattimani and Ray 2015), the first variation of the total potential energy of the overall PFGS plate can be expressed as

$$\delta T_p = \int_0^a \int_0^b \left[\frac{1}{2} \int_{-h/2}^{h/2} \left(\delta \{\varepsilon_b\}^T \{\sigma_b\} + \delta \{\varepsilon_s\}^T \{\sigma_s\} + \delta \{d_t\}^T \rho \left\{ \ddot{d}_t \right\} \right) dz - \delta \{d_t\}^T \{F\} \right] dx\, dy \tag{2.22}$$

where $\{\mathrm{F}\} = \{0\ 0\ \mathrm{p}\}^T$ is externally applied surface traction acting over a surface area, p is transverse load, ρ is the mass density of the PFGS plate, and δ is the symbol that describes the first variation.

2.2.3. Nonlinear finite element modeling of PFGS plate

The overall PFGS plate is discretized into eight-node iso-parametric quadrilateral elements with five degrees of freedom (three translational and two rotational) for each node. Making use of Eq. (2.8), the generalized displacement vectors $\{d_{tn}\}$ and $\{d_{rn}\}$ associated with the n^{th} (n = 1,2,3, …,8) node of an element can be written as

$$\{d_{tn}\} = \begin{bmatrix} u_{1n}\ v_{1n}\ w_{1n} \end{bmatrix}^T ; \{d_{rn}\} = \begin{bmatrix} \theta_{xn}\ \theta_{yn} \end{bmatrix}^T \tag{2.23}$$

subsequently, the generalized displacement vectors at any given point within an element can be expressed as

$$\{d_t\} = [N_t]\{d_t^e\} ; \{d_r\} = [N_r]\{d_r^e\} \tag{2.24}$$

in which, $\{d_t^e\}$ and $\{d_r^e\}$ are the nodal generalized translational and rotational displacement vectors, respectively; $[N_t]$ and $[N_r]$ are the shape function matrices of the order $[3\times 24]$ and $[2\times 16]$, respectively, and are expressed as

$$\{d_t^e\} = \left[\{d_{t1}^e\}^T \{d_{t2}^e\}^T \{d_{t3}^e\}^T \ldots \{d_{t8}^e\}^T\right]^T;$$

$$\{d_r^e\} = \left[\{d_{r1}^e\}^T \{d_{r2}^e\}^T \{d_{r3}^e\}^T \ldots \{d_{r8}^e\}^T\right]^T;$$

$$[N_t] = [N_{t1}\, N_{t2}\, N_{t3} \ldots N_{t8}];\ [N_r] = [N_{r1}\, N_{r2}\, N_{r3} \ldots N_{r8}];$$

$$N_{tn} = \mathrm{n}_n \mathrm{I}_t \text{ and } N_{rn} = \mathrm{n}_n \mathrm{I}_r \tag{2.25}$$

where n_n is the shape function in which the natural coordinates are associated with node n. I_t and I_r are the identity matrices. Now, from Eqs. (2.13) and (2.25), the generalized strain vectors at any point within an element are obtained as follows:

$$\{\varepsilon_{tb}\} = [ß_{tb}]\{d_t^e\};\ \{\varepsilon_{tbNL}\} = \frac{1}{2}[ß_1][ß_2]\{d_t^e\};\ \{\varepsilon_{rb}\} = [ß_{rb}]\{d_r^e\}$$

$$\{\varepsilon_{ts}\} = [ß_{ts}]\{d_t^e\} \text{ and } \{\varepsilon_{rs}\} = [ß_{rs}]\{d_r^e\} \tag{2.26}$$

in which, $[ß_{tb}]$, $[ß_1]$, $[ß_2]$, $[ß_{rb}]$, $[ß_{ts}]$ and $[ß_{rs}]$ are the generalized nodal strain displacement matrices and are given as follows:

$$[ß_{tb}] = [ß_{tb1}\, ß_{tb2}\, ß_{tb3} \ldots ß_{tb8}],\ [ß_1][ß_2] = [ß_1][ß_{21}\, ß_{21}\, ß_{23} \ldots ß_{28}],$$

$$[ß_{rb}] = [ß_{rb1}\, ß_{rb2}\, ß_{rb3} \ldots ß_{rb8}],\ [ß_{ts}] = [ß_{ts1}\, ß_{ts2}\, ß_{ts3} \ldots ß_{ts8}],$$

$$[ß_{rs}] = [ß_{rs1}\, ß_{rs2}\, ß_{rs3} \ldots ß_{rs8}] \tag{2.27a}$$

whereas, $[ß_{tbn}]$, $[ß_{1n}]$, $[ß_{2n}]$, $[ß_{rbn}]$, $[ß_{tsn}]$ and $[ß_{rsn}]$ (n=1,2,3, …, 8) are the sub-matrices and are given by

$$[ß_{tbn}] = \begin{bmatrix} \frac{\partial \mathrm{n}_n}{\partial x} & 0 & 0 \\ 0 & \frac{\partial \mathrm{n}_n}{\partial y} & 0 \\ \frac{\partial \mathrm{n}_n}{\partial y} & \frac{\partial \mathrm{n}_n}{\partial x} & 0 \end{bmatrix},\ [ß_1] = \begin{bmatrix} \frac{\partial w_1}{\partial x} & 0 & \frac{\partial w_1}{\partial y} \\ 0 & \frac{\partial w_1}{\partial y} & \frac{\partial w_1}{\partial x} \end{bmatrix}^T,\ [ß_{2n}] = \begin{bmatrix} 0 & 0 & \frac{\partial \mathrm{n}_n}{\partial x} \\ 0 & 0 & \frac{\partial \mathrm{n}_n}{\partial y} \end{bmatrix};$$

$$\left[ß_{rbn}\right]=\begin{bmatrix} \frac{\partial n_n}{\partial x} & 0 \\ 0 & \frac{\partial n_n}{\partial y} \\ \frac{\partial n_n}{\partial y} & \frac{\partial n_n}{\partial x} \end{bmatrix}, \quad \left[ß_{tsn}\right]=\begin{bmatrix} 0 & 0 & \frac{\partial n_n}{\partial x} \\ 0 & 0 & \frac{\partial n_n}{\partial y} \end{bmatrix} \text{ and } \left[ß_{rsn}\right]=\begin{bmatrix} n_n & 0 \\ 0 & n_n \end{bmatrix} \quad (2.27b)$$

substituting Eqs. (2.13), (2.15), and (2.26) into Eq. (2.22) and applying the principle of minimum total potential energy, i.e., $\delta T_p{}^e = 0$, and simplifying, the elemental equations of motion for PFGS plate are as follows

$$\left[M^e\right]\left\{\ddot{d}_t^e\right\}+\left[K_{tt}^e\right]\left\{d_t^e\right\}+\left[K_{tr}^e\right]\left\{d_r^e\right\}=\left\{F_t^e\right\} \quad (2.28)$$

$$\left[K_{rt}^e\right]\left\{d_t^e\right\}+\left[K_{rr}^e\right]\left\{d_t^e\right\}=0 \quad (2.29)$$

where, $\left[M^e\right]$ is the elemental mass matrix, $\left[K_{tt}^e\right]$, $\left[K_{tr}^e\right]$, $\left[K_{rt}^e\right]$ and $\left[K_{rr}^e\right]$ are the elemental elastic stiffness matrices and $\left\{F_t^e\right\}$ is the elemental mechanical load vector. For the sake of simplicity, elemental bending stiffness matrices and shear stiffness matrices are developed separately and computed using the selective integration method. On simplification, the elemental matrices and vectors are obtained as follows:

$$\left[K_{tt}^e\right]=\left[K_{tb}^e\right]+\left[K_{ts}^e\right]+\left[K_{tbNL}^e\right]; \quad \left[K_{tr}^e\right]=\left[K_{trb}^e\right]+\left[K_{trbNL}^e\right]+\left[K_{trs}^e\right]$$

$$\left[K_{rt}^e\right]=\left[K_{trb}^e\right]^T+\frac{1}{2}\left[K_{trbNL}^e\right]^T+\left[K_{trs}^e\right]^T; \quad \left[K_{rr}^e\right]=\left[K_{rrb}^e\right]+\left[K_{rrs}^e\right]; \text{ and}$$

$$\left\{F_t^e\right\}=\int_0^a\int_0^b\left[N_t\right]^T\left\{f\right\}dx\,dy \quad (2.30)$$

The elemental stiffness matrices, which correspond to bending and stretching deformations and transverse shear deformations, evolved in Eq. (2.30), and the various rigidity matrices and vectors appearing in the elemental matrices are presented as follows:

$$\left[K_{tb}^e\right]=\int_0^a\int_0^b\left[ß_{tb}\right]^T\left[Ð_{tb}\right]\left[ß_{tb}\right]dxdy, \quad \left[K_{trb}^e\right]=\int_0^a\int_0^b\left[ß_{tb}\right]^T\left[Ð_{trb}\right]\left[ß_{rb}\right]dxdy$$

$$\left[K_{rrb}^e\right]=\int_0^a\int_0^b\left[ß_{rb}\right]^T\left[Ð_{rrb}\right]\left[ß_{rb}\right]dxdy$$

$$\left[K_{tbNL}^e\right]=\int_0^a\int_0^b\left(\frac{1}{2}\left[ß_{tb}\right]^T\left[Ð_{tb}\right]\left[ß_1\right]\left[ß_2\right]+\left[ß_2\right]^T\left[ß_1\right]^T\left[Ð_{tb}\right]\left[ß_{tb}\right]+\frac{1}{2}\left[ß_2\right]^T\left[ß_1\right]^T\left[Ð_{tb}\right]\left[ß_1\right]\left[ß_2\right]\right)dxdy$$

$$\left[K^e_{trbNL}\right]=\int_0^a\int_0^b\left(\left[ß_2\right]^T\left[ß_1\right]^T\left[Ð_{trb}\right]\left[ß_{rb}\right]\right)dxdy \quad , \quad \left[K^e_{rtbNL}\right]=\frac{1}{2}\left[K^e_{trbNL}\right]^T$$

$$\left[M^e\right]=\int_0^a\int_0^b\left[N_t\right]^T\overline{m}\left[N_t\right]dxdy \qquad \text{where,} \quad \overline{m}=\int_{-h/2}^{h/2}\rho(z)\,dz$$

$$\left[K^e_{ts}\right]=\int_0^a\int_0^b\left[ß_{ts}\right]^T\left[Ð_{ts}\right]\left[ß_{ts}\right]dxdy \quad , \quad \left[K^e_{trs}\right]=\int_0^a\int_0^b\left[ß_{ts}\right]^T\left[Ð_{trs}\right]\left[ß_{rs}\right]dxdy$$

$$\left[K^e_{rrs}\right]=\int_0^a\int_0^b\left[ß_{rs}\right]^T\left[Ð_{rrs}\right]\left[ß_{rs}\right]dxdy \qquad (2.31a)$$

The various rigidity vectors and the rigidity matrices are given by

$$\left[Ð_{tb}\right]=\int_{-h/2}^{h/2}\left[Q_b(z)\right]dz \quad ; \quad \left[Ð_{trb}\right]=\int_{-h/2}^{h/2}\left[Q_b(z)\right]z\,dz \quad ; \quad \left[Ð_{rrb}\right]=\int_{-h/2}^{h/2}\left[Q_b(z)\right]z^2dz \quad ;$$

$$\left[Ð_{ts}\right]=\int_{-h/2}^{h/2}\left[Q_s(z)\right]dz \quad ; \quad \left[Ð_{trs}\right]=\int_{-h/2}^{h/2}\left[Q_s(z)\right]dz \quad ; \quad \left[Ð_{rrs}\right]=\int_{-h/2}^{h/2}\left[Q_s(z)\right]dz \qquad (2.31b)$$

The elemental governing equations are assembled into the global space in a straightforward manner to obtain the global equations of equilibrium as follows:

$$\left[M\right]\left\{\ddot{X}_t\right\}+\left[K_{tt}\right]\left\{X_t\right\}+\left[K_{tr}\right]\left\{X_r\right\}=\left\{\mathrm{F}\right\}$$

$$\left[K_{rt}\right]\left\{X_t\right\}+\left[K_{rr}\right]\left\{X_r\right\}=0 \qquad (2.32)$$

in which, $\left[M\right]$ is the global mass matrix, $\left[K_{tt}\right]$, $\left[K_{tr}\right]$, $\left[K_{rt}\right]$ and $\left[K_{rr}\right]$ are the global stiffness matrices, it may be noted that the stiffness matrices $\left[K_{tt}\right]$, $\left[K_{tr}\right]$ and $\left[K_{rt}\right]$ include both global linear and nonlinear components. $\left\{\mathrm{F}\right\}$ is the global mechanical load vector, $\left\{X_t\right\}$ and $\left\{X_r\right\}$ are the global generalized translational and rotational displacement vectors, respectively. After enforcing the displacement boundary conditions, the global rotational degrees of freedom are reduced to obtain the global equilibrium equations concerning the global nodal translational degrees of freedom as follows:

$$\left[M\right]\left\{\ddot{X}_t\right\}+\left[K\right]\left\{X_t\right\}=\left\{\mathrm{F}\right\} \qquad (2.33)$$

in which,

$$\left[K\right]=\left[K_{tt}\right]-\left[K_{tr}\right]\left[K_{rr}\right]^{-1}\left[K_{rt}\right] \qquad (2.34)$$

Eq. (2.33) presents the nonlinear FE model for the PFGS plate. The eigenvalues and eigenvectors for the PFGS plate can be obtained using Eq. (2.33) and rearranged in the form as follows:

$$\left(\left[K\right]-\omega^2\left[M\right]\right)\left\{X\right\}=0 \tag{2.35}$$

Where, ω and X are the natural frequency and corresponding eigenvector of the PFGS plate, respectively. The transient response of the plate can be obtained by incorporating Newmark's integration technique. Further, the nonlinear frequency-amplitude relationship is determined from Eq. (2.35) using a direct iterative method associated with FE formulations.

2.2.4. Skew Boundary Transformation

It can be observed from the PFGS plate shown in Figure 2.1 that the boundary elements support two adjacent edges. These edges may or may not be parallel to the global coordinate axes (x, y, z). Therefore, the nodal displacements are defined in terms of axes of local coordinates. Then, the axes of local coordinates are transformed into the global coordinate axes. Further, the boundary conditions are defined in terms of the axes of the global coordinates. The transformation of coordinates between the global degrees of freedom and local degrees of freedom of each node can be written as (Garg et al. 2006; Vinyas et al. 2020)

$$\mathrm{L}_n=\left[T_{s1}\right]\mathrm{L}_n^{'} \tag{2.36}$$

where, L_n and $\mathrm{L}_n^{'}$ are displacement vectors in the global edge and local edge coordinates at the n^{th} node, respectively, and are given by

$$\mathrm{L}_n=\left[u_{1n}\ v_{1n}\ w_{1n}\ \theta_{xn}\ \theta_{yn}\right]^{\mathrm{T}};\ \mathrm{L}_n^{'}=\left[u_{1n}^{'}\ v_{1n}^{'}\ w_{1n}^{'}\ \theta_{xn}^{'}\ \theta_{yn}^{'}\right]^{\mathrm{T}} \tag{2.37}$$

The transformation matrices for node n on the skew boundary is

$$\left[T_{s1}\right]=\begin{bmatrix} c & s & 0 & 0 & 0 \\ -s & c & 0 & 0 & 0 \\ 0 & 0 & 1 & 0 & 0 \\ 0 & 0 & 0 & c & s \\ 0 & 0 & 0 & -s & c \end{bmatrix} \tag{2.38}$$

where, $c=\cos\left(\Phi\right)$ and $s=\sin\left(\Phi\right)$.

It can be noted from the above transformation matrices that the transformation from the global coordinate system to the local coordinate system is unnecessary for the nodes not resting on the skew edges of the FG plate. In such a case, the transformation matrix has diagonal matrices, and the values assigned to the principal diagonal elements are equal to one.

The transformation matrices for the complete element is

$$T_s = eye\left(\left[T_{s1}\right]\right) \tag{2.39}$$

where, *eye* is the identity matrices of the order $[8\times 8]$, the order of identity matrices is equal to the number of nodes in an element. The elemental mass and stiffness matrices of an element having the nodes which lie on skew edges are as follows

$$\left[\overline{k_e}\right] = \left[T_s\right]^T \left[k_e\right]\left[T_s\right] \; ; \; \left[\overline{M_e}\right] = \left[T_s\right]^T \left[M_e\right]\left[T_s\right] \tag{2.40}$$

where $\left[\overline{k_e}\right]$ and $\left[\overline{M_e}\right]$ are transformed stiffness matrix and mass matrix, respectively.

2.3. Solution methodology

2.3.1. Nonlinear frequency parameter analysis

The solutions to the vibration problems are obtained using the eigenvalue formulation while an iterative method is adopted to solve the nonlinear eigenvalue problems of the PFGS plate (Han and Petyt 1997; Sundararajan et al. 2005). Firstly, utilizing a standard eigenvalue extraction algorithm, Eq. (2.35) is used to extract the linear eigenvalue and eigenvectors from the global mass and stiffness matrices by neglecting nonlinear stiffness matrices. Next, by normalizing the mode shape vector, and then the normalized eigenvector is scaled up to the amplitude ratio. Thus, the desired value should be equal to the maximum displacement values. This provides the initial vector. The initial nonlinear vector is then obtained by computing the nonlinear stiffness matrices by numerical integration technique and then solved for the nonlinear eigenvalues and corresponding eigenvectors. These steps are repeated until the values of nonlinear frequency, and its mode shape converges (Bergan and Clough 1972) at a specified rate as given by

$$\left(\frac{\left|\omega_{itr} - \omega_{itr-1}\right|}{\omega_{itr}}\right) \le 0.0001 \tag{2.41}$$

where the suffix *itr* indicates the iteration number.

2.3.2. Nonlinear transient analysis

In the nonlinear dynamic analysis, the nonlinear governing equation (Eq. (2.33)) depends on both linear and nonlinear stiffness matrices. The nonlinear stiffness matrix (K_{NL}) depends on both unknown displacement (X_t) and time-domain (t_i). Therefore, for the complete discretization of the nonlinear governing equation, the time derivatives appearing in Eq. (2.33) are approximated using Newmark's direct integration technique and Picard's methods. Here, the initial values of displacement, velocity, and acceleration are set to zero at time t_i = 0. Now, determining the velocities and accelerations at $t_i = (ń+1)\Delta t_i$ can be written as

$$\ddot{X}_{ń+1} = a_1(X_{ń+1} - X_{ń}) - a_2\dot{X}_{ń} - a_3\ddot{X}_{ń} \tag{2.42}$$

$$\dot{X}_{ń+1} = \dot{X}_{ń} + a_4\ddot{X}_{ń} + a_5\ddot{X}_{ń+1} \tag{2.43}$$

where, $a_1 = \dfrac{1}{\beta\,\Delta t_i^2}$; $a_2 = a_1\,\Delta t_i$; $a_3 = \left(\dfrac{1}{2\beta} - 1\right)$; $a_4 = (1-\eta)\Delta t_i$ and $a_5 = \eta\,\Delta t_i$, with the constants β= 0.25 and η=0.50 are taken.

Substituting Eqs. (2.42) and (2.43) into Eq. (2.33), we get

$$\left[\tilde{K}\right]\left\{X_{ń+1}\right\} = \left\{\tilde{F}_{ń+1}\right\} \tag{2.44}$$

with, $\left[\tilde{K}\right] = [K] + a_1[M]$;

$$\left\{\tilde{F}_{ń+1}\right\} = \left\{F_{ń+1}\right\} + [M]\left(a_1 X_{ń} + a_2\dot{X}_{ń} + a_3\ddot{X}_{ń}\right) \tag{2.45}$$

It may be noted that all the parameters can be determined at the initial time $t_i = ń\,\Delta t_i$ from Eqs. (2.44 - 2.45) except for the nonlinear stiffness matrix (K_{NL}), which depends on the unknown displacement $X_{ń+1}$. Therefore, the nonlinear equation from Eq. (2.44) is re-approximated by adopting the Picard-type iteration method. After re-approximation, the equation appears as follows:

$$\left[\tilde{K}\left(\left\{X^{itr}\right\}_{ń+1}\right)\right]\left\{X^{itr+1}\right\}_{ń+1} = \left\{\tilde{F}_{ń+1}\right\} \tag{2.46}$$

where the superscript *itr* indicates the number of iterations and successive iterations continue until the error of $X_{ń+1}$ is satisfied as

$$\frac{\left\| X_{ń+1}^{itr+1} - X_{ń+1}^{itr} \right\|}{\left\| X_{ń+1}^{itr} \right\|} \leq 0.0001 \tag{2.47}$$

2.4. RESULTS AND DISCUSSIONS

The PFGS plate is considered to investigate the effects of porosity distributions and skewness on the large amplitude free vibration and nonlinear transient responses. The PFGS plate consists of a ceramic surface at the top and a metallic surface at the bottom; in between, there is a gradation of these two constituent materials in conjunction with porosities. Validation studies have been conducted to evaluate the accuracy of the proposed FE model. Parametric studies are conducted for various parameters to evaluate the nonlinear frequency and dynamic response of the PFGS plate.

Further, to decrease the number of unknowns and to avoid the rigid body motion, various boundary conditions simply supported (S), clamped (C), free (F), and their combinations employed in this study are shown as follows:

Clamped (CCCC) : $u_1 = v_1 = w_1 = \theta_x = \theta_y = 0$

Free (FFFF): $u_1 = v_1 = w_1 = \theta_x = \theta_y \neq 0$

Simply supported (SSSS) : $u_1 = \theta_x \neq 0$; $v_1 = w_1 = \theta_y = 0$ at $x = 0, a$

$v_1 = \theta_y \neq 0$; $u_1 = w_1 = \theta_x = 0$ at $y = 0, b$ (2.48)

Table 2.1: The Properties of isotropic materials (Huang and Shen 2004).

Materials	Properties		
	E (N/m^2)	ϑ	ρ (kg/m^3)
ZrO_2 (Zirconium Oxide)	151.00×10^9	0.300	3000
Ti-6Al-4V (Titanium Alloy)	105.70×10^9	0.298	4429
Si_3N_4 (Silicon Nitride)	322.27×10^9	0.280	2370
SUS304 (Stainless Steel)	207.79×10^9	0.280	8166

2.5. Convergence and validation

Example 1: To examine the accuracy and effectiveness of the present FE model. The fundamental natural frequency parameter for a simply supported Si_3N_4 / SUS304 FG square plate for different volume fraction grading indexes (m) is compared with the results that Huang and Shen (2004) reported for the similar geometrical parameters and material properties of the plate. It can be observed from Table 2.2 that the results obtained with the present model closely resemble the reference literature (Huang and Shen 2004). The mesh size of [8 × 8] is adequate based on the progressive mesh refinement to model the PFGS plate.

Table 2.2: Comparing the fundamental natural frequency parameter for Si_3N_4 / SUS304 FGM square plate (a = 0.2; b = 0.2; h = 0.025, SSSS).

Sources	α				
	0.0	0.5	1.0	2.0	∞
Reference (Huang and Shen 2004)	12.495	8.675	7.555	6.777	5.405
Present [2 ×2]	12.3944	8.5641	7.5151	6.7418	5.3616
Present [4 ×4]	12.5893	8.6977	7.6357	6.8544	5.4459
Present [6 ×6]	12.6166	8.7160	7.6519	6.8692	5.4577
Present [8 ×8]	12.6251	8.7218	7.6569	6.8738	5.4614
Difference in %	1.030	0.536	1.330	1.408	1.032

Table 2.3: Comparison of fundamental frequency for an isotropic skew plate (a/b = 1, SSSS).

a/h	Sources	Skew Angle (Φ)			
		0°	15°	30°	45°
10	Present	1.9441	2.0852	2.5250	3.3911
	Liew et al. (1993)	1.9311	2.0379	2.4195	3.3548
5	Present	1.8010	1.8888	2.1727	2.7318
	Liew et al. (1993)	1.7661	1.8560	2.1719	2.9129

Example 2: An additional validation study is carried out for the dimensionless natural frequency of the isotropic skew plate with skew angles of 0°, 15°, 30°, and 45° with SSSS boundary condition for the aspect ratio $a/b = 1$ and thickness ratio $a/h = 5$ and 10. It can be seen that the results reported in Table 2.3 display excellent agreement with the reference literature (Liew et al. 1993).

Example 3: To validate further, a dimensionless frequency parameter for porous FG plates is determined and compared with the results reported in the literature by Rezaei et al. (2017) for the Al_2O_3 / Al FG porous plate with simply supported boundary conditions for various volume fraction grading index (m) and porosity volume index (e_p). It can be witnessed from Table 2.4 that the results hold a firm agreement for both evenly distributed porosity (P_e) and centrally distributed porosity (P_c) with the reference (Rezaei et al. 2017).

Table 2.4: Comparison of fundamental natural frequency for different porosity volume index for simply supported square Al_2O_3 / Al porous FGM plate.

b/a	e_p	Sources (Rezaei et al. 2017)	$m = 0$		$m = 0.5$		$m = 1$	
			P_e	P_c	P_e	P_c	P_e	P_c
$h/a = 0.05$								
1	0	Rezaei et al.	0.0291	0.0291	0.0247	0.0247	0.0222	0.0222
		Present	0.0292	0.0292	0.0247	0.0247	0.0223	0.0223
	0.2	Rezaei et al.	0.0300	0.0300	0.0246	0.0252	0.0210	0.0225
		Present	0.0296	0.0299	0.0242	0.0251	0.0207	0.0224
	0.4	Rezaei et al.	0.0314	0.0310	0.0242	0.0259	0.0182	0.0227
		Present	0.0305	0.0308	0.0235	0.0257	0.0177	0.0225
$h/a = 0.1$								
0.5	0	Rezaei et al.	0.0719	0.0719	0.0610	0.0610	0.0550	0.0550
		Present	0.0721	0.0721	0.0611	0.0611	0.0551	0.0551
	0.2	Rezaei et al.	0.0742	0.0740	0.0607	0.0624	0.0521	0.0555
		Present	0.0732	0.0739	0.0599	0.0622	0.0513	0.0554
	0.4	Rezaei et al.	0.0775	0.0765	0.0599	0.0640	0.0450	0.0561
		Present	0.0755	0.0762	0.0584	0.0636	0.0438	0.0557

Example 4: The nonlinear frequency ratio (NLFR) for different amplitude ratios W_{max}/h is validated with the results reported by Sundararajan et al. (2005), and good agreement with the present model for the simply supported Si_3N_4 / SUS304 FG plate is observed as shown in Table 2.5.

Table 2.5: Comparison of nonlinear frequency ratio (NLFR) (ω_{NL}/ω) with different values of amplitude ratios for Si_3N_4 / SUS304 FGM square plate (a/h = 10, m = 1, and SSSS).

Amplitude ratio (W_{max}/h)	0.2	0.4	0.6	0.8	1
Present	1.0066	1.0663	1.1719	1.3132	1.4805
Sundararajan et al. (2005)	1.0063	1.0654	1.1707	1.3155	1.4789
% Difference	0.029	0.084	0.102	0.174	0.108

Example 5: Furthermore, to check the reliability and accuracy of the approach adopted for the analysis of nonlinear transient responses, the present method is also validated with the Chen et al. (2000) for an orthotropic plate with $a = b = 0.250$, $h = 0.005$, $E_1 = 525$ GPa, $E_2 = 21$ GPa, $G_{12} = G_{23} = G_{13} = 10.50$ GPa, $\vartheta = 0.25$, and $\rho = 800$ kg/m^3 under the uniform step load of q_0=1N/mm^2. It can be observed from Figure 2.4 that in this case also, the dimensionless nonlinear transient deflection $(w_c = w/h)$ exhibits a very close agreement compared to the reference (Chen et al. 2000).

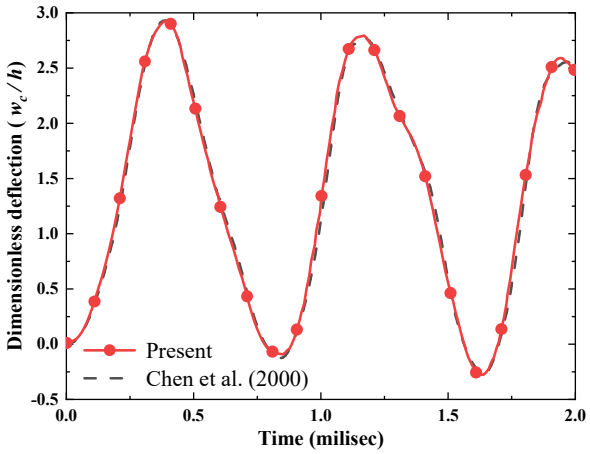

Figure 2.4: Comparison of dimensionless nonlinear transient deflection of the simply supported orthotropic plate.

2.6. Parametric Studies

Based on the comparison studies presented in section 2.3.1, the proposed approach extracts accurate results for carrying out the parametric studies on the PFGS plate. The influence of various boundary conditions like SSSS (simply supported), CCCC (clamped and clamped), SCSC (simply supported and clamped), SSSF (simply supported and free edge), and CCCF (clamped and free edge) are considered in the present analysis. The mesh size [8 × 8] used for the validation is adopted to extract the results for all parametric studies. The porous FG plate consists of two sets of combinations of materials: Si_3N_4/SUS304 and ZrO_2/Ti-6Al-4V. The properties such as Young's modulus (E), density (ρ), and Poisson's ratio (ϑ) of these constituent materials are provided in Table 2.1.

Further, the nonlinear frequency parameter (NLFP) of ZrO_2 / Ti-6Al-4V PFGS plates for various geometrical parameters, the following non-dimensional NLFP (ω_{NL}) equation is adopted.

$$\omega_{NL} = \bar{\omega}_{NL}\left(\frac{a^2}{h}\right)\sqrt{\frac{\rho_c}{E_c}} \tag{2.49}$$

where, ρ_c and E_c are the density and Young's modulus, respectively, for the ceramic material.

2.7. Nonlinear frequency analysis

2.7.1. Effect of volume fraction grading index (*m*)

In this section, the nonlinear free vibration characteristics of the PFGS plate are analyzed considering the parameters that influence the nonlinear frequency ratio (NLFR), such as skew angle, porosity distributions, porosity volume index, volume fraction grading index, and geometrical parameters of the plate. The results presented in Table 2.6 are focused on investigating the influence of porosity distributions for the skew angle Φ = 0°, volume fraction grading index (*m* = 0, 0.5, 1, 2, 5, and 10), and porosity volume index e_p = 0.10 on the fundamental NLFR (ω_{NL}/ω). It can be seen that for a given porosity distribution, increasing the value of volume fraction grading index (*m*) leads to a decrease in the NLFR till *m* = 2 whereas, from *m* = 5, it enhances. It indicates that the NLFR has the lowest values in the gradation region m = 1 to 5 for all porosity distributions.

Table 2.6: Effect of volume fraction grading index for different porosity distributions on the NLFR (ω_{NL}/ω) of Si_3N_4 / SUS304 PFGS plate ($a/b = 1$, $a/h = 50$, $e_p = 0.10$, $\Phi = 0°$, and SSSS).

P_d	m	Amplitude Ratio (W_{max}/h)					
		0.2	0.4	0.6	0.8	1.0	1.2
P_e	0.0	1.0256	1.0989	1.2120	1.3557	1.5220	1.7049
	0.5	1.0091	1.0691	1.1729	1.3112	1.4752	1.6577
	1.0	1.0031	1.0569	1.1552	1.2889	1.4492	1.6286
	2.0	1.0011	1.0514	1.1453	1.2743	1.4297	1.6045
	5.0	1.0061	1.0593	1.1540	1.2818	1.4348	1.6062
	10	1.0122	1.0710	1.1703	1.3014	1.4567	1.6297
P_c	0.0	1.0251	1.0971	1.2083	1.3498	1.5137	1.6940
	0.5	1.0095	1.0687	1.1708	1.3066	1.4677	1.6471
	1.0	1.0040	1.0573	1.1542	1.2855	1.4430	1.6194
	2.0	1.0021	1.0523	1.1450	1.2719	1.4248	1.5964
	5.0	1.0068	1.0598	1.1531	1.2789	1.4294	1.5981
	10	1.0125	1.0705	1.1680	1.2969	1.4494	1.6194
P_{tb}	0.0	1.0264	1.1020	1.2183	1.3657	1.5361	1.7230
	0.5	1.0105	1.0733	1.1812	1.3240	1.4927	1.6792
	1.0	1.0046	1.0617	1.1644	1.3030	1.4684	1.6525
	2.0	1.0027	1.0565	1.1551	1.2893	1.4502	1.6303
	5.0	1.0077	1.0644	1.1639	1.2972	1.4558	1.6328
	10	1.0137	1.0760	1.1800	1.3166	1.4777	1.6565

It is due to the decrease in ceramic composition as the volume fraction grading index increases and thus reduces the stiffness of the plate. As the stiffness of the plate decreases for higher values of volume fraction grading index, the linear frequency also decreases rapidly, and the difference between nonlinear frequency and linear frequency increases. Hence, the NLFR increases for higher volume fraction grading index values. Analogously, for a given value of *m*, the effect of porosity distributions on the NLFR follows the trend as centrally distributed porosity (P_c) < evenly distributed porosity (P_e) < P_{tb} type of porosity distribution. This signifies that the presence of porosity in the

gradation region has considerably less impact on the NLFR and that the distribution of porosities in the FG material can vary the NLFR.

Furthermore, the influence of various volume fraction grading indexes on the NLFP (ω_{NL}) for clamped and simply supported boundary conditions of the PFGS plate for all the porosity distributions is depicted in Figure 2.5. The geometrical parameters $a/b = 1$, $a/h = 40$, $\Phi = 30°$, and $e_p = 0.2$ are considered for the investigation. It can be observed from these figures that as the amplitude ratio increases, the NLFP also increases monotonically. Hence, it displays the hardening behavior characteristics. Further, the NLFP decreases with the increase in the volume fraction grading index m. It can also be seen that NLFP is maximal for the clamped case compared to simply supported boundary conditions of the plate. Moreover, each type of porosity distribution exhibits a different impact on influencing the NLFP. The P_c type of distribution has the highest, and the P_{tb} type of distribution has the lowest influence on the NLFP. The influence of porosity distributions on NLFP follows the trend as $P_c > P_e > P_{tb}$. The change in the NLFP is attributed to the decrease and variation of the stiffness of the plate due to the presence of a different type of porosity distribution, which significantly decreases the NLFP values as porosity volume increases.

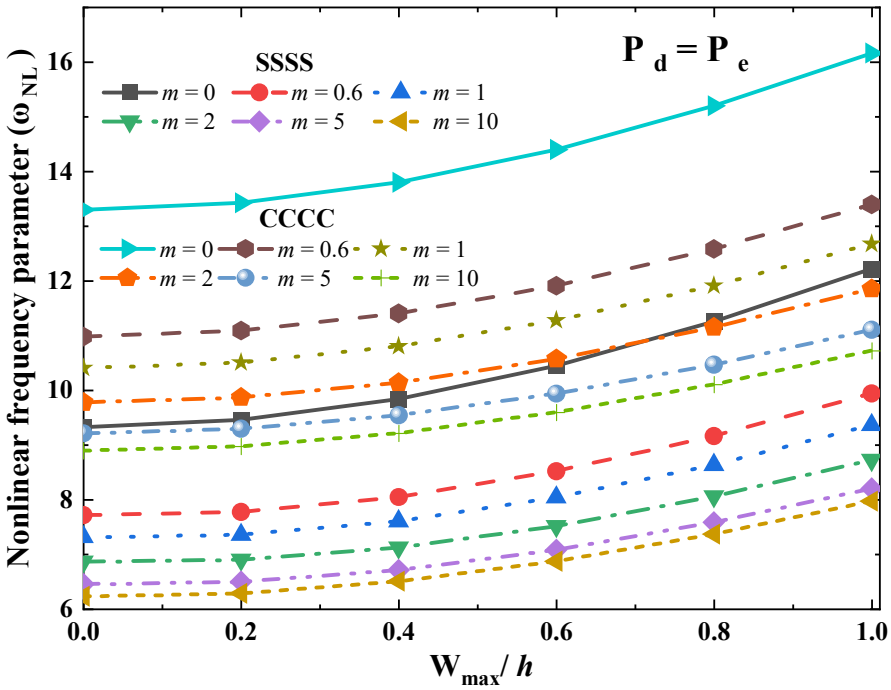

(a) P_e

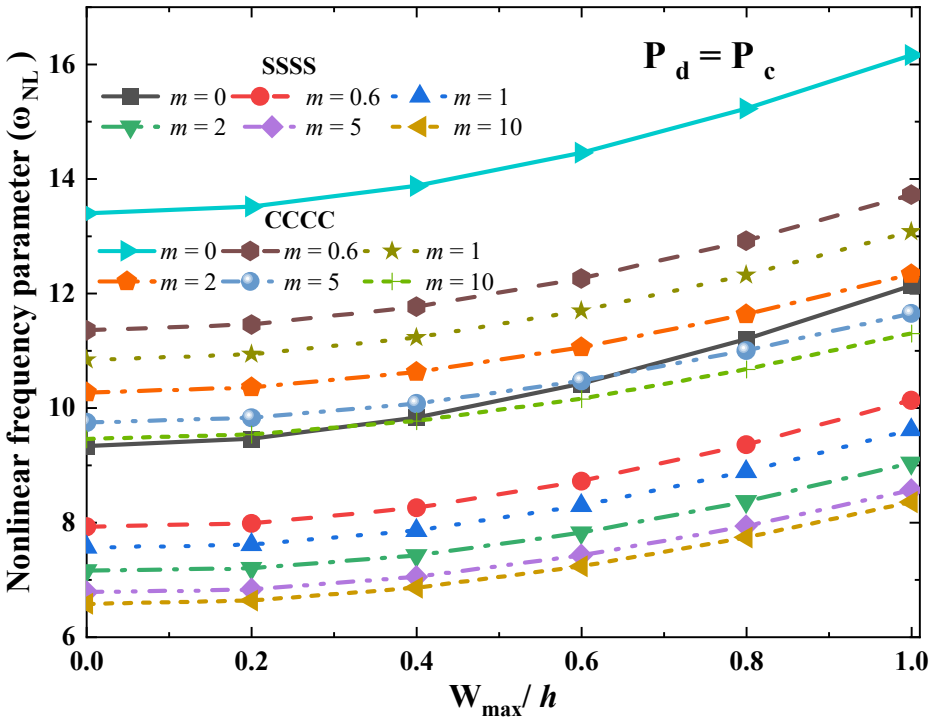

(b) P_c

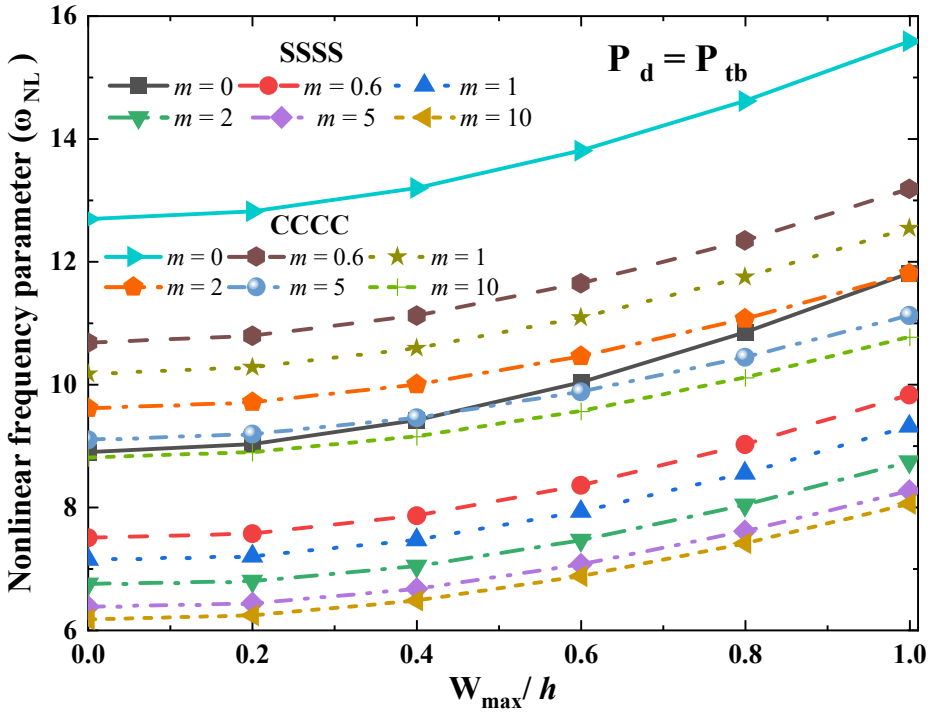

(c) P_{tb}

Figure 2.5: Effect of different volume fraction grading indices on NLFP of ZrO_2 / Ti-6Al-4V PFGS plate for various porosity distributions and boundary conditions.

2.7.2. Effect of skew angle on porosity distributions

The influence of porosity distributions for different skew angles on the fundamental NLFR (ω_{NL}/ω) is shown in Table 2.7. The effect of porosity distributions (P_e, P_c, and P_{tb}) with porosity volume index $e_p = 0.10$ for different skew angles ($\Phi = 0°$, 10°, 20°, 30°, and 40°) are considered. Further, the porous FG plate comprises of Si_3N_4/SUS304 with the boundary condition SSSS is considered for the analysis.

Table 2.7: Influence of Skew angle for different porosity distributions on the NLFR (ω_{NL}/ω) of Si_3N_4 / SUS304 PFGS plate. ($a/b = 1$, $a/h = 50$, $e_p = 0.10$, $m = 2$, and SSSS).

P_d	Skew angle (Φ)	Amplitude Ratio (W_{max}/h)					
		0.2	0.4	0.6	0.8	1.0	1.2
	0°	1.0011	1.0514	1.1453	1.2743	1.4297	1.6045
	10°	1.0022	1.0458	1.1266	1.2384	1.3744	1.5290
P_e	20°	1.0038	1.0393	1.1039	1.1934	1.3034	1.4298
	30°	1.0047	1.0358	1.0913	1.1681	1.2626	1.3717
	40°	1.0051	1.0335	1.0835	1.1526	1.2378	1.3363
	0°	1.0021	1.0523	1.1450	1.2719	1.4248	1.5964
	10°	1.0030	1.0465	1.1265	1.2368	1.3710	1.5234
P_c	20°	1.0042	1.0395	1.1032	1.1916	1.3001	1.4246
	30°	1.0049	1.0356	1.0901	1.1655	1.2585	1.3657
	40°	1.0052	1.0331	1.0820	1.1497	1.2331	1.3295
	0°	1.0027	1.0565	1.1551	1.2893	1.4502	1.6303
	10°	1.0036	1.0500	1.1347	1.2510	1.3919	1.5513
P_{tb}	20°	1.0048	1.0424	1.1099	1.2030	1.3168	1.4472
	30°	1.0055	1.0382	1.0961	1.1758	1.2736	1.3860
	40°	1.0057	1.0356	1.0876	1.1592	1.2472	1.3486

From Table 2.7, it can be observed that in the presence of porosities, the NLFR increases as the amplitude ratio W_{max}/h increases for all porosity distributions and skew angles. This indicates that the amplitude ratio exhibits hardening-type behavior in the presence of porosity and the amplitude ratio determines the extent of nonlinearity. Where W_{max} indicates the maximum flexural amplitude of the plate and h is the

thickness of the plate. If the amplitude ratio is set to zero, the porous FG plate undergoes linear vibration and gives a linear frequency.

Table 2.8: Effect of thickness ratio for various skew angles on the fundamental NLFR (ω_{NL}/ω) for different porosity distributions of Si3N4 / SUS304 PFGS plate (a/b = 1, m = 2, e_p = 0.10, W_{max}/h = 1.0, and SSSS).

Skew angle (Φ)	a/h	Porosity distributions (P_d)		
		P_e	P_c	P_{tb}
0°	10	1.4485	1.4443	1.4692
	20	1.4338	1.4290	1.4543
	50	1.4297	1.4248	1.4502
	100	1.4291	1.4242	1.4496
10°	10	1.4311	1.4273	1.4508
	20	1.4052	1.4012	1.4241
	50	1.3744	1.3710	1.3919
	100	1.3385	1.3356	1.3538
20°	10	1.3888	1.3858	1.4061
	20	1.3474	1.3442	1.3631
	50	1.3034	1.3001	1.3168
	100	1.2764	1.2725	1.2882
30°	10	1.3411	1.3383	1.3555
	20	1.2962	1.2929	1.3089
	50	1.2626	1.2585	1.2736
	100	1.2493	1.2445	1.2593
40°	10	1.3008	1.2979	1.3126
	20	1.2603	1.2564	1.2708
	50	1.2378	1.2331	1.2472
	100	1.2300	1.2250	1.2389

Further, it can also be observed from Table 2.7 that with the increase in skew angle, the NLFR decreases for all porosity distributions, porosity volume index, and volume fraction grading index. It may be due to the increase in linear frequency with an increase in stiffness of the plate as the skew angle increases. Hence, it reduces the NLFR. Besides, for a given skew angle, the effect of porosity distributions on the NLFR

follows the same trend as that followed in volume fraction grading index, such as the centrally distributed porosity (P_c) < evenly distributed porosity (P_e) < P_{tb} type of porosity distribution.

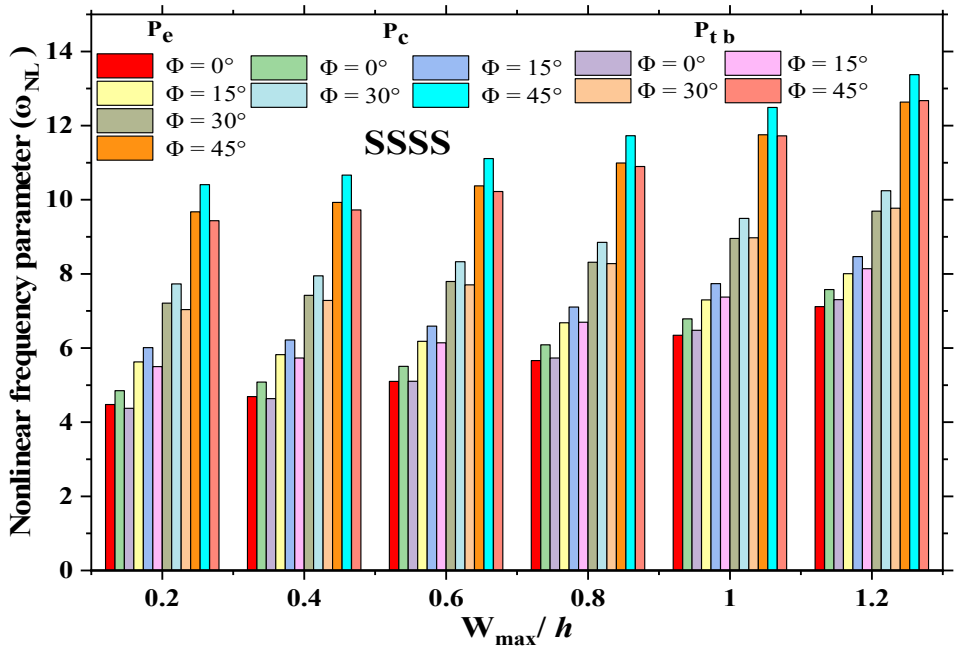

(a) SSSS

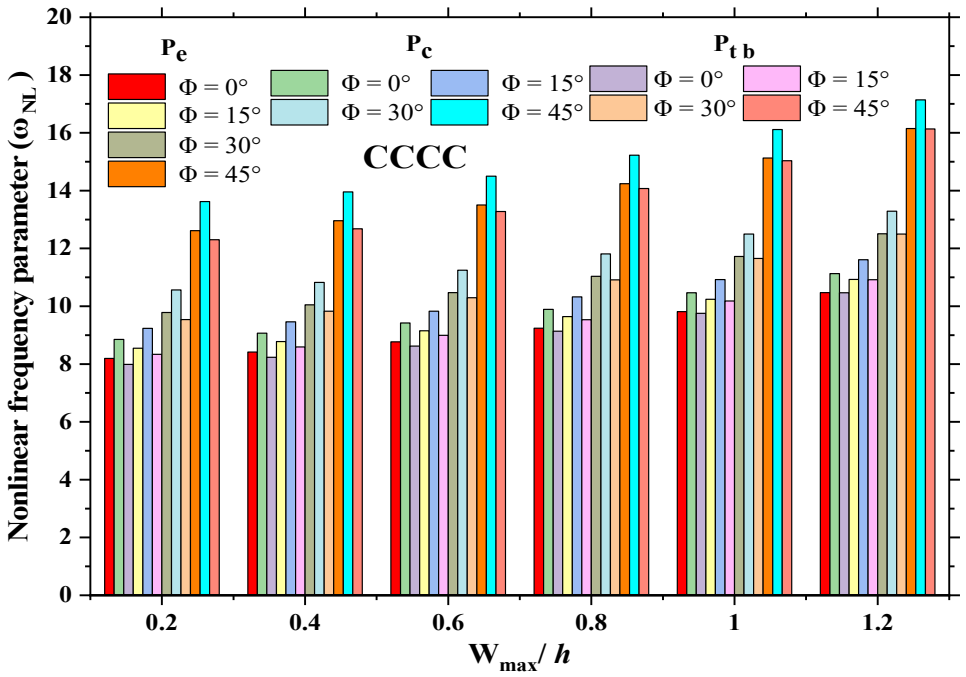

(b) CCCC

Figure 2.6: Effect of skew angle on NLFP of ZrO_2 / Ti-6Al-4V PFGS plate for various porosity distributions and boundary conditions. (a/b = 1, a/h = 80, m = 2, e_p = 0.3).

Additionally, the effect of the skew angle on NLFP of the PFGS plate for different porosity distributions (P_e, P_c, and P_{tb}) is shown in Figure 2.6. It can be seen that with an increase in skew angle, there is a reduction in plate area, due to which the stiffness of the porous plate increases. Hence, the rise in NLFP is observed. A significant increase in the NLFP can be noticed for the skew angle $\Phi = 45°$ as compared to lower skew angles ($\Phi = 0°$, 15°, and 30°). Besides, NLFP is high for the clamped case compared to the corresponding values of the simply supported boundary conditions. However, there is a reduction in the plate's stiffness due to the presence of porosity compared to the perfect FG skew plate. Figure 2.6 show that the P_c type of porosity distribution gives the highest NLFP while the P_{tb} exhibits the lowest NLFP. This indicates that the presence of porosity in the gradation region increases the NLFP.

2.7.3. Effect of thickness and aspect ratio

The influence of side-to-thickness ratio (a/h) for different skew angles and porosity distributions on NLFR of simply supported Si_3N_4 / SUS304 PFGS plate (m = 2, e_p = 0.10, and W_{max}/h = 1.0) is depicted in Table 2.8. It can be witnessed that the NLFR decreases as the thickness ratio increases. The physical significance of this behavior is the decrease of the plate's stiffness as the thickness of the plate decreases due to the presence of porosities. Besides, porosity distribution P_c has the lowest NLFR while P_{tb} exhibits the highest for all the cases of thickness ratios and skew angles ($P_c < P_e < P_{tb}$). It shows that porosities away from the gradation region have a more significant impact on the NLFR. For all the types of porosity distributions considered, a noticeable difference in the NLFR can be detected at the corresponding values of the thickness ratios.

The influence of aspect ratio variation (b/a) for various skew angles and porosity distributions on the nonlinear behavior of simply supported PFGS plates has been studied, considering m = 2, e_p = 0.10, and W_{max}/h = 1.0. It can be noticed from Table 2.9 that for an increase in aspect ratio, the NLFR decreases and then increases for lower skew angles. However, for higher skew angles ($\Phi = 30°$ and 40°), the NLFR increases gradually with an increase in aspect ratio. This is due to the decrease in linear frequencies as the aspect ratio increases with the presence of porosities; however, it is not presented here for the sake of brevity.

Table 2.9: Effect of aspect ratio for various skew angles on the fundamental NLFR (ω_{NL}/ω) for different porosity distributions of Si_3N_4 / SUS304 PFGS plate. (a/h = 50, m = 2, e_p = 0.10, W_{max}/h = 1.0, and SSSS).

Skew angle (Φ)	*b/a*	Porosity distributions (P_d)		
		P_e	P_c	P_{tb}
0°	0.6	1.4974	1.4905	1.5194
	0.8	1.4440	1.4387	1.4647
	1.0	1.4297	1.4248	1.4502
	1.2	1.4391	1.4338	1.4597
	1.4	1.4605	1.4546	1.4816
10°	0.6	1.4076	1.4034	1.4256
	0.8	1.3742	1.3708	1.3913
	1.0	1.3744	1.3710	1.3919
	1.2	1.3940	1.3900	1.4121
	1.4	1.4227	1.4180	1.4418
20°	0.6	1.2806	1.2774	1.2921
	0.8	1.2806	1.2776	1.2928
	1.0	1.3034	1.3001	1.3168
	1.2	1.3386	1.3347	1.3536
	1.4	1.3789	1.3742	1.3955
30°	0.6	1.1971	1.1935	1.2045
	0.8	1.2225	1.2186	1.2313
	1.0	1.2626	1.2585	1.2736
	1.2	1.3104	1.3057	1.3235
	1.4	1.3602	1.3548	1.3754
40°	0.6	1.1398	1.1363	1.1446
	0.8	1.1823	1.1782	1.1891
	1.0	1.2378	1.2331	1.2472
	1.2	1.2981	1.2928	1.3102
	1.4	1.3575	1.3514	1.3721

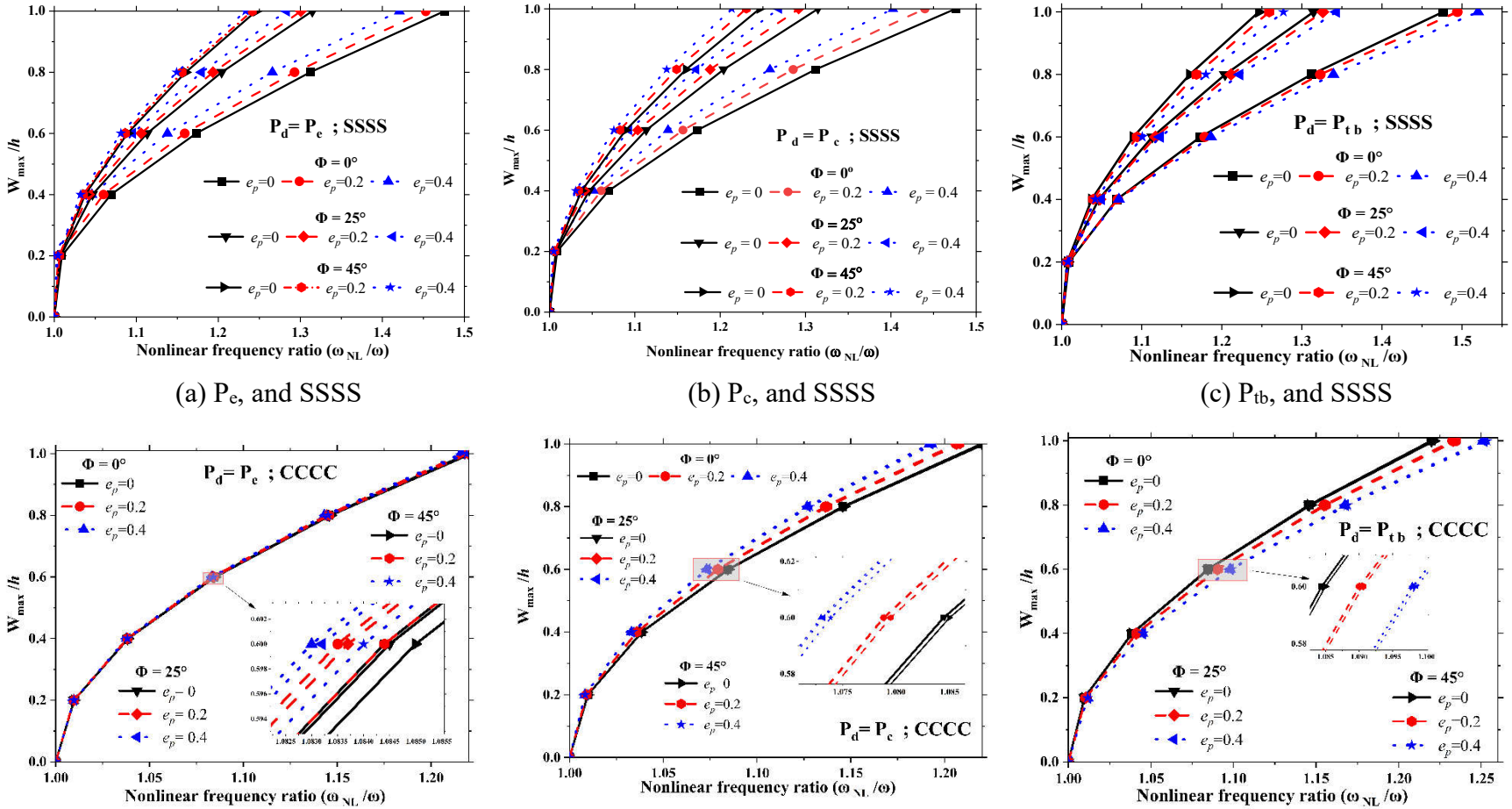

(a) P_e, and SSSS (b) P_c, and SSSS (c) P_{tb}, and SSSS

(d) P_e, and CCCC (e) P_c, and CCCC (f) P_{tb}, and CCCC

Figure 2.7: Effect of porosity volume index for different skew angles on the NLFR of ZrO_2 / Ti-6Al-4V PFGS plates with various porosity distributions and boundary conditions.

Furthermore, the lowest NLFR is observed for the porosity distribution $P_{c,}$ while P_{tb} exhibits the highest for all the instances of aspect ratio ($P_c < P_e < P_{tb}$). It may be due to the increase in porosities as the aspect ratio increases and the degradation of material properties.

2.7.4. Effect of porosity volume index (e_p)

The effect of various porosity volume indices for different skew angles on the NLFR of simply supported Si_3N_4/SUS304 PFGS plate for m = 1 at an amplitude ratio of W_{max}/h = 1.0 is shown in Table 2.10. It can be observable that, irrespective of skew angles for the porosity distributions P_e and P_c, the NLFR decreases with an increase in porosity volume index while it increases for the P_{tb} type of porosity distribution. It can be due to the degradation of the properties of the PFGS plate in the presence of distributions of porosities and geometric nonlinearity in the gradation region. Comparatively, the P_{tb} type of porosity distribution has a higher value of NLFR for all the porosity volume indices, and P_c exhibits the lowest values of NLFR ($P_c < P_e < P_{tb}$). It implies that P_c's porosity distribution has less significance in varying NLFR for different porosity volume indices. Also, it can be noted that as the skewness of the plate increases, the NLFR decreases gradually for all types of porosity distributions.

The influence of the porosity volume index for various boundary conditions on NLFR for P_e, $P_{c,}$ and P_{tb} types of porosity distributions is revealed in Figure 2.7. The geometrical parameters used for the PFGS plate are a/b = 1, a/h = 40, and m = 1 for skew angles Φ= 0°, 25°, and 45°. It can be seen that the NLFR has higher values for SSSS boundary conditions compared to clamped boundary conditions for all porosity distributions. It signifies that the stiffness of the plate increases for clamped plate in the presence of porosities and leads to an increase in the linear frequency. Therefore, NLFR decreases for the clamped case and increases for the simply supported case. Further, the noticeable difference in NLFR is discerned in clamped boundary conditions for variation of porosity volume index and skew angles. Also, P_c has the lowest NLFR values than P_e and P_{tb} type of porosity distributions irrespective of skew angles. This infers that the presence of porosities in the middle portion of the plate has a lower impact on the NLFR. Besides, the NLFR decreases steadily as the porosity volume index and skew angle increase for both the boundary conditions.

2.7.5. Effect of boundary conditions

The influence of porosity distributions on the NLFR for various boundary conditions is shown in Figure 2.8. The geometrical parameters used for the PFGS plate are $a/b = 1$, $a/h = 10$, $m = 1$, $e_p = 0.10$, and $\Phi = 15°$, and the porous material is ZrO_2 / Ti-6Al-4V. It can be seen from Figure 2.8 that the NLFR values are minimum for the CCCF boundary condition and maximum for the simply supported condition. For the cases of both fully clamped and simply supported edges of the plate, the simply supported plates exhibit maximum values of NLFR compared to a fully clamped plate. The effect of boundary conditions on the NLFR follows the trend as SSSS > SSSF > SCSC > CCCC > CCCF. It may be attributed to porosity and increased linear frequencies for clamped boundary conditions.

Table 2.10: Effect of porosity volume index for various skew angles on the NLFR (ω_{NL}/ω) for different porosity distributions of simply supported Si_3N_4 / SUS304 PFGS plate. ($a/h = 20$, $a/b = 1$, $m = 1$, and $W_{max} / h = 1.0$).

Φ	P_d	Porosity volume index (e_p)						
		0.0	0.05	0.15	0.25	0.35	0.45	0.55
	P_e	1.4568	1.4511	1.4384	1.4235	1.4056	1.3831	1.3531
5°	P_c	1.4568	1.4480	1.4302	1.4121	1.3935	1.3744	1.3548
	P_{tb}	1.4568	1.4601	1.4676	1.4766	1.4876	1.5012	1.5186
	P_e	1.4041	1.3988	1.3871	1.3738	1.3582	1.3389	1.3138
15°	P_c	1.4041	1.3964	1.3809	1.3651	1.3490	1.3325	1.3155
	P_{tb}	1.4041	1.4066	1.4125	1.4197	1.4286	1.4398	1.4543
	P_e	1.3416	1.3374	1.3283	1.3180	1.3059	1.2913	1.2728
25°	P_c	1.3416	1.3353	1.3227	1.3099	1.2967	1.2832	1.2693
	P_{tb}	1.3416	1.3438	1.3490	1.3553	1.3631	1.3730	1.3859
	P_e	1.2934	1.2905	1.2842	1.2768	1.2682	1.2578	1.2446
35°	P_c	1.2934	1.2883	1.2780	1.2675	1.2567	1.2456	1.2340
	P_{tb}	1.2934	1.2957	1.3010	1.3073	1.3151	1.3249	1.3374
	P_e	1.2605	1.2587	1.2545	1.2495	1.2435	1.2360	1.2267
45°	P_c	1.2605	1.2563	1.2477	1.2389	1.2298	1.2203	1.2104
	P_{tb}	1.2605	1.2630	1.2686	1.2752	1.2831	1.2927	1.3049

Also, the NLFR increases as the amplitude ratio increases for all the edge constraining cases of the PFGS plate. Besides, irrespective of boundary constraints, porosity distribution P_{tb} dominates the other two (P_e and P_c) by exhibiting the highest NLFR, and P_c displays the lowest NLFR ($P_c < P_e < P_{tb}$). This infers that the presence of porosities in the middle portion of the plate is less affected by boundary constraints than the porosity distribution P_{tb} on NLFR.

2.8. Nonlinear transient deflection analysis

This section investigates the nonlinear transient deflection of the PFGS plate. The influence of skew angle, porosity distribution, porosity volume index, and volume fraction grading index on the nonlinear transient deflection is studied. The geometrical parameters of the plate $a/h = 40$, $a/b = 1$ under a uniform step load of q_0=1 N/mm^2 with a time step of $\Delta t_i = 1\times10^{-5}$ being considered for the simply supported Si_3N_4/SUS304 PFGS plate. The dimensionless central deflection parameter considered for the study is $\overline{w_c} = w_c / h$.

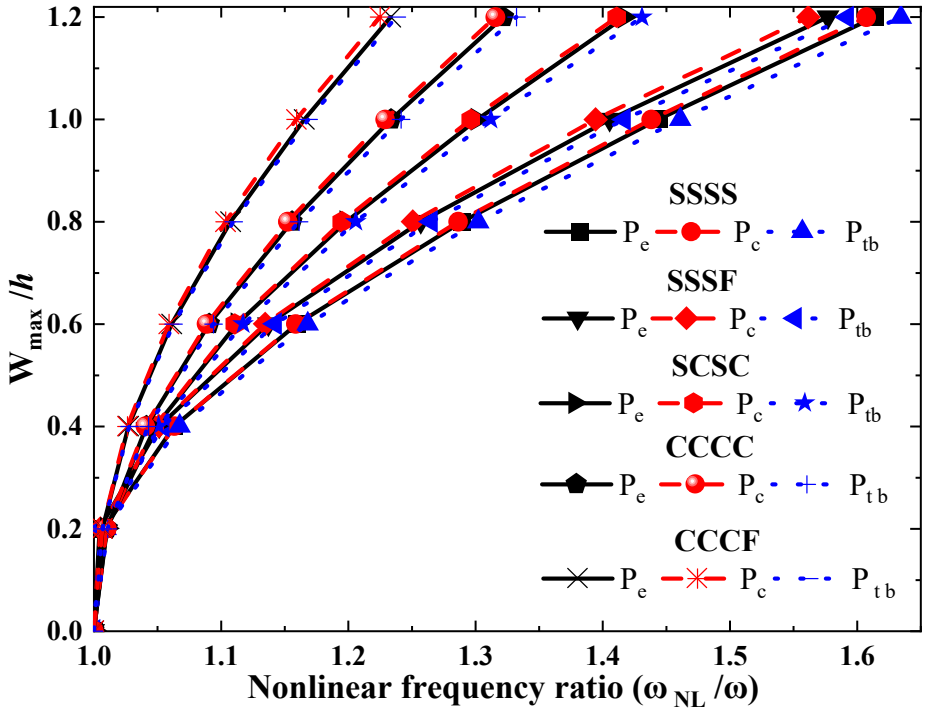

Figure 2.8: Influence of porosity distributions on the NLFR for various boundary conditions for ZrO_2 / Ti-6Al-4V PFGS plate.

2.8.1. Effect of porosity volume index

The effects of porosity volume indices e_p= 0.1, 0.2, and 0.3 on various skew angles Φ = 15°, 30°, and 45° for P_e, P_c, and P_{tb} types of porosity distributions are investigated. It can be observed from Figure 2.9 that the nonlinear transient deflection decreases with an increase in skew angle. This may be due to the increase in stiffness of the plate, which increases with an increase in the skew angle. Besides, the porosity volume index also influences deflection. As a result, the nonlinear deflection also increases for an increase in the porosity volume index. It can also be seen that for the P_e type distribution, the transient deflection is highest. In contrast, the P_c type distribution exhibits the lowest nonlinear transient deflection irrespective of skew angles. Analogously, for a given value of e_p and skew angle, the effect of porosity distributions on the transient deflections follows the trend as $P_c < P_{tb} < P_e$. Moreover, for the P_c type porosity distribution, a noticeable difference is discerned for all the porosity volume index values.

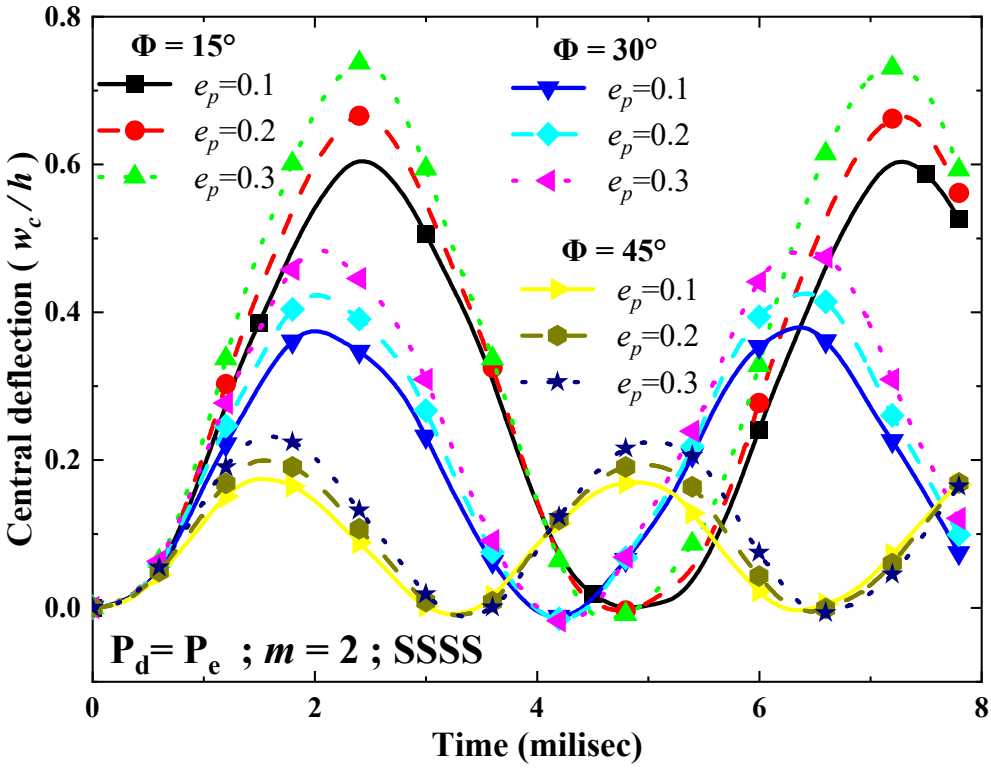

(a) P_e

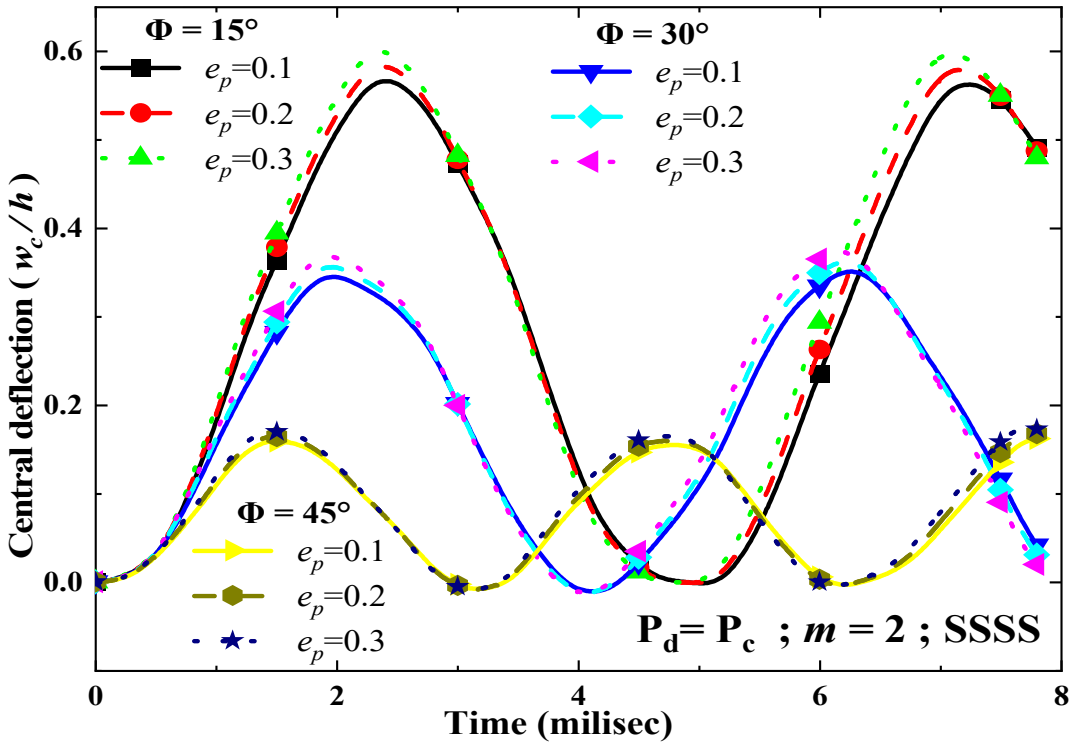

(b) P_c

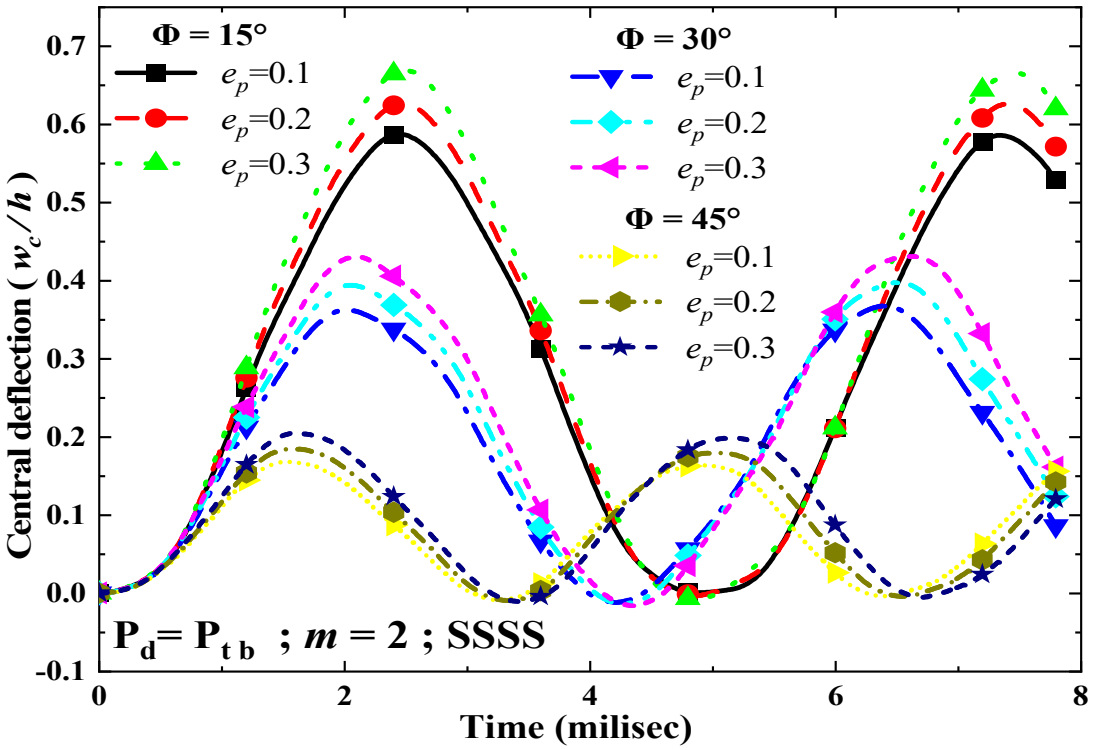

(c) P_{tb}

Figure 2.9: Effect of porosity volume index on central deflection (w_c / h) for various skew angles and porosity distributions on simply supported Si_3N_4 / SUS304 PFGS plate.

2.8.2. Effect of volume fraction grading index

The effects of various volume fraction grading indexes m = 0, 0.5, 2, 10, and ∞ for P_e, P_c, and P_{tb} types of distributions on a transient deflection of the PFGS plate are shown in Figure 2.10. It can be seen that the nonlinear transient deflection increases with an increase in the volume fraction grading index (m). It is due to a decrease in the plate's ceramic composition as m increases, hence the reduction in the stiffness of the plate. Figure 2.10 reveals that the P_e type of distribution exhibits the highest, and the P_c type presents the lowest nonlinear transient deflections for each value of m and follows the trend as $P_e > P_{tb} > P_c$. Hence, the distribution of porosity influences the deflection of the PFGS plate.

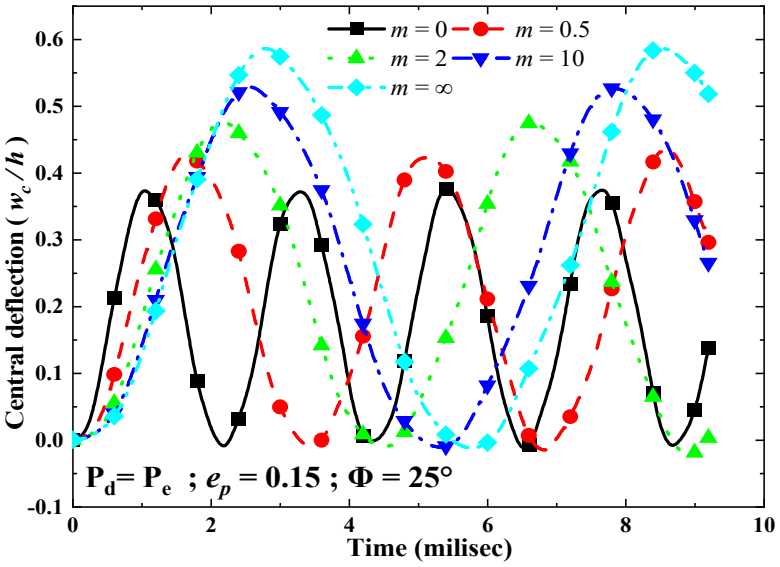

(a) P_e

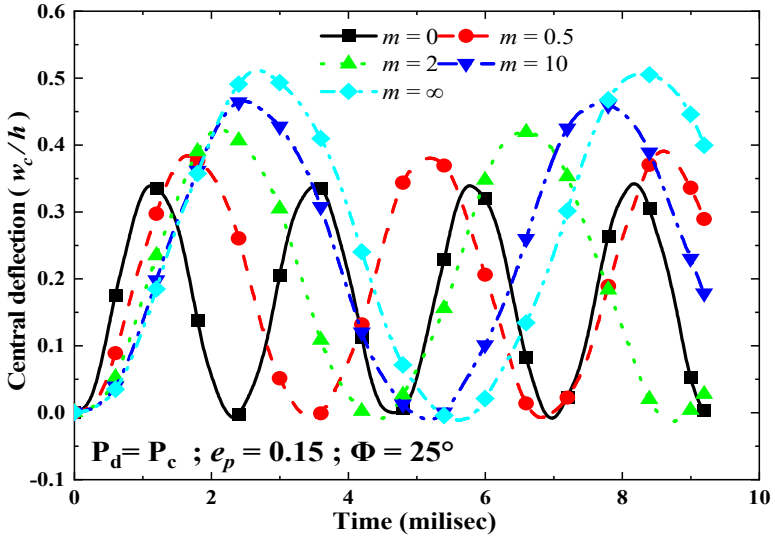

(b) P_c

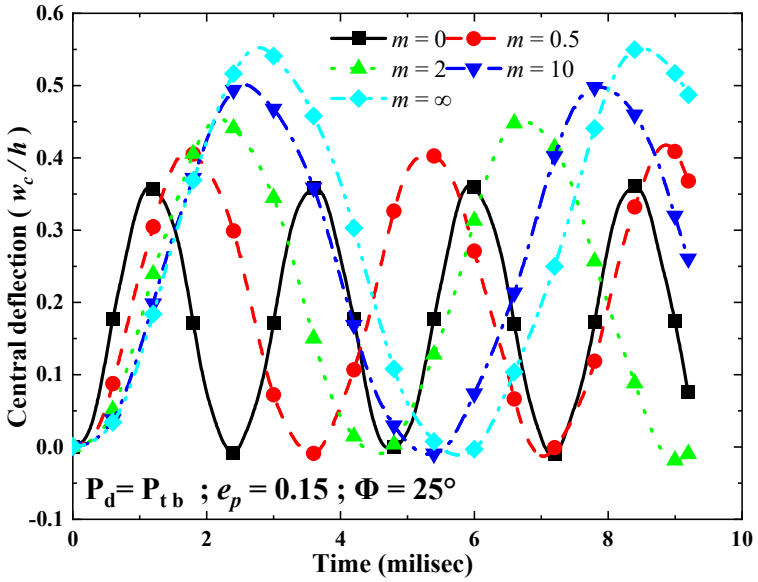

(c) P_{tb}

Figure 2.10: Effect of volume fraction grading index on central deflection (w_c / h) for different porosity distribution on the simply supported Si_3N_4 / SUS304 PFGS plate.

2.9. CONCLUSIONS

This chapter investigates the impact of porosity distributions for skewness on nonlinear free vibration and transient responses of porous functionally graded skew plates. The nonlinear FE formulation is adopted in the framework of FSDT in conjunction with von Karman's nonlinear relations. The effective material properties are extracted from the modified power-law distribution considering the different types of porosity distributions in the plate. The governing equations of the PFGS plates are derived using the principle of virtual work, incorporating a direct iterative technique to extract nonlinear frequency parameters and Newmark's integration technique for the nonlinear transient response.

From the detailed parametric analysis, the following observations are made. The NLFR decreases while the NLFP increases with the skew angle rise. The NLFR and NLFP are more sensitive to the centrally distributed porosity (P_c) than the P_e and P_{tb} porosity distributions for all skew angles. The NLFR decreases with an increase in porosity volume index for evenly distributed and centrally distributed porosities while it increases for the P_{tb} type of porosity distribution. For any given type of porosity distribution, the NLFR value is minimum for the CCCF boundary condition and maximum for the simply supported case. The nonlinear transient deflections of the

PFGS plate increase with the increase in porosity volume index and volume fraction grading index. In contrast, it decreases with the rise in skew angle. Besides, the distributions of porosities exhibit a significant impact on reducing the stiffness of the PFGS plates.

CHAPTER 3

EFFECT OF DIFFERENT GEOMETRICAL NON-UNIFORMITIES ON NONLINEAR VIBRATION OF POROUS FUNCTIONALLY GRADED SKEW PLATES

This chapter presents the investigation of nonlinear vibration analysis of tapered porous functionally graded skew (TPFGS) plate considering the effects of geometrical non-uniformities to optimize the thickness in the structural design. The TPFGS plate is studied with a thickness that varies linearly, bi-linearly, and exponentially. The nonlinear finite element formulation derived in chapter 2 is used for the analysis of TPFGS plates. The influence of the porosity distributions and porosity volume indices on the nonlinear frequency responses of the TPFGS plate for different skew angles and variable thicknesses is studied with various geometrical parameters. The influence of taper ratio, variable thickness, skewness, porosity distributions, gradation, and boundary conditions on the plate's nonlinear vibration is demonstrated. The nonlinear frequency analysis reveals that the geometrical non-uniformities and porosities significantly influence the porous functionally graded plates with varying thicknesses rather than the uniform thickness. Besides, exponentially and linearly variable thicknesses can be considered for the thickness optimizations of TPFGS plates in the structural design.

3.1. INTRODUCTION

Geometrically non-uniform FG porous plates are critical in various engineering applications, as geometric variations on the rectangular FG porous plate affect the variability of response characteristics. Hence, this chapter presents the influence of porosity distributions on the nonlinear free vibration analysis of the functionally graded porous plates with various geometrical non-uniformities. The effective material properties of the FG porous plate are computed using a modified power-law

distribution. A nonlinear FE model is developed in conjunction with von Karman's geometric nonlinearity, considering the porosities with the aid of Hamilton's principle under the framework of shear deformation theory. Further, the research focuses on the influence of the porosity distributions and the geometric non-uniformities such as skewness and various kinds of variable thickness, i.e., linearly, bi-linearly, and exponentially varying thickness. Besides, the influence of taper ratio, skewness, porosity distributions, gradation, and boundary conditions on the plate's structural behavior is investigated in detail.

3.2. PROBLEM DESCRIPTION AND GOVERNING EQUATION

3.2.1. TPFGS plate geometry

The schematic diagram of the tapered porous functionally graded skew (TPFGS) plate is depicted in Figure 3.1. The dimensional parameters refer to a Cartesian coordinate with the x, y, and z coordinate axes spanning its length a, width b, and tapered thickness h (x, y).

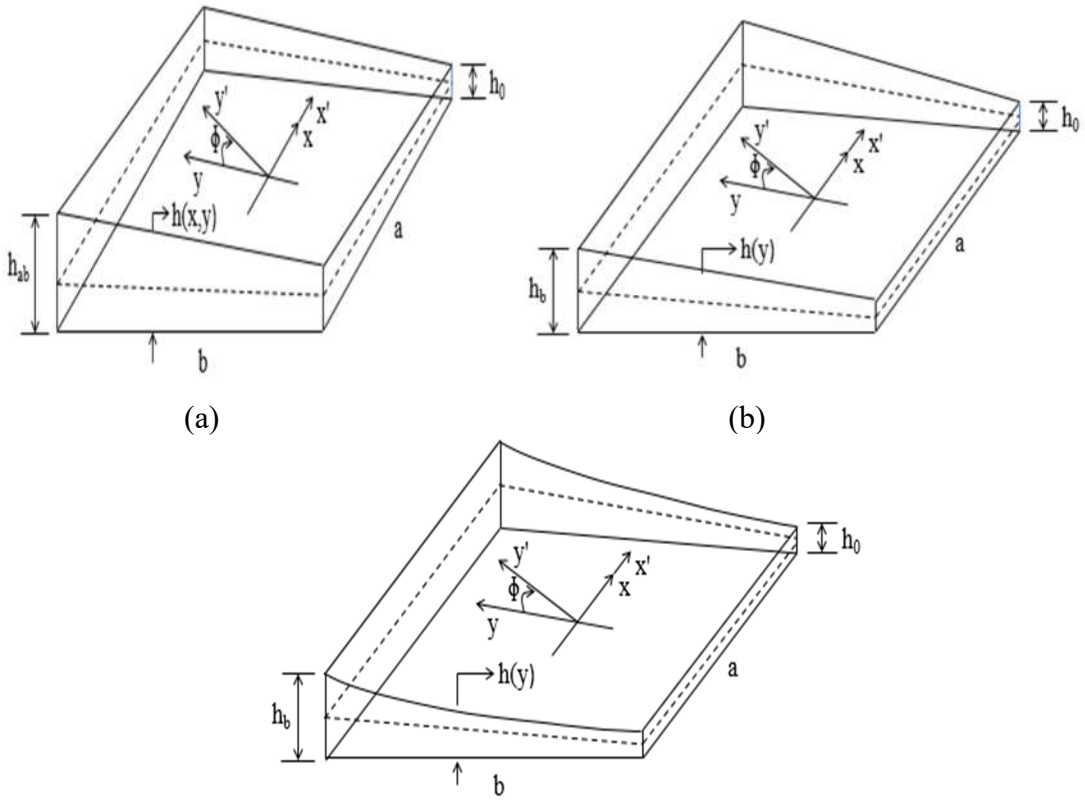

Figure 3.1: The geometry of the TPFGS plate. (a) Bi-linearly variable thickness, (b) Linearly variable thickness, and (c) Exponentially variable thickness.

The geometrical skewness of the TPFGS plate is measured by rotating the coordinate y at an angle Φ called the skew angle. The TPFGS plate consists of different types of variable thickness, *viz.* linearly (h (y)), bi-linearly (h (x, y)), and exponentially (h (y)) variable thickness, as shown in Figures 3.1 (a) – (c), where h is a function of both x and y coordinates for bi-linearly variable thickness, while h is a function of the only y coordinate for linearly and exponentially variable thicknesses.

The effective material properties of the TPFGS plate represented are identical to Section 2.2.1 of Chapter 2. However, the evenly distributed and centrally distributed porosity distributions are considered for the present analysis. Besides, the tapered thickness h depends on the type of variable thickness, such as linearly (h (y)), bi-linearly (h (x, y)), and exponentially (h (y)) variable thickness, used in the analysis for the derivation of the formulation for TPFGS plate. In addition, the displacement equations, von Kármán's strain-displacement equations, the constitutive equations, the governing equations, the nonlinear FE formulation and solution methodologies are provided in the same manner as in Sections 2.2 and 2.3.

3.2.2. Variable thickness

(a) *Bi-linearly variable thickness* (h (x,y)): If non-uniformity of thickness changes in both the directions, i.e., x- and y- directions of the TPFGS plate as depicted in Figure 3.1(a), *i.e.,* taper ratio's $\beta = \chi \neq 0$. Then the function for *bi-linearly variable thickness* (h (x,y)) varies in both x and y directions can be stated as follows:

$$h(x,y) = h_0\left(1+\beta\left(\frac{y}{b}\right)\right)\left(1+\chi\left(\frac{x}{a}\right)\right) \tag{3.1}$$

whereas, $\beta = \dfrac{h_{ab}-h_0}{h_0}$; $\chi = \dfrac{h_{ab}-h_0}{h_0}$ (3.2)

where β and χ are taper ratios in the y and x directions, respectively; h_0 is the initial thickness of the bi-linearly tapered PFGS plate; h_{ab} is the plate's maximum thickness varies in both x and y directions, and x/a and y/b are the dimensionless parameters.

(b) *Linearly variable thickness* ($h(y)$): If the non-uniformity of thickness is considered only in the y-direction as shown in Figure 3.1(b), i.e., taper ratio $\beta \neq 0$, and $\chi = 0$. Then, the function for *linearly variable thickness* h (y) in the y-direction can be expressed as follows:

$$h(y) = h_0\left(1+\beta\left(\frac{y}{b}\right)\right) \tag{3.3}$$

whereas,
$$\beta = \frac{h_b - h_0}{h_0} \tag{3.4}$$

where β is the taper ratio in y-direction; h_0 is the initial thickness of the linearly tapered PFGS plate; h_b is the maximum thickness of the TPFGS plate, which varies y-direction, and y/b is the dimensionless parameter.

(c) Exponentially variable thickness ($h(y)$): If the non-uniformity of thickness varies exponentially in the y-direction as represented in Figure 3.1(c), i.e., taper ratio $\beta \neq 0$, and $\chi = 0$. Then, the function for *exponentially variable thickness* $h(y)$ in the y-direction can be expressed as follows:

$$h(y) = h_0\, e^{\left(\left(\frac{y}{b}\right)\log(\beta+1)\right)} \tag{3.5}$$

whereas,
$$\beta = \frac{h_b - h_0}{h_0} \tag{3.6}$$

where β is the taper ratio in y-direction; h_0 is the initial thickness of the linearly tapered PFGS plate; h_b is the maximum thickness of the TPFGS plate, which varies y-direction, and y/b is the dimensionless parameter.

3.3. RESULTS AND DISCUSSIONS

The TPFGS plate made of Si_3N_4 / SUS304 is considered to investigate the influence of porosity distributions coupled with geometrical non-uniformities on the nonlinear free vibration responses. The plate's top surface is tapered and consists of ceramic material, while its bottom metallic surface is flat. These materials, including porosities, are graded between the tapered top surface and the bottom surface. The TPFGS plate consists of Si_3N_4/SUS304 material with the properties of Young's modulus (E), Poisson's ratio (ϑ), and density (ρ) for the ceramic (Si_3N_4) and metal (SUS304) given in Table 2.1.

Furthermore, numerous examples are demonstrated to study the significance of porosity distributions, porosity volume index, volume fraction grading index, aspect ratio, and span-thickness ratio for various skew angles and the taper ratios of different types of variable thicknesses on the large amplitude free vibrations of the TPFGS plate.

Table 3.1: Comparison of the square isotropic tapered plate with various boundary conditions.

Boundary conditions	*a*/*h*	Methods	Taper ratio (β)	ω
SSSS	100	Mizusawa (1993)	0.50	24.543
		Manna (2012)		25.0594
		Kumar et al. (2021)		24.543
		Present		24.6638
		Mizusawa (1993)	1	29.184
		Manna (2012)		30.8965
		Kumar et al. (2021)		29.184
		Present		29.5910
CCCC	100	Manna (2012)	0.25	40.309
		Kumar et al. (2021)		41.9982
		Present		40.5676
	5	Manna (2012)	0.25	28.154
		Kumar et al. (2021)		30.976
		Present		29.1148
CCSS	100	Manna (2012)	0.25	32.441
		Kumar et al. (2021)		32.3085
		Present		32.5515
	10	Manna (2012)	0.25	29.339
		Kumar et al. (2021)		29.8564
		Present		29.8499

3.3.1. Convergence and validation

This section is devoted to verifying the proposed nonlinear FE formulation. The fundamental natural frequencies of a square isotropic tapered plate are compared with the earlier results (Kumar et al. 2021; Manna 2012; Mlzusawa 1993) for the span ratio (a / h_0) 100, 10, and 5, and the taper ratio for linearly varying thickness (β) 0.25, 0.50, and 1.0. The mesh size of [8 × 8] is used based on progressive mesh refinement. The results in Table 3.1 shows an excellent agreement with the reference literature (Kumar et al. 2021; Manna 2012; Mlzusawa 1993). Further, all validation studies presented in

section 2.5 except Example 5 have also been implemented for the present analysis. The nonlinear FE formulation derived in the present study is used for the parametric studies on porosity distribution's influence on TPFGS plates with variable thickness and skewness. The mesh size [8 × 8] used for the validation is adopted to extract all parametric results.

3.3.2. Numerical results

This section presents a study on the nonlinear to linear frequency ratios (NLFR) (ω_{NL}/ω) of the TPFGS plate with geometrical skewness for different taper ratios of various non-uniform thicknesses (linear, bi-linear, and exponentially varying thicknesses). Besides, the plots illustrate the non-dimensional nonlinear frequency parameter (NLFP) of the TPFGS plate with different boundary conditions, taper ratios, skew angles, porosity volume index, variable thicknesses, and porosity distributions. Unless otherwise stated, the following dimensionless equation is considered for the parametric study of the square Si_3N_4/SUS304 TPFGS plate to extract NLFP:

$$\omega_{NL} = \bar{\omega}_{NL}\, a^2 \sqrt{12\rho_c(1-\upsilon_c^2)/\mathrm{E}_c h_0^2} \tag{3.7}$$

3.3.3. Effect of volume fraction grading index and taper ratio

This section presents a study on the nonlinear frequency ratios (NLFR) (ω_{NL}/ω) of the TPFGS plate with geometrical skewness for different taper ratios of various non-uniform thicknesses such as linear, bi-linear, and exponentially varying thicknesses. Tables 3.2 – 3.4 present the NLFR for different taper ratios for each type of variable thickness and the plate's porosity distributions. The influence of a porosity distribution is computed for a different value of the volume fraction grading index (m = 0, 0.5, 1, 2, 5, 10). The taper ratios for both the linearly and exponentially varying thicknesses are β = 0, 0.25, 0.50, and 1.0 meanwhile, the taper ratio for bi-linearly varying thickness is $\beta = \chi$ = 0, 0.25, 0.50, and 1.0.

A comparative study of two types of porosity distribution P_e and P_c, is presented for the plate edge supported by SSSS boundary conditions. It is depicted from the results that with an increase in the volume fraction index (m) for both P_e and P_c, the NLFR decreases till m = 2, whereas the trend reverses from m = 5. The same trend is noticed for uniform

plate thickness and all variable plate thickness types, irrespective of taper ratios and porosity distributions. It may be due to the decrease in ceramic composition with an increase in the volume fraction grading index, leading to a decrease in the plate's stiffness, and the frequency is proportionally dependent on it.

Table 3.2: Effect of volume fraction grading index on the NLFR (ω_{NL}/ω) of linearly variable thickness Si_3N_4 / SUS304 TPFGS plate for the different taper ratio (β). (a/b = 1, h_0 = 1/10, e_p = 0.1, $\Phi = 0°$, $\chi = 0$, and SSSS).

m	W_{max}/h									
	0.2		0.4		0.6		0.8		1.0	
	P_e	P_c	P_e	P_c	P_e	P_c	P_e	P_c	P_e	P_c
$\beta = 0$										
0	1.0267	1.0262	1.1031	1.1014	1.2204	1.2170	1.3688	1.3633	1.5397	1.5320
0.5	1.0102	1.0107	1.0733	1.0731	1.1816	1.1798	1.3248	1.3207	1.4934	1.4866
1	1.0042	1.0051	1.0612	1.0618	1.1640	1.1632	1.3027	1.2998	1.4677	1.4622
2	1.0022	1.0033	1.0557	1.0568	1.1542	1.1542	1.2882	1.2864	1.4485	1.4443
5	1.0072	1.0080	1.0636	1.0642	1.1629	1.1623	1.2958	1.2933	1.4537	1.4490
10	1.0133	1.0136	1.0753	1.0749	1.1790	1.1771	1.3152	1.3111	1.4753	1.4687
$\beta = 0.25$										
0	1.0270	1.0266	1.1042	1.1026	1.2227	1.2194	1.3724	1.3671	1.5447	1.5372
0.5	1.0106	1.0110	1.0745	1.0743	1.1840	1.1823	1.3286	1.3246	1.4985	1.4920
1	1.0045	1.0054	1.0624	1.0630	1.1664	1.1657	1.3065	1.3038	1.4729	1.4676
2	1.0025	1.0036	1.0569	1.0580	1.1567	1.1567	1.2921	1.2904	1.4538	1.4498
5	1.0075	1.0083	1.0648	1.0654	1.1653	1.1648	1.2996	1.2974	1.4589	1.4544
10	1.0136	1.0140	1.0765	1.0762	1.1814	1.1796	1.3190	1.3150	1.4805	1.4741
$\beta = 0.50$										
0	1.0273	1.0269	1.1055	1.1039	1.2254	1.2221	1.3765	1.3714	1.5503	1.5429
0.5	1.0109	1.0114	1.0758	1.0757	1.1867	1.1850	1.3328	1.3290	1.5042	1.4979
1	1.0049	1.0058	1.0637	1.0644	1.1692	1.1686	1.3108	1.3082	1.4787	1.4769
2	1.0029	1.0040	1.0582	1.0594	1.1594	1.1596	1.2964	1.2949	1.4597	1.4560
5	1.0079	1.0087	1.0662	1.0668	1.1681	1.1676	1.3040	1.3018	1.4649	1.4606
10	1.0140	1.0143	1.0778	1.0775	1.1841	1.1824	1.3233	1.3195	1.4864	1.4803
$\beta = 1.0$										
0	1.0281	1.0277	1.1085	1.1070	1.2314	1.2284	1.3860	1.3812	1.5633	1.5565
0.5	1.0117	1.0122	1.0789	1.0788	1.1930	1.1915	1.3426	1.3391	1.5173	1.5117
1	1.0057	1.0066	1.0668	1.0675	1.1755	1.1751	1.3208	1.3185	1.4921	1.4877
2	1.0037	1.0048	1.0613	1.0626	1.1658	1.1661	1.3065	1.3053	1.4734	1.4701
5	1.0087	1.0095	1.0692	1.0700	1.1744	1.1742	1.3140	1.3122	1.4786	1.4749
10	1.0148	1.0152	1.0809	1.0807	1.1904	1.1889	1.3332	1.3298	1.5000	1.4975

Table 3.3: Effect of volume fraction index on the NLFR (ω_{NL}/ω) of bi-linearly variable thickness Si_3N_4 / SUS304 TPFGS plate for the different taper ratio ($\beta = \chi$). ($a/b = 1$, $h_0 = 1/10$, $e_p = 0.1$, $\Phi = 0°$, and SSSS).

m	W_{max}/h									
	0.2		0.4		0.6		0.8		1.0	
	P_e	P_c	P_e	P_c	P_e	P_c	P_e	P_c	P_e	P_c
$\beta = \chi = 0$										
0	1.0267	1.0262	1.1031	1.1014	1.2204	1.2170	1.3688	1.3634	1.5396	1.5320
0.5	1.0102	1.0107	1.0733	1.0731	1.1816	1.1797	1.3248	1.3207	1.4933	1.4867
1	1.0042	1.0051	1.0612	1.0618	1.1640	1.1632	1.3027	1.2998	1.4677	1.4622
2	1.0022	1.0033	1.0557	1.0568	1.1542	1.1542	1.2883	1.2864	1.4485	1.4443
5	1.0072	1.0080	1.0636	1.0642	1.1629	1.1623	1.2958	1.2933	1.4536	1.4490
10	1.0133	1.0136	1.0753	1.0749	1.1790	1.1771	1.3152	1.3111	1.4753	1.4687
$\beta = \chi = 0.25$										
0	1.0274	1.0270	1.1057	1.1041	1.2257	1.2225	1.3770	1.3719	1.5509	1.5437
0.5	1.0110	1.0114	1.0760	1.0759	1.1871	1.1854	1.3333	1.3295	1.5050	1.4987
1	1.0049	1.0059	1.0639	1.0645	1.1695	1.1689	1.3114	1.3088	1.4795	1.4745
2	1.0029	1.0040	1.0584	1.0596	1.1598	1.1599	1.2970	1.2954	1.4605	1.4568
5	1.0079	1.0087	1.0663	1.0670	1.1684	1.1680	1.3045	1.3024	1.4656	1.4615
10	1.0140	1.0144	1.0780	1.0777	1.1845	1.1827	1.3238	1.3200	1.4872	1.4811
$\beta = \chi = 0.50$										
0	1.0284	1.0280	1.1093	1.1079	1.2331	1.2301	1.3887	1.3840	1.5670	1.5603
0.5	1.0119	1.0125	1.0798	1.0797	1.1947	1.1933	1.3453	1.3419	1.5213	1.5156
1	1.0059	1.0069	1.0676	1.0684	1.1772	1.1769	1.3235	1.3213	1.4959	1.4916
2	1.0039	1.0051	1.0622	1.0634	1.1675	1.1680	1.3093	1.3082	1.4771	1.4741
5	1.0089	1.0098	1.0701	1.0709	1.1762	1.1760	1.3168	1.3151	1.4824	1.4789
10	1.0150	1.0154	1.0817	1.0816	1.1922	1.1907	1.3360	1.3326	1.5037	1.4983
$\beta = \chi = 1.0$										
0	1.0315	1.0312	1.1208	1.1197	1.2563	1.2541	1.4253	1.4218	1.6101	1.6001
0.5	1.0150	1.0157	1.0914	1.0918	1.2185	1.2178	1.3827	1.3806	1.5725	1.4347
1	1.0090	1.0101	1.0794	1.0805	1.2012	1.2017	1.3683	1.3604	1.4302	1.4292
2	1.0070	1.0083	1.0740	1.0756	1.1917	1.1929	1.3474	1.3476	1.5315	1.5285
5	1.0120	1.0130	1.0819	1.0830	1.2003	1.2009	1.3550	1.3547	1.5381	1.5336
10	1.0181	1.0186	1.0935	1.0937	1.2161	1.2154	1.3738	1.3718	1.5487	1.4295

As a result, a rapid decrease in the linear frequency is observed for higher values of the volume fraction grading index, leading to an increase in the difference between nonlinear frequency and linear frequency. Hence, the NLFR increases for higher values of volume fraction grading index.

Table 3.4: Effect of volume fraction index on the NLFR (ω_{NL}/ω) of exponentially variable thickness Si_3N_4 / SUS304 TPFGS plate for the different taper ratio (β). (a/b = 1, h_0 = 1/10, e_p = 0.1, Φ = 0°, χ = 0, and SSSS).

m	W_{max}/h									
	0.2		0.4		0.6		0.8		1.0	
	P_e	P_c	P_e	P_c	P_e	P_c	P_e	P_c	P_e	P_c
$\beta = 0$										
0	1.0267	1.0262	1.1031	1.1014	1.2204	1.2170	1.3688	1.3633	1.5397	1.5320
0.5	1.0102	1.0107	1.0733	1.0731	1.1816	1.1798	1.3248	1.3207	1.4934	1.4866
1	1.0042	1.0051	1.0612	1.0618	1.1640	1.1632	1.3027	1.2998	1.4677	1.4622
2	1.0022	1.0033	1.0557	1.0568	1.1542	1.1542	1.2882	1.2864	1.4485	1.4443
5	1.0072	1.0080	1.0636	1.0642	1.1629	1.1623	1.2958	1.2933	1.4537	1.4490
10	1.0133	1.0136	1.0753	1.0749	1.1790	1.1771	1.3152	1.3111	1.4753	1.4687
$\beta = 0.25$										
0	1.0270	1.0265	1.1042	1.1025	1.2227	1.2193	1.3723	1.3670	1.5445	1.5370
0.5	1.0105	1.0110	1.0745	1.0743	1.1840	1.1822	1.3284	1.3244	1.4983	1.4918
1	1.0045	1.0054	1.0623	1.0629	1.1664	1.1657	1.3064	1.3036	1.4727	1.4674
2	1.0025	1.0036	1.0568	1.0579	1.1566	1.1566	1.2920	1.2902	1.4536	1.4496
5	1.0075	1.0083	1.0648	1.0654	1.1652	1.1647	1.2995	1.2972	1.4587	1.4543
10	1.0136	1.0140	1.0764	1.0761	1.1813	1.1795	1.3188	1.3149	1.4803	1.4740
$\beta = 0.50$										
0	1.0273	1.0269	1.1053	1.1037	1.2250	1.2217	1.3760	1.3707	1.5494	1.5421
0.5	1.0109	1.0113	1.0757	1.0755	1.1864	1.1846	1.3322	1.3284	1.5034	1.4970
1	1.0048	1.0058	1.0635	1.0642	1.1688	1.1682	1.3102	1.3076	1.4779	1.4728
2	1.0028	1.0039	1.0580	1.0592	1.1590	1.1592	1.2959	1.2942	1.4589	1.4551
5	1.0078	1.0086	1.0660	1.0666	1.1677	1.1672	1.3034	1.3012	1.4640	1.4598
10	1.0139	1.0143	1.0776	1.0773	1.1838	1.1820	1.3227	1.3189	1.4856	1.4794
$\beta = 1.0$										
0	1.0279	1.0275	1.1078	1.1063	1.2299	1.2269	1.3837	1.3788	1.5600	1.5531
0.5	1.0115	1.0120	1.0782	1.0781	1.1914	1.1899	1.3402	1.3366	1.5143	1.5082
1	1.0055	1.0064	1.0660	1.0668	1.1739	1.1735	1.3183	1.3160	1.4888	1.4874
2	1.0035	1.0046	1.0605	1.0618	1.1642	1.1645	1.3040	1.3027	1.4700	1.4666
5	1.0085	1.0093	1.0685	1.0692	1.1728	1.1726	1.3116	1.3097	1.4752	1.4714
10	1.0146	1.0150	1.0801	1.0799	1.1889	1.1873	1.3308	1.3272	1.4966	1.4909

Further, the NLFR increases with an increase in the taper ratio. It can be seen from Tables 3.2 – 3.4 that with an increase in the taper ratio, the degree of hardening nonlinearity increases. Consequently, the amplitude ratio significantly affects the NLFR for different values of the taper ratios. Analogously, for a given value of m, the

influence of different types of variable thickness on NLFR follows the trend as exponentially variable thickness < linearly variable thickness < bi-linearly variable thickness. An increase in the taper ratio increases the plate's stiffness, which results in a higher nonlinear frequency.

Additionally, the effect of porosity distribution on the NLFR follows the trend as centrally distributed porosity (P_c) < evenly distributed porosity (P_e), irrespective of different types of porosity distributions and taper ratio. The presence of porosities in the gradation region has significantly reduced the stiffness and weight of the plate. Hence, it has considerably less impact on the NLFR.

Table 3.5: Effect of porosity volume index on the NLFR (ω_{NL}/ω) of linearly variable thickness Si_3N_4 / SUS304 TPFGS plate for the different taper ratio (β) and skew angle (Φ). ($a/b = 1$, $h_0 = 1/10$, $m = 2$, $W_{max}/h = 1.0$, $\chi = 0$, and SSSS).

Φ	e_p	$\beta = 0$		$\beta = 0.1$		$\beta = 0.25$		$\beta = 0.50$	
		P_e	P_c	P_e	P_c	P_e	P_c	P_e	P_c
0°	0	1.4636	1.4636	1.4658	1.4658	1.4692	1.4692	1.4754	1.4754
	0.1	1.4485	1.4443	1.4506	1.4464	1.4538	1.4498	1.4597	1.4560
	0.2	1.4309	1.4246	1.4328	1.4267	1.4359	1.4300	1.4415	1.4361
	0.4	1.3826	1.3838	1.3843	1.3859	1.3871	1.3891	1.3922	1.3951
15°	0	1.4258	1.4258	1.4291	1.4291	1.4340	1.4340	1.4425	1.4425
	0.1	1.4118	1.4084	1.4150	1.4116	1.4198	1.4164	1.4279	1.4247
	0.2	1.3956	1.3907	1.3986	1.3938	1.4032	1.3985	1.4110	1.4066
	0.4	1.3516	1.3539	1.3543	1.3569	1.3584	1.3614	1.3654	1.3691
30°	0	1.3518	1.3518	1.3561	1.3561	1.3627	1.3627	1.3736	1.3736
	0.1	1.3411	1.3383	1.3453	1.3425	1.3516	1.3489	1.3621	1.3596
	0.2	1.3286	1.3245	1.3326	1.3286	1.3386	1.3348	1.3487	1.3453
	0.4	1.2950	1.2957	1.2985	1.2996	1.3038	1.3055	1.3127	1.3153
45°	0	1.2919	1.2919	1.2960	1.2960	1.3022	1.3022	1.3129	1.3129
	0.1	1.2850	1.2818	1.2890	1.2860	1.2951	1.2921	1.3049	1.3027
	0.2	1.2767	1.2715	1.2805	1.2756	1.2865	1.2817	1.2956	1.2917
	0.4	1.2539	1.2497	1.2573	1.2536	1.2625	1.2595	1.2714	1.2696

3.3.4. Effect of porosity volume index

The effect of geometrical skewness and porosity volume index on the NLFR for different types of variable thickness of the TPFGS plate is studied. Tables 3.5 – 3.7 depict the results of the NLFR for different skew angles, porosity volume index, taper ratio, and various types of variable thickness of the plate. A comparative study between P_e and P_c porosity distributions with geometrical skewness for several inconstant

thickness types is presented. As expected, with an increase in the porosity volume index for both P_e and P_c, the NLFR decreases irrespective of the taper ratio, skew angle, and the type of variable thickness. It can be due to the reduction in the TPFGS plate's stiffness on which the frequency depends proportionally. This kind of impulsive behavior arises because of non-dimensionalized parameters.

Further evaluation reveals that irrespective of the porosity distributions, taper ratio, and type of variable thickness, the NLFR decreases with an increase in the skew angle. The decrease in NLFR attributes to the rise in the plate's stiffness. The stiffness increases with the plate's skewness, on which the linear frequency rises. Meanwhile, the effect of porosity distributions on the NLFR follows the trend as centrally distributed porosity (P_c) < evenly distributed porosity (P_e), irrespective of the skew angle, taper ratio, and various types of variable thickness.

Table 3.6: Effect of porosity parameter index on the NLFR (ω_{NL}/ω) of bi-linearly variable thickness Si_3N_4 / SUS304 TPFGS plate for the different taper ratio ($\beta = \chi$) and skew angle (Φ). ($a/b = 1$, $h_0 = 1/10$, $m = 2$, $W_{max}/h = 1.0$, and SSSS).

Φ	e_p	$\beta = \chi = 0$		$\beta = \chi = 0.1$		$\beta = \chi = 0.25$		$\beta = \chi = 0.50$	
		P_e	P_c	P_e	P_c	P_e	P_c	P_e	P_c
0°	0	1.4636	1.4636	1.4681	1.4681	1.4762	1.4762	1.4939	1.4939
	0.1	1.4485	1.4443	1.4528	1.4487	1.4605	1.4568	1.4771	1.4741
	0.2	1.4309	1.4246	1.4350	1.4290	1.4423	1.4369	1.4580	1.4540
	0.4	1.3826	1.3838	1.3863	1.3881	1.3928	1.3959	1.4071	1.4128
15°	0	1.4258	1.4258	1.4326	1.4326	1.4435	1.4435	1.4648	1.4648
	0.1	1.4118	1.4084	1.4183	1.4150	1.4289	1.4258	1.4493	1.4467
	0.2	1.3956	1.3907	1.4018	1.3971	1.4120	1.4077	1.4316	1.4283
	0.4	1.3516	1.3539	1.3572	1.3600	1.3662	1.3701	1.3841	1.3902
30°	0	1.3518	1.3518	1.3607	1.3607	1.3749	1.3749	1.4006	1.4006
	0.1	1.3411	1.3383	1.3497	1.3470	1.3634	1.3609	1.3883	1.3863
	0.2	1.3286	1.3245	1.3368	1.3330	1.3500	1.3466	1.3740	1.3711
	0.4	1.2950	1.2957	1.3022	1.3037	1.3138	1.3166	1.3356	1.3407
45°	0	1.2919	1.2919	1.3006	1.3006	1.3139	1.3139	1.3359	1.3359
	0.1	1.2850	1.2818	1.2934	1.2902	1.3068	1.3040	1.3292	1.3267
	0.2	1.2767	1.2715	1.2846	1.2798	1.2970	1.2931	1.3186	1.3153
	0.4	1.2539	1.2497	1.2609	1.2577	1.2722	1.2708	1.2925	1.2936

3.3.5. Effect of thickness and aspect ratio

The influence of the thickness-to-length ratio of different types of variable thickness on the NLFR for various taper ratios and the plate's skewness are tabulated in

Tables 3.8 - 3.10. The NLFR decreases with an increase in the thickness-to-length ratio. This decrease is irrespective of the different types of variable thickness, taper ratio, skew angles, and porosity distributions. Such a kind of behavior happens when the parameters are non-dimensionalized. It may be because of the rise in the plate's stiffness with an increase in thickness, and thus, the corresponding linear fundamental frequency increases. As expected, as the taper ratio increases, the NLFR increases irrespective of thickness-to-length ratio, porosity distribution, and the skew angle.

Table 3.7: Effect of porosity parameter index on the NLFR (ω_{NL}/ω) of exponentially variable thickness Si_3N_4 / SUS304 TPFGS plate for the different taper ratio (β) and skew angle (Φ). ($a/b = 1$, $h_0 = 1/10$, $m = 2$, $W_{max}/h = 1.0$, $\chi = 0$, and SSSS).

Φ	e_p	$\beta = 0$		$\beta = 0.1$		$\beta = 0.25$		$\beta = 0.50$	
		P_e	P_c	P_e	P_c	P_e	P_c	P_e	P_c
0°	0	1.4636	1.4636	1.4657	1.4657	1.4690	1.4690	1.4745	1.4745
	0.1	1.4485	1.4443	1.4505	1.4464	1.4536	1.4496	1.4589	1.4551
	0.2	1.4309	1.4246	1.4328	1.4267	1.4357	1.4298	1.4408	1.4353
	0.4	1.3826	1.3838	1.3843	1.3859	1.3869	1.3889	1.3914	1.3934
15°	0	1.4258	1.4258	1.4290	1.4290	1.4337	1.4337	1.4413	1.4413
	0.1	1.4118	1.4084	1.4149	1.4116	1.4194	1.4161	1.4268	1.4236
	0.2	1.3956	1.3907	1.3986	1.3938	1.4029	1.3982	1.4099	1.4055
	0.4	1.3516	1.3539	1.3543	1.3568	1.3581	1.3611	1.3644	1.3681
30°	0	1.3518	1.3518	1.3561	1.3561	1.3623	1.3623	1.3722	1.3722
	0.1	1.3411	1.3383	1.3452	1.3425	1.3512	1.3485	1.3607	1.3582
	0.2	1.3286	1.3245	1.3325	1.3285	1.3382	1.3344	1.3474	1.3438
	0.4	1.2950	1.2957	1.2984	1.2995	1.3035	1.3051	1.3115	1.3140
45°	0	1.2919	1.2919	1.2961	1.2961	1.3016	1.3016	1.3116	1.3116
	0.1	1.2850	1.2818	1.2890	1.2860	1.2942	1.2916	1.3036	1.3009
	0.2	1.2767	1.2715	1.2804	1.2755	1.2860	1.2813	1.2949	1.2903
	0.4	1.2539	1.2497	1.2573	1.2535	1.2620	1.2592	1.2700	1.2681

Analogously, for a given value of the thickness-to-length ratio, the influence of different types of variable thickness on NLFR follows the trend observed in the previous examples, i.e., exponentially variable thickness < linearly variable thickness < bi-linearly variable thickness.

Furthermore, the effects of aspect ratio on the NLFR for different types of variable thickness, taper ratio, and geometrical skewness are presented in Tables 3.11 - 3.13. These tables disclose that with an increase in the aspect ratio, the NLFR decreases and then increases for lower skew angles (Φ = 0° and 15°) and increases progressively for

Table 3.8: Effect of thickness-to-length ratio (a/h_0) on the NLFR (ω_{NL}/ω) of linearly variable thickness Si_3N_4 / SUS304 TPFGS plate for the different taper ratio (β) and skew angle (Φ). ($a/b = 1$, $m = 2$, $e_p = 0.1$, $W_{max}/h = 1.0$, $\chi = 0$, and SSSS).

Φ	a/h_0	$\beta = 0$		$\beta = 0.1$		$\beta = 0.25$		$\beta = 0.50$	
		P_e	P_c	P_e	P_c	P_e	P_c	P_e	P_c
0°	10	1.4485	1.4443	1.4506	1.4464	1.4538	1.4498	1.4597	1.4560
	20	1.4338	1.4290	1.4343	1.4296	1.4351	1.4304	1.4366	1.4319
	50	1.4297	1.4248	1.4298	1.4249	1.4299	1.4250	1.4302	1.4252
	100	1.4291	1.4242	1.4292	1.4242	1.4292	1.4242	1.4293	1.4243
15°	10	1.4118	1.4084	1.4150	1.4116	1.4198	1.4164	1.4279	1.4247
	20	1.3770	1.3736	1.3792	1.3757	1.3823	1.3788	1.3871	1.3836
	50	1.3349	1.3318	1.3373	1.3342	1.3406	1.3375	1.3456	1.3424
	100	1.2997	1.2963	1.3021	1.2989	1.3057	1.3025	1.3112	1.3080
30°	10	1.3411	1.3383	1.3453	1.3425	1.3516	1.3489	1.3621	1.3596
	20	1.2962	1.2929	1.2987	1.2954	1.3023	1.2991	1.3082	1.3051
	50	1.2626	1.2585	1.2639	1.2598	1.2658	1.2617	1.2688	1.2648
	100	1.2493	1.2445	1.2500	1.2453	1.2511	1.2463	1.2528	1.2482
45°	10	1.2850	1.2818	1.2890	1.2860	1.2951	1.2921	1.3049	1.3027
	20	1.2472	1.2431	1.2489	1.2449	1.2515	1.2476	1.2560	1.2522
	50	1.2284	1.2236	1.2290	1.2242	1.2299	1.2251	1.2314	1.2267
	100	1.2217	1.2166	1.2221	1.2171	1.2227	1.2177	1.2237	1.2186

Table 3.9: Effect of thickness-to-length ratio (a/h_0) on the NLFR (ω_{NL}/ω) of bi-linearly variable thickness Si_3N_4 / SUS304 TPFGS plate for the different taper ratio ($\beta = \chi$) and skew angle (Φ). ($a/b = 1$, $m = 2$, $e_p = 0.1$, $W_{max}/h = 1.0$, and SSSS).

Φ	a/h_0	$\beta = \chi = 0$		$\beta = \chi = 0.1$		$\beta = \chi = 0.25$		$\beta = \chi = 0.50$	
		P_e	P_c	P_e	P_c	P_e	P_c	P_e	P_c
0°	10	1.4485	1.4443	1.4528	1.4487	1.4605	1.4568	1.4771	1.4741
	20	1.4338	1.4290	1.4349	1.4301	1.4367	1.4321	1.4409	1.4363
	50	1.4297	1.4248	1.4299	1.4250	1.4302	1.4253	1.4309	1.4259
	100	1.4291	1.4242	1.4292	1.4242	1.4293	1.4243	1.4294	1.4245
15°	10	1.4118	1.4084	1.4183	1.4150	1.4289	1.4258	1.4493	1.4467
	20	1.3770	1.3736	1.3814	1.3779	1.3877	1.3842	1.3979	1.3944
	50	1.3349	1.3318	1.3397	1.3365	1.3462	1.3430	1.3560	1.3527
	100	1.2997	1.2963	1.3047	1.3014	1.3118	1.3086	1.3227	1.3195
30°	10	1.3411	1.3383	1.3497	1.3470	1.3634	1.3609	1.3883	1.3863
	20	1.2962	1.2929	1.3012	1.2980	1.3090	1.3058	1.3223	1.3193
	50	1.2626	1.2585	1.2652	1.2611	1.2692	1.2652	1.2762	1.2724
	100	1.2493	1.2445	1.2507	1.2460	1.2530	1.2484	1.2570	1.2526
45°	10	1.2850	1.2818	1.2934	1.2902	1.3068	1.3040	1.3292	1.3267
	20	1.2472	1.2431	1.2508	1.2468	1.2566	1.2528	1.2677	1.2642
	50	1.2284	1.2236	1.2297	1.2248	1.2316	1.2268	1.2351	1.2305
	100	1.2217	1.2166	1.2226	1.2175	1.2238	1.2188	1.2258	1.2208

Table 3.10: Effect of thickness-to-length ratio (a/h_0) on the NLFR (ω_{NL}/ω) of exponentially variable thickness Si_3N_4 / SUS304 TPFGS plate for the different taper ratio (β) and skew angle (Φ). ($a/b = 1$, $m = 2$, $e_p = 0.1$, $W_{max}/h = 1.0$, $\chi = 0$, and SSSS).

Φ	a/h_0	$\beta = 0$		$\beta = 0.1$		$\beta = 0.25$		$\beta = 0.50$	
		P_e	P_c	P_e	P_c	P_e	P_c	P_e	P_c
0°	10	1.4485	1.4443	1.4505	1.4464	1.4536	1.4496	1.4589	1.4551
	20	1.4338	1.4290	1.4343	1.4296	1.4351	1.4303	1.4364	1.4316
	50	1.4297	1.4248	1.4298	1.4249	1.4299	1.4250	1.4301	1.4252
	100	1.4291	1.4242	1.4292	1.4242	1.4292	1.4242	1.4293	1.4243
15°	10	1.4118	1.4084	1.4149	1.4116	1.4194	1.4161	1.4268	1.4236
	20	1.3770	1.3736	1.3792	1.3757	1.3821	1.3786	1.3865	1.3830
	50	1.3349	1.3318	1.3373	1.3341	1.3404	1.3373	1.3450	1.3418
	100	1.2997	1.2963	1.3021	1.2988	1.3055	1.3022	1.3105	1.3073
30°	10	1.3411	1.3383	1.3452	1.3425	1.3512	1.3485	1.3607	1.3582
	20	1.2962	1.2929	1.2986	1.2953	1.3021	1.2988	1.3074	1.3043
	50	1.2626	1.2585	1.2639	1.2597	1.2656	1.2616	1.2684	1.2644
	100	1.2493	1.2445	1.2500	1.2452	1.2510	1.2463	1.2526	1.2479
45°	10	1.2850	1.2818	1.2890	1.2860	1.2942	1.2916	1.3036	1.3009
	20	1.2472	1.2431	1.2489	1.2449	1.2514	1.2474	1.2554	1.2516
	50	1.2284	1.2236	1.2290	1.2242	1.2299	1.2251	1.2312	1.2264
	100	1.2217	1.2166	1.2221	1.2171	1.2227	1.2176	1.2236	1.2185

the higher skew angles, say Φ = 30° and 45°. This erratic change of the NLFR for a higher aspect ratio is due to reduced actual inertia due to porosities and reduced stiffness. This kind of unexpected behavior appears due to the non-dimensionalizing of the parameters. An additional interesting observation is that for a given aspect ratio value, the influence of different types of variable thickness on NLFR follows the trend as linearly < bi-linearly < exponentially changing thickness. It may be due to the degradation of material properties and increased porosity as the aspect ratio increases. Furthermore, the NLFR is lower in the centrally distributed porosities than in evenly distributed porosities ($P_c < P_e$).

3.3.6. Effect of porosity volume index on the NLFP with different boundary conditions

The plots (Figures 3.2 - 3.4) illustrate the non-dimensional nonlinear frequency parameter (NLFP) of the TPFGS plate with different boundary conditions, taper ratios, skew angles, porosity volume index, variable thickness, and porosity distributions. Unless otherwise stated, the following geometrical parameters are considered for the

Table 3.11: Effect of aspect ratio (a/b) on the NLFR (ω_{NL}/ω) of linearly variable thickness Si_3N_4 / SUS304 TPFGS plate for the different taper ratio (β) and skew angle (Φ). (h_0 = 1/10, m = 2, e_p = 0.1, W_{max}/h = 1.0, χ = 0, and SSSS).

Φ	a/b	$\beta = 0$		$\beta = 0.1$		$\beta = 0.25$		$\beta = 0.50$	
		P_e	P_c	P_e	P_c	P_e	P_c	P_e	P_c
	0.6	1.5102	1.5037	1.5117	1.5054	1.5140	1.5078	1.5184	1.5123
	0.8	1.4593	1.4546	1.4610	1.4563	1.4638	1.4591	1.4687	1.4643
0°	1.0	1.4485	1.4443	1.4506	1.4464	1.4538	1.4498	1.4597	1.4560
	1.2	1.4627	1.4584	1.4652	1.4610	1.4693	1.4652	1.4765	1.4728
	1.4	1.4903	1.4856	1.4935	1.4889	1.4985	1.4941	1.5075	1.5037
	0.6	1.4154	1.4110	1.4187	1.4133	1.4236	1.4195	1.4303	1.4279
	0.8	1.4004	1.3969	1.4035	1.4000	1.4082	1.4047	1.4160	1.4126
15°	1.0	1.4118	1.4084	1.4150	1.4116	1.4198	1.4164	1.4279	1.4247
	1.2	1.4403	1.4365	1.4437	1.4400	1.4490	1.4454	1.4581	1.4547
	1.4	1.4774	1.4730	1.4812	1.4771	1.4874	1.4832	1.4980	1.4946
	0.6	1.2547	1.2524	1.2584	1.2562	1.2637	1.2612	1.2729	1.2702
	0.8	1.2910	1.2884	1.2948	1.2923	1.3005	1.2981	1.3097	1.3074
30°	1.0	1.3411	1.3383	1.3453	1.3425	1.3516	1.3489	1.3621	1.3596
	1.2	1.3980	1.3947	1.4028	1.3995	1.4097	1.4069	1.4221	1.4192
	1.4	1.4563	1.4523	1.4616	1.4578	1.4702	1.4685	1.4836	1.4796
	0.6	1.1319	1.1302	1.1331	1.1314	1.1349	1.1328	1.1376	1.1357
	0.8	1.1986	1.1960	1.2012	1.1985	1.2049	1.2024	1.2109	1.2085
45°	1.0	1.2850	1.2818	1.2890	1.2860	1.2951	1.2921	1.3049	1.3027
	1.2	1.3752	1.3713	1.3793	1.3561	1.3896	1.3864	1.4030	1.3993
	1.4	1.4578	1.4518	1.4648	1.3353	1.3326	1.4743	1.4868	1.3245

parametric study of the square Si_3N_4/SUS304 TPFGS plate: a/b = 1, h_0=1/10, m = 2, Φ = 0°,15°,30°, and 45°. Figure 3.3 depict the results for non-dimensional NLFP of linearly TPFGS plate. The taper ratio taken for non-uniform thickness (h_b / h_0) is 1 and 1.5, considering different boundary conditions for evenly distributed (P_e) and centrally distributed (P_c) porosities. Results show that for a given taper ratio and skew angle, the NLFP obtained is maximum at the ideal tapered FGS plate (e_p = 0); meanwhile, the NLFP trend decreases with an increase in porosity parameter index (e_p) for the TPFGS plate. Thus, this signifies that the ideal FGS plates are stiffer than the TPFGS plates. Besides, results reveal a rapid decrease in the NLFP for the evenly distributed porosities (P_e) with an increase in the porosity volume index (e_p). In contrast, the decrease rate is slow and steady for the centrally distributed porosities (P_c). The NLFP can be assumed constant for the centrally distributed porosities (P_c) with an increase in the porosity volume index (e_p). Thus, the NLFP of P_c is more harmful than that of P_e.

Table 3.12: Effect of aspect ratio (a/b) on the NLFR (ω_{NL}/ω) of bi-linearly variable thickness Si_3N_4 / SUS304 TPFGS plate for the different taper ratio ($\beta = \chi$) and skew angle (Φ). ($h_0 = 1/10$, $m = 2$, $e_p = 0.1$, $W_{max}/h = 1.0$, and SSSS).

Φ	a/b	$\beta = \chi = 0$		$\beta = \chi = 0.1$		$\beta = \chi = 0.25$		$\beta = \chi = 0.50$	
		P_e	P_c	P_e	P_c	P_e	P_c	P_e	P_c
	0.6	1.5102	1.5037	1.5133	1.5071	1.5190	1.5129	1.5312	1.5257
	0.8	1.4593	1.4546	1.4630	1.0054	1.4694	1.4650	1.4833	1.4795
0°	1.0	1.4485	1.4443	1.4528	1.4487	1.4605	1.4568	1.4771	1.4741
	1.2	1.4627	1.4584	1.4680	1.4639	1.4775	1.4738	1.4977	1.4946
	1.4	1.4903	1.4856	1.4969	1.4925	1.5090	1.5050	1.5344	1.5321
	0.6	1.4154	1.4110	1.4219	1.4179	1.4327	1.4286	1.4508	1.4481
	0.8	1.4004	1.3969	1.4068	1.4033	1.4169	1.4136	1.4356	1.4325
15°	1.0	1.4118	1.4084	1.4183	1.4150	1.4289	1.4258	1.4493	1.4467
	1.2	1.4403	1.4365	1.4474	1.4437	1.4592	1.4558	1.4979	1.4576
	1.4	1.4774	1.4730	1.4856	1.4815	1.5002	1.4958	1.5253	1.5264
	0.6	1.2547	1.2524	1.2622	1.2595	1.2740	1.2712	1.2925	1.2898
	0.8	1.2910	1.2884	1.2988	1.2963	1.3109	1.3085	1.3320	1.3300
30°	1.0	1.3411	1.3383	1.3497	1.3470	1.3634	1.3609	1.3883	1.3863
	1.2	1.3980	1.3947	1.4078	1.4046	1.4225	1.4207	1.4513	1.4494
	1.4	1.4563	1.4523	1.4269	1.4370	1.4853	1.4832	1.3561	1.3543
	0.6	1.1319	1.1302	1.1343	1.1322	1.1381	1.1360	1.1428	1.1409
	0.8	1.1986	1.1960	1.2037	1.2013	1.2116	1.2093	1.2238	1.2219
45°	1.0	1.2850	1.2818	1.2934	1.2902	1.3068	1.3040	1.3292	1.3267
	1.2	1.3752	1.3713	1.3871	1.3819	1.4016	1.4000	1.4410	1.3278
	1.4	1.4578	1.4518	1.4709	1.4713	1.3253	1.4993	1.3160	1.3132

A further exciting comparison is that the NLFP increases with an increase in the taper ratio (h_b/h_0) for a given skew angle. However, increasing NLFP is seen with an increase in the TPFGS plate's geometrical skewness for a given taper ratio. It is due to the stiffness of the TPFGS plate increasing with an increase in the skew angle and taper ratio. Furthermore, Figures 3.2 (a) – (f) illustrate that the dimensionless NLFP increases with the number of boundary edge constraints. However, the non-dimensional NLFP for the ideal tapered FGS plate ($e_p = 0$) exhibits a higher side than the TPFGS plate for all boundary conditions. Thus, the order of increasing the dimensionless NLFP with boundary constraints is SSSS < SCSC < CCCC. The increase in the NLFP from SSSS to CCCC is an average of almost 30%. This is attributed to the fact that the flexural rigidity increases with an increase in boundary constraints.

Table 3.13: Effect of aspect ratio (a/b) on the NFR (ω_{NL}/ω) of exponentially variable thickness Si_3N_4 / SUS304 TPFGS plate for the different taper ratio (β) and skew angle (Φ). (h_0 = 1/10, m = 2, e_p = 0.1, W_{max}/h = 1.0, χ = 0, and SSSS).

Φ	a/b	$\beta = 0$		$\beta = 0.1$		$\beta = 0.25$		$\beta = 0.50$	
		P_e	P_c	P_e	P_c	P_e	P_c	P_e	P_c
	0.6	1.5102	1.5037	1.5404	1.5350	1.5463	1.5414	1.5560	1.5523
	0.8	1.4593	1.4546	1.4713	1.4671	1.4754	1.4712	1.4822	1.4784
0°	1.0	1.4485	1.4443	1.4505	1.4464	1.4536	1.4496	1.4589	1.4551
	1.2	1.4627	1.4584	1.4569	1.4524	1.4596	1.4551	1.4641	1.4598
	1.4	1.4903	1.4856	1.4768	1.4717	1.4793	1.4742	1.4835	1.4785
	0.6	1.4154	1.4110	1.4639	1.4577	1.4702	1.4400	1.4819	1.4773
	0.8	1.4004	1.3969	1.4198	1.4165	1.4253	1.4221	1.4341	1.4311
15°	1.0	1.4118	1.4084	1.4149	1.4116	1.4194	1.4161	1.4268	1.4236
	1.2	1.4403	1.4365	1.4318	1.4279	1.4357	1.4319	1.4422	1.4384
	1.4	1.4774	1.4730	1.4590	1.4542	1.4626	1.4579	1.4683	1.4638
	0.6	1.2547	1.2524	1.3032	1.3010	1.3094	1.3073	1.3190	1.3158
	0.8	1.2910	1.2884	1.3142	1.3119	1.3206	1.3184	1.3305	1.3286
30°	1.0	1.3411	1.3383	1.3452	1.3425	1.3512	1.3485	1.3607	1.3582
	1.2	1.3980	1.3947	1.3862	1.3827	1.3923	1.3883	1.4006	1.3974
	1.4	1.4563	1.4523	1.4300	1.4248	1.4352	1.4309	1.4436	1.4393
	0.6	1.1319	1.1302	1.1417	1.1396	1.1393	1.1429	1.1490	1.1460
	0.8	1.1986	1.1960	1.2137	1.2115	1.2177	1.2155	1.2233	1.2213
45°	1.0	1.2850	1.2818	1.2890	1.2860	1.2942	1.2916	1.3036	1.3009
	1.2	1.3752	1.3713	1.3615	1.3576	1.3678	1.3642	1.3779	1.3745
	1.4	1.4578	1.4518	1.4269	1.4222	1.4336	1.4275	1.4434	1.4399

Figures 3.3 – 3.4 depict the results for non-dimensional NLFP of both bi-linearly and exponentially variable thickness of the TPFGS plate with different boundary conditions for evenly distributed (P_e) and centrally distributed (P_c) porosities. The taper ratio for uniform and non-uniform thickness for bi-linearly (h_{ab} / h_0) and exponentially (h_b / h_0) variable thickness is 1 and 1.5, respectively.

The figures show that a similar trend is observed for both bi-linearly and exponentially variable thickness, as presented in linearly variable thickness. In addition, for a given value of skew angle and taper ratio, the effects of different types of varying thickness on the NLFP follow a trend as exponentially < linearly < bi-linearly variable thickness and exhibits the highest NLFP in the centrally distributed porosities compared to evenly distributed porosities ($P_e < P_c$) for all the boundary conditions considered. It can also be

noticed that the NLFP of the TPFGS plate is always more significant than the uniform PFGS plate.

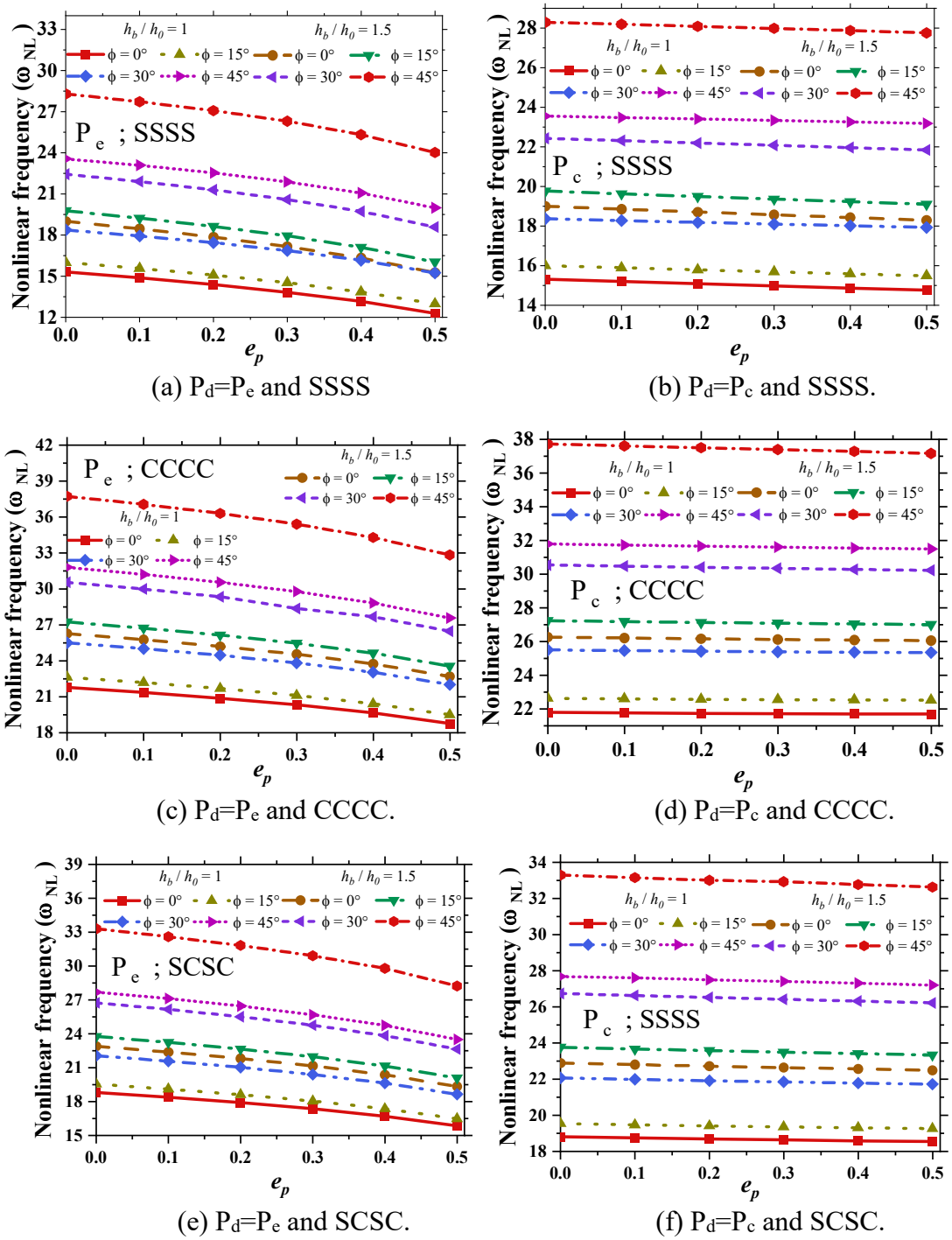

(a) P_d=P_e and SSSS (b) P_d=P_c and SSSS.

(c) P_d=P_e and CCCC. (d) P_d=P_c and CCCC.

(e) P_d=P_e and SCSC. (f) P_d=P_c and SCSC.

Figure 3.2: Effect of taper ratio and porosity volume index on the NLFP for the Linearly variable thickness of the TPFGS plate. (a) P_d=P_e and SSSS, (b) P_d=P_c and SSSS, (c) P_d=P_e and SCSC, (d) P_d=P_c and SCSC, (e) P_d=P_e and SCSC, and (f) P_d=P_c and SCSC.

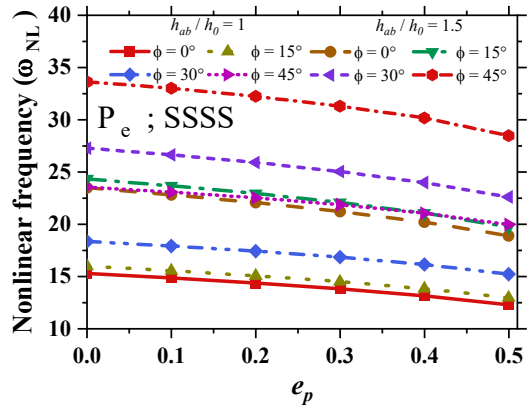

(a) P_d=P_e and SSSS

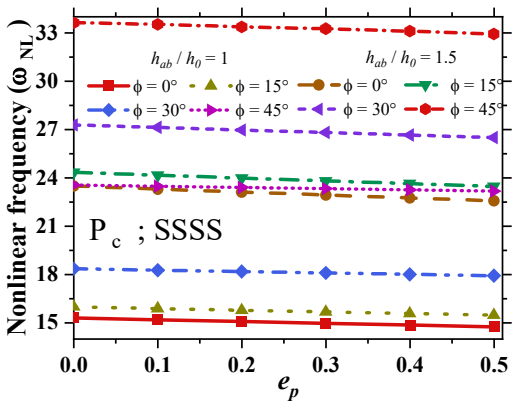

(b) P_d=P_c and SSSS

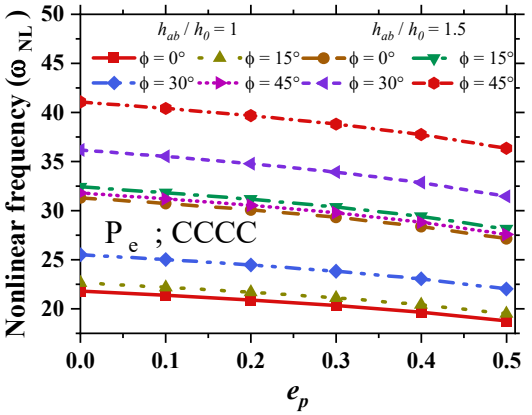

(c) P_d=P_e and CCCC

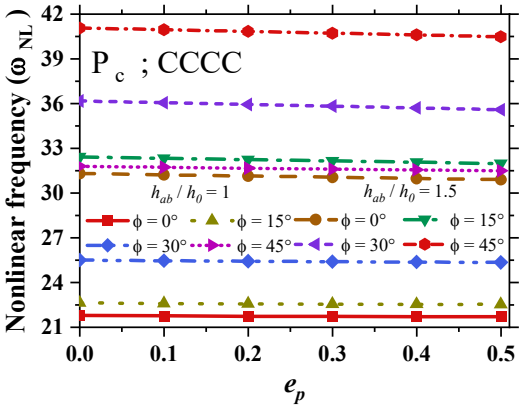

(d) P_d=P_c and CCCC

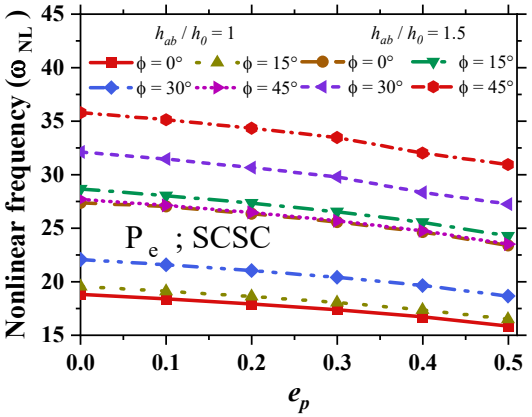

(e) P_d=P_e and SCSC

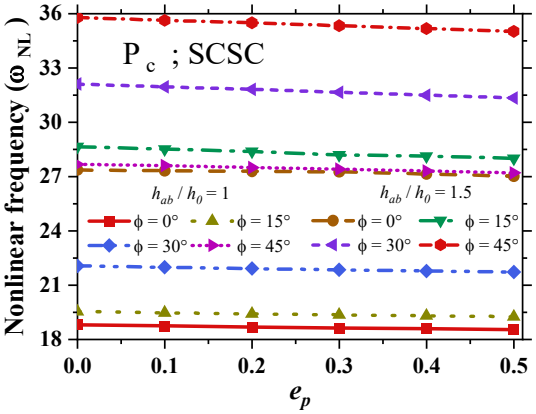

(f) P_d=P_c and SCSC.

Figure 3.3: Effect of taper ratio and porosity parameter index on the NLFP for the Bi-linearly Variable thickness of the TPFGS plate. (a) P_d=P_e and SSSS, (b) P_d=P_c and SSSS, (c) P_d=P_e and SCSC, (d) P_d=P_c and SCSC, (e) P_d=P_e and SCSC, and (f) P_d=P_c and SCSC.

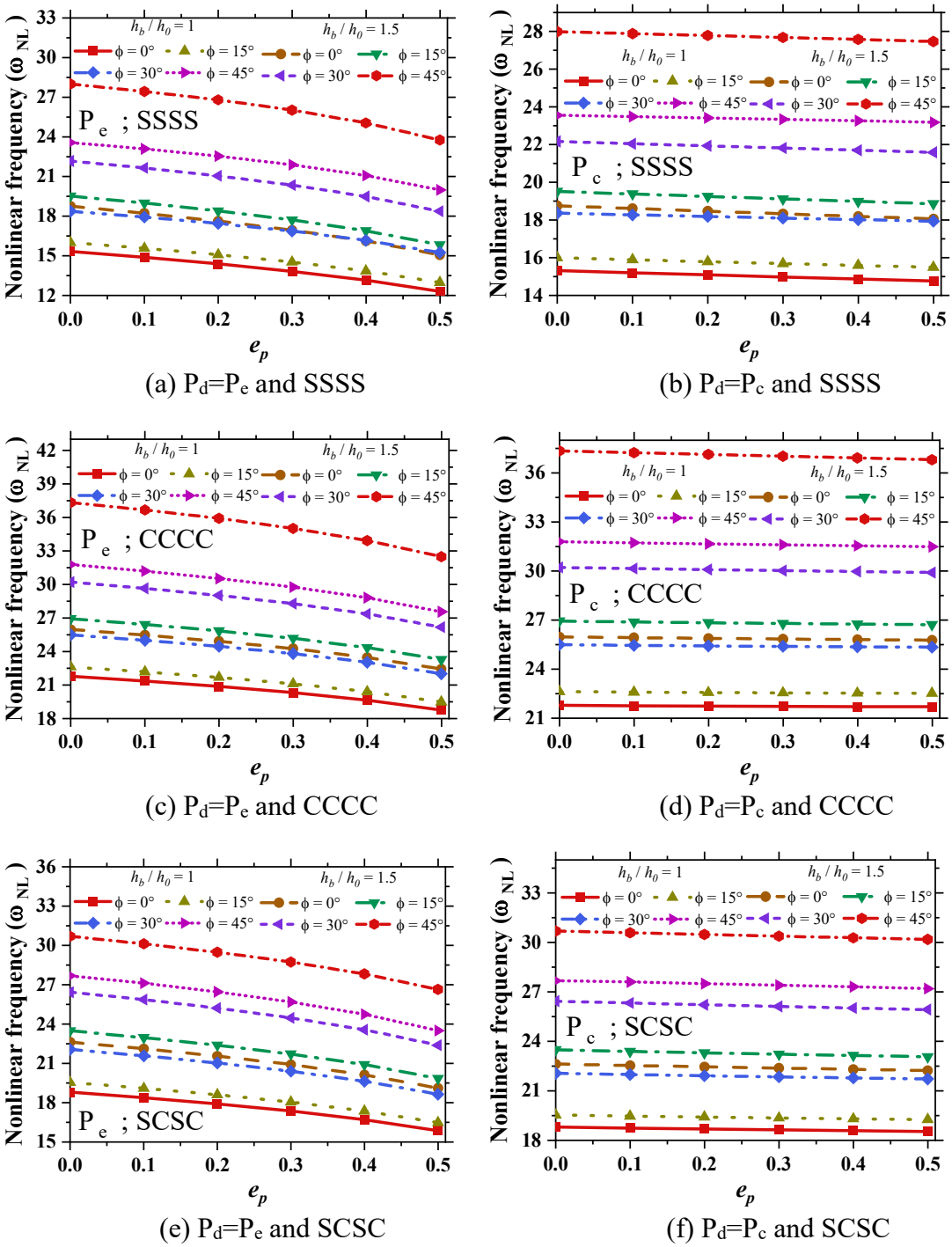

(a) P_d=P_e and SSSS (b) P_d=P_c and SSSS

(c) P_d=P_e and CCCC (d) P_d=P_c and CCCC

(e) P_d=P_e and SCSC (f) P_d=P_c and SCSC

Figure 3.4: Effect of taper ratio and porosity parameter index on the NLFP for the exponentially Variable thickness of the TPFGS plate. (a) P_d=P_e and SSSS, (b) P_d=P_c and SSSS, (c) P_d=P_e and SCSC, (d) P_d=P_c and SCSC, (e) P_d=P_e and SCSC, and (f) P_d=P_c and SCSC.

3.4. CONCLUSIONS

The present study uses the nonlinear FE formulation in the framework of FSDT in colligation with von Karman's assumptions to investigate the influence of porosity distributions on the nonlinear free vibrations of a tapered porous functionally graded plate with the consideration of geometrical skewness and various types of variable thickness. The equations of motion are derived using Hamilton's principle. The useful material properties of the TPFGS plate are predicted using the modified power-law distribution and Voigt's model. The nonlinear frequency results are computed through the direct iterative method. Validations and comparison studies have been carried out to check the proposed model's reliability.

The following are the concluded outcomes from the present study. In the presence of porosities, the NLFR (ω_{NL}/ω) decreases initially and then increases with an increase in the volume fraction grading index (m) for all the types of variable thickness, taper ratio, skew angles, and porosity distributions. NLFR increases with an increase in the taper ratio and amplitude ratio. In contrast, NLFR decreases with the rise in the plate's skewness and porosity volume index, irrespective of various types of variable thickness and porosity distributions. Further, the effect of bi-linearly variable thickness is high compared to linearly variable and exponentially variable thickness on both NLFR and NLFP. It follows the trend as exponentially variable thickness < linearly variable thickness < bi-linearly variable thickness. Hence, exponentially and linearly varying thicknesses can be considered for the thickness optimizations of TPFGS plates. The geometrical non-uniformities on the PFG plate are always more significant than the PFG plate with uniform thickness for both NLFR and NLFP cases. Besides, the NLFP of the centrally distributed porosity (P_c) decreases steadily for all boundary conditions and various types of variable thickness with an increase in porosity volume index. In contrast, the NLFP of the evenly distributed porosities decreases rapidly. Hence, the NLFR and NLFP are more susceptible to centrally distributed porosity than evenly distributed porosity. The influence of porosity distributions on the NLFR follows the trend as $P_c < P_e$, and for the NLFP, the tendency is $P_c > P_e$. The NLFP follows the sequence of increasing order with boundary conditions as SSSS > SCSC > CCCC. The average of almost 30% is the increase in the NLFP from SSSS to CCCC.

CHAPTER 4

GEOMETRICALLY NONLINEAR VIBRATION AND TRANSIENT RESPONSES OF POROUS FG SKEW PLATE SUBJECTED TO THERMAL LOADS

This chapter investigates the influence of distributions of porosities on the nonlinear analysis of PFGS plates in a thermal environment. The modified power-law series has been used to determine the temperature-dependent effective material properties in the thickness direction. A nonlinear finite element formulation is derived using an improved first-order shear deformation theory (IFSDT) and von Kármán's type nonlinearity. Numerical results like the nonlinear frequency and nonlinear transient deflections have been extracted. The detailed numerical investigations are performed for various material and geometrical parameters. At the same time, emphasis is placed on investigating the effect of the distribution of porosities and geometrical skewness under thermal loads.

4.1. INTRODUCTION

Geometrical skewness in FG plate allows designers to have different alignment options for hurdles in structural applications such as aerospace, biomedical, civil, defence, mechanical, etc. The FG skew plates gain limited space in the literature even though it makes it easier for an engineer to have versatility in aligning the edges of plates in the occurrence of complications. The plate's area varies depending on the plate's skewness. Consequently, the change in the plate's stiffness is proportional to the skewness. However, the stiffness also depends on the variation of the temperature and porosity distribution. In Chapter 2, the influence of porosity distributions on the nonlinear behaviour of the PFGS plate without thermal loads has been investigated. This chapter extends a similar investigation into PFGS plates under thermal loads.

The main objective of this chapter is to investigate the influence of porosity distributions and temperature on the nonlinear behaviour of the PFGS plate under thermal loads. A nonlinear FE model for the PFGS plates based on the improved first-order shear deformation theory (IFSDT) concatenated with von Kármán assumptions in the thermal environment has been proposed. The modified power-law series determines the temperature-dependent effective material properties of the PFGS plate. The governing equations are derived using Hamilton's principle, and solutions are obtained using the direct iterative method and Newmark's integration method. The predominant effects of the porosity distributions in conjunction with the geometrical skewness on the nonlinear free vibration and transient responses of the PFGS plate for various thermal loadings are investigated.

4.2. PROBLEM DESCRIPTION AND GOVERNING EQUATION

The geometrical parameters of the PFGS plate considered in the present analysis are identical to those of the plate studied in Figure 2.1. Further, skew boundary transformation and solution methodologies are presented identically to sections 2.2.4 and 2.3. However, temperature-dependent effective material properties, the displacement equations, the constitutive equations, and the nonlinear FE formulation considering the IFSDT are explained in the subsequent section.

4.2.1. Temperature-dependent effective material properties

The temperature-dependent effective material properties of the PFGS plate constantly vary in the thickness direction, and the distribution of porosities formed during PFGS plate fabrication is theoretically predicted using mathematical models. As depicted in Figure 2.2, the PFGS plate is studied using two different models: evenly (P_e) and centrally (P_c) distributed porosities.

The modified power-law series for different porosity distributions is employed to derive the generalized temperature-dependent effective material properties of the PFGS plate (P_{fg} (z, T)) for modulus of elasticity (E_{fg} (z, T)), Poisson's ratio (ϑ_{fg} (z, T)), and mass density (ρ_{fg} (z, T)) at each location in the PFGS plate. Eqs. (4.1) and (4.2) determine the generalized temperature-dependent effective material properties of the PFGS plate for P_e and P_c.

Evenly distributed porosity (*EDP*) (P_e):

$$\mathrm{P_{fg}}\left(\mathrm{z,T}\right)=\left(P_t(T)-P_b(T)\right)\left(\frac{1}{2}+\frac{z}{h}\right)^m+P_b(T)-\left(\frac{e_p}{2}\right)\left(P_t(T)+P_b(T)\right) \tag{4.1}$$

Centrally distributed porosity (*CDP*) (P_c):

$$\mathrm{P_{fg}}\left(z,T\right)=\left(P_t(T)-P_b(T)\right)\left(\frac{1}{2}+\frac{z}{h}\right)^m+P_b(T)-\left(\frac{e_p}{2}\right)\left(P_t(T)+P_b(T)\right)\left(1-\frac{2|z|}{h}\right) \tag{4.2}$$

$\mathrm{P_{fg}}$ (z, T) represents the temperature-dependent effective material characteristics in the transverse direction, while $P_t(T)$ and $P_b(T)$ denote ceramic and metal material properties, respectively.

The temperature-dependent material properties of each constituent material are stated with the function of nonlinear temperature distribution (Reddy and Chin 1998) as follows:

$$P(\mathrm{T})=\varsigma_0\left(\frac{\varsigma_{-1}}{\mathrm{T}}+1+\varsigma_1\mathrm{T}+\varsigma_2\mathrm{T}^2+\varsigma_3\mathrm{T}^3\right) \tag{4.3}$$

where ς_0, ς_{-1}, ς_1, ς_2, and ς_3 are the coefficients of temperature T (K) and are specific to each material constituent, $P_b(T)$ and $P_t(T)$, respectively. T is the nonlinear temperature distribution. Besides, the mass density (ρ), thermal conductivity (k), and Poisson's ratio (ϑ) are weakly influenced by temperature fluctuations and are presumed to be constant (Huang and Shen 2004).

Further, the nonlinear temperature distribution is presumed to occur in the path of gradation. A steady-state one-dimensional Fourier heat conduction equation can be used to solve temperature distribution problems. A thermal field is assumed to be constant in any *x*-*y* plane of the PFGS plate. The temperature distribution through the thickness can thus be solved using the steady-state heat transfer equation as follows (Javaheri and Eslami 2002a; b) :

$$-\frac{\mathrm{d}}{\mathrm{dx}}\left[k(z)\frac{\mathrm{dT}}{\mathrm{d}z}\right]=0 \tag{4.4}$$

Eq. (4.4) can be simplified by applying the boundary conditions as $\mathrm{T=T_b}$ at $z=-h/2$ and $\mathrm{T=T_t}$ at $z=h/2$.

$$T(z) = T_b - (T_t - T_b)\frac{\left(\int_{-h/2}^{Z} \frac{1}{k_{fg}(z)}\,dz\right)}{\left(\int_{-h/2}^{h/2} \frac{1}{k_{fg}(z)}\,dz\right)} \tag{4.5}$$

Now, by utilizing polynomial series to solve Eq. (4.5) and after simplification, Eq. (4.5) can be expressed as follows (Javaheri and Eslami 2002a; b):

$$T(Z) = T_b + (T_t - T_b)\,\chi(Z) \tag{4.6}$$

in which,

$$\chi(z) = \frac{1}{\lambda}\left[\left(\frac{z}{h}+\frac{1}{2}\right) - \frac{k_{tb}}{(2m+1)k_b}\left(\frac{z}{h}+\frac{1}{2}\right)^{m+1} + \frac{k_{tb}^2}{(2m+1)k_b^2}\left(\frac{z}{h}+\frac{1}{2}\right)^{2m+1} - \frac{k_{tb}^3}{(3m+1)k_b^3}\left(\frac{z}{h}+\frac{1}{2}\right)^{3m+1} + \frac{k_{tb}^4}{(4m+1)k_b^4}\left(\frac{z}{h}+\frac{1}{2}\right)^{4m+1} - \frac{k_{tb}^5}{(5m+1)k_b^5}\left(\frac{z}{h}+\frac{1}{2}\right)^{5m+1}\right] \tag{4.7a}$$

$$\lambda = 1 - \frac{k_{tb}}{(2m+1)k_b} + \frac{k_{tb}^2}{(2m+1)k_b^2} - \frac{k_{tb}^3}{(3m+1)k_b^3} + \frac{k_{tb}^4}{(4m+1)k_b^4} - \frac{k_{tb}^5}{(5m+1)k_b^5} \tag{4.7b}$$

and

$$k_{tb} = k_t - k_b \tag{4.7c}$$

Further, Figure 4.1 illustrates the effect of temperature rise on the modulus of elasticity of Si_3N_4/SUS304 PFGS plates as an initial step in investigating the temperature-dependent nonlinear vibration and dynamic behaviour of the PFGS plates.

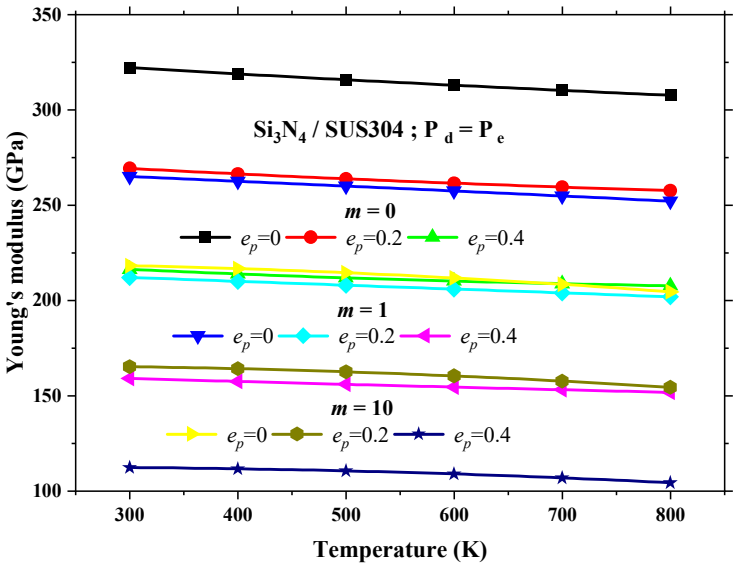

(a) P_e

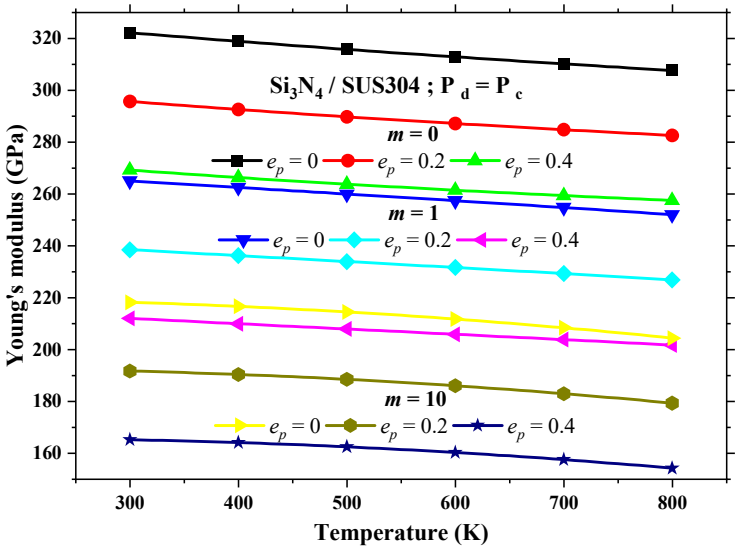

(b) P_c

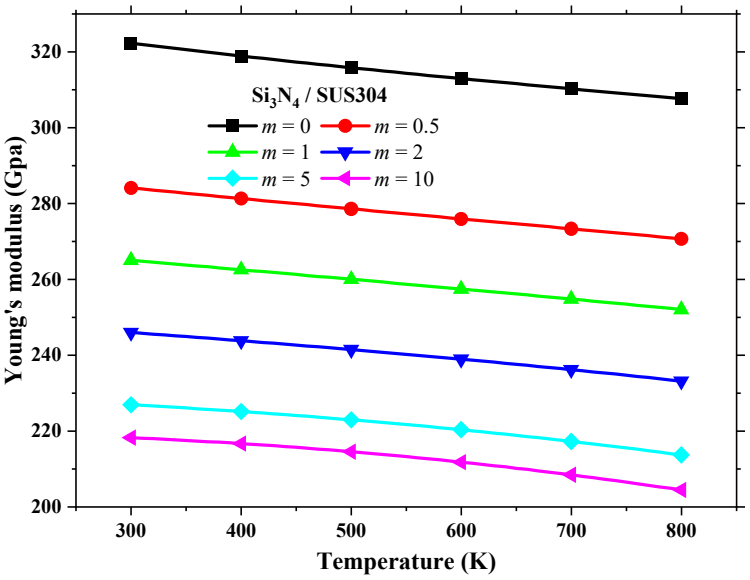

(c) Perfect FG plate

Figure 4.1: Young modulus as a function of temperature for Si_3N_4 / SUS304 FG porous plate with different VFGI. (a) P_e, (b) P_c, and (c) Perfect FG plate.

4.2.2. Constitutive equations

For any position in the entire PFGS plate, the state of stress and associated state of strain are defined as follows (Sundararajan et al. 2005):

$$\{\sigma_b\}=\begin{Bmatrix}\sigma_{xx}\\ \sigma_{yy}\\ \sigma_{xy}\end{Bmatrix}=\left[Q_b\left(z,T\right)\right]\left(\begin{Bmatrix}\varepsilon_{xx}\\ \varepsilon_{yy}\\ \varepsilon_{xy}\end{Bmatrix}-\begin{Bmatrix}\alpha_{xx}\left(z,T\right)\\ \alpha_{yy}\left(z,T\right)\\ 0\end{Bmatrix}\Delta T\right);$$

$$\{\sigma_s\}=\begin{Bmatrix}\tau_{yz}\\ \tau_{xz}\end{Bmatrix}=\left[Q_s\left(z,T\right)\right]\begin{Bmatrix}\gamma_{yz}\\ \gamma_{xz}\end{Bmatrix} \tag{4.8}$$

where $\Delta\mathrm{T}=\mathrm{T}(z)-\mathrm{T}_0$

The normal stresses σ_{xx} and σ_{yy} are present in the *x*- and *y*- directions, respectively. In-plane and transverse shear stresses are given by τ_{xy}, τ_{xz}, and τ_{yz}, respectively. $\left[Q_b\left(z,\mathrm{T}\right)\right]$ and $\left[Q_s\left(z,\mathrm{T}\right)\right]$ are the temperature-dependent elastic coefficient matrices and are the function of the *z*- coordinate. $\alpha_{xx}\left(z,\mathrm{T}\right)$ and $\alpha_{yy}\left(z,\mathrm{T}\right)$ are the coefficients of thermal expansion in the *x*- and *y*- directions, respectively. T(*z*) represents the temperature at any point on the PFGS plate, T_0 is the reference temperature, and ΔT represents the temperature increase over the reference temperature.

$$\left[Q_b\left(z,\mathrm{T}\right)\right]=\begin{bmatrix}Q_{11} & Q_{12} & 0\\ Q_{12} & Q_{22} & 0\\ 0 & 0 & Q_{66}\end{bmatrix};\quad \left[Q_s\left(z,\mathrm{T}\right)\right]=\begin{bmatrix}Q_{55} & 0\\ 0 & Q_{44}\end{bmatrix} \tag{4.9}$$

From Eq. (4.9), the expressions for elastic coefficients can be stated as follows:

$$Q_{11}=Q_{22}=\frac{E_{fg}\left(z,\mathrm{T}\right)}{1-\left(\vartheta_{fg}\left(z\right)\right)^2};\quad Q_{12}=Q_{21}=\frac{\vartheta_{fg}\left(z\right)E_{fg}\left(z,\mathrm{T}\right)}{1-\left(\vartheta_{fg}\left(z\right)\right)^2}$$

$$Q_{44}=Q_{55}=Q_{66}=\frac{E_{fg}\left(z,\mathrm{T}\right)}{2\left(1+\vartheta_{fg}\left(z\right)\right)} \tag{4.10}$$

where $E_{fg}\left(z,\mathrm{T}\right)$ and $\vartheta_{fg}\left(z\right)$ are the position and temperature-dependent effective Young's modulus and position-dependent effective Poisson's ratio of the PFGS plate, respectively.

4.2.3. Strain-displacement relations

As described in Eq. (4.11), the displacement fields of the PFGS plate are built on the mid-plane using the IFSDT model (Vinyas et al. 2019).

$$u_0(x,y) = u_1(x,y) + z\,\theta_x(x,y,z) - \left(\frac{4z^3}{3h^2}\right)\left(\theta_x(x,y,z) + \frac{\partial w_1}{\partial x}\right)$$

$$v_0(x,y) = v_1(x,y) + z\theta_y(x,y,z) - \left(\frac{4z^3}{3h^2}\right)\left(\theta_y(x,y,z) + \frac{\partial w_1}{\partial y}\right)$$

$$w_0(x,y) = w_1(x,y) \tag{4.11}$$

where the displacements along the *x*, *y*, and *z* coordinates at each location in a given PFGS plate are u_0, v_0, and w_0. The midplane displacements are denoted by u_1, v_1, and w_1. The generalized transverse normal rotations of the *x*- and *y*-axes are θ_y and θ_x, respectively.

4.2.4. Nonlinear strain displacement equations

The nonlinear strains ($\{\varepsilon_b\}$: bending and $\{\varepsilon_s\}$: shear) associated with the displacement fields of Eq. (4.11) for the PFGS plate are constructed based on von Karman's assumptions to deliberate geometric distortion as follows (Kattimani and Ray 2015; Tanov and Tabiei 2000):

$$\{\varepsilon_b\} = \begin{Bmatrix} \varepsilon_{xx} \\ \varepsilon_{yy} \\ \gamma_{xy} \end{Bmatrix} = \begin{Bmatrix} u_{1,x} + \frac{1}{2}\left(w_{1,x}\right)^2 \\ v_{1,y} + \frac{1}{2}\left(w_{1,y}\right)^2 \\ u_{1,y} + v_{1,x} + \left(w_{1,x}\right)\left(w_{1,y}\right) \end{Bmatrix} + z\begin{Bmatrix} \theta_{x,x} \\ \theta_{y,y} \\ \theta_{x,y} + \theta_{y,x} \end{Bmatrix} \tag{4.12a}$$

$$\{\varepsilon_s\} = \begin{Bmatrix} \gamma_{xz} \\ \gamma_{yz} \end{Bmatrix} = \begin{Bmatrix} w_{1,x} \\ w_{1,y} \end{Bmatrix} + C_1\begin{Bmatrix} \theta_x \\ \theta_y \end{Bmatrix} \tag{4.12b}$$

where $C_1 = 1 - 4\left(\frac{z}{h}\right)^2$ (4.12c)

It can be assumed from Eq. (4.12a) that the first two terms in the expressions $\{\varepsilon_b\}$ signify that the in-plane strains are distributed through the thickness with sufficient accuracy (Tanov and Tabiei 2000). Hence, Eq. (4.12) represents the simplified form of strain relations identical to FSDT by neglecting the contribution of the higher-order terms except for the transverse strain expressions (Tanov and Tabiei 2000). Further, the

transverse shear strains in Eq. (4.12) are employed with the second-order polynomial to define the variation of the transverse shear strains along with the thickness of the plate.

Henceforth, in the present IFSDT, the traditional FSDT is considered for further analysis to simplify and accelerate computations, and the transverse stress resultants are multiplied directly by the Eq. (4.12c). The second-order polynomial in Eq. (4.12c) distributes shear strains and stress along with the thickness and vanishes at the bottom and top of the plate. As a result, the shear locking phenomena are avoided in this unique approach of IFSDT, which produces reasonably accurate results compared to HSDT.

4.2.5. Nonlinear finite element formulation

The nonlinear FE formulation implemented in this chapter is identical to section 2.2.3 of Chapter 2. However, the effect of the geometric stiffness matrix that occurs due to nonlinear temperature distribution across the thickness of the PFGS plate is considered for the present analysis. This induces thermal stresses and directly impacts the PFGS plate's vibration characteristics. As a result of the deformed geometry of the PFGS plate generated by thermal forces, it necessitates the measurement of the geometric stiffness matrix. The PFGS plate's elementary equations of motion subjected to thermal loads can be obtained by using Eq. (2.22) and applying Hamilton's principle, i.e. $\delta T_p^{\,e} = 0$, followed by unifying and simplifying the terms based on the stiffness matrices and degrees of freedom:

$$\begin{gathered}\left[M^{e}\right]\left\{\ddot{d}_t^{e}\right\}+\left(\left[K_{tb}^{e}-K_{Temp-tt}^{e}\right]\right)\left\{d_t^{e}\right\}+\left[K_{tr}^{e}\right]\left\{d_r^{e}\right\}=\left\{F_t^{e}\right\} \\ \left[K_{rt}^{e}\right]\left\{d_t^{e}\right\}+\left[K_{rr}^{e}\right]\left\{d_t^{e}\right\}=0\end{gathered} \tag{4.13}$$

in which,

$$\begin{gathered}\left[K_{tt}^{e}\right]=\left[K_{tb}^{e}\right]+\left[K_{ts}^{e}\right]+\left[K_{tbNL}^{e}\right];\ \left[K_{tr}^{e}\right]=\left[K_{trb}^{e}\right]+\left[K_{trbNL}^{e}\right]+\left[K_{trs}^{e}\right] \\ \left[K_{rt}^{e}\right]=\left[K_{trb}^{e}\right]^{T}+\frac{1}{2}\left[K_{trbNL}^{e}\right]^{T}+\left[K_{trs}^{e}\right]^{T};\ \left[K_{rr}^{e}\right]=\left[K_{rrb}^{e}\right]+\left[K_{rrs}^{e}\right]; \\ \left[K_{Temp-tt}^{e}\right]=\left[K_{Temp-tb}^{e}\right]+\left[K_{Temp-ts}^{e}\right] \text{ and } \left\{\mathrm{F}_t^{e}\right\}=\int_0^a\int_0^b\left[N_t\right]^{T}\left\{f\right\}dx\,dy\end{gathered} \tag{4.14}$$

where $\left[M^e\right]$ is the elemental mass matrix; $\left[K_{tt}^e\right]$, $\left[K_{tr}^e\right]$, $\left[K_{rt}^e\right]$ and $\left[K_{rr}^e\right]$ are the elemental stiffness matrices; $\left[K_{Temp-tt}^e\right]$ is the elemental stiffness matrices under thermal loading; $\left\{\mathrm{F}_t^e\right\}$ is the elemental mechanical load vector. The various nodal strain displacement matrices $[ß]$, elemental stiffness, rigidity matrices, and vectors used in Eq. (4.14) are derived in Appendix - I.

Finally, Eq. (4.13) is condensed to provide a more simplified form of global equations of equilibrium for the PFGS plate:

$$[M]\left\{\ddot{X}_t\right\}+\left(\left[K_{eq}^L+K_{eq}^{NL}\right]-K_{Temp-tt}\right)\left\{X_t\right\}=\left\{\mathrm{F}_{eq}\right\} \tag{4.15a}$$

$$[M]\left\{\ddot{X}_t\right\}+\left[\overline{K_{eq}}\right]\left\{X_t\right\}=\left\{\mathrm{F}_{eq}\right\} \tag{4.15b}$$

in which,

$$\left[\overline{K_{eq}}\right]=\left(\left[K_{tt}-K_{Temp-tt}\right]\right)-\left[K_{tr}\right]\left[K_{rr}\right]^{-1}\left[K_{rt}\right] \tag{4.16}$$

where $\left[K_{eq}^L+K_{eq}^{NL}\right]$ is a set of linear and nonlinear stiffness matrices known as generalized equivalent stiffness matrices, and the force vector is represented by $\left\{\mathrm{F}_{eq}\right\}$.

Further, the eigenvalues and corresponding eigenvectors of the PFGS plate can be obtained by rearranging Eq. (4.15) as follows:

$$\left(\left[\left(\overline{K_{eq}}-K_{Temp-tt}\right)\right]-\left(\omega^2[\mathrm{M}]\right)\right)\{\mathrm{X}\}=0 \tag{4.17}$$

where ω and X are the PFGS plate's natural frequency and corresponding eigenvector, respectively.

4.3. RESULTS AND DISCUSSIONS

The PFGS plate is considered to investigate the effects of porosity and geometrical skewness on the geometrically nonlinear free vibration and transient deflections subjected to thermal loads. Several validation studies have been carried out to check the accuracy of the proposed nonlinear FE model.

The reference temperature (T_0) and the temperature on the metal surface (T_m) are assumed to be 300 K. The properties such as thermal conductivity (k), density, and

Poisson's ratio of the ceramic and metal constituents are presumed to be independent of temperature, as they are weakly dependent on temperature changes. The mass density (ρ_c) and thermal conductivity (k_c) for ceramic material (silicon nitride - Si_3N_4) are 2370 kg/m^3 and 9.19 W/m K, respectively; meanwhile; 8166 kg/m^3 and 12.04 W/m K are the mass density (ρ_m) and thermal conductivity (k_m) of metal (stainless steel - SUS304), respectively. The thermal expansion coefficient and Young's modulus are dependent on the temperature. Table 4.1 provides the temperature-dependent coefficients of the materials Si_3N_4 and SUS304 used in the present investigation. For Si_3N_4 / SUS304, the Poisson's ratio is presumed to be constant at 0.28. Various parameters are considered in parametric studies to investigate the nonlinear frequency and transient responses of the PFGS plate under thermal load.

The non-dimensional equation $\omega_{NL} = \bar{\omega}_{NL}\left(a^2/h\right)\sqrt{\rho_m(1-\upsilon_m^2)/E_m}$ is used to assess the nonlinear frequency parameter (NLFP) of the Si_3N_4 / SUS304 PFGS plate under a thermal loading for various geometrical parameters. Where E_m , ρ_m, and υ_m are Young's modulus, density, and Poisson's ratio of the metal (SUS304) at a reference temperature (T_0 = 300 K), respectively.

Table 4.1: Coefficients of the temperature-dependent constituent materials Si_3N_4 and SUS304: Young's modulus E (Pa) and the coefficient of thermal expansion α (1/K) (Reddy and Chin 1998).

Materials	Properties	ς_0	ς_{-1}	ς_1	ς_2	ς_3	P(T=300 K)
Si_3N_4	E (Pa)	348.43e9	0.0	-3.070e-4	2.160e-7	-8.946e-11	322.2715e9
	α (1/K)	5.8723e-6	0.0	9.095e-4	0.0	0.0	7.4746e-6
SUS304	E (Pa)	201.04e9	0.0	3.079e-4	-6.534e-7	0.0	207.7877e9
	α (1/K)	12.330e-6	0.0	8.086e-4	0.0	0.0	15.321e-6

4.4. Convergence and validation

The robustness of the proposed nonlinear finite element model enables the parametric analyses to be carried out by validating and comparing the obtained results with solutions available in the open literature.

Example 1: The natural frequency of the FG plate from the present analysis is compared with the various open literature (Hosseini-Hashemi et al. 2010, 2011; Matsunaga 2008; Zhao et al. 2009) for different thickness ratios. It can be observed from Table 4.2 that the percentile error is less than 1 % compared to the reference literature (Hosseini-Hashemi et al. 2010, 2011; Matsunaga 2008; Zhao et al. 2009). Hence, the obtained results from the proposed IFSDT formulation display excellent agreement with the reference literature (Hosseini-Hashemi et al. 2010, 2011; Matsunaga 2008; Zhao et al. 2009).

Example 2: The dimensionless fundamental frequency for a simply supported Si_3N_4 / SUS304 FG square plate under thermal loading is compared with Huang and Shen's (2004) results for different volume fraction grading indexes (m). The plate's ceramic surface is exposed to two thermal loadings (T_c), 400 K and 600 K, respectively. The metal surface has a temperature (T_m) of 300 K. Table 4.3 shows that the current model's results are very similar to those reported in the reference literature (Huang and Shen 2004). Besides, [8 × 8] mesh size is considered sufficient to model the PFGS plate based on progressive mesh refinement.

Example 3: The fundamental natural frequency is computed to check the reliability of the present model on the skewness of the isotropic plate with skew angles of 0°, 15°, 30°, and 45°. Table 4.4 shows that the findings presented in the table agree very well with reference literature (Liew et al. 1993).

Example 4: Table 4.5 compares the linear frequency responses of the SSSS FG porous plate with geometry for EDP (P_e) and CDP (P_c) under the drained condition to those in the literature (Rezaei et al. 2017). The validation parameters are identical to those in the reference literature (Rezaei et al. 2017), and the porous FG material used is Al_2O_3/Al. Table 4.5 illustrates that the findings agree with the available literature (Rezaei et al. 2017).

Example 5: Figure 4.2 shows the comparison of the SSSS FG (Si_3N_4/ SUS304) plate for the geometrical parameters m = 1, a/h =10, and a/b = 1 on the nonlinear frequency ratio (NLFR) (ω_{NL}/ω). The validation and comparison of the current model are based on the same material properties and boundary conditions as those utilized in the

literature (Sundararajan et al. 2005). The obtained results are identical to those found in the reference literature (Sundararajan et al. 2005), as shown in Figure 4.2.

Table 4.2: Comparison of the fundamental natural frequency of simply supported Al/Al_2O_3 FG square plates.

h/*a*	Method	Volume fraction grading index (*m*)					
		0	0.5	1	4	10	∞
0.05	Present [2×2]	0.0153	0.0130	0.0118	0.0101	0.0096	-
	Present [4×4]	0.0148	0.0125	0.0113	0.0098	0.0094	-
	Present [6×6]	0.0148	0.0125	0.0113	0.0098	0.0094	-
	Present [8×8]	0.0148	0.0125	0.0113	0.0098	0.0094	-
	TSDT (Hosseini-Hashemi et al. 2011)	0.0148	0.0125	0.0113	0.0098	0.0094	-
	FSDT (Hosseini-Hashemi et al. 2010)	0.0148	0.0128	0.0115	0.0101	0.0096	-
	FSDT (Zhao et al. 2009)	0.0146	0.0124	0.0112	0.0097	0.0093	-
0.1	Present [8×8]	0.0577	0.0491	0.0442	0.0380	0.0363	0.0295
	TSDT (Hosseini-Hashemi et al. 2011)	0.0577	0.0490	0.0442	0.0381	0.0364	0.0293
	HSDT (Matsunaga 2008)	0.0577	0.0492	0.0443	0.0381	0.0364	0.0293
	FSDT (Hosseini-Hashemi et al. 2010)	0.0577	0.0492	0.0445	0.0383	0.0363	0.0294
	FSDT (Zhao et al. 2009)	0.0568	0.0482	0.0435	0.0376	0.3592	-
0.2	Present [8×8]	0.2106	0.1807	0.1631	0.1370	0.1283	0.1077
	TSDT (Hosseini-Hashemi et al. 2011)	0.2113	0.1807	0.1631	0.1378	0.1301	0.1076
	HSDT (Matsunaga 2008)	0.2121	0.1819	0.1640	0.1383	0.1306	0.1077
	FSDT (Hosseini-Hashemi et al. 2010)	0.2112	0.1806	0.1650	0.1371	0.1304	0.1075
	FSDT (Zhao et al. 2009)	0.2055	0.1757	0.1587	0.1356	0.1284	-

Furthermore, Figure 4.2 shows that the current NLFR results are slightly higher than the reference values. The IFSDT and FSDT with von Karman's assumptions utilized by the current model and reference material (Sundararajan et al. 2005) lead to this

disparity. As a result, the nonlinear frequency is influenced by the mass, linear stiffness, and nonlinear stiffness matrices.

Table 4.3: Comparison of fundamental natural frequency for simply supported Si_3N_4 / SUS304 square FG plate under thermal loading. ($a = b = 0.2$, $a/h = 8$).

Temperature (K)	Ref. (Huang and Shen 2004)	Volume fraction grading index (m)				
		Ceramic	0.5	1	2	Metal
$T_c = 400$ $T_m=300$	Present [2×2]	12.2104	8.4184	7.3791	6.6124	5.2374
	Present [4×4]	12.3919	8.5404	7.4884	6.7138	5.3104
	Present [6×6]	12.4182	8.5579	7.5037	6.7278	5.3214
	Present [8×8]	12.4264	8.5634	7.5085	6.7322	5.3248
	Ref.	12.397	8.615	7.474	6.693	5.311
	% Diff	0.236	0.598	0.459	0.582	0.259
$T_c = 600$ $T_m=300$	Present [2×2]	11.8264	8.1076	7.0847	6.3268	4.9202
	Present [4×4]	11.9785	8.2042	7.1693	6.4039	4.9671
	Present [6×6]	12.0025	8.2199	7.1829	6.4161	4.9761
	Present [8×8]	12.0101	8.2249	7.1871	6.4200	4.9790
	Ref.	11.984	8.269	7.171	6.398	4.971
	% Diff	0.217	0.533	0.224	0.342	0.160

Table 4.4: The dimensionless natural frequency comparison for an isotropic skew plate ($a/b = 1$, SSSS).

a/h	Ref. (Liew et al. 1993)	Skew angle (Φ)			
		0°	15°	30°	45°
10	Present	1.9491	2.0945	2.5447	3.4285
	Ref.	1.9311	2.0379	2.4195	3.3548
5	Present	1.8170	1.9084	2.2035	2.7864
	Ref.	1.7661	1.8560	2.1719	2.9129

Example 6: The proposed model is validated with Chen et al. (2000) to verify the reliability and accuracy of the methodology used to study nonlinear transient

deflections for an orthotropic plate. It can be observed from Figure 4.3 that the nonlinear transient deflection exhibits a very similar response compared to the reference literature (Chen et al. 2000).

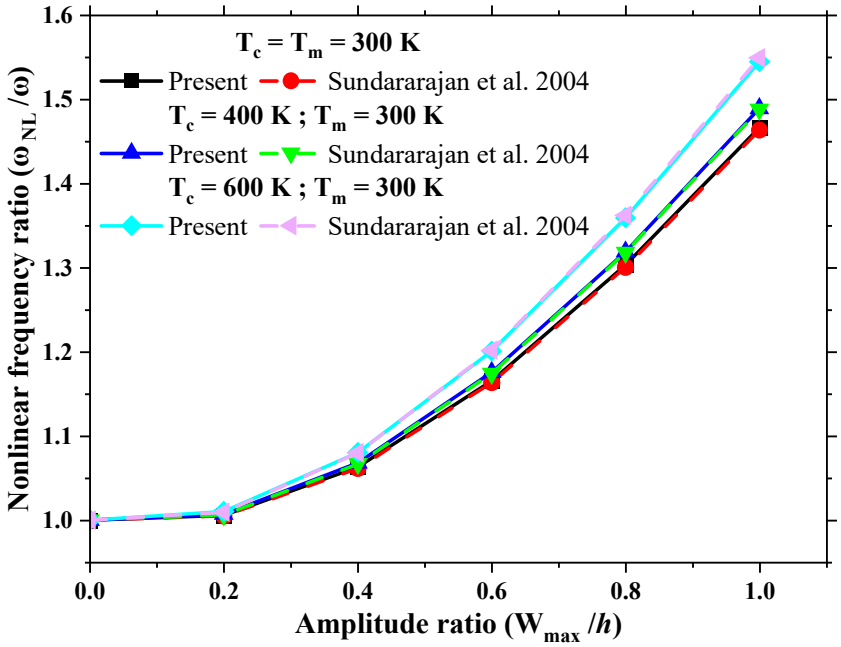

Figure 4.2: Nonlinear frequency ratio (NLFR) comparison of a SSSS Si_3N_4 / SUS304 FG plate in under thermal loading ($a = b = 1$, $a/h = 10$, and $m = 2$).

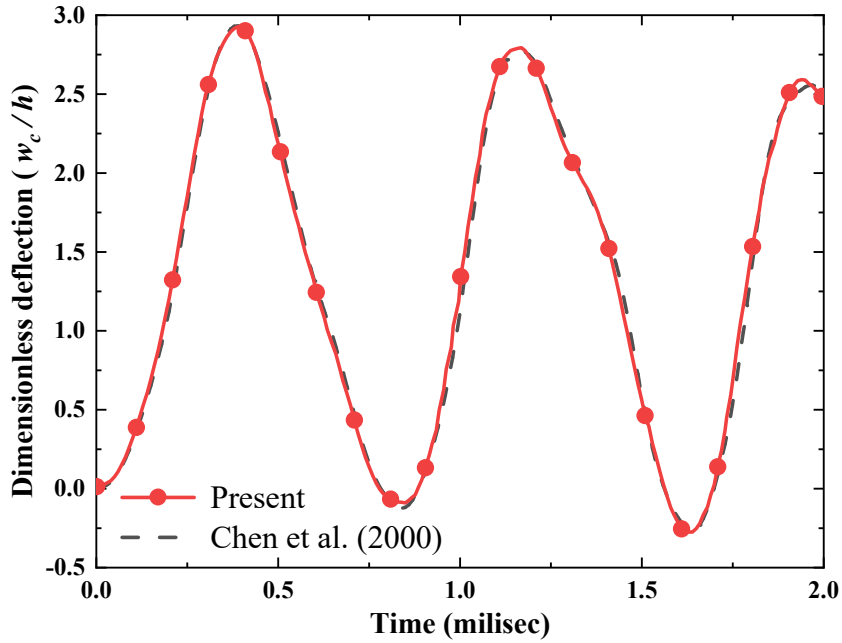

Figure 4.3: Comparison of dimensionless nonlinear transient deflection of the simply supported orthotropic plate.

Table 4.5: Natural frequency comparison for SSSS Al_2O_3/Al porous FG plate with various porosity volume indexes.

b/a	e_p	Sources (Rezaei et al. 2017)	m = 0		m = 0.5		m = 1	
			P_e	P_c	P_e	P_c	P_e	P_c
h/a = 0.05								
1	0	Ref.	0.0291	0.0291	0.0247	0.0247	0.0222	0.0222
		Present	0.0291	0.0291	0.0247	0.0247	0.0222	0.0222
	0.2	Ref.	0.0300	0.0300	0.0246	0.0252	0.0210	0.0225
		Present	0.0295	0.0298	0.0241	0.0251	0.0207	0.0223
	0.4	Ref.	0.0314	0.0310	0.0242	0.0259	0.0182	0.0227
		Present	0.0305	0.0307	0.0235	0.0257	0.0176	0.0225
h/a = 0.1								
0.5	0	Ref.	0.0719	0.0719	0.0610	0.0610	0.0550	0.0550
		Present	0.0718	0.0718	0.0610	0.0610	0.0549	0.0549
	0.2	Ref.	0.0742	0.0740	0.0607	0.0624	0.0521	0.0555
		Present	0.0729	0.0736	0.0597	0.0620	0.0512	0.0552
	0.4	Ref.	0.0775	0.0765	0.0599	0.0640	0.0450	0.0561
		Present	0.0753	0.0758	0.0583	0.0634	0.0438	0.0555

4.5. Nonlinear frequency analysis of the PFGS plate

4.5.1. Effect of temperature rise on the NLFR

The effects of temperature rise on the NLFR of the PFGS plate at a skew angle ($\Phi = 0°$) and the porosity volume index for different porosity distributions are shown in Figure 4.4. The ceramic surface has a different temperature, i.e., T_c = 300 K, 400 K, 500 K, 600 K, 700 K, and 800 K. It can be seen that as the temperature gradient ($\Delta T = T_c - T_m$) increases, the NLFR increases for a given porosity distribution. This is due to the rapid decrease in linear frequency relative to NLFP with an increase in the temperature gradient. Furthermore, as the temperature increases, the PFGS plate's Young's modulus decreases, lowering the corresponding linear frequency. The NLFR thus increases with an increase in temperature gradient and amplitude ratio.

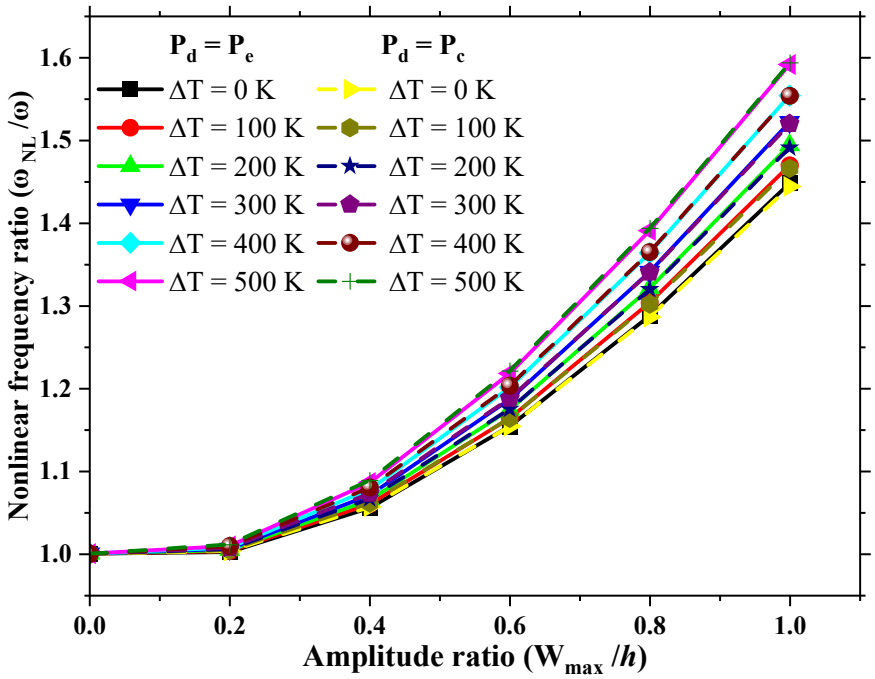

Figure 4.4: Effects of temperature rise on NLFR for the porosity distributions P_e and P_c ($a/b = 1$, $a/h = 10$, $e_p = 0.1$, $\Phi = 0°$, $m = 2$, and SSSS).

Furthermore, evenly distributed porosities have slightly higher NLFR values than centrally distributed porosities regardless of temperature change ($P_c < P_e$). This implies that NLFR depends on the distribution of porosity in the PFGS plate, besides the temperature change. This is because arrangements of the porosities in the P_e facilitate the uniform distribution of materials across the thickness. In contrast, more materials are accumulated far away from the middle plane for P_c leading to high stiffness in the plate. In addition, for all the temperature gradient and porosity distributions, the plate shows nonlinear behaviour for the value of amplitude ratio (W_{max} /h) greater than 0.2, which indicates the increase in hardening behaviour. Hence, the NLFR of the PFGS plate increases as the amplitude ratio (W_{max} /h) rises.

4.5.2. Effect of skew angle

The influence of skew angle on the NLFR of the PFGS plate for various porosity distributions with temperature rise is demonstrated in Table 4.6. The NLFR values are considered at the amplitude ratio $W_{max}/ h = 1.0$. It can be seen that as the skew angle of the plate increases, the NLFR decreases for a given temperature gradient. Besides, the NLFR increases with an increase in temperature gradient for a given skew angle. As

the skew angle increases, the plate's flexural stiffness also rises, leading to an increase in the linear frequency. Thus, the disparity between nonlinear and linear frequency decreases. As a result, a change in skewness in the PFGS plate can vary the NLFR. Furthermore, centrally distributed porosities have lower NLFR values relative to the evenly distributed porosities ($P_e > P_c$), in addition to the rise in temperature gradient and skew angle, respectively. This is because the porosities in the P_e are arranged with a uniform material distribution over the thickness. On the other hand, P_c accumulates more materials away from the middle plane, resulting in a plate with high rigidity.

Table 4.6: Influence of various skew angles on the NLFR for the porosity distributions P_e and P_c ($a/b = 1$, $a/h = 10$, $e_p = 0.1$, $m = 2$, $W_{max}/h = 1.0$, and SSSS).

P_d	Φ	ΔT					
		0	100	200	300	400	500
P_e	0°	1.4485	1.4700	1.4943	1.5221	1.5540	1.5919
	15°	1.4118	1.4297	1.4496	1.4722	1.4979	1.5275
	30°	1.3411	1.3525	1.3649	1.3785	1.3935	1.4103
	45°	1.2850	1.2914	1.2983	1.3055	1.3134	1.3215
P_c	0°	1.4443	1.4663	1.4914	1.5203	1.5540	1.5939
	15°	1.4084	1.4267	1.4474	1.4709	1.4979	1.5294
	30°	1.3383	1.3500	1.3629	1.3771	1.3930	1.4109
	45°	1.2819	1.2885	1.2957	1.3033	1.3115	1.3205

4.5.3. Effect of porosity volume index

The influence of different porosity volume indices with porosity distributions on the NLFR of the PFGS plate for different thermal loadings and skew angles at an amplitude ratio (W_{max}/h) 1.0 is presented in Table 4.7. It can be found that the NLFR steadily decreases with an increase in the porosity volume index for a given value of temperature gradient and skew angle. Besides, both the porosity distributions (P_e and P_c) show a similar pattern. It is due to the plate's properties deteriorating in the presence of porosities in a thermal environment. The P_e type of porosity distribution has higher NLFR values for all porosity volume indices, while P_c has the lowest NLFR value (P_e

> P_c). Hence, the effects of porosities are lower in the centrally distributed porosity (P_c) than in the evenly distributed porosity (P_e) for NLFR.

Table 4.7: Influence of porosity volume index on NLFR for different thermal loadings ($a/b = 1$, $a/h = 10$, $m = 2$, $W_{max}/h = 1.0$, and SSSS).

Φ	ΔT (K)	P_d	e_p					
			0.0	0.1	0.2	0.3	0.4	0.5
0°	0 K	P_e	1.4636	1.4485	1.4309	1.4096	1.3826	1.3460
		P_c	1.4636	1.4443	1.4246	1.4045	1.3838	1.3625
	200 K	P_e	1.5164	1.4943	1.4702	1.4428	1.4103	1.3686
		P_c	1.5164	1.4914	1.4665	1.4418	1.4171	1.3923
	500 K	P_e	1.6355	1.5919	1.5487	1.5043	1.4567	1.4008
		P_c	1.6355	1.5939	1.5550	1.5183	1.4834	1.4499
15°	0 K	P_e	1.4258	1.4118	1.3956	1.3761	1.3516	1.3188
		P_c	1.4258	1.4084	1.3907	1.3725	1.3539	1.3347
	200 K	P_e	1.4694	1.4496	1.4281	1.4036	1.3746	1.3377
		P_c	1.4694	1.4474	1.4255	1.4037	1.3818	1.3597
	500 K	P_e	1.5640	1.5275	1.4909	1.4531	1.4119	1.3636
		P_c	1.5640	1.5294	1.4967	1.4657	1.4359	1.4070
30°	0 K	P_e	1.3518	1.3411	1.3286	1.3136	1.2950	1.2705
		P_c	1.3518	1.3383	1.3245	1.3103	1.2957	1.2805
	200 K	P_e	1.3791	1.3649	1.3492	1.3313	1.3099	1.2828
		P_c	1.3791	1.3629	1.3466	1.3303	1.3138	1.2970
	500 K	P_e	1.4338	1.4103	1.3863	1.3607	1.3322	1.2983
		P_c	1.4338	1.4109	1.3890	1.3677	1.3468	1.3263
45°	0 K	P_e	1.2919	1.2850	1.2767	1.2666	1.2539	1.2372
		P_c	1.2919	1.2819	1.2715	1.2608	1.2497	1.2382
	200 K	P_e	1.3070	1.2983	1.2883	1.2767	1.2626	1.2446
		P_c	1.3070	1.2957	1.2841	1.2723	1.2603	1.2479
	500 K	P_e	1.3348	1.3215	1.3077	1.2923	1.2745	1.2527
		P_c	1.3348	1.3205	1.3063	1.2922	1.2781	1.2639

Furthermore, Figure 4.5 display the influence of porosity volume indexes on the NLFP (ω_{NL}) for different temperature gradients and skew angles. For the SSSS and CCCC boundary conditions of the PFGS plate, the influence of temperature change (ΔT = 0 K, 200 K, and 400 K) for different skew angles of 0°, 15°, 30°, and 45° on NLFP is considered for the investigation. Figure 4.5 show that, for any given temperature gradient and skew angle, the NLFP decreases gradually with an increase in the porosity volume index for an evenly distributed porosity distribution. On the other hand, the NLFP decreases steadily and is considered stable as the porosity volume index increases for centrally distributed porosity distributions. It may be due to the more material accretion away from the middle surface stabilizing the PFGS plate's flexural stiffness for porosity distributions of type P_c. Meanwhile, the distribution of porosities in the P_e leads to uniform material distribution over the thickness, resulting in a sudden decrease in the stiffness. This means that the gradation area's porosities significantly affect the NLFP more than evenly distributed porosities.

In addition, for any given temperature gradient and skew angle, NLFP is less susceptible to changes in porosity volume density for centrally distributed porosities than for evenly dispersed porosities. Hence, the NLFP of P_c is greater than the NLFP of P_e. The same trend is observed for both the SSSS and CCCC boundary conditions. Interestingly, for any given porosity volume index and skew angle, the NLFP decreases as the temperature gradient increases. This is because Young's modulus of the PFGS plate decreases as temperature increases. Moreover, the temperature effects of the clamped PFGS plate's nonlinear vibrational frequencies are greater than those of the simply supported PFGS plates. Compared to the simply supported PFGS plates for the nonlinear rise in temperature, the thermal stresses are fully developed for the supported edges of fully constrained (clamped boundary condition). Thus, the NLFP has greater values for CCCC boundary conditions than the SSSS case. Furthermore, for any given temperature gradient and porosity volume index, the NLFP increases as the skew angle increases. Besides, as compared to the P_e type of porosity distribution, NLFP has the highest values for the P_c type ($P_c > P_e$). This infers that the NLFP is more sensitive to the P_c than the P_e.

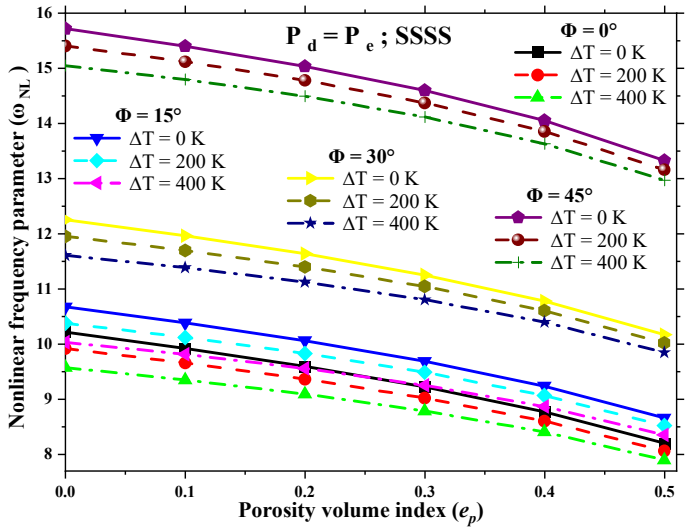

(a) P_e and SSSS

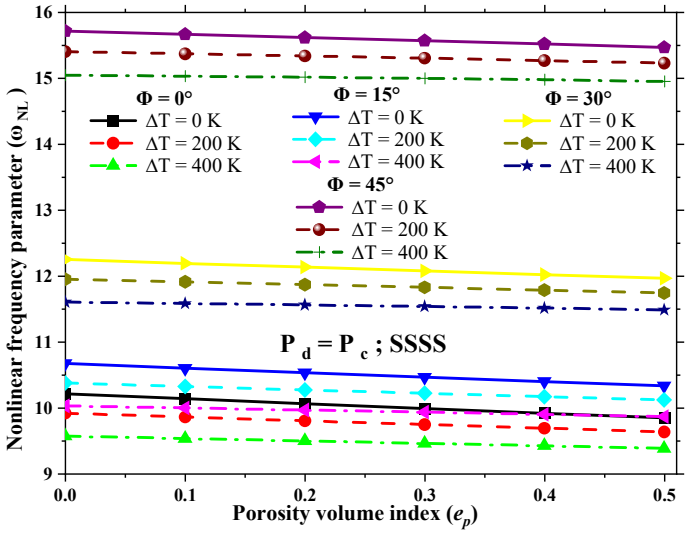

(b) P_c and SSSS

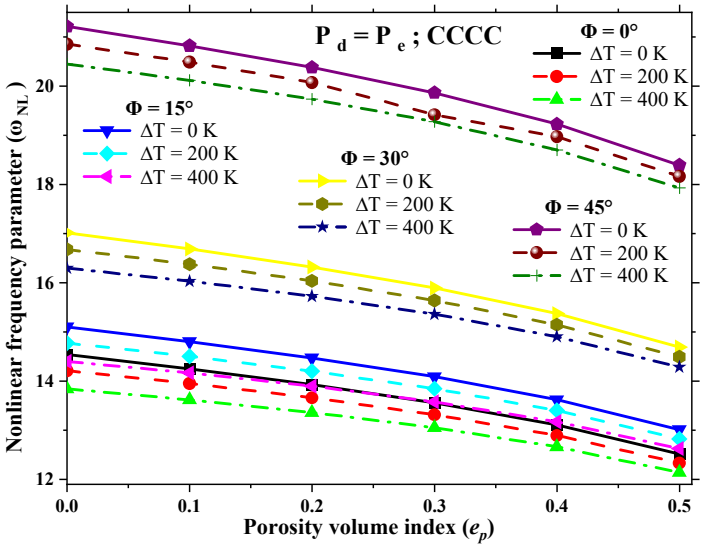

(c) P_e and CCCC

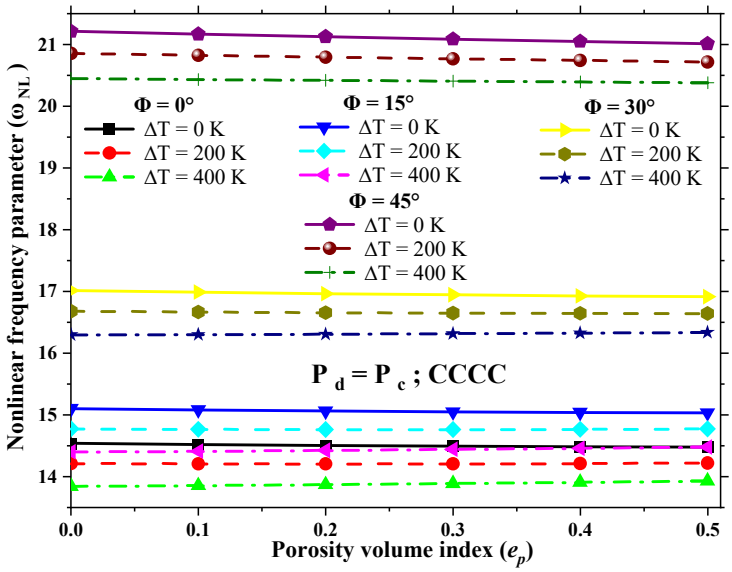

(d) P_c and CCCC

Figure 4.5: Influence of various porosity volume indices for different temperatures on NLFP (a/b = 1, a/h = 10, m = 2, and W_{max}/h = 1.0).

4.5.4. Effect of thickness and aspect ratio

The porosity distribution's influence at a various thickness to length ratios (h/a) on the NLFR of the PFGS plate with different skew angles is shown in Table 4.8. The temperature gradients ΔT = 0 K, 200 K, and 400 K are considered for the analysis. Table 4.8 shows that the NLFR decreases until h/a = 0.10, but it enhances with an increase in the thickness-to-length ratio from h/a = 0.12. This trend is observed for less skewed (Φ = 0° and 15°) PFGS plates. Meanwhile, the NLFR increases steadily by increasing the thickness ratio for highly skewed (Φ = 30° and 45°) plates. This increase or decrease in the NLFR trend can be observed irrespective of porosity distributions and temperature gradients. It may be because greater stiffness is achieved by having lower thickness ratios. Also, the plate's hardening behavior is enhanced in the presence of porosities in a thermal environment. Also, for any given thickness-to-length ratio, the P_c has the lowest NLFR while the P_e shows the highest ($P_e > P_c$). However, a noticeable meager difference between the two porosity distributions (P_c and P_e) can also be observed.

Table 4.8: Effect of thickness ratio on NLFR under different thermal loadings (a/b=1, m = 2, e_p = 0.1, W_{max}/h = 1.0, and SSSS).

Φ	ΔT (K)	P_d	*h/a*					
			0.06	0.08	0.10	0.12	0.14	0.16
0°	0 K	P_e	1.4360	1.4414	1.4485	1.4573	1.4676	1.4801
		P_c	1.4312	1.4369	1.4443	1.4538	1.4641	1.4766
	200 K	P_e	1.5616	1.5098	1.4943	1.4917	1.4953	1.5032
		P_c	1.5610	1.5073	1.4914	1.4887	1.4926	1.5007
	400 K	P_e	1.8263	1.6122	1.5540	1.5334	1.5274	1.5294
		P_c	1.8452	1.6148	1.5540	1.5323	1.5262	1.5283
15°	0 K	P_e	1.3852	1.3991	1.4118	1.4246	1.4379	1.4522
		P_c	1.3817	1.3956	1.4084	1.4214	1.4349	1.4496
	200 K	P_e	1.4777	1.4533	1.4496	1.4538	1.4620	1.4729
		P_c	1.4776	1.4515	1.4474	1.4514	1.4597	1.4707
	400 K	P_e	1.6493	1.5306	1.4979	1.4887	1.4894	1.4958
		P_c	1.6615	1.5329	1.4979	1.4880	1.4885	1.5063
30°	0 K	P_e	1.3059	1.3239	1.3411	1.3579	1.3747	1.3916
		P_c	1.3027	1.3210	1.3383	1.3553	1.3723	1.3895
	200 K	P_e	1.3556	1.3558	1.3649	1.3773	1.3914	1.4052
		P_c	1.3542	1.3539	1.3629	1.3753	1.3895	1.4041
	400 K	P_e	1.4318	1.3975	1.3935	1.3995	1.4098	1.4209
		P_c	1.4350	1.3978	1.3930	1.3986	1.4087	1.4216
45°	0 K	P_e	1.2542	1.2692	1.2850	1.3010	1.3164	1.3312
		P_c	1.2503	1.2657	1.2819	1.2985	1.3141	1.3295
	200 K	P_e	1.2797	1.2863	1.2983	1.3127	1.3266	1.3415
		P_c	1.2766	1.2834	1.2957	1.3098	1.3247	1.3390
	400 K	P_e	1.3134	1.3067	1.3134	1.3239	1.3379	1.3493
		P_c	1.3120	1.3049	1.3115	1.3230	1.3355	1.3483

Furthermore, Table 4.9 presents the influence of porosity distributions on the width-to-length (b/a) aspect ratio under the various thermal loadings and skew angles. It can be

observed from Table 4.9 that the NLFR decreases till b/a = 1; however, it enhances with an increase in width-to-length ratio from 1.2.

Table 4.9: Effect of aspect ratio on NLFR under thermal loading (a/h =10, m = 2, e_p = 0.1, W_{max}/h = 1.0, and SSSS).

Φ	ΔT (K)	P_d	b/a					
			0.6	0.8	1.0	1.2	1.4	1.6
0°	0 K	P_e	1.5362	1.4687	1.4485	1.4552	1.4753	1.5010
		P_c	1.5308	1.4643	1.4443	1.4506	1.4700	1.4949
	200 K	P_e	1.5684	1.5073	1.4973	1.5090	1.5376	1.5716
		P_c	1.5285	1.5039	1.4914	1.5058	1.5339	1.5674
	400 K	P_e	1.6059	1.5552	1.5540	1.5825	1.6254	1.6740
		P_c	1.6029	1.5539	1.5540	1.5828	1.6259	1.6744
15°	0 K	P_e	1.4587	1.4160	1.4118	1.4291	1.4566	1.4873
		P_c	1.4545	1.4126	1.4084	1.4252	1.4518	1.4820
	200 K	P_e	1.4835	1.4468	1.4496	1.4750	1.5110	1.5505
		P_c	1.4782	1.4443	1.4474	1.4724	1.5078	1.5465
	400 K	P_e	1.3397	1.4840	1.4979	1.5360	1.5856	1.6386
		P_c	1.5097	1.4834	1.4979	1.5363	1.5858	1.6391
30°	0 K	P_e	1.2984	1.3097	1.3411	1.3823	1.4264	1.4695
		P_c	1.2960	1.3074	1.3383	1.3788	1.4220	1.4634
	200 K	P_e	1.3111	1.3271	1.3649	1.4139	1.4664	1.5164
		P_c	1.3089	1.3253	1.3629	1.4113	1.4630	1.5135
	400 K	P_e	1.3247	1.3472	1.3935	1.4533	1.5175	1.5804
		P_c	1.3237	1.3463	1.3930	1.4527	1.5167	1.5792
45°	0 K	P_e	1.1439	1.2109	1.2850	1.3568	1.4226	1.4788
		P_c	1.1414	1.2084	1.2819	1.3530	1.4177	1.4745
	200 K	P_e	1.1473	1.2186	1.2983	1.3775	1.4504	1.3447
		P_c	1.1431	1.2165	1.2957	1.3741	1.4462	1.5083
	400 K	P_e	1.1511	1.2270	1.3134	1.4010	1.4836	1.5840
		P_c	1.1493	1.2252	1.3115	1.3987	1.4809	1.3656

This trend is observed for PFGS plates that are less skewed (Φ = 0° and 15°). Meanwhile, the NLFR increases steadily with an increase in the width-to-length ratio for highly skewed (Φ = 30° and 45°) plates. The increase or decrease in NLFR can be observed regardless of porosity distributions and temperature gradients. This could be because the geometrical instability increases as the structural elements become thinner in the presence of porosities in a thermal environment, which affects the plate's dynamic behaviour. Also, the porosity distribution P_c has the lowest, and P_e has the highest values of NLFR for a given aspect ratio ($P_c < P_e$).

4.5.5. Effect of boundary conditions

The effect of porosity distributions on the NLFR of the PFGS plate for different boundary conditions is depicted in Figure 4.6. For simplicity, the results are extracted only for the skew angle Φ = 30° and the temperature gradient ΔT = 300 K. Figure 4.6 shows that regardless of boundary conditions, porosities, and temperature, an increase in NLFR is correlated with an increase in amplitude ratio. Furthermore, NLFR is high for the simply supported case and lowest for the CCCF case. This is because the flexural stiffness increases with an increase in boundary constraints, leading to an increase in the linear frequency. Thus, the NLFR decreases.

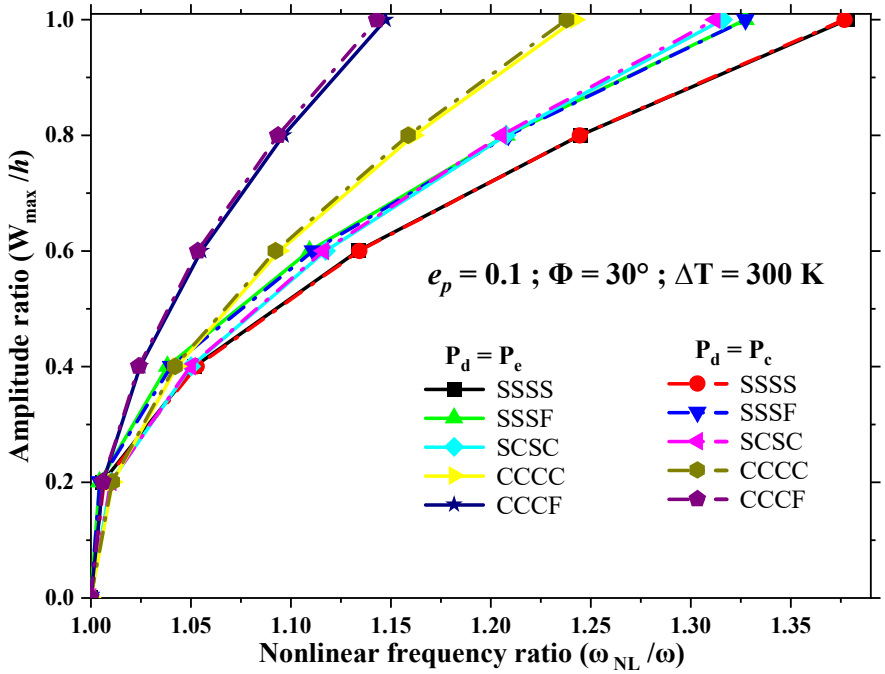

Figure 4.6: Influence of various boundary conditions for the porosity distributions P_e and P_c on NLFR. (a/b = 1, a/h = 10, m = 2, e_p = 0.1, Φ = 30°, and ΔT = 300).

However, free edges have no constraints, which contributes to a lower plate stiffness value. Hence, the structure becomes stiffer for clamped boundary constraints. Therefore, for the CCCF case, the NLFR has the lowest value. The NLFR decreases with the following boundary condition pattern: SSSS > SSSF > SCSC > CCCC > CCCF. Furthermore, a noticeable difference is shallow between the P_e and P_c types of porosity distributions for any given boundary conditions. In contrast, the NLFR exhibits the lowest values for P_c type compared to the P_e type of porosity distributions. Besides, for given support conditions and porosity distribution, the PFGS plate displays nonlinear behavior for a value of amplitude ratio (W_{max} /h) greater than 0.2. Thus, the NLFR of the plate increases as the amplitude ratio (W_{max} /h) rises, exhibiting the hardening behavior.

4.6. Geometrically nonlinear transient response analysis

The significance of porosity distributions on the nonlinear transient deflections of the PFGS plate in a thermal environment is investigated in this section. The effects of skew angle, temperature gradient, porosity distributions, porosity volume index, and volume fraction grading index are analyzed on the geometrically nonlinear transient deflection. A uniform step load of q_0 = 1 N/mm^2, a time step of $\Delta t_i = 1\times10^{-5}$, and a dimensionless transient deflection function $w = w_c / h$ are used for the present analysis.

4.6.1. Effect of porosity volume index and skew angle

The effect of porosity volume indices (e_p = 0.1, 0.2, and 0.3) and different skew angles (Φ = 0° and 40°) on the nonlinear transient deflections of the PFGS plates is shown in Figure 4.7. It can be observed from Figure 4.7 that the amplitude and time period of motion decrease as the skew angle increases. This may be due to an increase in the stiffness of the plate as the skew angle increases. In addition, the porosity volume index affects the deflection due to the variance in the bending stiffness and the thermal strains in the presence of porosities. Consequently, at lower temperatures (T_c = 400 K), a rectangular PFGS plate deflection increases as the porosity volume index increases. In contrast, the deflection decreases for higher temperatures as the porosity volume index increases (T_c = 600 K). Furthermore, deflection increases as the porosity volume index increases for any given temperature of the angled plate and evenly dispersed

porosities. In comparison, the trend is reversed for centrally distributed porosities. This is due to the porous effect that causes the plate stiffness to decrease. For porosity distributions of type P_c, it could be because more material accretion away from the middle surface leads to the PFGS plate's high flexural stiffness. Meanwhile, the porosity dispersion in the P_e results in a consistent material distribution over the thickness, decreasing stiffness.

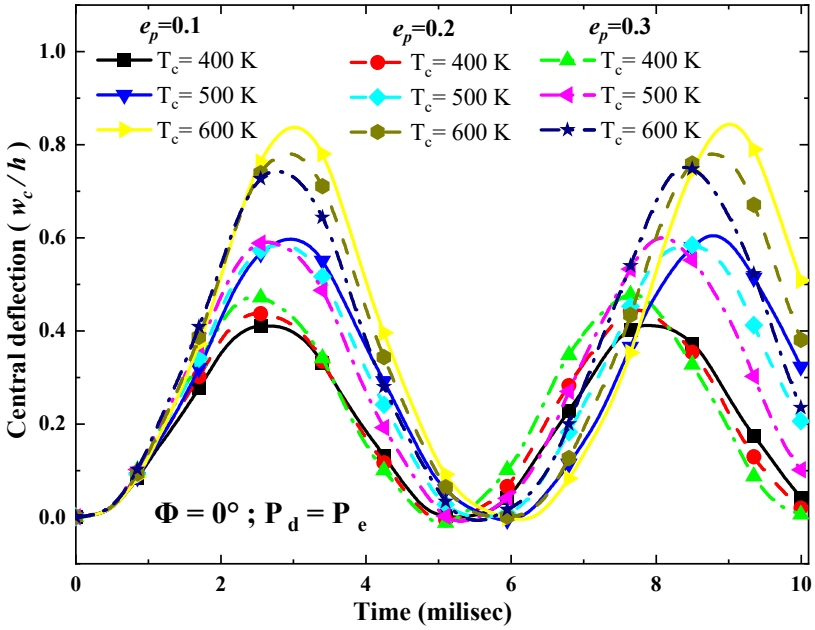

(a) P_e and Φ =0°

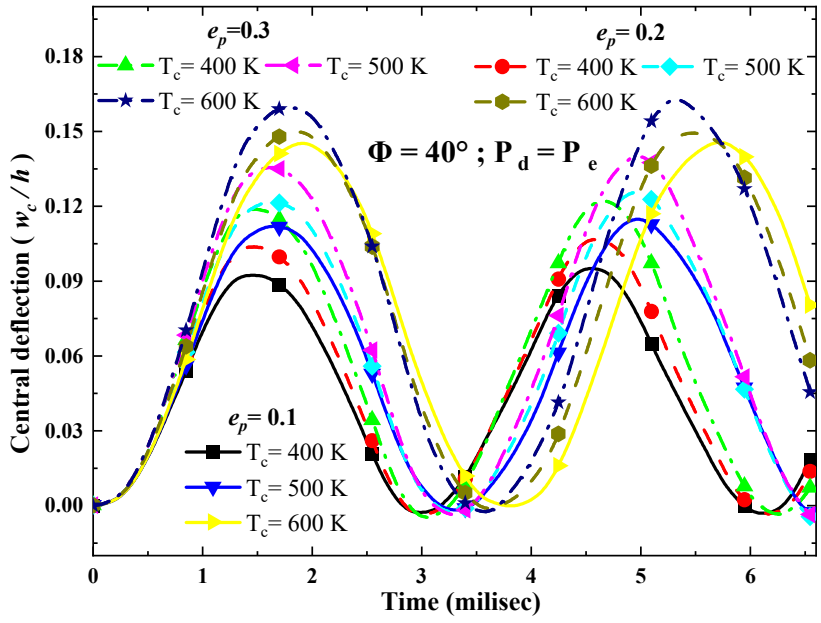

(b) P_e and Φ =40°

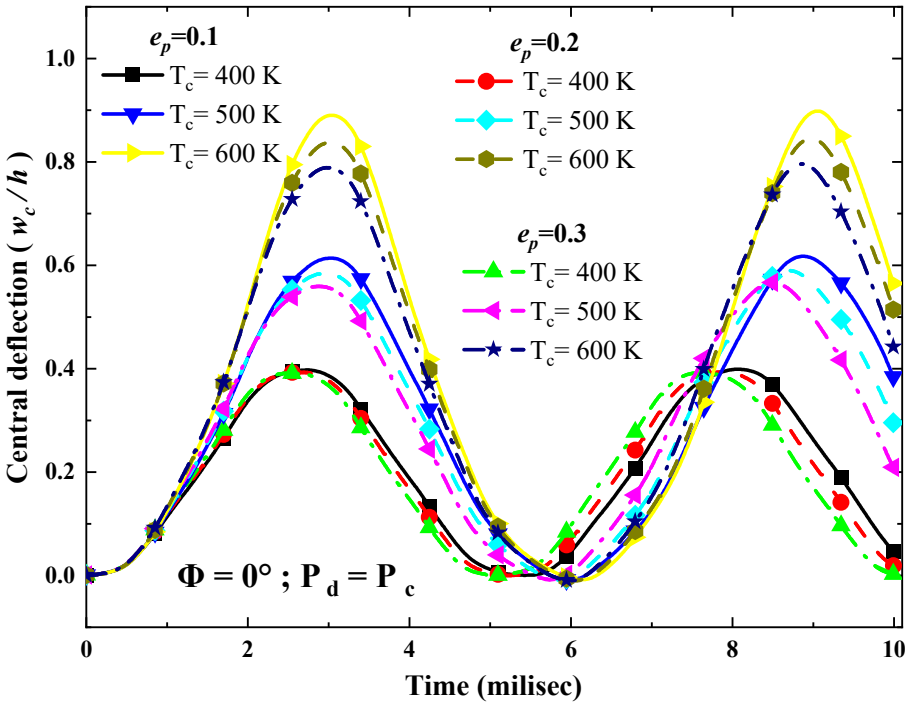

(c) P_c and Φ =0°

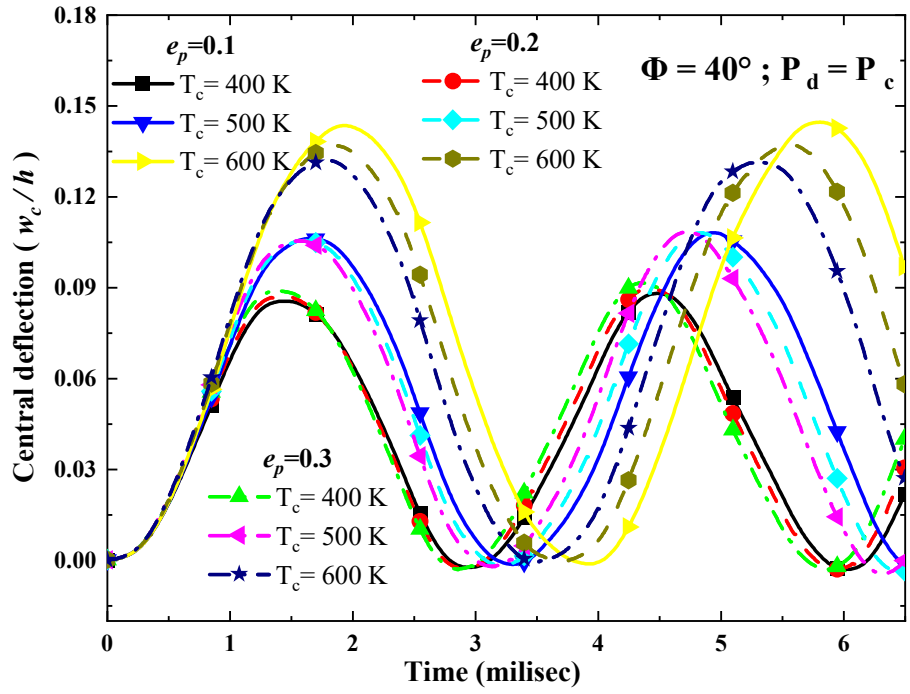

(d) P_c and Φ =40°

Figure 4.7: Influence of porosity volume index on transient deflections of the PFGS plate with different skew angles and temperature rise (a/b = 1, a/h = 30, m = 2, and SSSS).

The impact of thermal loading on the nonlinear transient response of the PFGS plate reveals that as temperature rises, the amplitude and time period of motion increase. Moreover, Figure 4.7 show that under thermal loadings, for the square porous FG plates, the P_c has the highest transient deflections ($P_c > P_e$), and the pattern is reversed for skewed PFGS plates ($P_e > P_c$). It may be due to the porosity distribution leading to the stiffness variation. In addition, the PFGS plate with P_c has higher stiffness for a given skew angle than the P_e due to the distribution of porosities.

4.6.2. Effect of volume fraction grading index

The influence of the volume fraction grading index for P_e and P_c type porosity distributions on the nonlinear transient responses of the PFGS plate under thermal loading is shown in Figure 4.8. It can be seen from Figure 4.8 that with an increase in the volume fraction grading index (m) and temperature, the amplitude and time-period of motion increase. Therefore, as bending rigidity increases, the magnitude of the deflection decreases. Besides, the metallic plate has the highest vibration amplitude, whereas the ceramic plate has the lowest. This is due to a decline in the ceramic composition of the plate as m rises. As a result, the PFGS plate's stiffness decreases as the m increases but increases as the skew angle rises. Thus, increasing the skew angle reduces the plate's transient deflection. Consequently, the influence of volume fraction grading indices seems to be predominant for property determination of PFGS plate, which is subsequently proportional to the stiffness.

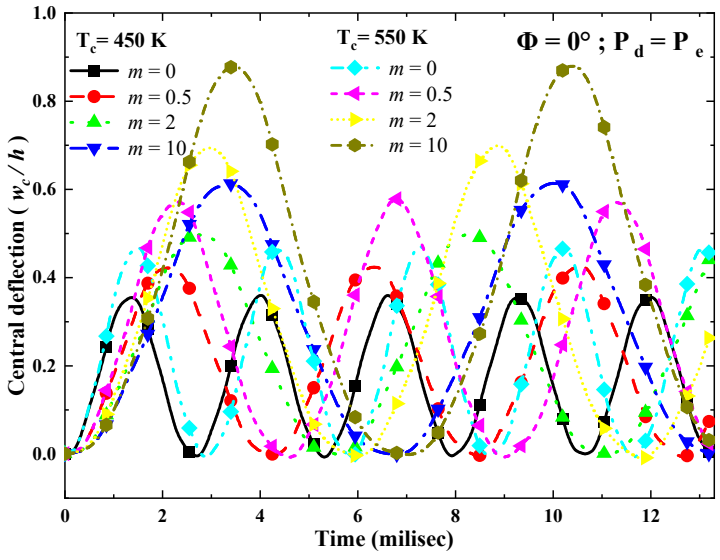

(a) P_e and Φ =0°

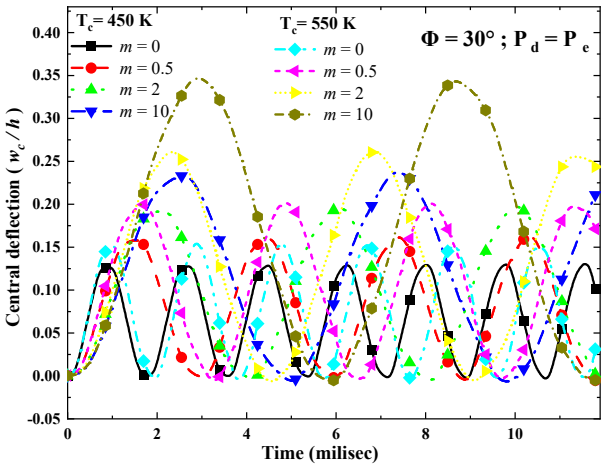

(b) P_e and Φ =30°

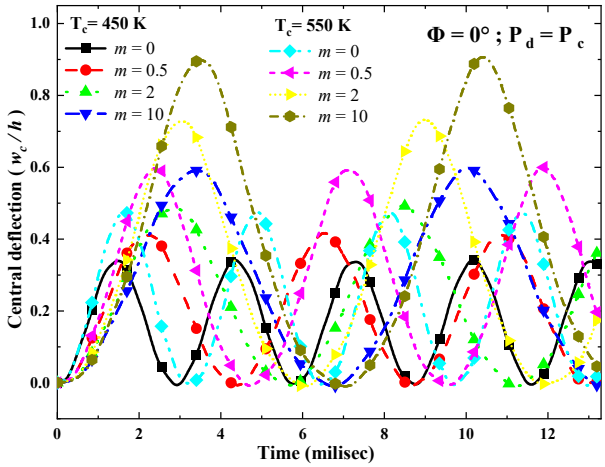

(c) P_c and Φ =0°

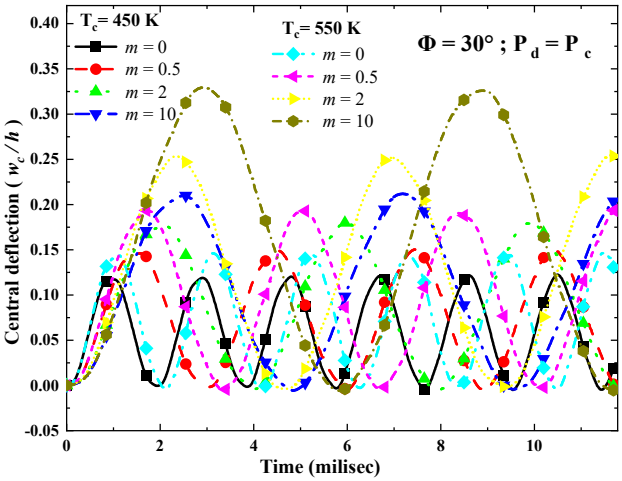

(d) P_c and Φ =30°

Figure 4.8: Influence of volume fraction grading index (m) on transient deflections of the PFGS plate with different skew angles and temperature rise (a/b = 1, a/h = 30, e_p = 0.15, and SSSS).

Figure 4.8 shows that for each value of *m* and T_c, the P_e type of porosity distribution has the lowest nonlinear transient deflections. In contrast, the P_c type has the highest ($P_c > P_e$). As a result, the porosity distribution affects the PFGS plate's deflection. It may be because the distribution of materials in the plate depends on the arrangement of porosities and temperature, which leads to the variation of stiffness.

4.7. CONCLUSIONS

This chapter investigates the influence of porosity distributions on nonlinear free vibration and transient deflections of geometrically skewed functionally graded plates with porosity in a thermal environment. Nonlinear FE formulations are developed by using the IFSDT with von Kármán assumptions. The temperature-dependent effective material properties are estimated using a modified power-law series, which accounts for the different porosity distributions. The nonlinear temperature distribution is considered one-dimensional steady-state heat conduction through the PFGS plate thickness. Using the direct iterative and Newmark's integration approaches, the governing equations of the PFGS plates are extracted using Hamilton's principle. The proposed model's reliability is assessed through various convergence and validation studies.

The following observations are made from the detailed parametric evaluation. With an increase in the amplitude ratio (W_{max}/h) in the presence of porosities and temperature, both NLFR (ω_{NL}/ω) and NLFP (ω_{NL}) increase. Conversely, the NLFR decreases as the skew angle rises, while the NLFP rises. Further, for a given plate skewness, increasing the temperature gradient increases the NLFR while decreasing the NLFP. In contrast, the NLFR decreases with increasing the porosity volume index for both the porosity distributions (P_e and P_c) and the skew angle for a given temperature gradient. The NLFR and NLFP are more vulnerable to centrally dispersed (Pc) than evenly dispersed (Pe) porosity distributions in the thermal environment for all skew angles. The impact of porosity distributions follows the pattern $P_c < P_e$ for NLFR, while on the NLFP, the trend is $P_c > P_e$. For lower skew angles, the NLFR decreases to a particular value for a given porosity distribution and temperature gradient, then increase for both thickness and aspect ratios, respectively. On the other hand, the NLFR steadily increases for higher skew angles. The NLFR has the highest values for the simply supported case

and the lowest values for CCCF boundary conditions for all types of porosity distributions under different thermal loadings used in the analysis. The NLFR decreases in the following pattern: SSSS > SSSF > SCSC > CCCC > CCCF. In the case of NLFP, the temperature effects of the clamped PFGS plate are greater than simply supported boundary conditions. Besides, with increasing volume fraction index and temperature, the nonlinear transient deflection of the PFGS plate in a thermal environment increases and decreases as the skew angle increases. The P_e type has a slight impact, while the P_c type significantly affects geometrically nonlinear deflections.

CHAPTER 5

NONLINEAR ANALYSIS OF TWO-DIRECTIONAL FUNCTIONALLY GRADED DOUBLY CURVED PANELS WITH POROSITIES

This chapter investigates the nonlinear behavior of two-directional functionally graded materials (TDFGM) doubly curved panels with porosities. The composition of TDFGM constitutes four different materials, and the modified power-law function is employed to vary the material properties continuously in both thickness and longitudinal directions. A nonlinear finite element formulation derived in chapter 4 is extended for the analysis of TDFGM shells. Then, the direct iterative method is incorporated to accomplish the numerical results using the frequency-amplitude, nonlinear central deflection relations. Finally, the influence of volume fraction grading indices, porosity distributions, porosity volume, curvature ratio, thickness ratio, and aspect ratio provides a thorough insight into the linear and nonlinear responses of the porous curved panels. Meanwhile, this study emphasizes the influence of the volume fraction gradation profiles in conjunction with the various material and geometrical parameters on the linear frequency, nonlinear frequency, and deflection of the TDFGM porous shells.

5.1. INTRODUCTION

Traditional FGM has been limited to only changing the material properties in a single direction (Jha et al. 2013), usually in the thickness direction. However, this approach may be ineffective in designing propulsion systems and space application components, often exposed to significant stresses or temperature differences in multiple directions (Nemat-Alla 2003, 2009; Nemat-Alla et al. 2009). As a result, bi-directional FGM (BDFGM) was developed by adding another material into the traditional FGM to withstand the induced extreme thermal stresses in advanced engineering applications

such as spacecraft and space shuttles. BDFGM has inherited the advantages of the higher capability to reduce the thermal, mechanical, and residual stresses. Besides, BDFGM contributes to a more flexible design than one-dimensional FGM (1-D FGM) by varying volume fractions of the constituent materials in two or more directions (Asemi et al. 2011; Van Do et al. 2017a; Nemat-Alla 2009; Nie and Zhong 2007; Shariyat and Alipour 2011; Sobhani Aragh and Hedayati 2012). Hence, developing bi-directional or multi-directional FGM is necessary and valuable in advanced structural elements.

In this chapter, a modified power-law series is employed to obtain the effective material properties of the TDFGM porous shells that vary smoothly as an arbitrary function of the volume fractions in longitudinal and transverse directions. The composition of TDFGM comprises four different materials. A nonlinear FE model is developed based on the improved first-order shear deformation theory (IFSDT) in conjunction with von Karman's nonlinearity. The equations of motion are obtained through Hamilton's principle. The equations of motion solutions are incurred using the direct iterative method. The linear and nonlinear vibration characteristics and deflection analysis of the TDFGM porous shells through the different shell geometries such as cylindrical, spherical, hyperboloid, and ellipsoid shells with four different material phases are analyzed for various geometrical and material parameters.

5.2. PROBLEM DESCRIPTION AND GOVERNING EQUATION

The displacement equations, the governing equations, and the nonlinear FE formulation are presented identical to sections 4.2.3 – 4.2.5 of Chapter 4 by ignoring the thermal effects. The solution methodologies are adapted from section 2.3. However, TDFGM shell geometry, homogenization technique for determining the effective material properties, nonlinear strain-displacement equations, and constitutive equations are explained in the following sections.

5.2.1. TDFGM shell geometry

The TDFGM porous shell made of four different material compositions is shown in Figure 5.1. The geometry of the TDFGM shell is referred to as a cartesian coordinate with sides a and b, uniform thickness h, and radii of curvatures R_1 and R_2

along with x and y directions, respectively. The TDFGM shell with four forms of shell geometry based on the curvature such as cylindrical shell ($R_1 = R$, $R_2 = \infty$), spherical shell ($R_1 = R_2 = R$), hyperboloid shell ($R_1 = R$, $R_2 = -R$), and elliptical shell ($R_1 = 2R$, $R_2 = R$) as shown in Figure 5.2 are taken for numerical evaluation in this chapter.

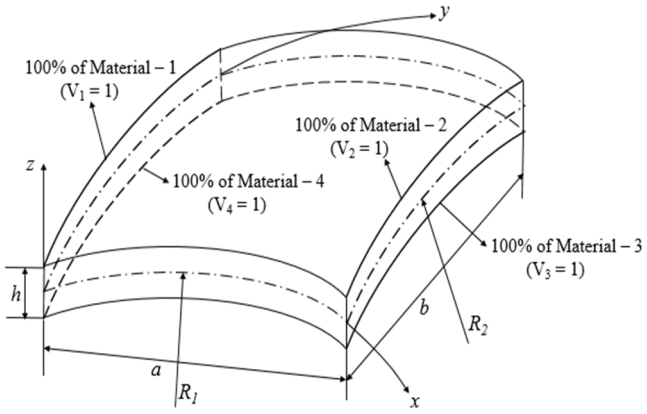

(a)

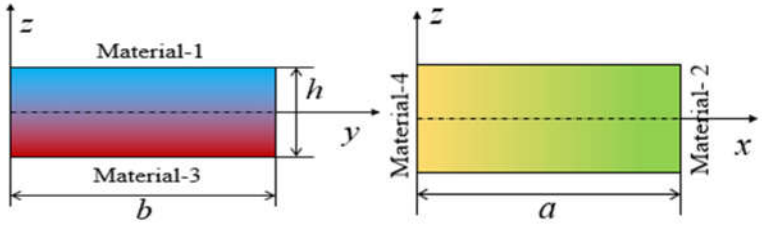

(b) (c)

Figure 5.1: TDFGM doubly curved porous shell geometry.

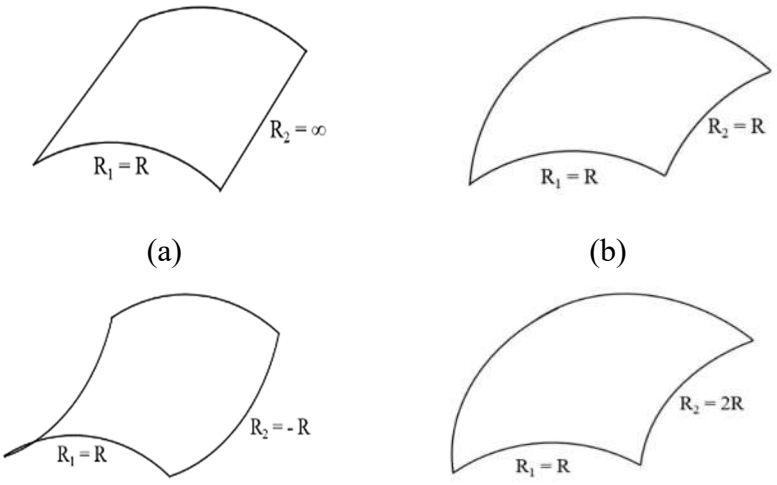

(a) (b)

(c) (d)

Figure 5.2: The TDFGM doubly curved porous shells schematic diagram (a) Cylindrical, (b) Spherical, (c) Hyperboloid, and (d) Ellipsoid.

5.2.2. Effective material properties

The TDFGM porous shell is heterogeneous and consists of four different material compositions. Two are ceramics (material – 1 and 2), and the other is metallic (material – 3 and 4) phases, as shown in Figure 5.1. Here, the top and bottom surfaces of the TDFGM shell are made of two distinct pure ceramic and metallic phases, respectively. The material and physical properties of the shell are assumed to vary in longitudinal (*x*-axis) and transverse (*z*-axis) directions, respectively.

The distribution of porosities during the manufacturing of the TDFGM shell is mathematically modeled to obtain effective material properties. In the present study, the TDFGM shells are considered with three types of models, *viz*. ideal TDFGM shells (with zero pores), evenly (P_e), and centrally (P_c) distributed TDFGM porous shells, as shown in Figure 5.3.

(a) (b)

Figure 5.3: The geometry of the porosity distributions in the TDFGM porous shell (a) Evenly distributed porosity (P_e) and (b) Centrally distributed porosity (P_c).

The generalized effective material properties of TDFGM porous shell panel ($P_{fg}(x, z)$) for modulus of elasticity ($E_{fg}(x, z)$), mass density ($\rho_{fg}(x, z)$), and Poisson's ratio ($\vartheta_{fg}(x, z)$) at each point in the shell panel can be obtained by using a modified power-law series for different porosity distributions are as follows (Van Do et al. 2017b; Ebrahimi and Dabbagh 2019):

Ideal TDFGM shell:

$$P_{fg}\left(x,z\right) = P_1V_1 + P_2V_2 + P_3V_3 + P_4V_4 \tag{5.1}$$

TDFGM shell with evenly distributed porosity (P_e):

$$P_{fg}\left(x,z\right) = P_1V_1 + P_2V_2 + P_3V_3 + P_4V_4 - \left(\left(\frac{e_p}{2}\right)\left(P_1 + P_2 + P_3 + P_4\right)\right) \tag{5.2}$$

TDFGM shell with centrally distributed porosity (P_c):

$$P_{fg}\left(x,z\right)=P_1V_1+P_2V_2+P_3V_3+P_4V_4-\left(\left(\frac{e_p}{2}\right)\left(P_1+P_2+P_3+P_4\right)\left(1-\frac{2|z|}{h}\right)\right) \tag{5.3}$$

where P_i (i = 1, 2, 3, and 4) are the generic material properties of the material – 1 to 4, such as Young's modulus and density of the material. V_1 to V_4 are the volume fractions of the four constituent materials (material – 1 to 4). The material characteristics at a point by varying volume fractions of each material are expressed as follows (Asemi et al. 2011; Rad and Shariyat 2013):

$$V_1=\left(\frac{1}{2}+\frac{x}{a}\right)^{m_x}\left(\frac{1}{2}+\frac{z}{h}\right)^{m_z};$$

$$V_2=\left(1-\left(\frac{1}{2}+\frac{x}{a}\right)^{m_x}\right)\left(\frac{1}{2}+\frac{z}{h}\right)^{m_z};$$

$$V_3=\left(\frac{1}{2}+\frac{x}{a}\right)^{m_x}\left(1-\left(\frac{1}{2}+\frac{z}{h}\right)^{m_z}\right);$$

$$V_4=\left(1-\left(\frac{1}{2}+\frac{x}{a}\right)^{m_x}\right)\left(1-\left(\frac{1}{2}+\frac{z}{h}\right)^{m_z}\right) \tag{5.4}$$

where m_z and m_x are non-negative real numbers for the volume fraction grading indexes along the -z and -x directions.

From Eqs. (5.1) – (5.4), ($P_{fg}(x, z)$) reduces to conventional perfect 1D-FGM shell for m_x = e_p = 0, and the material properties changes constantly through the thickness direction (along z-axis) for $P_1 = P_{ceramic}$ and $P_3 = P_{metal}$. Hence, the upper and lower surfaces are made of pure ceramic and metallic materials.

5.2.3. Nonlinear strain displacement equations

The nonlinear strains ($\{\varepsilon_b\}$: bending and $\{\varepsilon_s\}$: shear) are associated with the displacement fields of Eq. (4.11) for the TDFGM shell is established based on von Karman's type nonlinearity to consider the geometric distortion as follows (Ebrahimi and Dabbagh 2020; Tanov and Tabiei 2000):

$$\{\varepsilon_b\}=\begin{Bmatrix}\varepsilon_{xx}\\ \varepsilon_{yy}\\ \gamma_{xy}\end{Bmatrix}=\begin{Bmatrix}\overline{u}_{1,x}+\dfrac{w_1}{R_1}+\dfrac{1}{2}\left(\overline{w}_{1,x}\right)^2\\ \overline{v}_{1,y}+\dfrac{w_1}{R_2}+\dfrac{1}{2}\left(\overline{w}_{1,y}\right)^2\\ \overline{u}_{1,y}+\overline{v}_{1,x}+\left(\overline{w}_{1,x}\right)\left(\overline{w}_{1,y}\right)\end{Bmatrix}+z\begin{Bmatrix}\theta_{x,x}\\ \theta_{y,y}\\ \theta_{x,y}+\theta_{y,x}\end{Bmatrix}$$

$$\{\varepsilon_s\}=\begin{Bmatrix}\gamma_{xz}\\ \gamma_{yz}\end{Bmatrix}=\begin{Bmatrix}w_{1,x}\\ w_{1,y}\end{Bmatrix}+C_1\begin{Bmatrix}\theta_x\\ \theta_y\end{Bmatrix} \tag{5.5}$$

5.2.4. Constitutive equations

The stress-strain relations for any TDFGM curved panel can be stated as follows:

$$\{\sigma_b\}=\begin{Bmatrix}\sigma_{xx}\\ \sigma_{xx}\\ \sigma_{xy}\end{Bmatrix}=\begin{bmatrix}\dfrac{E_{fg}(x,z)}{1-\left(\vartheta_{fg}(x,z)\right)^2} & \dfrac{\vartheta_{fg}(x,z)E_{fg}(x,z)}{1-\left(\vartheta_{fg}(x,z)\right)^2} & 0\\ \dfrac{\vartheta_{fg}(x,z)E_{fg}(x,z)}{1-\left(\vartheta_{fg}(x,z)\right)^2} & \dfrac{E_{fg}(x,z)}{1-\left(\vartheta_{fg}(x,z)\right)^2} & 0\\ 0 & 0 & \dfrac{E_{fg}(x,z)}{2\left(1+\left(\vartheta_{fg}(x,z)\right)\right)}\end{bmatrix}\begin{Bmatrix}\varepsilon_{xx}\\ \varepsilon_{yy}\\ \gamma_{xy}\end{Bmatrix}$$

$$\{\sigma_s\}=\begin{Bmatrix}\sigma_{xz}\\ \sigma_{yz}\end{Bmatrix}=\begin{bmatrix}\dfrac{E_{fg}(x,z)}{2\left(1+\left(\vartheta_{fg}(x,z)\right)\right)} & 0\\ 0 & \dfrac{E_{fg}(x,z)}{2\left(1+\left(\vartheta_{fg}(x,z)\right)\right)}\end{bmatrix}\begin{Bmatrix}\gamma_{xz}\\ \gamma_{yz}\end{Bmatrix} \tag{5.6}$$

where $\{\sigma_b\}$ and $\{\sigma_s\}$ are the stress vector at any point in the TDFGM shell.

5.3. RESULTS AND DISCUSSIONS

In this section, the nonlinear FE solutions are obtained to illustrate the nonlinear frequency responses and nonlinear central deflection of the TDFGM shells with the proposed approach of IFSDT. The material properties of the TDFGM for four different material compositions tabulated in Table 5.1 are considered for the analysis. The investigation presents the parametric studies on the influence of different shell geometries, porosity distributions, porosity volume index, volume fraction grading indexes, curvature ratio, aspect ratio, and thickness-length ratio on the linear and

nonlinear frequency, and nonlinear central deflection of the TDFGM shells. Special attention is given to evaluating the effects of porosity and porosity distributions with combined volume fraction gradations along x and z directions with the geometrical parameters of the TDFGM shell panels. The present study employs the uniformly distributed load (q_0) of – 10^5 N/m^2 for central deflection. The results are extracted based on the non-dimensionalized linear frequency and deflection parameters. The non-dimensionalized quantities used are as follows:

Non-dimensionalized linear frequency $\omega = \bar{\omega} a^2 \sqrt{\rho_{M_1} h / D_0}$

where $D_0 = E_{M_1} h^3 \Big/ 12\left(1 - \vartheta_{M_1}^2\right)$

Non-dimensionalized central deflection $w = w_c \big/ h$

Non-dimensionalized load parameter $P = \left(\dfrac{q_0 a^4}{(E_{M_3}) h^4} \right)$ (5.7)

where E_{M_1}, ρ_{M_1}, and ϑ_{M_1} are Young's modulus, density, and Poisson's ratio of the material – 1 made of Si_3N_4; q_0 is the applied uniformly distributed mechanical load and E_{M_3} is the material – 3 made of SUS304.

5.3.1. Convergence and comparison study

The accuracy of the developed nonlinear FE model assures the carrying out of parametric studies by validating and comparing the computed results with existing solutions available in the open literature. A mesh size converged at [10 × 10] is adopted in this article.

Example 1: The fundamental frequency of the in-plane FG plate for different longitudinal volume fraction indices (m_x) and boundary conditions is validated with the literature (Chu et al. 2014) tabulated in Table 5.2. It can be observed that the obtained results are very close to the reference literature (Chu et al. 2014).

Example 2: Table 5.3 compares linear frequency responses of the SSSS FG porous curved panel having spherical geometry for evenly distributed porosity (P_e) with the literature (Amir and Talha 2019; Zare Jouneghani et al. 2017). The parameters considered for the validation are a/h =100, a/b = 1, R/a = 1, and m_x = 0, and the porous

FG material is taken as Al_2O_3/SUS304. It can be seen from Table 5.3 that the results from the present model show a definitive agreement with the open literature (Amir and Talha 2019; Zare Jouneghani et al. 2017).

Table 5.1: Material properties of the doubly curved TDFGM shells (Ebrahimi and Dabbagh 2021; Zhao et al. 2009).

Properties	Material – 1 (Si_3N_4)	Material – 2 (Aluminium oxide)	Material – 3 (SUS304)	Material – 4 (Al)
E (Gpa)	322.2715	320.20	207.7877	70
ρ (kg/m^3)	2370	3750	8166	2707
ϑ	0.30	0.30	0.30	0.30

Table 5.2: Comparison of fundamental frequency of in-plane FG plate for different m_x (a/h =100, a/b = 1, $R/a = \infty$).

Boundary condition	Sources	In-plane VFGI (m_x)	
		0	2
SSSS	Analytical (Chu et al. 2014)	19.7392	19.8948
	HRBCM (Chu et al. 2014)	19.6632	19.9094
	Present	19.7321	20.1746
SCSC	Analytical (Chu et al. 2014)	28.9509	29.5147
	HRBCM (Chu et al. 2014)	28.9445	29.5180
	Present	28.9221	29.5707

Example 3: The convergence and comparison of the nonlinear frequency ratio (NLFR) (ω_{NL}/ω) of the SSSS FG curved panel made of ZrO_2/Al for the geometrical parameter's a/h =100, m_z = 2, m_x = 0, a/b = 1, R/a = 50 are shown in Table 5.4. In order to show the stability and efficiency of the present model, various shell geometries are considered for comparison. The same material properties and boundary conditions considered in the literature (Kar and Panda 2016) are used for the present model's validation and comparison. It can be observed from Table 5.4 that the obtained results resemble the reference literature very well (Kar and Panda 2016). Besides, it can be observed from Table 4 that the present NLFR results are relatively higher than the reference values.

This difference arises due to the IFSDT with von Karman's assumptions and HSDT with Green-Lagrange's assumptions used by the present model and reference literature (Kar and Panda 2016). Thus, the nonlinear frequency depends on the mass and linear stiffness matrices and nonlinear stiffness matrices.

Table 5.3: Comparison of fundamental frequency of SSSS square porous FG spherical shell panels composed of Al_2O_3/SUS304 for different e_p and m_z (a/h =100, a/b = 1, R/a = 1, m_x = 0, P_e, and SSSS).

e_p	Sources	Volume fraction grading index (m_z)		
		0.6	1	5
0	Ref. (Zare Jouneghani et al. 2017)	73.5029	67.7563	54.9591
	Ref. (Amir and Talha 2019)	73.5668	67.9406	55.1755
	Present	73.4906	67.7546	54.9521
0.1	Ref. (Zare Jouneghani et al. 2017)	74.2942	67.8636	53.7906
	Ref. (Amir and Talha 2019)	74.2638	67.9719	53.9476
	Present	74.2883	67.8696	53.7900
0.2	Ref. (Zare Jouneghani et al. 2017)	75.2655	67.9668	52.3336
	Ref. (Amir and Talha 2019)	75.1476	68.0110	52.4470
	Present	75.2676	67.9825	53.1440

Table 5.4: Comparison of NLFR square FG shell panels composed of ZrO_2/Al (a/h =100, m_z = 2, m_x = 0, R/a = 50, and SSSS).

Shell geometry	Ref.	Amplitude ratio (W_{max}/h)				
		0.4	0.8	1.2	1.6	2.0
Cylindrical	Present [2 × 2]	1.0341	1.1005	1.1935	1.3070	1.4356
	Present [4 × 4]	1.0693	1.1900	1.3464	1.5261	1.6936
	Present [6 × 6]	1.0697	1.1903	1.3455	1.5221	1.6883
	Present [8 × 8]	1.0697	1.1901	1.3448	1.5192	1.6669
	Present [10 × 10]	1.0697	1.1901	1.3449	1.5195	1.6672
	Kar and Panda (2016)	1.0566	1.1488	1.2672	1.4035	1.5513
Hyperboloid	Present [10 × 10]	1.0326	1.1234	1.2563	1.4139	1.5874
	Kar and Panda (2016)	1.0227	1.0875	1.1857	1.3082	1.4468
Ellipsoid	Present [10 × 10]	1.0853	1.2167	1.3782	1.5573	1.7244
	Kar and Panda (2016)	1.0710	1.1738	1.2992	1.4394	1.5892

Example 4: The nonlinear central deflection of the FG plate for different volume fraction indexes (m_z = 0.5 and 2) of the proposed model is compared with the reference literature (Praveen and Reddy 1998) is shown in Figure 5.4. The material and

geometrical parameters considered are the same as in the reference solution (Praveen and Reddy 1998). It can be noticed that the present solutions match very well with the reference literature (Praveen and Reddy 1998).

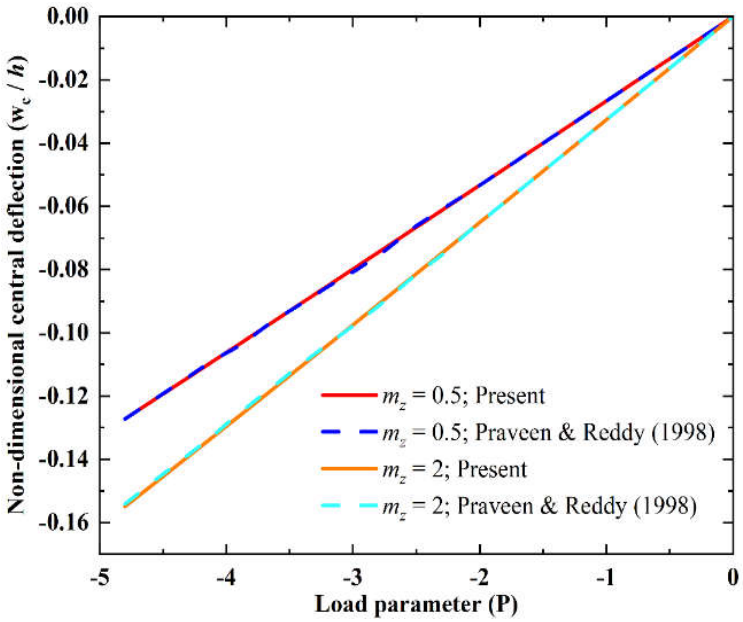

Figure 5.4: Comparison of nonlinear central deflection (w_c/h) of FGM plate.

5.3.2. Effect of TDFGM volume fractions

The volume fraction grading index is considered one of the significant parameters for determining the properties of TDFGM shells, which subsequently affects the material's stiffness. The effects of the coupled variation of volume fraction grading indexes in both the directions m_x and m_z on the NLFR for different amplitude ratios of the simply supported TDFGM shell without porosities are tabulated in Tables 5.5 – 5.8. The various shell geometries considered for the study are cylindrical, spherical, hyperboloid, and ellipsoid shells. These results show that the NLFR decreases with increasing the transverse volume fraction grading indices (m_z) for all shell geometries. At the same time, the downward trend of the NLFR gradually reverses with a further increase in both the volume fraction grading indices m_x and m_z. It may be due to increased ceramic-rich particles as the longitudinal volume fraction index (m_x) increases.

Table 5.5: NLFR (ω_{NL} /ω) of square TDFGM porous cylindrical shell panels for different volume fraction grading index (a/h =20, R/a = 20, e_p = 0, and SSSS).

m_x	m_z	Amplitude ratio (W_{max}/h)					ω
		0.25	0.50	0.75	1.0	1.25	
0	0.0	1.0257	1.0752	1.1448	1.2296	1.3262	19.6310
	0.5	1.0263	1.0770	1.1481	1.2355	1.3327	13.5190
	2.0	1.0255	1.0745	1.1432	1.2276	1.3227	10.6380
	10.0	1.0246	1.0719	1.1386	1.2204	1.3130	9.2121
0.5	0.5	1.0264	1.0771	1.1482	1.2350	1.3328	13.5190
	2.0	1.0255	1.0745	1.1434	1.2282	1.3228	10.6450
	10.0	1.0245	1.0719	1.1385	1.2202	1.3127	9.2188
2	0.5	1.0262	1.0768	1.1476	1.2340	1.3317	13.5190
	2.0	1.0254	1.0744	1.1433	1.2280	1.3226	10.5830
	10.0	1.0247	1.0723	1.1394	1.2216	1.3145	9.1636
10	0.5	1.0267	1.0782	1.1503	1.2390	1.3375	12.5470
	2.0	1.0293	1.0857	1.1643	1.2594	1.3657	8.8002
	10.0	1.0280	1.0820	1.1573	1.2486	1.3516	8.2710

In contrast, the non-dimensionalized linear frequency decreases with an increase in both the volume fraction grading indices. Besides, the linear frequency variation is insignificant irrespective of various shell geometries for a given m_z and m_x. It is evident that the TDFGM panel progressively becomes metal and ceramic rich as m_z and m_x increase, respectively, and metal-rich material has comparatively lower stiffness than ceramic material. Thus, it is interesting to note that a proportionate mixture of ceramic and metal particles yields a minor variance in stiffness with an increase in volume fraction grading indices in both transverse (m_z) and longitudinal (m_x) directions.

In addition, Figure 5.5 show the nonlinear central deflection (w_c/h) variation considering the porosity distributions P_e and P_c for different shell geometries. It can be noted that the predominant effects of volume fraction indices on the nonlinear deflection appear to be in the gradation region (m_x = m_z = 1 and 2). Meanwhile, a pronounced lower deflection can be observed for higher volume fraction grading

indices (m_z and m_x) due to the increased stiffness. Therefore, the influence of VFGI seems to be predominant in the property determination of TDFGM shells, which is subsequently proportional to the stiffness. In addition, the P_c type of porosity distribution has more effect on nonlinear deformations than evenly distributed porosity (P_e). It may be due to the distribution of the porosities leading to the stiffness variation.

Table 5.6: NLFR (ω_{NL}/ω) of square TDFGM porous spherical shell panels for different volume fraction grading index (a/h =20, R/a = 20, e_p = 0, and SSSS).

m_x	m_z	Amplitude ratio (W_{max}/h)					ω
		0.25	0.50	0.75	1.0	1.25	
0	0.0	1.0374	1.0971	1.1751	1.2666	1.3687	19.8370
	0.5	1.0383	1.0994	1.1790	1.2726	1.3759	13.6630
	2.0	1.0371	1.0961	1.1734	1.2644	1.3655	10.7470
	10.0	1.0358	1.0930	1.1679	1.2560	1.3542	9.3037
0.5	0.5	1.0384	1.0994	1.1791	1.2727	1.3760	13.6630
	2.0	1.0371	1.0962	1.1733	1.2644	1.3655	10.7540
	10.0	1.0358	1.0929	1.1677	1.2559	1.3544	9.3104
2	0.5	1.0382	1.0990	1.1784	1.2715	1.3747	13.6630
	2.0	1.0370	1.0961	1.1733	1.2640	1.3648	10.6920
	10.0	1.0360	1.0935	1.1688	1.2576	1.3564	9.2554
10	0.5	1.0389	1.1009	1.1818	1.2766	1.3811	12.6880
	2.0	1.0426	1.1102	1.1979	1.2998	1.4127	8.9082
	10.0	1.0408	1.1055	1.1896	1.2883	1.3965	8.3667

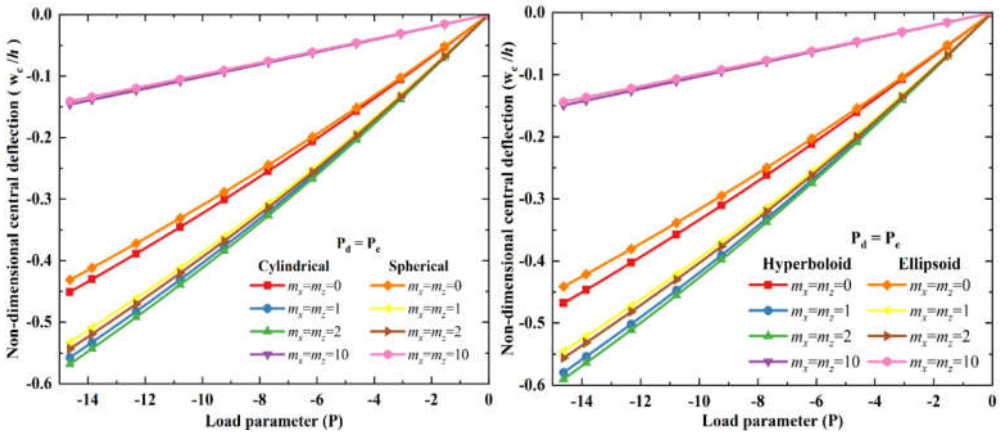

(a) P_e, Cylindrical, and Spherical (b) P_e, Hyperboloid, and Ellipsoid

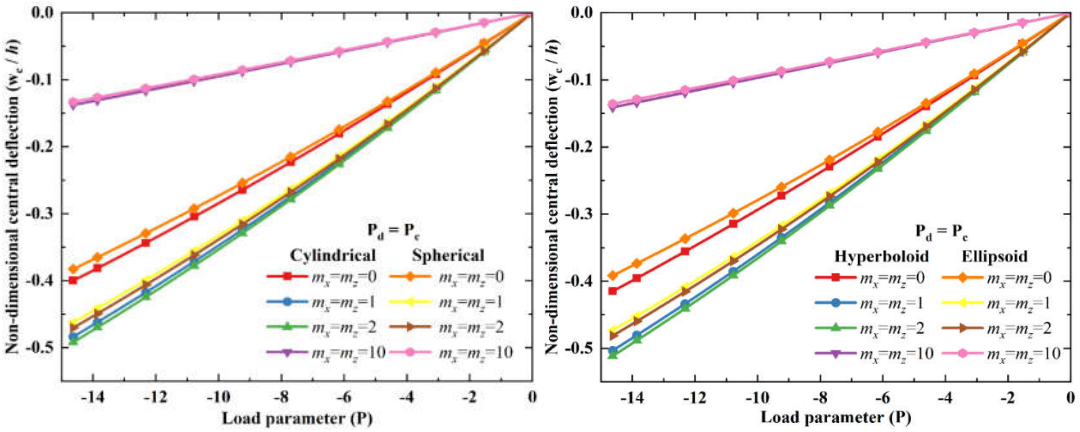

(c) P_c, Cylindrical, and Spherical (d) P_c, Hyperboloid, and Ellipsoid

Figure 5.5: Nonlinear central deflection of square TDFGM porous panels for different volume fraction grading index and porosity distributions (a/h = 20, e_p = 0.1, and R/a = 20).

Table 5.7: NLFR (ω_{NL} /ω) of square TDFGM porous hyperboloid shell panels for different volume fraction grading index (a/h =20, R/a = 20, e_p = 0, and SSSS).

m_x	m_z	Amplitude ratio (W_{max}/h)					ω
		0.25	0.50	0.75	1.0	1.25	
0	0.0	1.0131	1.0511	1.1106	1.1876	1.2762	19.5550
	0.5	1.0135	1.0524	1.1133	1.1915	1.2823	13.4670
	2.0	1.0130	1.0506	1.1095	1.1854	1.2737	10.5980
	10.0	1.0125	1.0489	1.1059	1.1795	1.2665	9.1786
0.5	0.5	1.0135	1.0524	1.1133	1.1916	1.2824	13.4670
	2.0	1.0130	1.0506	1.1096	1.1854	1.2737	10.6060
	10.0	1.0125	1.0488	1.1058	1.1798	1.2651	9.1852
2	0.5	1.0134	1.0522	1.1129	1.1908	1.2814	13.4670
	2.0	1.0130	1.0506	1.1095	1.1858	1.2735	10.5440
	10.0	1.0126	1.0491	1.1065	1.1804	1.2666	9.1300
10	0.5	1.0136	1.0531	1.1150	1.1943	1.2863	12.4930
	2.0	1.0149	1.0583	1.1257	1.2117	1.3106	8.7597
	10.0	1.0143	1.0558	1.1205	1.2035	1.2985	8.2356

Table 5.8: NLFR (ω_{NL}/ω) of square TDFGM porous ellipsoid shell panels for different volume fraction grading index (a/h =20, R/a = 20, e_p = 0, and SSSS).

m_x	m_z	Amplitude ratio (W_{max}/h)					ω
		0.25	0.50	0.75	1.0	1.25	
0	0.0	1.0317	1.0865	1.1603	1.2488	1.3479	19.7180
	0.5	1.0325	1.0885	1.1640	1.2552	1.3552	13.5800
	2.0	1.0314	1.0856	1.1589	1.2465	1.3448	10.6840
	10.0	1.0303	1.0827	1.1537	1.2395	1.3344	9.2507
0.5	0.5	1.0325	1.0886	1.1642	1.2544	1.3559	13.5800
	2.0	1.0314	1.0856	1.1588	1.2467	1.3448	10.6910
	10.0	1.0303	1.0827	1.1536	1.2388	1.3342	9.2574
2	0.5	1.0324	1.0882	1.1635	1.2535	1.3542	13.5800
	2.0	1.0314	1.0856	1.1587	1.2466	1.3446	10.6290
	10.0	1.0305	1.0832	1.1546	1.2402	1.3361	9.2023
10	0.5	1.0330	1.0899	1.1667	1.2584	1.3603	12.6060
	2.0	1.0362	1.0984	1.1818	1.2804	1.3900	8.8459
	10.0	1.0346	1.0941	1.1741	1.2692	1.3751	8.3114

5.3.3. Effect of porosity volume index

The influence of the porosity volume index (e_p) and porosity distributions P_e and P_c for different shell geometries is investigated and tabulated in Table 5.9. For the sake of brevity, only the volume fraction grading index two is considered for both m_x and m_z. It can be observed that the NLFR increases with an increase in the porosity volume index for a P_e type of porosity distribution. However, the responses are not showing a monotonous behavior for spherical and ellipsoid shell geometries. Meanwhile, the trend is reversed for the P_c type of porosity distribution. Besides, the linear frequency decreases for an evenly distributed porosity while it increases for a centrally distributed porosity distribution with an increase in e_p. It may be due to the more material accretion away from the middle surface leading to an enhancing the flexural stiffness of the TDFGM shell for the porosity distribution type P_c. For a given e_p and porosity distribution, the variation of NLFR for various shell geometries follows the trend as $NLFR_{hyperboloid} < NLFR_{cylindrical} < NLFR_{ellipsoid} < NLFR_{spherical}$.

In comparison, the linear frequency follows the trend as spherical > ellipsoid > cylindrical > hyperboloid. It may be because the hyperboloid shells account for the lower stiffness due to the anticlastic behavior. Also, porosities' effects are higher in the centrally distributed porosity (P_c) than in the evenly distributed porosity (P_e) for linear responses contrary to the NLFR.

Table 5.9: NLFR (ω_{NL}/ω) of square TDFGM porous shell panels for different porosity volume index (a/h =20, R/a = 20, $m_x = m_z = 2$, W_{max}/h = 1.5, and SSSS).

TDFGP Shell geometry	e_p	P_e		P_c	
		NLFR	ω	NLFR	ω
Cylindrical	0	1.4254	10.5830	1.4254	10.5830
	0.1	1.4287	10.0960	1.4072	10.6390
	0.2	1.4313	9.5247	1.3877	10.7130
	0.3	1.4362	8.7359	1.3669	10.8050
Spherical	0	1.4721	10.6920	1.4721	10.6920
	0.1	1.4681	10.2030	1.4489	10.7460
	0.2	1.4640	9.6287	1.4251	10.8170
	0.3	1.4633	8.8341	1.4006	10.9060
Hyperboloid	0	1.3703	10.5440	1.3703	10.5440
	0.1	1.3813	10.0570	1.3579	10.6000
	0.2	1.3908	9.4875	1.3437	10.6740
	0.3	1.4017	8.7011	1.3273	10.7660
Ellipsoid	0	1.4498	10.6290	1.4498	10.6290
	0.1	1.4495	10.1410	1.4290	10.6840
	0.2	1.4488	9.5685	1.4073	10.7570
	0.3	1.4508	8.7772	1.3845	10.8480

Furthermore, the nonlinear central deflection of the TDFGM shell influenced by porosity volume index (e_p) and porosity distributions P_e and P_c for various shell geometries is depicted in Figure 5.6. It can be observed that the hyperboloid shell geometry has a maximum deflection compared to other shell geometries. It is due to the reduced stiffness in the hyperboloid shell geometry because of its anticlastic deportment. The deflections increase with an increase in the porosity volume index (e_p)

for all porosity distributions. Meanwhile, P_c's porosity distribution shows the minimum deflection than the evenly distributed porosity P_e and a noticeable difference is observed in P_e between the porosity volume index. Also, the deflection rate is very high for the P_e type of porosity distribution compared to P_c for a given porosity volume index and shell geometry. This is because the arrangements of the porosities in the P_e facilitate the uniform distribution of materials across the thickness. In contrast, more materials are accumulated far away from the middle plane for P_c leading to high stiffness in the shell. For particular e_p and porosity distributions, the nonlinear deflection variation of the different shell geometries follows the trend as hyperboloid > cylindrical > ellipsoid > spherical. Besides, the nonlinear deflections increase with an increase in load parameters.

5.3.4. Effect of thickness and aspect ratios

The NLFR and linear frequency (ω) of the TDFGM porous shells for different shell geometries and thickness ratios are tabulated in Table 5.10. For a given shell geometry and porosity distribution, the NLFR and linear frequency values increase with an increase in the thickness ratio. It may be because greater stiffness is achieved by having lower thickness ratios. However, due to their anticlastic nature, NLFR does not have the same trend for hyperboloid porous shells. Besides, there is a sudden drop in NLFR values, increasing the a/h ratio from 50 to 100. This is because of the change in stiffness values, thus leading to degradation in the material properties at a higher amplitude ratio $W_{max}/h = 1.5$. The structure transforms into thin panels along with the geometric nonlinearity included in the panel due to the porosities.

Besides, the aspect ratio can be considered a significant parameter in the shell's geometry, particularly for thin shell structures. The geometrical instability increases as the structural elements become thinner, which affects the shell's dynamic behavior. The influence of the aspect ratio on the NLFR and linear frequency of the TDFGM porous shells is shown in Table 5.11. The NLFR of porous shell panels decreases with an increase in the aspect ratio. In contrast, the linear frequency responses show a reversed trend for a given shell geometry and porosity distribution. For both thickness and aspect ratio cases, the P_c's NLFR exhibits lower values than the P_e. Meanwhile, the linear responses show a reversal trend for all shell geometries. In addition, the influence of

thickness and aspect ratio on the NLFR and linear frequency value increases in the order as follows hyperboloid < cylindrical < ellipsoid < spherical for a given e_p and porosity distribution.

Table 5.10: NLFR (ω_{NL} /ω) of square TDFGM porous shell panels with different thickness ratios (R/a = 20, e_p = 0.1, $m_x = m_z$ = 2, W_{max}/h = 1.5, and SSSS).

TDFGP Shell geometry	Thickness ratio (a/h)	P_e		P_c	
		NLFR	ω	NLFR	ω
Cylindrical	10	1.4093	9.8244	1.3878	10.3250
	20	1.4287	10.0960	1.4072	10.6390
	50	1.4812	10.3570	1.4592	10.9120
	100	1.5292	11.0140	1.3941	11.5630
Spherical	10	1.4342	9.8497	1.4139	10.3500
	20	1.4682	10.2030	1.4489	10.7460
	50	1.5291	11.0030	1.5148	11.5500
	100	1.3313	13.2900	1.3468	13.8210
Hyperboloid	10	1.3825	9.8140	1.3599	10.3140
	20	1.3812	10.0570	1.3579	10.6000
	50	1.3791	10.1290	1.3558	10.6840
	100	1.3722	10.1390	1.3496	10.6970
Ellipsoid	10	1.4221	9.8352	1.4011	10.3360
	20	1.4495	10.1410	1.4290	10.6840
	50	1.4987	10.6310	1.4980	11.1830
	100	1.3546	12.0150	1.5175	12.5550

5.3.5. Effect of curvature ratio

The TDFGM with curved geometry is stronger enough to carry a larger load than the flat plates. It is apparent that the curved panels make the structure more rigid. Thus, the effects of the shallowness ratio on the NLFR and linear responses of the TDFGM porous shell for various curved panel geometries are presented in Table 5.12. It can be observed that the NLFR and the linear frequency responses decrease with an increase in the shallowness ratio for all shell geometries and porosity distributions. Since the curved panel tends to flat plate as the shallowness ratio increases to infinity, it decreases

stiffness. However, the effect of the shallowness ratio on the NLFR is insignificant for hyperboloid porous shells. Further, the NLFR of the P_c exhibits lower values than the P_e, whereas the linear responses show an opposite movement for all types of shell geometries. In addition, the influence of the shallowness ratio on the NLFR increases in the order as follows: $NLFR_{hyperboloid} < NLFR_{cylindrical} < NLFR_{ellipsoid} < NFR_{spherical}$ for a given e_p and porosity distribution.

Table 5.11: NLFR (ω_{NL}/ω) of TDFGM porous shell panels with different aspect ratios (a/h = 20, R/a = 50, e_p = 0.1, $m_x = m_z = 2$, W_{max}/h = 1.5, and SSSS).

TDFGP Shell geometry	a/b	P_e		P_c	
		NLFR	ω	NLFR	ω
Cylindrical	1.0	1.4012	10.0680	1.3785	10.6110
	1.5	1.2941	16.4040	1.2773	17.2940
	2.0	1.1785	25.2580	1.1677	26.6310
	2.5	1.1056	36.6320	1.0981	38.6250
Spherical	1.0	1.4199	10.0850	1.3979	10.6280
	1.5	1.3349	16.4200	1.3172	17.3100
	2.0	1.2267	25.2700	1.2147	26.6430
	2.5	1.1556	36.6410	1.1489	38.6340
Hyperboloid	1.0	1.3814	10.0620	1.3581	10.6040
	1.5	1.2517	16.3940	1.2358	17.2830
	2.0	1.1234	25.2480	1.1168	26.6200
	2.5	1.0494	36.6240	1.0463	38.6160
Ellipsoid	1.0	1.4107	10.0750	1.3884	10.6180
	1.5	1.3334	16.4020	1.3147	17.2920
	2.0	1.2281	25.2470	1.2129	26.6190
	2.5	1.1540	36.6140	1.1452	38.6060

5.3.6. Effect of boundary conditions

The influence of the support conditions on the NLFR and linear frequency responses of the TDFGM porous shell is shown in Figure 5.7. For a given shell geometry and porosity distribution, the linear frequency responses decline with the

decrease in the number of boundary constraints (CCCC > SCSC > SSSS). Meanwhile, the nonlinearity effect for the NLFR responses is more predominant in the simply supported boundary condition than in the other boundary conditions. It can be noted that the impact of various shell geometries for a given boundary condition and porosity distribution on the variation of linear responses are insignificant. In addition, the NLFR of the P_c shows lower values than the P_e, whereas the opposite trend is followed for the linear responses for a given type of shell geometry.

Table 5.12: NLFR (ω_{NL} /ω) of square TDFGM porous shell panels with different curvature ratios (a/h =20, e_p = 0.1, $m_x = m_z = 2$, W_{max}/h = 1.5, and SSSS).

TDFGP Shell geometry	Curvature ratio (R/a)	P_e		P_c	
		NLFR	ω	NLFR	ω
Cylindrical	5	1.5218	10.5970	1.4822	11.1340
	10	1.4681	10.1980	1.4489	10.7410
	20	1.4287	10.0960	1.4072	10.6390
	50	1.4012	10.0680	1.3785	10.6110
	∞	1.3815	10.0620	1.3581	10.6050
Spherical	5	1.5445	12.1350	1.5440	12.6550
	10	1.5216	10.6180	1.5086	11.1550
	20	1.4682	10.2030	1.4489	10.7460
	50	1.4199	10.0850	1.3979	10.6280
	∞	1.3815	10.0620	1.3581	10.6050
Hyperboloid	5	1.3754	9.9805	1.3536	10.5190
	10	1.3807	10.0420	1.3574	10.5840
	20	1.3813	10.0570	1.3579	10.6000
	50	1.3814	10.0620	1.3581	10.6040
	∞	1.3814	10.0620	1.3581	10.6050
Ellipsoid	5	1.5449	11.2700	1.5410	11.7990
	10	1.4991	10.3770	1.4827	10.9170
	20	1.4495	10.1410	1.4290	10.6840
	50	1.4107	10.0750	1.3884	10.6180
	∞	1.3815	10.0620	1.3581	10.6050

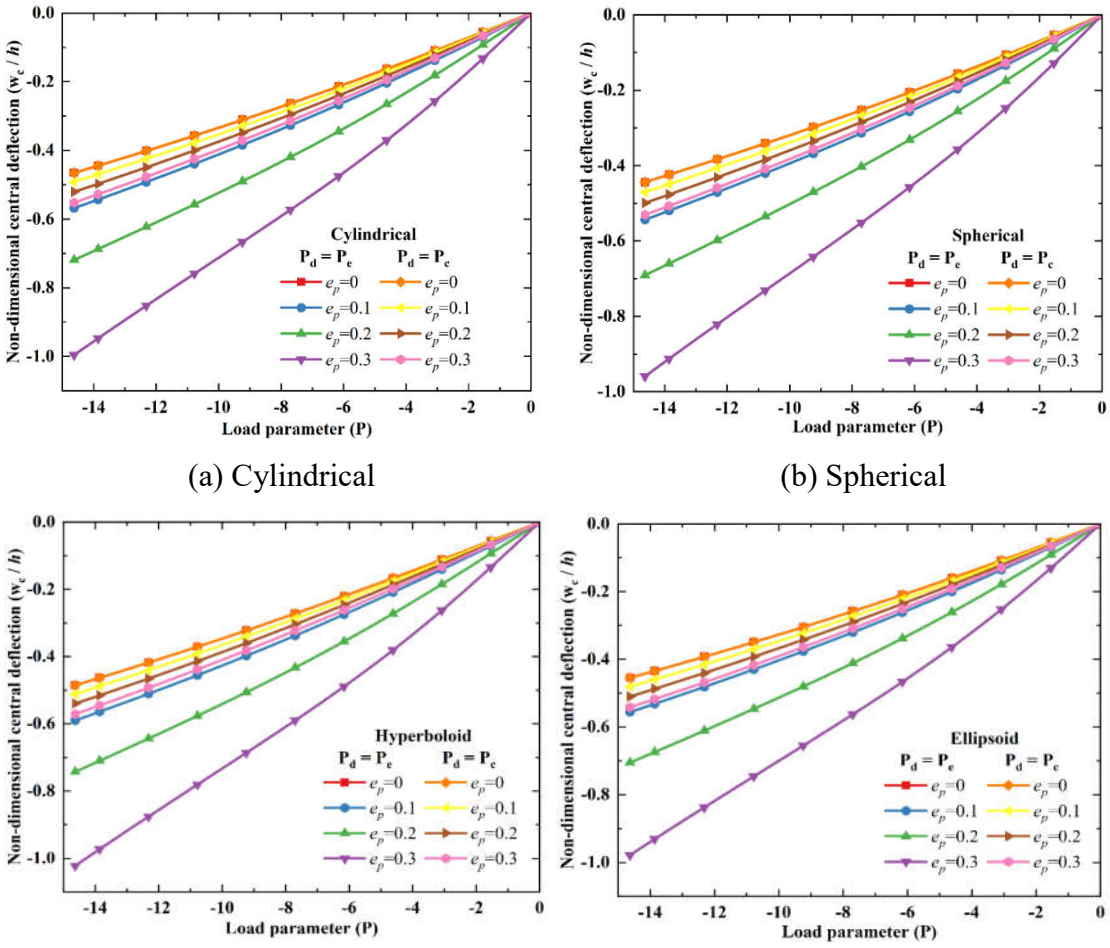

(a) Cylindrical (b) Spherical

(c) Hyperboloid (d) Ellipsoid

Figure 5.6: Nonlinear central deflection of square TDFGM porous panels for different porosity distributions and porosity volume index (a/h = 20, $m_x = m_z$ = 2, R/a = 20).

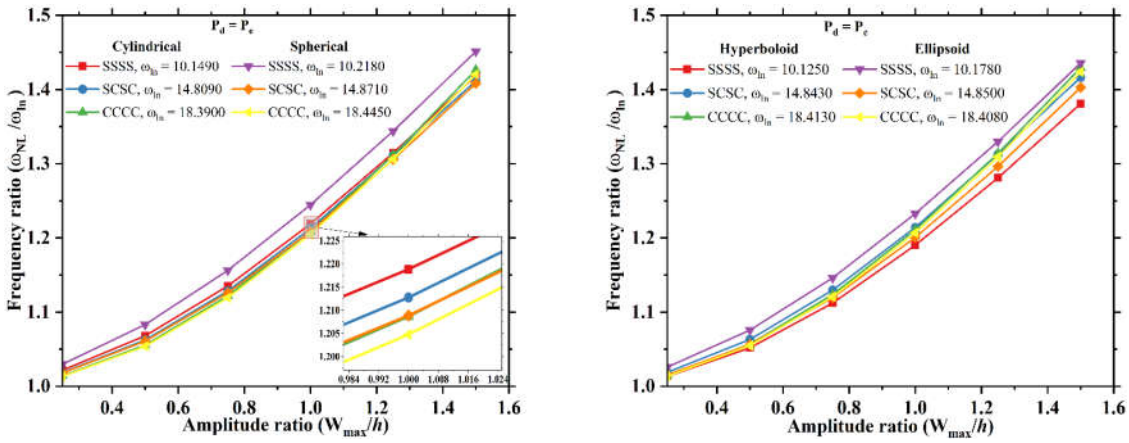

(a) P_e (b) P_e

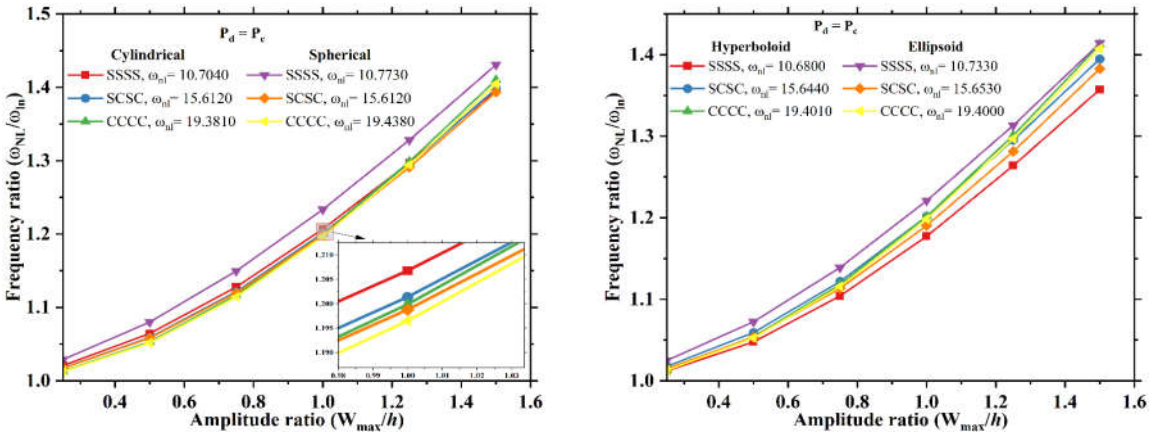

(c) P_c (d) P_c

Figure 5.7: NLFR (ω_{NL} /ω) of square TDFGM porous panels for different porosity distributions and support conditions (a/h =40, R/a = 50, e_p = 0.1, and $m_x = m_z = 2$).

5.4. CONCLUSIONS

The present study makes the first attempt to assess the linear frequency, nonlinear frequency, and nonlinear deformations of the TDFGM porous shells. To this end, the modified power-law series is used to integrate four different compositions of materials incorporating the porosities and determine the effective TDFGM porous shell properties in both longitudinal and thickness directions. A nonlinear FE formulation is developed based on the IFSDT and von Karman's geometric nonlinearity. The solutions are extracted using the direct iterative method.

The following beneficial conclusions can be drawn from the several exciting outcomes observed in the numerical studies. The linear frequency, nonlinear frequency, and nonlinear deformations can be changed and controlled significantly by altering the volume fraction gradation profiles in the required direction for each material with the proper combination of materials. The highest linear frequency is noticed for the porosity distribution P_c, while the highest NLFR and nonlinear deflections are observed for P_e. The hyperboloid shell has the maximum nonlinear deformations due to its anticlastic nature, whereas the spherical shell has the maximum NLFR. The nonlinear deflection rate is very high and has a maximum for evenly distributed porosity than the centrally distributed porosity for a given porosity volume index and shell geometry. The NLFR increases with an increase in the thickness ratio, whereas it decreases with an increase in aspect ratio and curvature ratio. Meanwhile, the linear frequency increases for an

increase in thickness ratio and aspect ratio while decreases in curvature ratio. The linear frequency variation and nonlinear deformations for a given boundary condition, shell geometry, and porosity distribution are insignificant. The interpretation of nonlinear deflections and NLFR in connection with the various shell geometries is SSSS > SCSC > CCCC.

CHAPTER 6

GEOMETRICALLY NONLINEAR BEHAVIOR OF TWO-DIRECTIONAL FUNCTIONALLY GRADED POROUS PLATES WITH FOUR DIFFERENT MATERIALS

This chapter investigates the influence of porosity distributions on the nonlinear behavior of two-directional functionally graded porous plates (TDFGPP) made from four distinct materials. The constitutive equations and nonlinear finite element formulation derived in the previous chapters have been extended for the present analysis. The influence of volume fraction grading indices, porosity distributions, porosity volume, thickness ratio, and aspect ratio for different support conditions provides a thorough insight into the linear and nonlinear responses of the porous plate. In addition, this study emphasizes the influence of the volume fraction gradation profiles with four different materials on the linear frequency, nonlinear frequency, and deflections of the TDFGPP.

6.1. INTRODUCTION

In Chapter 5, the influence of porosity distributions on the nonlinear vibration behavior of the two-directional functionally graded porous (TDFGP) curved panels has been investigated. In this chapter, a similar investigation is extracted for TDFGP plates. The main objective of this chapter is to investigate the linear vibration, nonlinear free vibration, and deflection analysis of two-directional FG porous plates with four distinct material compositions. The present work's certainty appears to be more apparent for structures with changing VFGI values for the various constituent materials in two different directions (longitudinal and transverse). A modified power-law series is used to quantify the material properties of the TDFGPP that vary smoothly as an arbitrary function of the VFGI in longitudinal and transverse directions. A nonlinear FE model is established based on the IFSDT and von Karman's nonlinearity. The solutions are

found using the direct iterative and Newmark's integration procedures, and the equations of motion are determined using Hamilton's principle. The linear and geometrically nonlinear vibration characteristics and deflection analysis of the TDFGPP have been evaluated for various geometrical and material parameters.

6.2. PROBLEM DESCRIPTION AND GOVERNING EQUATION

6.2.1. The geometry of the TDFGPP

The TDFGPP made of four different material compositions is shown in Figure 6.1. In this article, the TDFGPP's geometry is characterized as a Cartesian coordinate with sides *a* and *b* and uniform thickness *h*, as shown in Figure 6.1.

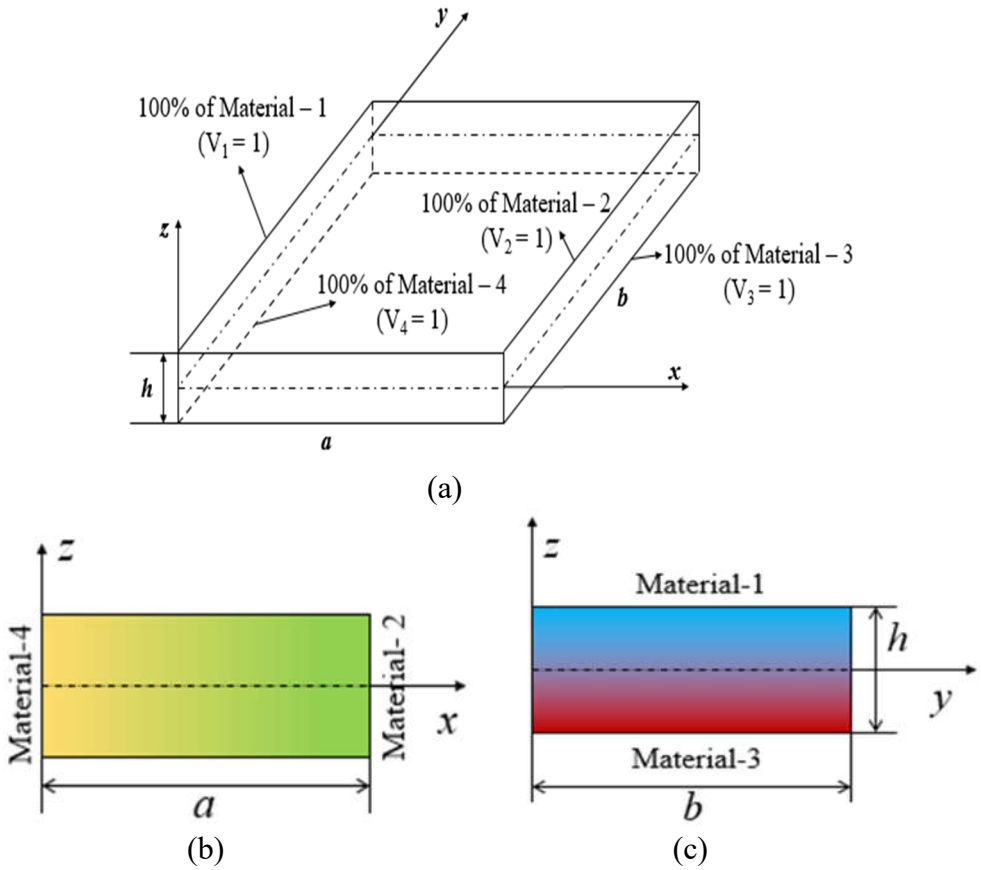

Figure 6.1: TDFGPP geometry is composed of Si_3N_4/SUS304 and Al/Aluminium oxide.

6.2.2. Nonlinear FE formulation and governing equations of motion

The displacement equations, von Kármán's strain-displacement equations, the governing equations, and the nonlinear FE formulation derived in sections 4.2.3 – 4.2.5

are adopted without thermal effects for the present analysis of TDFGPP also. The homogenization technique for determining the effective material properties (Eqs. (5.1) – (5.4)) and the constitutive equations (Eq. (5.6)) derived in Chapter 5 are adopted for the analysis of TDFGPP also. Further, the solution methodologies are adapted from section 2.3 of Chapter 2.

6.3. RESULTS AND DISCUSSIONS

Validation studies presented in section 4.4 (Examples 1, 4, 5, and 6) and section 5.3.1 (Examples 1 and 4) of chapters 4 and 5, respectively, have also been implemented for the present analysis. However, the validation has been carried out without the effects of temperature, i.e., T = 300 K of Example 5 in section 4.4 (Chapter 4) for the present analysis of TDFGPP. Since the validation is executed for nonlinear free vibration studies, the results corresponding to the nonlinear free vibration behavior of TDFGPP appear before the dynamic analysis in the subsequent section. The material properties of the TDFGPP with four different material compositions tabulated in Table 5.1 are considered for the analysis. Further, the present study employs the uniformly distributed load (q_0) – 10^2 N/m^2 and – 10^6 N/m^2 for central and transient deflections. The time increment Δt = 10 μs is used for all the examples of transient deflection. The results are extracted based on the non-dimensionalized parameters for frequency and deflections. The non-dimensionalized quantities used are identical to those in Eq. (5.7).

6.3.1. Effect of TDFGPP volume fractions

The volume fraction grading index is considered one of the significant parameters to determine the properties of the TDFGPP, which subsequently affects the material's stiffness. The effects of variation of VFGI in both the directions m_x and m_z on the NLFR for different amplitude ratios are tabulated in Table 6.1. The analysis is performed on the SSSS TDFGPP plate with no porosity. These results show that the NLFR decreases with increased transverse VFGI (m_z). At the same time, the downward trend of the NLFR gradually reverses with a further increase in the VFGI in both m_x and m_z directions. It may be due to increased ceramic-rich particles as the longitudinal VFGI (m_x) increases. In contrast, the non-dimensionalized linear frequency decreases with an increase in the VFGI. It is evident that the TDFGPP becomes progressively

more metal and ceramic rich as m_z and m_x increase. Also, the metal-rich material has a comparatively lower stiffness than the ceramic material. Thus, it is interesting to note that a proportionate mixture of both ceramic and metal particles as m_z and m_x increase leads to a minor variation in the stiffness.

Table 6.1: NLFR (ω_{NL} /ω) of the TDFGPP for different VFGI (a/h =100, a/b = 1, e_p = 0, and SSSS).

m_x	m_z	Amplitude ratio (W_{max}/h)						ω
		0.25	0.50	0.75	1.0	1.25	1.50	
0	0.0	1.0130	1.0507	1.1100	1.1868	1.2759	1.3746	19.7321
	0.5	1.0133	1.0519	1.1125	1.1906	1.2818	1.3821	13.5854
	2.0	1.0128	1.0500	1.1086	1.1847	1.2729	1.3706	10.6972
	10.0	1.0124	1.0483	1.1050	1.1787	1.2645	1.3601	9.2679
0.5	0.5	1.0133	1.0519	1.1125	1.1911	1.2819	1.3823	13.5852
	2.0	1.0128	1.0501	1.1086	1.1846	1.2729	1.3706	10.7046
	10.0	1.0123	1.0483	1.1049	1.1786	1.2643	1.3603	9.2748
2	0.5	1.0132	1.0517	1.1121	1.1904	1.2809	1.3810	13.5861
	2.0	1.0128	1.0500	1.1086	1.1846	1.2732	1.3714	10.6418
	10.0	1.0124	1.0486	1.1056	1.1795	1.2659	1.3619	9.2180
10	0.5	1.0136	1.0530	1.1148	1.1948	1.2871	1.3900	12.6063
	2.0	1.0150	1.0582	1.1257	1.2125	1.3118	1.4208	8.8283
	10.0	1.0142	1.0555	1.1200	1.2028	1.2994	1.4043	8.3017

In addition, Figure 6.2 shows the nonlinear central deflection (w_c /h) variation considering P_e and P_c's porosity distributions for the TDFGPP. It can be noted that the predominant effects of VFGI on the nonlinear deflection appear to be in the gradation region ($m_x = m_z$ = 1 and 2). Meanwhile, a pronounced lower deflection can be observed for higher VFGI (m_z and m_x) due to increased stiffness. Therefore, the influence of VFGI seems to be predominant for property determination of TDFGPP material, which is subsequently proportional to the stiffness. In addition, the P_e type of porosity distribution has more effect on the nonlinear deformations than the CDP (P_c), i.e., (P_e > P_c). It is due to the distribution of porosities in TDFGPP material, leading to a stiffness

variation. Besides, Figure 6.3 show the nonlinear transient deflection's (w_c /h) variation considering P_e and P_c's porosity distributions for the TDFGPP. It can be noticed from Figure 6.3 that a similar kind of trend is observed as seen in the nonlinear central deflections of the TDFGPP.

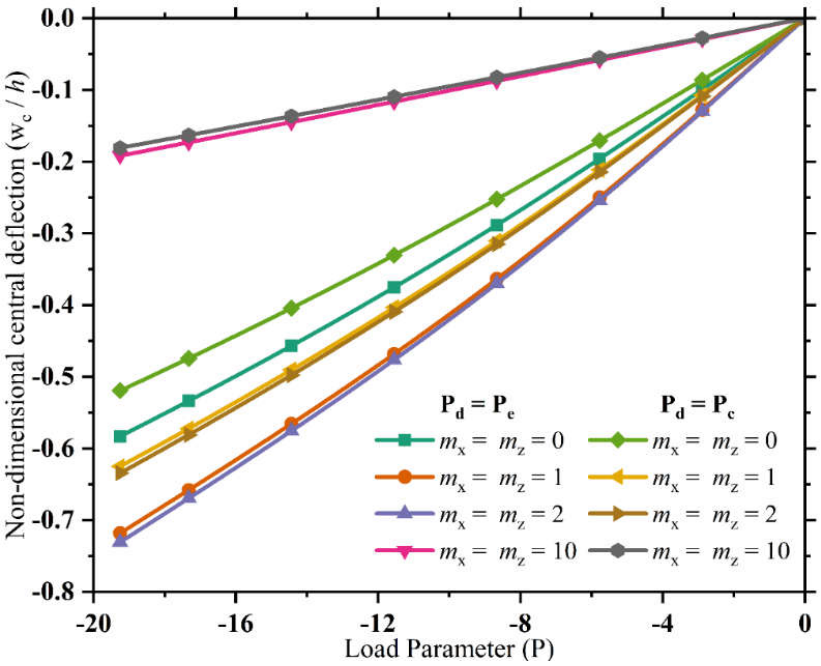

Figure 6.2: Nonlinear central deflections of square TDFGM porous plate for different VFGI (m_x and m_z) (a/h = 100, and e_p = 0.1).

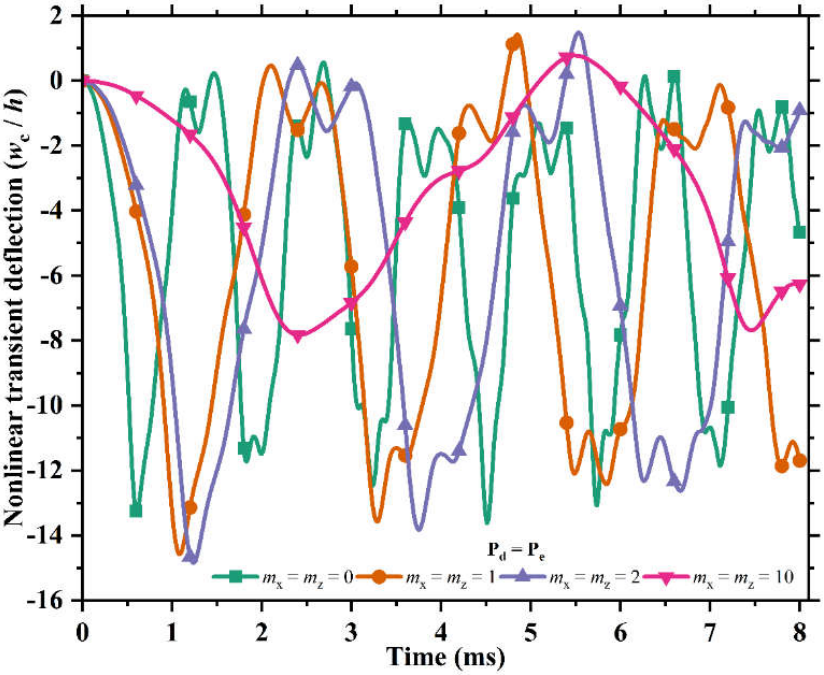

(a) EDP (P_e)

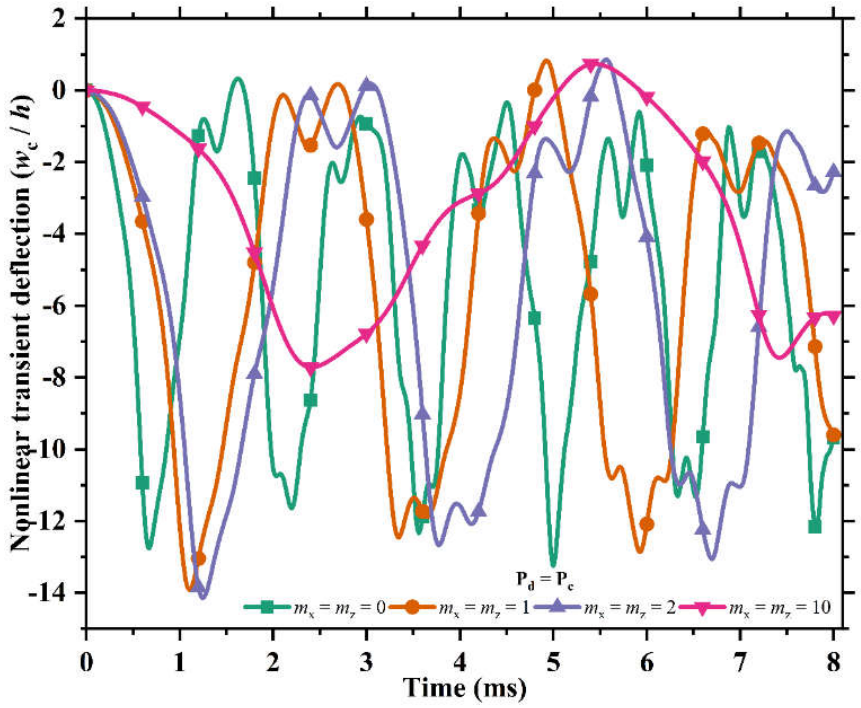

(b) CDP (P_c)

Figure 6.3: Nonlinear transient deflections of square TDFGPP for different VFGI (a/h = 100, e_p = 0.1). (a) EDP (P_e), and (b) CDP (P_c).

Table 6.2: NLFR (ω_{NL}/ω) of the square TDFGPP for different PVI (e_p) (a/h =100, m_x = m_z = 2, and SSSS).

P_d	e_p	Amplitude ratio (W_{max}/h)						ω
		0.25	0.50	0.75	1.00	1.25	1.50	
	0.0	1.0128	1.0500	1.1086	1.1846	1.2732	1.3714	10.6418
	0.1	1.0133	1.0518	1.1123	1.1906	1.2817	1.3816	10.1443
P_e	0.2	1.0137	1.0533	1.1155	1.1960	1.2891	1.3911	9.5643
	0.3	1.0141	1.0551	1.1192	1.2020	1.2972	1.4020	8.7673
	0.4	1.0155	1.0602	1.1299	1.2193	1.3213	1.4329	7.3333
	0.0	1.0128	1.0500	1.1086	1.1846	1.2732	1.3714	10.6418
	0.1	1.0126	1.0487	1.1055	1.1790	1.2650	1.3604	10.7020
P_c	0.2	1.0123	1.0471	1.1017	1.1727	1.2555	1.3483	10.7822
	0.3	1.0118	1.0450	1.0970	1.1645	1.2443	1.3331	10.8839
	0.4	1.0112	1.0423	1.0912	1.1551	1.2309	1.3144	11.0093

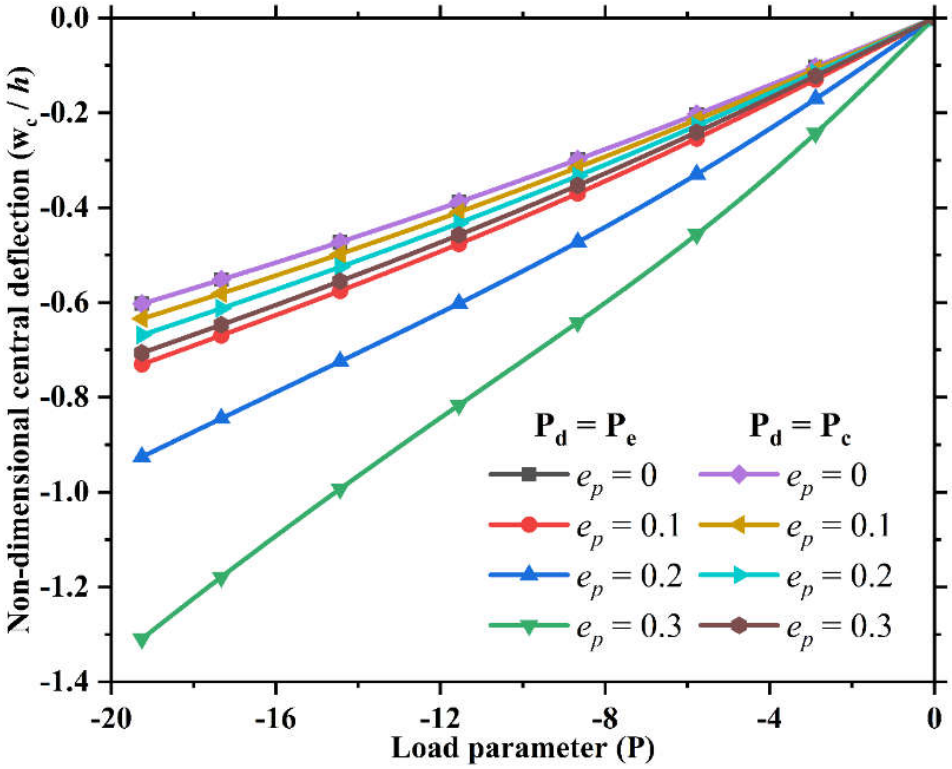

Figure 6.4: Nonlinear central deflections of TDFGPP for different porosity distributions and PVI (e_p) (a/h = 100, and $m_x = m_z = 2$).

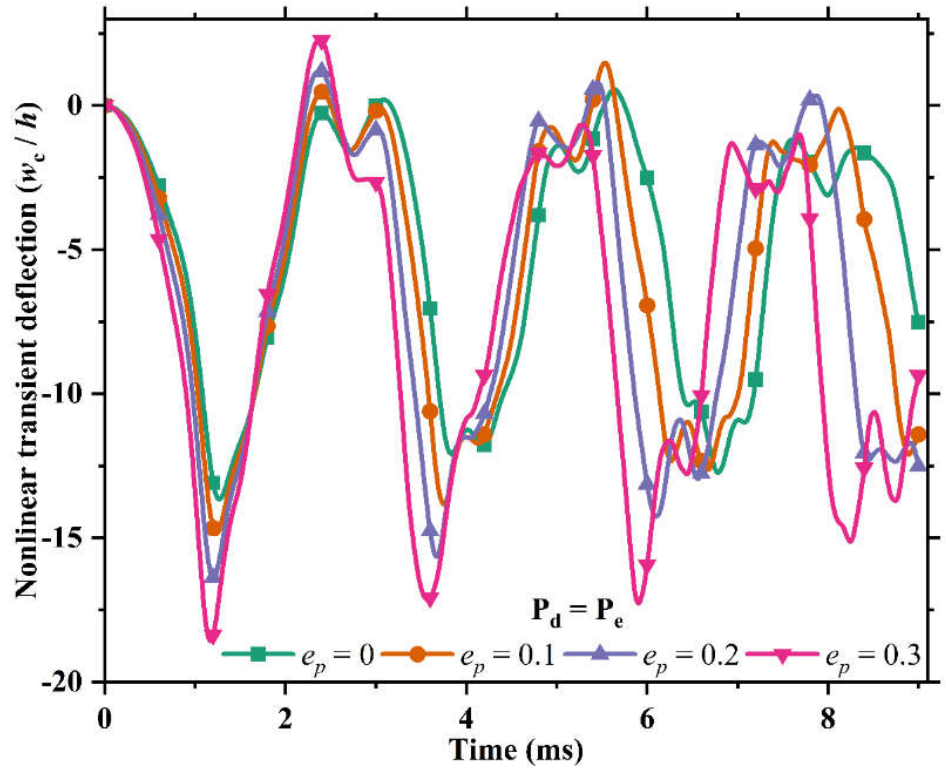

(a) EDP (P_e)

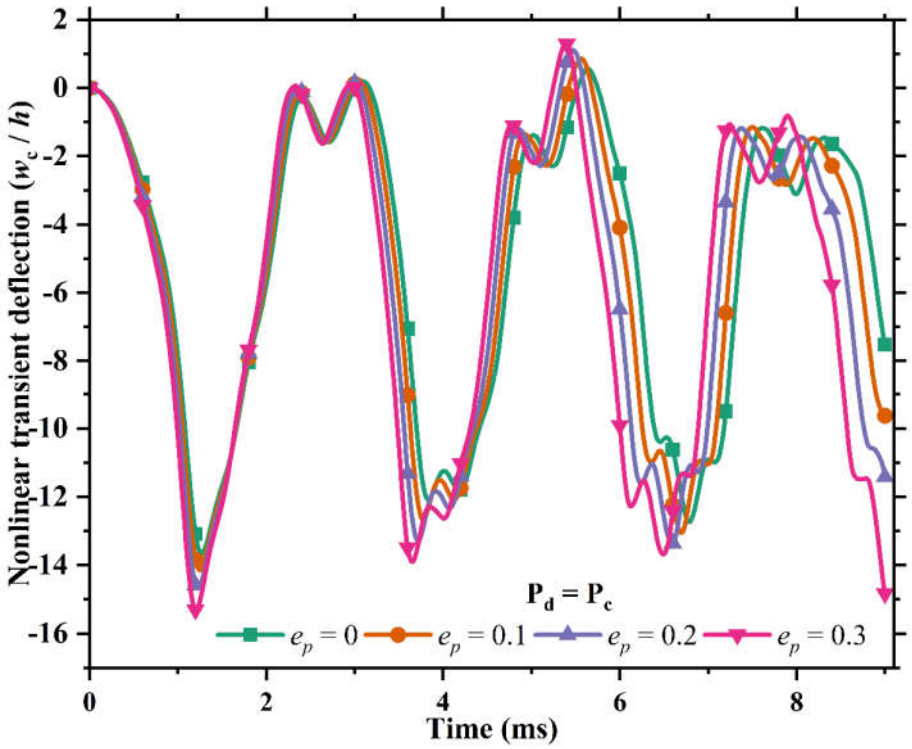

(b) CDP (P_c)

Figure 6.5: Nonlinear transient deflections of the TDFGPP with CDP (P_c) for different PVI (e_p) (a/h = 100, a/b = 1, and $m_x = m_z$ = 2). (a) EDP (P_e), and (b) CDP (P_c).

6.3.2. Effect of porosity volume index (PVI)

The influence of the PVI (e_p) and porosity distributions P_e and P_c on the TDFGPP are investigated and tabulated in Table 6.2. For the sake of brevity, only the VFGI two is considered for both m_x and m_z. It can be seen that the NLFR increases with an increase in the PVI (e_p) for an EDP (P_e). Meanwhile, the trend is reversed for the CDP (P_c). Besides, the linear frequency decreases for an EDP while it increases for the CDP with an increase in e_p. Also, porosities' effects are higher in the CDP (P_c) than in the EDP (P_e) for linear responses contrary to the NLFR. It can be due to the more material accretion away from the middle surface, which enhances the flexural stiffness of the TDFGPP for the porosity distributions type P_c.

Furthermore, the nonlinear central deflection of the TDFGPP influenced by PVI (e_p) and porosity distributions P_e and P_c is depicted in Figure 6.4. It can be observed that the deflections increase with an increase in the PVI (e_p) for all porosity distributions. Meanwhile, P_c's porosity distribution shows the minimum deflection than the EDP (P_e), and a noticeable difference is observed in P_e between the PVI. Also, the deflection rate

is very high for P_e type of porosity distributions compared to P_c for a given PVI. It is because the arrangements of the porosities in the P_e facilitate the uniform distribution of materials across the thickness. In contrast, more materials are accumulated far away from the middle plane for P_c leading to high stiffness in the plate. Besides, the nonlinear deflections increase with an increase in the load parameters. Furthermore, Figure 6.5 shows the nonlinear transient deflections of the TDFGPP influenced by PVI (e_p) and porosity distributions P_e and P_c. It can be observed from Figure 6.5 that the nonlinear transient deflections of the TDFGPP follow a similar pattern of nonlinear central deflections, as illustrated in Figure 6.4.

6.3.3. Effect of thickness and aspect ratios

The NLFR and linear frequency of the TDFGPP for different thickness ratios are tabulated in Table 6.3. The NLFR and linear frequency values increase with the thickness ratio for a given porosity distribution. It is because greater stiffness is achieved by having lower thickness ratios.

Table 6.3: NLFR (ω_{NL} /ω) of the square TDFGPP for different thickness ratios (e_p = 0.1, $m_x = m_z = 2$, $W_{max}/h = 1.5$, and SSSS).

Thickness ratio (a/h)	P_e		P_c	
	NLFR	ω	NLFR	ω
5	1.3753	8.9906	1.3582	9.3622
10	1.3772	9.8168	1.3620	10.3164
20	1.3801	10.0618	1.3591	10.6044
50	1.3811	10.1338	1.3598	10.6895
100	1.3815	10.1443	1.3604	10.7020

Besides, the aspect ratio can be considered a significant parameter in the plate's geometry, particularly for thin structures. The geometrical instability increases as the structural elements become thinner, which affects the plate's dynamic behavior. The aspect ratio's influence on the NLFR and linear frequency of the TDFGPP are shown in Table 6.4. The NLFR of porous plates decreases with an increase in the aspect ratio. In contrast, the linear frequency responses show a reversed trend for a given porosity distribution. For both thickness and aspect ratio cases, the P_c's NLFR exhibits lower

values than the P_e. Meanwhile, the linear responses show a reverse trend.

6.3.4. Effect of boundary conditions

The support condition's influence on the nonlinear central and transient deflection of the TDFGPP is shown in Figures 6.6 and 6.7, respectively. It can be inferred that, for a given boundary condition, the nonlinear deformations of the P_c have lower values than the P_e. The arrangements of the porosities in the P_e may facilitate the uniform distribution of materials across the thickness, leading to maximum deformation. In contrast, more materials are accumulated far away from the middle plane for P_c leading to high stiffness in the plate. However, clamped edges have lesser deflections while SSSS shows the highest deflection and follows the SSSS > SCSC > CCCC trend. It is commonly known that as boundary restrictions are clamped, the structure becomes stiffer.

Table 6.4: NLFR (ω_{NL}/ω) of the TDFGPP for different aspect ratios (a/h = 100, e_p = 0.1, $m_x = m_z = 2$, W_{max}/h = 1.5, and SSSS).

aspect ratio (a/b)	P_e		P_c	
	NLFR	ω	NLFR	ω
0.5	1.1764	6.3411	1.1656	6.6897
1.0	1.3815	10.1443	1.3604	10.7020
1.5	1.2908	16.4809	1.2741	17.3864
2.0	1.1774	25.3471	1.1651	26.7389
3.0	1.0611	50.6468	1.0574	53.4217

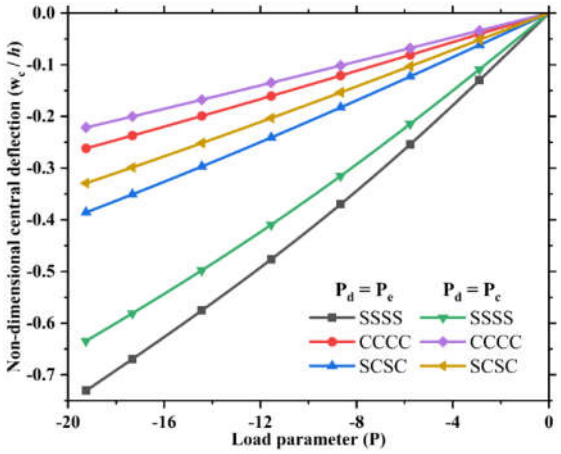

Figure 6.6: Nonlinear central deflections of TDFGPP for different support conditions (a/h = 100, a/b = 1, $m_x = m_z = 2$, and e_p = 0.1).

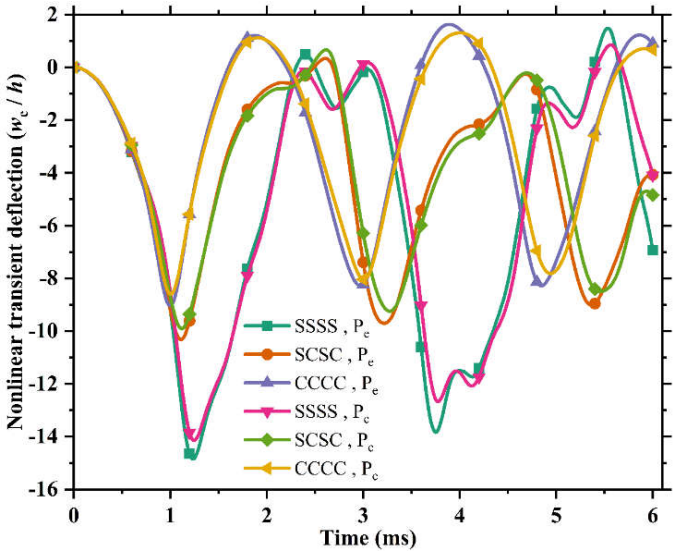

Figure 6.7: Nonlinear transient deflections of the TDFGPP for different support conditions and porosity distributions (a/h = 100, a/b = 1, $m_x = m_z$ = 2, and e_p = 0.1).

6.4. CONCLUSIONS

This chapter investigates the linear frequency, nonlinear frequency, and nonlinear deformations of the TDFGPP with four different material compositions. The modified power-law series integrates four different compositions of materials incorporating the porosities and determines the effective TDFGPP properties in longitudinal and thick directions. A nonlinear FE formulation is constructed based on the IFSDT and von Karman's geometric nonlinearity. The solutions are extracted using the direct iterative method and Newmark's integration techniques.

Following beneficial conclusions can be made from the several exciting outcomes observed in the numerical studies. The linear frequency, nonlinear frequency, and nonlinear deformations can be significantly varied and regulated by changing the volume fraction gradation profiles in the desired direction (transverse and longitudinal) for each material with suitable materials. The distribution of porosities has a more significant impact on the frequency variation. The porosity distribution CDP exhibits the highest linear frequency, while EDP exhibits the highest NLFR and nonlinear deflections. The nonlinear deflection rate is reasonably considerable for a given porosity volume index and reaches a maximum value for evenly distributed porosity (EDP) rather than centrally distributed porosity (CDP). The NLFR increases with an

increasing thickness ratio but decreases with increasing aspect ratios. Meanwhile, the linear frequency increases as the thickness and aspect ratios increase. The nonlinear deflections with respect to the various boundary conditions follow the pattern SSSS > SCSC > CCCC.

CHAPTER 7

GEOMETRICALLY NONLINEAR ANALYSIS OF FUNCTIONALLY GRADED SATURATED POROUS PLATES

This chapter investigates the nonlinear analysis of a functionally graded saturated porous material (FGSPM) plate under undrained conditions. The nonlinear finite element formulation derived in chapter 4 has been extended to analyze FGSPM plates. The effective material characteristics of the saturated porous plate change constantly in the thickness direction. The pores of the saturated porous plate are examined in fluid-filled conditions. Thus, the constitutive equations are established using Biot's linear poroelasticity theory. The emphasis is placed on exploring the effects of numerous parameters such as Skempton coefficient, volume fraction grading index, porosity volume index, porosity distributions, and boundary conditions during the extensive numerical analyses on the linear frequency, large amplitude frequencies, and nonlinear central deflection of the FGSPM plates. It is evident from the investigation that saturated fluid in the pores substantially impacts the nonlinear deflection and vibration behavior of FGSPM plates.

7.1. INTRODUCTION

Functionally graded saturated porous materials (FGSPM) comprise the pores and cavities filled with fluid, and the skeletal part is made of solid material. Fabricating the perfect FGM without the entrapment of fluids in the pores is inevitable using modern-day manufacturing techniques. Hence, it is crucial to investigate the effects of undrained pores on the structural behavior of FGSPM plates. FGSPM is widely used in the aircraft industry as a vibration damper meanwhile civil, mechanical, and maritime structures because of its low density. In this chapter, the investigation of nonlinear analysis of FG saturated porous plates has been carried out under drained conditions.

The poroelastic behavior of an FGSPM plate is modeled using the Biot theory, which considers the saturated pore fluid pressure. In addition, the FGSPM plate's effective material properties vary smoothly as an arbitrary function of the volume fractions in transverse directions, conferring a modified power-law series. The governing equations are developed and solved using the nonlinear finite element method, IFSDT, von Kármán's assumptions, the Hamilton principle, and the direct iterative technique. Finally, the linear and geometrically nonlinear vibration behavior of the FGSPM plate for the undrained conditions are extracted. Besides, the dynamic responses of the FGSPM plate are investigated for numerous parameters such as porosity and saturated porosity distributions, Skempton coefficients, and volume fraction grading index.

7.2. PROBLEM DESCRIPTION AND GOVERNING EQUATION

The nonlinear finite element formulation considering the IFSDT with von Kármán's nonlinearity has been derived in Chapter 4. The same formulation has been used to analyze porous FGSPM plates without considering the effects of temperature. Further, the homogenization technique to obtain the effective material properties and solution methodologies is employed identical to sections 2.2.1 and 2.3.1 of Chapter 2. However, the constitutive equations are developed using Biot's poroelasticity theory, which incorporates saturated fluids. The same has been presented in the subsequent section.

7.2.1. The geometry of functionally graded saturated porous material plates

Consider an FGSPM plate, as depicted in Figure 6.1, which is formed of porous material with fluid-saturated pores. For the numerical analysis in the present study, the sides a and b and the thickness h are referenced to the cartesian coordinate axis positioned on the plate's mid-plane, with the z-axis in the thickness direction.

The effective material properties of the functionally graded saturated porous material plate vary continuously in the thickness direction. The distribution of saturated porosities formed during FGSPM plate fabrication is theoretically predicted. As illustrated in Figure 7.1, the FGSPM plate is studied using two different models: evenly (P_e) and centrally (P_c) distributed porosities.

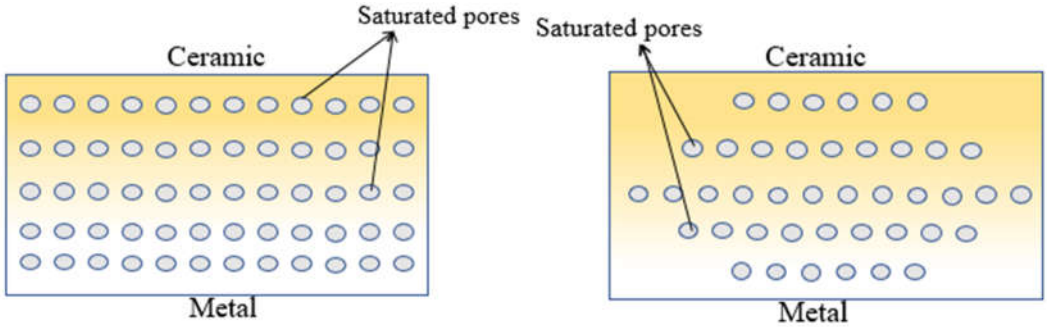

(a) (b)

Figure 7.1: Cross-section of the FGSPM plate showing the porosity distributions in an undrained state. (a) Evenly distributed porosity (P_e) and (b) Centrally distributed porosity (P_c).

7.2.2. Constitutive relations

The poroelastic behaviour of a FGSPM plate is modelled using the Biot constitutive law (Biot's linear poroelasticity theory). As a result, the stress–strain relationship is as follows (Babaei et al. 2020b; DETOURNAY and CHENG 1993):

$$\sigma_{ij} = 2G\varepsilon_{ii} + \frac{2G\vartheta_u}{1-2\vartheta_u}\varepsilon_{kk}\delta_{ij} - \alpha_s\, p\delta_{ij} \tag{7.1}$$

where

$$p = M\left(\xi - \alpha_s\, \varepsilon_{kk}\right) \tag{7.2}$$

$$M = \frac{2G((\vartheta_u - \vartheta)}{\alpha^2\left(1-2\vartheta_u\right)\left(1-2\vartheta\right)} \tag{7.3}$$

$$\vartheta_u = \frac{\vartheta + \frac{\alpha_s\, B\left(1-2\vartheta\right)}{3}}{1 - \frac{\alpha_s\, B\left(1-2\vartheta\right)}{3}} \tag{7.4}$$

The pore fluid pressure is represented by p; G stands for shear modulus; M indicates Biot's modulus; The undrained Poisson's ratio is denoted by ϑ_u $\left(0 < \vartheta < \vartheta_u < 0.5\right)$; The Biot coefficient of effective stress is represented by α_s $(0 < \alpha_s < 1)$ (for the present study, α is assumed to be 0.35); ε_{kk} is volumetric strain; ξ is a change in the volume of fluid. The influence of fluid in the pores on structure's response in an undrained state is

denoted by the Skempton coefficient B. It is also called the Skempton pore pressure coefficient.

By condensing Eq. (7.1) to the plane-stress condition in cartesian coordinates and under the undrained condition, the following equations emerge as ($\xi = 0$) (Jabbari et al. 2014b).

$$\begin{Bmatrix}\sigma_{xx}\\ \sigma_{yy}\\ \sigma_{xy}\end{Bmatrix} = \begin{bmatrix}Q_{ij}\end{bmatrix}\begin{Bmatrix}\varepsilon_{xx}\\ \varepsilon_{yy}\\ \varepsilon_{xy}\end{Bmatrix}, \quad \begin{Bmatrix}\tau_{yz}\\ \tau_{xz}\end{Bmatrix} = \begin{bmatrix}Q_{s(ij)}\end{bmatrix}\begin{Bmatrix}\gamma_{yz}\\ \gamma_{xz}\end{Bmatrix} \tag{7.5}$$

$$Q_{ij} = G(z)\begin{bmatrix}Q_1 & Q_2 & 0\\ Q_2 & Q_1 & 0\\ 0 & 0 & 1\end{bmatrix}, \quad Q_{s(ij)} = G(z)\begin{bmatrix}1 & 0\\ 0 & 1\end{bmatrix} \tag{7.6}$$

$$Q_1 = \left(\frac{2}{1-\vartheta_u^2}\right)\left[1+\vartheta_u + \frac{(\vartheta_u - \vartheta)(1+\vartheta_u)}{(1-2\vartheta)}\left(1-\frac{C_2}{C_1}\right)\right] \tag{7.7}$$

$$Q_2 = \left(\frac{2}{1-\vartheta_u^2}\right)\left[(1+\vartheta_u)\vartheta_u + \frac{(\vartheta_u - \vartheta)(1+\vartheta_u)}{(1-2\vartheta)}\left(1-\frac{C_2}{C_1}\right)\right] \tag{7.8}$$

$$C_1 = 2\left[1+\frac{\vartheta_u}{(1-2\vartheta_u)} + \frac{(\vartheta_u - \vartheta)}{(1-2\vartheta_u)(1-2\vartheta)}\right]G(z), \quad C_2 = C_1 - 2G(z) \tag{7.9}$$

7.3. RESULTS AND DISCUSSIONS

The nonlinear finite element solutions are obtained in this section to demonstrate the nonlinear frequency responses and nonlinear central deflections of the FGSPM plate using the proposed formulation. The material parameters of the Si_3N_4 / SUS304 FGSPM plate are listed in Table 2.1 for analysis. The parametric investigations on the Skempton coefficient (Pore fluid pressure), the influence of porosity volume index, saturated porosity distributions, VFGI, thickness-length ratio, and aspect ratio on linear and nonlinear frequency, nonlinear central deflections of the FGSPM plate are presented. Special emphasis is recorded on saturated porosity distributions and VFGI effects on the FGSPM plate. The uniformly distributed load (q_0) – 10^6 N/m^2 is used for nonlinear central deflections. The results are derived using non-dimensionalized linear

frequency and deflection parameters. The following are the non-dimensionalized quantities considered:

Non-dimensionalized linear frequency $\omega_{\text{ln}} = \bar{\omega} h\sqrt{\rho_c / E_c}$

Non-dimensionalized central deflection $(w) = w_c / h$

Non-dimensionalized load parameter $P = \left(\dfrac{q_0 a^4}{(E_m) h^4} \right)$ (7.12)

where E_m and E_c are the modulus of elasticity of the metal and ceramic materials respectively; ρ_c is the density of the ceramic material; the applied uniformly distributed mechanical load is q_0.

7.3.1. Convergence and comparison study

The robustness of the proposed nonlinear finite element model enables the parametric analyses to be carried out by validating and comparing the obtained results with solutions available in the open literature.

Validation studies presented in section 4.4 (Examples 4, 5, and 6) and section 5.3.1 (Example 4) of chapters 4 and 5, respectively, have also been implemented for the present analysis. However, the validation has been carried out without the effects of temperature, i.e., T = 300 K of Example 5 in section 4.4 (Chapter 4) for the present analysis of FGSPM plates.

Example 1: The non-dimensionalized linear frequency and deflection of the SSSS FG porous plate are shown in Tables 7.1 and 7.2. The acquired results are compared to those available in the open literature (Ebrahimi and Habibi 2016) for the same material and geometrical parameters used by the authors (Ebrahimi and Habibi 2016). Different Skempton coefficients (B), thickness ratios, and boundary conditions are considered for validation. The proposed model's responses converge at a mesh size of [8 × 8] and show remarkable agreement with the available literature (Ebrahimi and Habibi 2016).

7.3.2. Effect of Skempton coefficient (B) and volume fraction grading index (*m*)

The Skempton coefficient and VFGI are essential parameters in determining the characteristics of the FGSPM plate, which determines the material's stiffness. Tables 7.3 and 7.4 show the significance of changing the Skempton coefficient (B) and VFGI

(m) on natural frequency and NLFR (ω_{NL}/ω) for various amplitude ratios. The analysis is carried out for the simply supported FGSPM plate for EDP (P_e) and CDP (P_c). As noticed from the tables, the linear frequency and NLFR increase with the Skempton coefficient for a given VFGI (m). As also discernible, the FGSPM plate exhibits the lowest linear frequency and NLFR under a drained situation (no fluid; B = 0). It is due to the compressibility of the pores being high at this stage (no fluid in the pores). In contrast, in an undrained condition, the compressibility of the fluid reduces with the Skempton coefficient, and frequencies increase as well. Therefore, the behavior of the FGSPM plate replicates that of functionally graded porous plates without fluid when the compressibility of the fluid in pores is large (B = 0; drained state). Besides, the stiffness of the FGSPM plate is at its lowest in drained conditions. Hence, the frequencies are also at their lowest. Furthermore, when the compressibility of the fluid (B >> 0) in cavities is low, the highest frequencies can be attained. Hence, the behavior of the FGSPM plate is similar to that of rigid plates.

Moreover, for a given Skempton coefficient, the linear frequency and NLFR exhibit the lowest values for CDP (P_c) in the ceramic region compared to EDP (P_e). In contrast, the lowest values of linear frequencies are observed for EDP in the metallic region, with an increase in the VFGI (m). Besides, for a given Skempton coefficient, the NLFR decreases gradually and reverses the trend with an increase in VFGI (m) because the high concentration of the ceramic material is gradually changed to the metallic material. This gradual change in material reduces the plate's stiffness, resulting in a quick fall in the plate's linear frequency. As a result, there is a significant difference between nonlinear and linear frequency, resulting in an increase in NLFR for higher VFGI (m).

In addition, Figures 7.2 and 7.3 depict the influence of the VFGI (m) and Skempton coefficient on the geometrically nonlinear central deflection (w_c/h) of the FGSPM plate ($e_p = 0.1$, $a/h = 10$, $a/b = 1$, and SSSS). As observed from the plots, for a given Skempton coefficient and porosity volume index, the central deflection increases with an increase in VFGI (m) for both the types of porosity distributions (P_e and P_c) shown in Figure 7.2. It's due to a decrease in stiffness as the FGSPM plate becomes more metal-rich as the VFGI (m) rises.

Table 7.1: Dimensionless fundamental frequency of FG porous square plates (e_p = 0) (a/b =1).

h/a	Sources	B.C	Skempton coefficient (B)			
			0.1	0.3	0.5	0.7
0.05	Ebrahimi et al. (2016)	SSSS	0.01473	0.01495	0.01526	0.01549
	Present (IFSDT)		0.0149	0.0151	0.0153	0.0155
	Ebrahimi et al. (2016)	CCCC	0.0266	0.02702	0.02754	0.02784
	Present (IFSDT)		0.0265	0.0269	0.0272	0.0276
0.1	Ebrahimi et al. (2016)	SSSS	0.05783	0.05876	0.05954	0.06055
	Present (IFSDT)		0.0581	0.0589	0.0596	0.0604
	Ebrahimi et al. (2016)	CCCC	0.09965	0.10106	0.10243	0.10378
	Present (IFSDT)		0.0975	0.0986	0.0997	0.1007
0.2	Ebrahimi et al. (2016)	SSSS	0.21275	0.21563	0.21857	0.22162
	Present (IFSDT)		0.2118	0.2141	0.2164	0.2186
	Ebrahimi et al. (2016)	CCCC	0.33041	0.33373	0.33696	0.34011
	Present (IFSDT)		0.3091	0.3113	0.3134	0.3155

Table 7.2: Dimensionless deflection of FG porous square plates (e_p = 0) (a/b =1).

h/a	Sources	B.C	Skempton coefficient (B)			
			0.1	0.3	0.5	0.7
0.05	Ebrahimi et al. (2016)	SSSS	0.04543	0.04399	0.04263	0.04135
	Present (IFSDT)		0.0444	0.0432	0.0420	0.0409
	Ebrahimi et al. (2016)	CCCC	0.01456	0.01412	0.01369	0.01329
	Present (IFSDT)		0.0145	0.0141	0.0137	0.0134
0.1	Ebrahimi et al. (2016)	SSSS	0.04699	0.04555	0.04419	0.04291
	Present (IFSDT)		0.0466	0.0453	0.0442	0.0431
	Ebrahimi et al. (2016)	CCCC	0.01627	0.01582	0.01540	0.01500
	Present (IFSDT)		0.0169	0.0165	0.0161	0.0158
0.2	Ebrahimi et al. (2016)	SSSS	0.05323	0.05179	0.05043	0.04915
	Present (IFSDT)		0.0552	0.0540	0.0528	0.0517
	Ebrahimi et al. (2016)	CCCC	0.02269	0.02223	0.02181	0.02140
	Present (IFSDT)		0.0259	0.0255	0.0251	0.0248

Table 7.3: Effect of Skempton coefficient (B) and VFGI on the NLFR (ω_{NL}/ω) of Si_3N_4/SUS304 FGSPM square plate. (a/h =10, e_p = 0.1, $P_d = P_e$, & SSSS).

m	B	Amplitude ratio (W_{max}/h)				ω
		0.25	0.50	0.75	1.00	
0	0.0	1.0424	1.1610	1.3366	1.5509	0.0623
	0.1	1.0427	1.1619	1.3384	1.5538	0.0629
	0.3	1.0432	1.1637	1.3419	1.5591	0.0639
	0.5	1.0437	1.1654	1.3452	1.5640	0.0649
	0.7	1.0441	1.1669	1.3481	1.5685	0.0659
0.5	0.0	1.0220	1.1257	1.2931	1.5041	0.0403
	0.1	1.0222	1.1265	1.2947	1.5068	0.0406
	0.3	1.0224	1.1279	1.2978	1.5117	0.0413
	0.5	1.0227	1.1292	1.3007	1.5163	0.0419
	0.7	1.0229	1.1304	1.3033	1.5205	0.0426
1.0	0.0	1.0143	1.1106	1.2720	1.4785	0.0348
	0.1	1.0144	1.1113	1.2736	1.4810	0.0351
	0.3	1.0146	1.1126	1.2764	1.4858	0.0357
	0.5	1.0148	1.1137	1.2791	1.4902	0.0362
	0.7	1.0149	1.1148	1.2816	1.4942	0.0368
2.0	0.0	1.0116	1.1032	1.2590	1.4598	0.0309
	0.1	1.0117	1.1038	1.2605	1.4623	0.0311
	0.3	1.0118	1.1050	1.2633	1.4669	0.0316
	0.5	1.0119	1.1061	1.2658	1.4712	0.0321
	0.7	1.0121	1.1071	1.2682	1.4751	0.0326
10.0	0.0	1.0253	1.1262	1.2861	1.4872	0.0262
	0.1	1.0255	1.1270	1.2878	1.4898	0.0264
	0.3	1.0258	1.1284	1.2909	1.4948	0.0269
	0.5	1.0261	1.1298	1.2937	1.4993	0.0273
	0.7	1.0264	1.1310	1.2964	1.5035	0.0277

Table 7.4: Effect of Skempton coefficient (B) and VFGI on the NLFR (ω_{NL}/ω) of Si_3N_4/SUS304 FGSPM square plate. (a/h =10, e_p = 0.1, $P_d = P_c$, & SSSS).

m	Skempton coefficient (B)	Amplitude ratio (W_{max}/h)				ω
		0.25	0.50	0.75	1.00	
0	0.0	1.0416	1.1581	1.3309	1.5421	0.0602
	0.1	1.0419	1.1590	1.3327	1.5449	0.0607
	0.3	1.0424	1.1608	1.3362	1.5502	0.0617
	0.5	1.0428	1.1625	1.3394	1.5551	0.0627
	0.7	1.0433	1.1640	1.3424	1.5596	0.0636
0.5	0.0	1.0226	1.1249	1.2895	1.4970	0.0404
	0.1	1.0227	1.1257	1.2912	1.4997	0.0407
	0.3	1.0230	1.1271	1.2942	1.5046	0.0414
	0.5	1.0232	1.1284	1.2971	1.5091	0.0421
	0.7	1.0235	1.1296	1.2997	1.5133	0.0427
1.0	0.0	1.0155	1.1109	1.2698	1.4728	0.0352
	0.1	1.0156	1.1116	1.2713	1.4754	0.0355
	0.3	1.0158	1.1129	1.2742	1.4801	0.0361
	0.5	1.0160	1.1140	1.2769	1.4845	0.0367
	0.7	1.0162	1.1151	1.2794	1.4885	0.0372
2.0	0.0	1.0131	1.1041	1.2577	1.4554	0.0314
	0.1	1.0131	1.1047	1.2592	1.4578	0.0317
	0.3	1.0133	1.1059	1.2620	1.4625	0.0322
	0.5	1.0135	1.1071	1.2646	1.4668	0.0327
	0.7	1.0136	1.1081	1.2670	1.4707	0.0332
10.0	0.0	1.0257	1.1252	1.2824	1.4801	0.0269
	0.1	1.0259	1.1259	1.2841	1.4827	0.0272
	0.3	1.0262	1.1274	1.2872	1.4876	0.0276
	0.5	1.0265	1.1288	1.2900	1.4921	0.0280
	0.7	1.0268	1.1300	1.2926	1.4963	0.0285

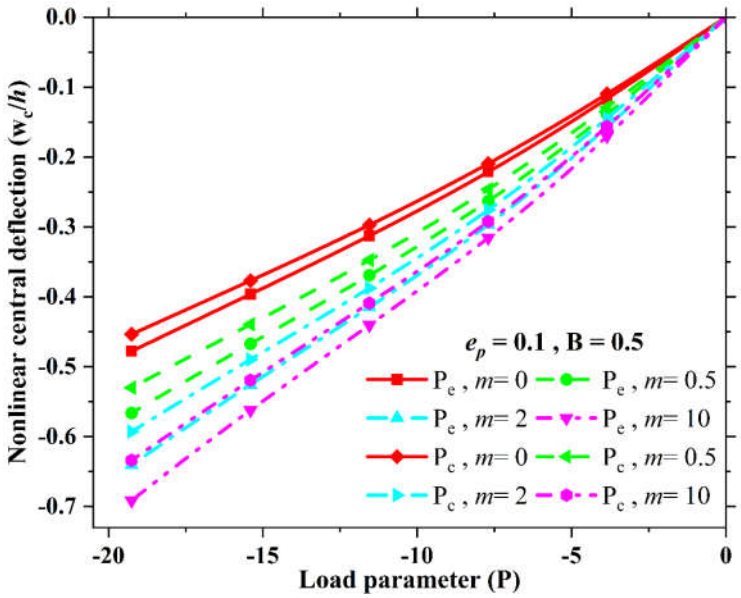

Figure 7.2: Effect of VFGI on the central deflection (w_c/h) of Si_3N_4/SUS304 FGSPM square plate for different porosity distributions. (a/h =10, B = 0.5, e_p = 0.1, & SSSS).

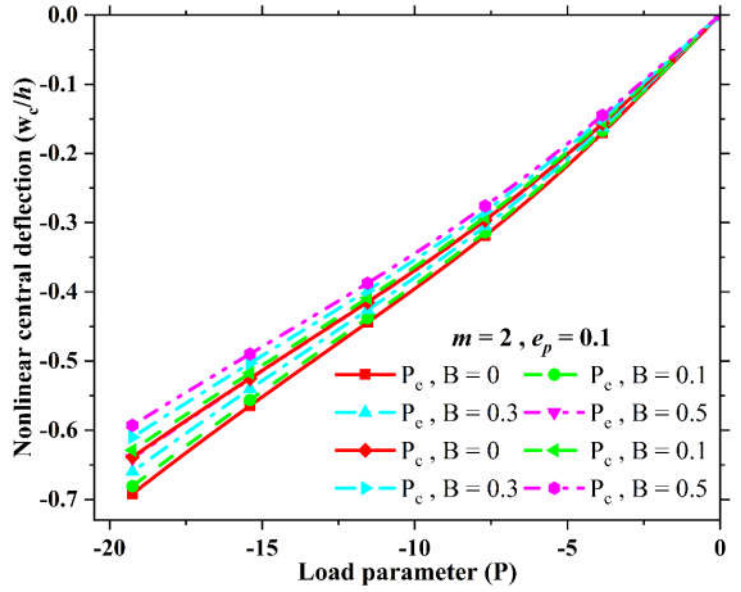

Figure 7.3: Effect of Skempton coefficient (B) on the central deflection (w_c/h) of Si_3N_4/SUS304 FGSPM square plate for different porosity distributions. (a/h =10, e_p = 0.1, m = 2, & SSSS).

Furthermore, the central deflection reduces as the Skempton coefficient (increase in pore fluid pressure) increases for a given VFGI and porosity volume index. The same trend is observed for both the types of porosity distributions (P_e and P_c), as illustrated in Figure 7.4. The physical significance of this trend is that, as the pore fluid pressure

increases, the compressibility of the plate decreases, leading to an increase in the stiffness of the FGSPM plate. Besides, EDP has the highest central deflection than the CDP. It is because the distribution of porosities is uniform in evenly distributed porosities, leading to a sudden decrease in the stiffness of the plate.

7.3.3. Influence of porosity volume index (e_p) for various Skempton coefficients

The effect of the porosity volume index (e_p) for various Skempton coefficients (B) on the linear frequency and NLFR of the FGSPM plate is illustrated in Figure 7.4 for SSSS and CCCC boundary conditions. The different porosity distributions considered for the study are EDP (P_e) and CDP (P_c). The figures show that the linear frequency gradually decreases as the porosity volume index increases for both types of boundary conditions. However, a gradual decrease and an increase in NLFR are observed for the SSSS and CCCC support conditions, respectively. Also, a noticeable difference in the NLFR is witnessed for each value of the Skempton coefficient with the CCCC boundary conditions compared to the SSSS boundary conditions. This trend is noticed for a Skempton coefficient with EDP (P_e). However, the decrease in the linear frequency and increase in the NLFR are seen with increased porosity volume index for the CDP (P_c) for SSSS and CCCC boundary conditions. Also, a noticeable difference in linear frequency is observed for each value of Skempton coefficient for both types of boundary conditions.

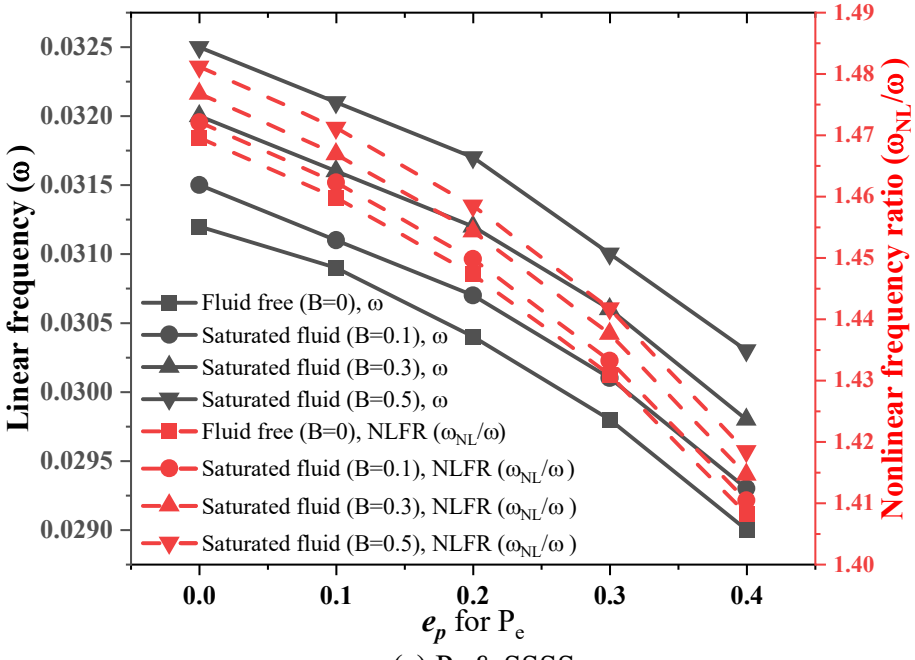

(a) P_e & SSSS

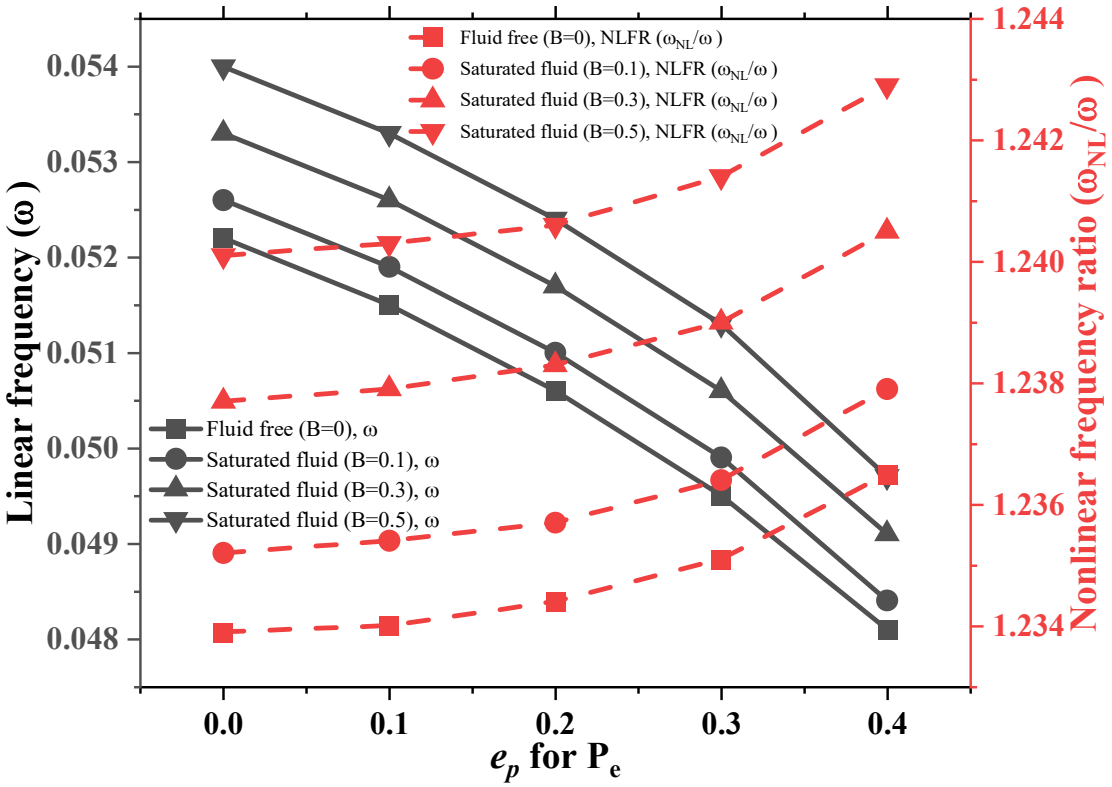

(b) P_e & CCCC

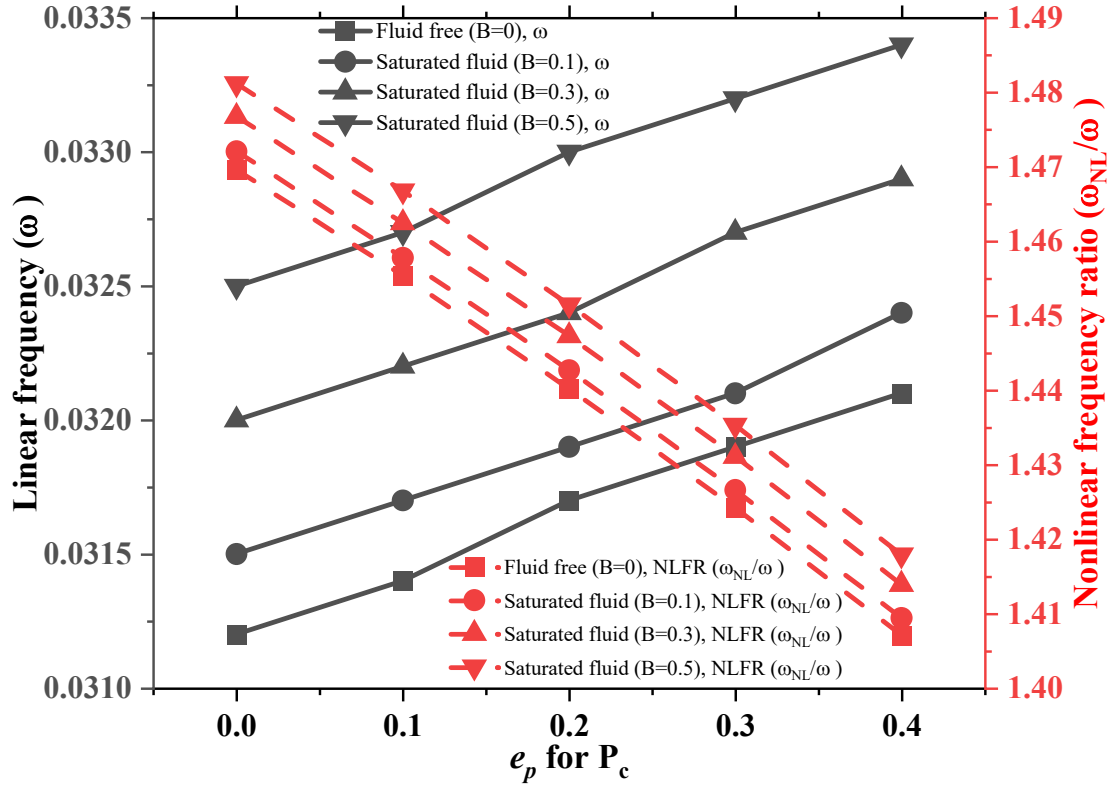

(c) P_c & SSSS

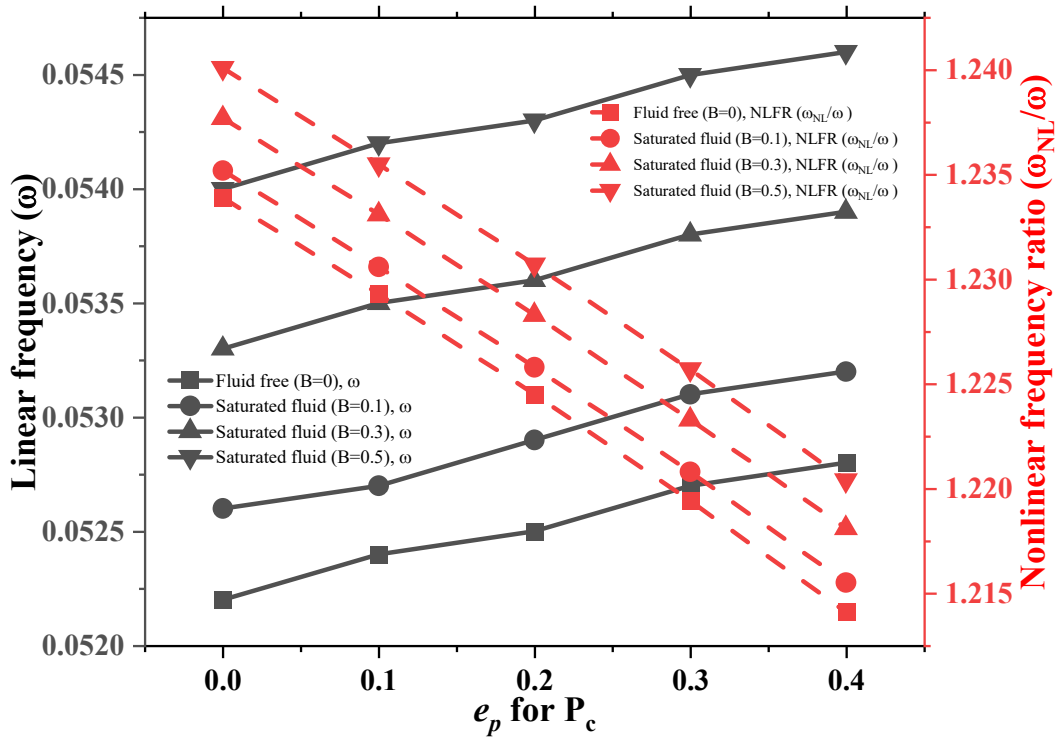

(d) P_c & CCCC

Figure 7.4: Influence of Skempton coefficient (B) on the linear frequency and NLFR (ω_{NL}/ω) of Si_3N_4/SUS304 FGSPM square plate for different porosity volume index. (a/h =10, m = 2, W_{max}/h = 1,). (a) P_e, & SSSS, (b) P_e, & CCCC, (c) P_c, & SSSS, and (d) P_c, & CCCC.

Further, clamped boundary conditions have higher values of linear frequency and the lowest values of NLFR compared to simply supported boundary conditions. Furthermore, the linear frequency and NLFR increase with the Skempton coefficient for a given porosity volume index. It is because the arrangements of the porosities in the P_e facilitate the uniform distribution of materials across the thickness. In contrast, more materials are accumulated far away from the middle plane for P_c leading to high stiffness in the plate.

Furthermore, the geometrically nonlinear central deflection of the FGSPM plate influenced by different porosity volume index and porosity distributions is shown in Figure 7.5. For all porosity distributions, it can be seen that deflections rise as the porosity volume index (e_p) increases. Meanwhile, the porosity distribution P_c exhibits the slightest deviation compared to the porosity distribution P_e with the variation of the Skempton coefficient. Besides, P_e has a clear difference between the porosity volume

index. Also, the deflection rate for P_e type porosity distributions is much higher than for P_c at a given porosity volume index. It could be because more material accretion away from the central region increases the FGSPM plate's flexural stiffness for porosity distributions of type P_c.

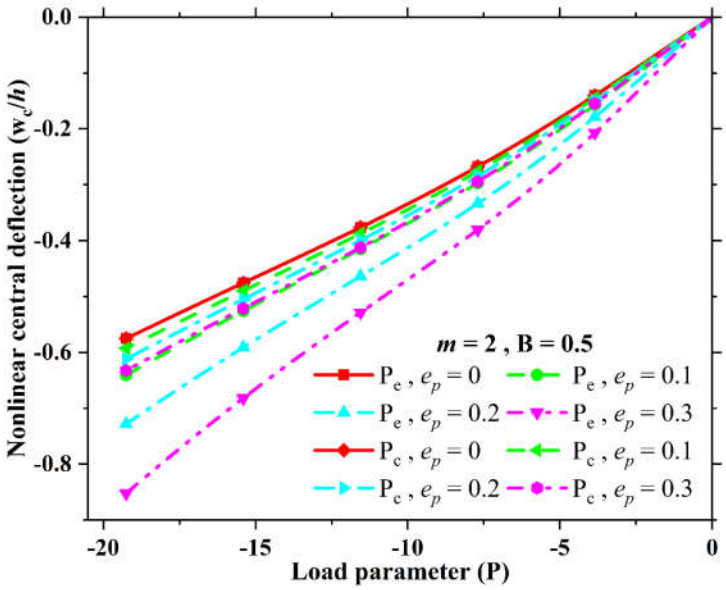

Figure 7.5: Influence of porosity volume index on the central deflection (w_c/h) of Si_3N_4/SUS304 FGSPM square plate for different porosity distributions. (a/h =10, B = 0.5, m = 2, & SSSS).

7.3.4. Effect of thickness and aspect ratios

The FGSPM plate's NLFR and linear frequency for numerous thickness ratios and boundary conditions are tabulated in Table 7.5. It can be observed that when the thickness ratio is increased for a given porosity distribution, the NLFR and linear frequency values reduce. The reason for this is that smaller thickness ratios result in increased rigidity. Additionally, for a given porosity distribution and boundary condition, no substantial difference can be found for thinner plates with an increase in the Skempton coefficient. As a result, the influence of pore fluid pressure is insignificant for thinner plates.

Further, in the case of thin plates, the aspect ratio could be considered a crucial parameter in the plate's geometry. The geometrical instability rises as the structural parts become thinner, affecting the plate's dynamic behavior. Table 7.6 considers the consequences of aspect ratios on the NLFR and linear frequency of the FGSPM plate.

The NLFR of FGSPM plates decreases and then increases as the aspect ratio increases. On the other hand, the linear frequency responses diminish for a given porosity distribution and boundary condition. It is because of material redistribution in the presence of porosities and a loss in plate stiffness as the area grows.

Table 7.5: Influence of thickness ratio on the NLFR (ω_{NL}/ω) of Si_3N_4/SUS304 FGSPM plate for different Skempton coefficient (B). ($a/b = 1$, $m = 2$, $W_{max}/h = 1.0$, $e_p = 0.1$).

P_d	a/h	Skempton coefficient (B)							
		0.0		0.25		0.50		1.00	
		NLFR	ω	NLFR	ω	NLFR	ω	NLFR	ω
P_e	SSSS								
	8	1.4750	0.0473	1.4820	0.0483	1.4905	0.0492	1.4994	0.0510
	10	1.4597	0.0309	1.4657	0.0315	1.4712	0.0321	1.4805	0.0333
	20	1.4396	0.0079	1.4444	0.0081	1.4486	0.0083	1.4554	0.0086
	50	1.4341	0.0013	1.4385	0.0013	1.4422	0.0013	1.4485	0.0014
	CCCC								
	8	1.2483	0.0763	1.2527	0.0775	1.2568	0.0787	1.2643	0.0809
	10	1.2340	0.0515	1.2373	0.0524	1.2403	0.0533	1.2455	0.0550
	20	1.2179	0.0140	1.2198	0.0143	1.2215	0.0146	1.2241	0.0151
	50	1.2141	0.0023	1.2158	0.0024	1.2171	0.0024	1.2191	0.0025
P_c	SSSS								
	8	1.4710	0.0482	1.4779	0.0491	1.8907	0.0501	1.4955	0.0519
	10	1.4554	0.0314	1.4614	0.0321	1.4478	0.0327	1.4762	0.0340
	20	1.4348	0.0081	1.4395	0.0083	1.4436	0.0084	1.4505	0.0088
	50	1.4291	0.0013	1.4335	0.0013	1.4372	0.0014	1.4434	0.0014
	CCCC								
	8	1.2439	0.0775	1.2484	0.0787	1.2525	0.0799	1.2601	0.0821
	10	1.2293	0.0524	1.2325	0.0533	1.2355	0.0542	1.2408	0.0559
	20	1.2126	0.0143	1.2145	0.0146	1.2161	0.0149	1.2187	0.0154
	50	1.2088	0.0024	1.2103	0.0024	1.2116	0.0025	1.2136	0.0026

Table 7.6: Influence of aspect ratio on the NLFR (ω_{NL}/ω) of Si_3N_4/SUS304 FGSPM plate for different Skempton coefficient (B). (a/h = 10, m = 2, W_{max}/h = 1.0, e_p = 0.1).

P_d	b/a	Skempton coefficient (B)							
		0.0		0.25		0.50		1.00	
		NLFR	ω	NLFR	ω	NLFR	ω	NLFR	ω
P_e	SSSS								
	0.75	1.4938	0.0423	1.4997	0.0432	1.5051	0.0440	1.5145	0.0456
	1.00	1.4597	0.0309	1.4657	0.0315	1.4712	0.0321	1.4805	0.0333
	1.25	1.4689	0.0255	1.4742	0.0260	1.4790	0.0265	1.4869	0.0275
	1.50	1.4960	0.0225	1.5002	0.0230	1.5038	0.0235	1.5099	0.0244
	CCCC								
	0.75	1.2485	0.0699	1.2523	0.0711	1.2559	0.0722	1.2624	0.0742
	1.00	1.2340	0.0515	1.2373	0.0524	1.2403	0.0533	1.2455	0.0550
	1.25	1.2322	0.0435	1.2349	0.0443	1.2374	0.0450	1.2417	0.0465
	1.50	1.2346	0.0395	1.2369	0.0403	1.2390	0.0410	1.2425	0.0423
P_c	SSSS								
	0.75	1.4894	0.0431	1.4953	0.0440	1.5007	0.0448	1.5102	0.0464
	1.00	1.4554	0.0314	1.4614	0.0321	1.4478	0.0327	1.4762	0.0340
	1.25	1.4643	0.0259	1.4695	0.0265	1.4742	0.0270	1.4823	0.0281
	1.50	1.4910	0.0229	1.4951	0.0234	1.4988	0.0239	1.5049	0.0248
	CCCC								
	0.75	1.2439	0.0710	1.2478	0.0722	1.2514	0.0732	1.2580	0.0753
	1.00	1.2293	0.0524	1.2325	0.0533	1.2355	0.0542	1.2408	0.0559
	1.25	1.2272	0.0442	1.2300	0.0450	1.2325	0.0458	1.2368	0.0473
	1.50	1.2295	0.0402	1.2318	0.0410	1.2338	0.0417	1.2374	0.0431

Besides, for both thickness and aspect ratios, the linear frequency and NLFR increase with the Skempton coefficient. This trend is observed irrespective of aspect ratio, boundary conditions, and porosity distributions. However, centrally distributed porosities and clamped boundary conditions have higher linear frequency values,

whereas evenly distributed porosities and simply supported boundary conditions have greater values for NLFR.

7.3.5. Effect of different support conditions

Figure 7.6 exhibits the support condition's influence on the nonlinear central deflection of the FGSPM plate for a given Skempton coefficient, VFGI, and porosity volume index. It can be deduced that the nonlinear deformations of the P_c have smaller values than the P_e for a given boundary condition. The configuration of the porosities in the P_e may enable uniform material distribution across the thickness simpler, resulting in maximum deformation. On the other hand, P_c accumulates more materials much away from the central plane, resulting in a plate with high rigidity. Clamped edges have lower deflections, while SSSS has the maximum deflection and follows the SSSS > SCSC > CCCC trend. It is commonly known that as boundary restrictions are clamped, the structure becomes stiffer.

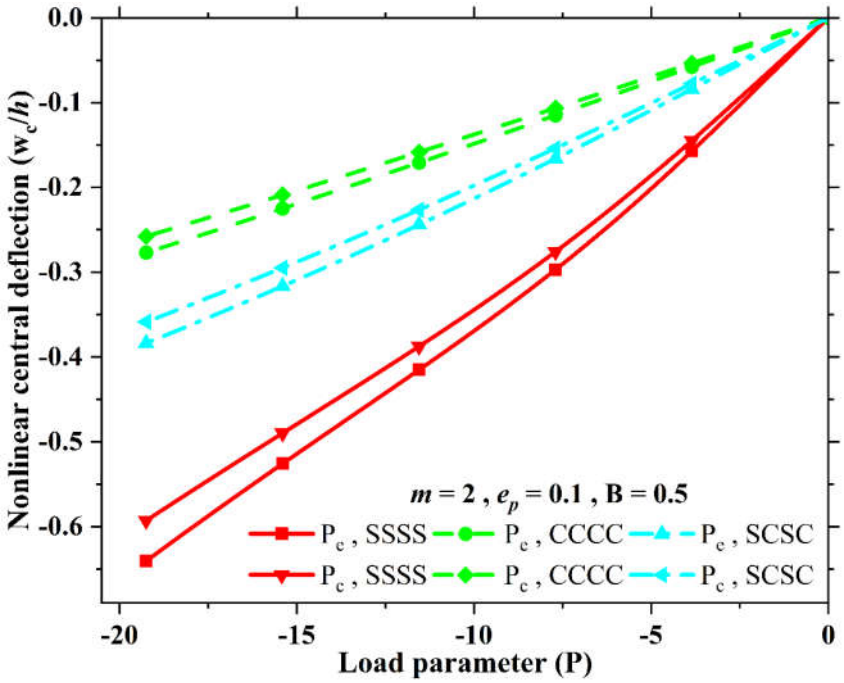

Figure 7.6: Influence of Skempton coefficient (B) on the central deflection (w_c/h) of Si_3N_4/SUS304 FGSPM square plate for various boundary conditions. (a/h =10, B = 0.5, e_p = 0.1, & m = 2).

7.4. CONCLUSIONS

The present work uses Biot's theory to investigate the FGSPM plate's linear frequency, nonlinear frequency, and nonlinear deformations by considering the fluid pore pressure. The modified power-law series is utilized to vary the material compositions for different porosity distributions to extract the effective material properties of the fluid-saturated porous plate along the thickness direction. A nonlinear FE formulation is developed based on the IFSDT and von Karman's geometric nonlinearities. The direct iterative method is used to extract the solutions.

The numerous exciting findings observed in the numerical studies can draw the following conclusions. The effect of solid-fluid interactions significantly influences the linear and nonlinear frequencies and nonlinear deformation compared to the fluid-free FG porous plate by varying fluid compressibility within the pores. For all the case studies carried out for the FGSPM plate for various boundary conditions, it has been discovered that the FGSPM plates under undrained conditions have greater linear frequency, NLFR, and lower deflections. The evenly distributed porosities are significantly more affected by pore fluid pressure than the centrally distributed porosities. For increased porosity volume index under simply supported and clamped boundary conditions, the Skempton coefficient significantly impacts the NLFR of FGSPM plates. Parametric studies on thickness ratio indicate that saturated fluid's effect on thinner plates has less significance, while the aspect ratio has been significantly affected by the saturated fluid. For various boundary conditions, the nonlinear deflections in relation to the Skempton coefficient follow the pattern SSSS > SCSC > CCCC.

CHAPTER 8

SUPERSONIC FLUTTER CHARACTERISTICS OF FUNCTIONALLY GRADED SATURATED POROUS PLATES UNDER THERMAL LOADING

This chapter investigates the aero-thermo-poroelastic supersonic flutter characteristics of the geometrically nonlinear functionally graded saturated porous material (FGSPM) plates subjected to yawed flow angles. The nonlinear finite element formulation and constitutive equations established in chapters 4 and 7 are extended for the present analysis. In addition, the supersonic piston theory considering the yawed flow angle effects is used to model the FGSPM plate. The emphasis is placed on understanding the effects of numerous parameters such as aerodynamic pressure, yawed airflow angle, Skempton coefficient, temperature gradients, porosity volume index, saturated porosity distributions, volume fraction grading index, and boundary conditions during the extensive numerical analyses on the nonlinear flutter bounds of the FGSPM plate. It is evident from the investigation that saturated fluid in the pores of the FGSPM plate substantially impacts the flutter bounds than the plates in drained conditions.

8.1. INTRODUCTION

Flutter is a type of dynamic instability that occurs while aircraft are in flight. It is the self-excited oscillation of the outer skin of an aircraft when subjected to supersonic airflow along its surface. In addition, aerodynamic heating can lead to dynamic instability such as flutter in high-speed flight vehicles because of the significant temperature rise on the external skin. Panel flutter occurs when two eigenmodes of a structure merge at a critical aerodynamic pressure due to aerodynamic pressure acting on the panel, causing dynamic instability. Thus, above a critical pressure, the panel's motion becomes unstable and increases exponentially over time.

A common solution to the flutter issue is to stiffen the panels in danger of fluttering, a process that typically adds weight to the design (Ibrahim et al. 2007a; Marzocca et al. 2011). Therefore, thin plates made of functionally graded materials (FGM) are a common structural component due to their enhanced strength, particularly in aerospace vehicles such as high-speed airplanes, rockets, and spacecraft subject to thermal loads owing to aerodynamic or solar radiation heating. This results in a temperature distribution over the surface and a thermal gradient through the thickness of the plate. The presence of these thermal fields results in a flutter motion at a lower dynamic pressure or a larger limit-cycle amplitude at the same dynamic pressure.

Additionally, it is inevitable to produce flawless FGM devoid of the entrapment of saturated fluid pores using contemporary production procedures (Alhaifi et al. 2021). However, saturated fluids in the FGM pores increase the structure's stiffness (Detournay and Cheng 1993). Consequently, it is essential to investigate the flutter behavior of functionally graded saturated porous materials (FGSPM) structures consisting of fluid-filled pores and solid material as a skeletal part.

The main objective of this chapter is to investigate the geometrically nonlinear flutter characteristics of the supersonic FGSPM plates subjected to thermal loading. The investigation considers the aero-thermo-poroelastic analysis of the FGSPM plate in which pores are filled with saturated fluid, saturated porosity distributions, and yawed flow angle at supersonic speed. The poroelastic behavior of the FGSPM plate is modeled using the Biot theory, which considers the fluid pore pressure. In addition, the FGSPM plate's temperature-dependent effective material properties vary smoothly as an arbitrary function of the volume fractions in transverse directions, conferring a modified power-law series. The governing equations are developed and solved using the IFSDT, nonlinear finite element method, supersonic piston theory, von Karman's assumptions, Hamilton principle, and the direct iterative technique. Geometrically nonlinear frequencies and aerodynamic pressure of the FGSPM plate in undrained conditions for different porosity distributions and various geometrical parameters are evaluated in detail.

8.2. PROBLEM DESCRIPTION AND GOVERNING EQUATION

The geometrical parameters of the FGSPM plate considered in the present analysis are identical to the plate studied in the previous chapter, as shown in Figure 7.1. Section 4.2 of Chapter 4 contains the displacement equations, the nonlinear strain-displacement relations, and a nonlinear FE formulation. The same formulation has been used for the present chapter. Further, the temperature-dependent material properties by considering different porosity distributions presented in section 4.2.1 of chapter 4 have also been implemented for the present analysis. However, the constitutive equations have been derived by incorporating the temperature and saturated pore fluid pressure in the following sections. Besides, the aerodynamic loading acting on the surface of the supersonic FGSPM plate has been derived using the first-order piston theory, as explained in the subsequent section.

8.2.1. Constitutive relations

The thermo-poroelastic behavior of the FGSPM plate is modeled using poroelastic constitutive equations, i.e., linear poroelasticity theory. As a result, the stress-strain relationship is as follows (Babaei et al. 2020b; Detournay and Cheng 1993):

$$\sigma_{ij} = 2G\left(z,T\right)\varepsilon_{ii} + \frac{2G\left(z,T\right)\vartheta_u}{1-2\vartheta_u}\varepsilon_{kk}\delta_{ij} - \alpha_s\, p\delta_{ij} \tag{8.1}$$

where $p = M\left(\xi - \alpha_s\,\varepsilon_{kk}\right)$; $M = \dfrac{2G\left(z,T\right)\left(\vartheta_u - \vartheta\right)}{\alpha_s^2\left(1-2\vartheta_u\right)\left(1-2\vartheta\right)}$; $\vartheta_u = \dfrac{\vartheta + \dfrac{\alpha_s B\left(1-2\vartheta\right)}{3}}{1-\dfrac{\alpha_s B\left(1-2\vartheta\right)}{3}}$ (8.2)

where *G(z, T)* stands for position and temperature-dependent shear modulus;

By condensing Eq. (8.1) to the plane-stress condition in cartesian coordinates and under the undrained condition, the following equations emerge as ($\xi = 0$) (Jabbari et al. 2014b).

$$\left\{\sigma_b\right\} = \begin{Bmatrix}\sigma_{xx}\\ \sigma_{yy}\\ \sigma_{xy}\end{Bmatrix} = \left[Q_{ij}\left(z,T\right)\right]\left(\begin{Bmatrix}\varepsilon_{xx}\\ \varepsilon_{yy}\\ \varepsilon_{xy}\end{Bmatrix} - \begin{Bmatrix}\alpha_{xx}\left(z,T\right)\\ \alpha_{yy}\left(z,T\right)\\ 0\end{Bmatrix}\Delta T\right);$$

$$\{\sigma_s\}=\begin{Bmatrix}\tau_{yz}\\ \tau_{xz}\end{Bmatrix}=\left[Q_{s(ij)}(z,T)\right]\begin{Bmatrix}\gamma_{yz}\\ \gamma_{xz}\end{Bmatrix} \tag{8.3}$$

where ΔT is the rise in temperature over the reference temperature, i.e., $\Delta \mathrm{T}=\mathrm{T}(z)-\mathrm{T}_0$. In which T($z$) is the temperature for any point in the FGSPM plate across the thickness, T_0 is the reference temperature.

$$Q_{ij}(z,T)=G(z,T)\begin{bmatrix}Q_1 & Q_2 & 0\\ Q_2 & Q_1 & 0\\ 0 & 0 & 1\end{bmatrix},\quad Q_{s(ij)}(z,T)=G(z,T)\begin{bmatrix}1 & 0\\ 0 & 1\end{bmatrix} \tag{8.4}$$

$$Q_1=\left(\frac{2}{1-\vartheta_u^2}\right)\left[1+\vartheta_u+\frac{(\vartheta_u-\vartheta)(1+\vartheta_u)}{(1-2\vartheta)}\left(1-\frac{C_2}{C_1}\right)\right] \tag{8.5}$$

$$Q_2=\left(\frac{2}{1-\vartheta_u^2}\right)\left[(1+\vartheta_u)\vartheta_u+\frac{(\vartheta_u-\vartheta)(1+\vartheta_u)}{(1-2\vartheta)}\left(1-\frac{C_2}{C_1}\right)\right] \tag{8.6}$$

$$C_1=2\left[1+\frac{\vartheta_u}{(1-2\vartheta_u)}+\frac{(\vartheta_u-\vartheta)}{(1-2\vartheta_u)(1-2\vartheta)}\right]G(z,T)\ ;\ C_2=C_1-2G(z,T) \tag{8.7}$$

8.2.2. Aerodynamic loading using first-order piston theory

The aerodynamic pressure load with yawed flow angle is developed based on the first-order piston theory (Dowell 1966, 1970) for supersonic FG porous plate can be expressed as (Prakash and Ganapathi 2006; Zhou et al. 2018)

$$\Delta P=-\frac{\rho_\infty U_\infty^2}{\sqrt{M_\infty^2-1}}\left(\frac{\partial w_1(x,y,t)}{\partial x}\cos\theta+\frac{\partial w_1(x,y,t)}{\partial x}\sin\theta+\left(\frac{M_\infty^2-2}{M_\infty^2-1}\right)\left(\frac{1}{U_\infty}\right)\frac{\partial w_1(x,y,t)}{\partial t}\right) \tag{8.9}$$

where U_∞, M_∞, and ρ_∞ signifies the free stream airflow velocity, Mach number, and density, respectively.

For the supersonic FGSPM plates with $M_\infty >> 1$, the following approximate equation can be written as follows (Zhou et al. 2018):

$$\left[\left(M_\infty^2-2\right)\Big/\left(M_\infty^2-1\right)\right]\mu\Big/\sqrt{M_\infty^2-1}\rightarrow\frac{\mu}{M_\infty} \tag{8.10}$$

8.2.3. The total potential energy principle

Using the total energy of the FGSPM plate, the following governing equations of motion are derived (Kattimani and Ray 2014):

$$\delta T_p = \int_0^a \int_0^b \left[\frac{1}{2} \int_{-h/2}^{h/2} \begin{pmatrix} \delta\{\varepsilon_b\}^T \{\sigma_b\} + \delta\{\varepsilon_s\}^T \{\sigma_s\} + \delta\{d_t\}^T \rho\left\{\ddot{d}_t\right\} \\ -\delta\{d_t\}^T \{\Delta p w\} \end{pmatrix} dz \right] dx\,dy = 0 \tag{8.11}$$

where Δp denotes the aerodynamic pressure loading.

The FGSPM plate's elementary equations of motion can be expressed by applying Hamilton's principle, i.e. $\delta T_p^{\,e} = 0$, followed by unifying and simplifying the terms based on the stiffness matrices and degrees of freedom:

$$\begin{gathered} \left[M^e\right]\left\{\ddot{d}_t^e\right\} + \left(\left[K_{tb}^e - K_{Temp-tt}^e\right] + \lambda\left[\overline{A}_{fe}\right]\right)\left\{d_t^e\right\} + \left[K_{tr}^e\right]\left\{d_r^e\right\} = \left\{F_t^e\right\} \\ \left[K_{rt}^e\right]\left\{d_t^e\right\} + \left[K_{rr}^e\right]\left\{d_t^e\right\} = 0 \end{gathered} \tag{8.12}$$

in which,

$$\left[K_{tt}^e\right] = \left[K_{tb}^e\right] + \left[K_{ts}^e\right] + \left[K_{tbNL}^e\right];\ \left[K_{tr}^e\right] = \left[K_{trb}^e\right] + \left[K_{trbNL}^e\right] + \left[K_{trs}^e\right];$$

$$\left[K_{rt}^e\right] = \left[K_{trb}^e\right]^T + \frac{1}{2}\left[K_{trbNL}^e\right]^T + \left[K_{trs}^e\right]^T;\ \left[K_{rr}^e\right] = \left[K_{rrb}^e\right] + \left[K_{rrs}^e\right];$$

$$\left[K_{Temp-tt}^e\right] = \left[K_{Temp-tb}^e\right] + \left[K_{Temp-ts}^e\right] \text{ and } \left\{\mathrm{F}_t^e\right\} = \int_0^a \int_0^b \left[N_t\right]^T \{f\}\, dx\, dy \tag{8.13}$$

where $\left[M^e\right]$ is the elemental mass matrix; $\left[K_{tt}^e\right]$, $\left[K_{tr}^e\right]$, $\left[K_{rt}^e\right]$ and $\left[K_{rr}^e\right]$ are the elemental stiffness matrices; $\left[K_{Temp-tt}^e\right]$ is the elemental stiffness matrices under thermal loading; $\left\{\mathrm{F}_t^e\right\}$ is the elemental mechanical load vector. The various elemental stiffness, rigidity matrices, and vectors used in Eq. (8.12) and (8.13) are derived in Appendix - II.

Finally, Eq. (8.12) is condensed to provide a more simplified form of global equations of equilibrium for the FGSPM plate:

$$\left[M\right]\left\{\ddot{X}_t\right\} + \left(\left[K_{eq}^L + K_{eq}^{NL}\right] - K_{eq}^G + \lambda\left[\overline{A}\right]\right)\left\{X_t\right\} = \left\{\mathrm{F}_{eq}\right\} \tag{8.14a}$$

$$\left[M\right]\left\{\ddot{X}_t\right\} + \left[\overline{K_{eq}}\right]\left\{X_t\right\} = \left\{\mathrm{F}_{eq}\right\} \tag{8.14b}$$

in which,

$$\left[\overline{K_{eq}}\right]=\left(\left[K_{tt}-K_{Temp-tt}\right]+\lambda\left[\overline{A}_f\right]\right)-\left[K_{tr}\right]\left[K_{rr}\right]^{-1}\left[K_{rt}\right] \tag{8.15}$$

where $\left[K_{eq}^{L}+K_{eq}^{NL}\right]$ is a set of linear and nonlinear stiffness matrices known as generalized equivalent stiffness matrices and $\left\{\mathrm{F}_{eq}\right\}$ is the force vector.

Furthermore, the governing differential Eq. (8.14) is solved using the direct iterative technique (Bergan and Clough 1972) to produce flutter bounds for the FGSPM plate (Prakash and Ganapathi 2006; Zhou et al. 2018).

8.3. RESULTS AND DISCUSSIONS

The proposed model is used to validate the accuracy and reliability by considering several numerical examples of nonlinear vibration and flutter bounds. Then, the nonlinear finite element solutions are obtained in this section to demonstrate the nonlinear frequency responses and critical aerodynamic pressure loads for different temperature gradients and yawed flow angles influenced by various significant parameters. Special emphasis is recorded on saturated porosity distributions on the critical aerodynamic loads with yawed flow angles of the FGSPM plate under various temperature gradients. The results are derived using non-dimensionalized nonlinear frequency parameters. The following are the non-dimensionalized quantities considered:

Non-dimensionalized nonlinear frequency $\omega_{NL}=\overline{\omega_{NL}}\,a^2\sqrt{\left(\rho_{m0}\,h/D_{m0}\right)}$ (8.16)

in which, $D_{m0}=\left(E_{m0}\,h^3\Big/12\left(1-\upsilon_{m0}^2\right)\right)$

where E_{m0}, ρ_{m0}, and υ_{m0} are the modulus of elasticity, density, and Poisson's ratio of the metallic constituent material (Si_3N_4), respectively, at the reference temperature (T_0).

Further, the temperature-dependent material parameters of the Si_3N_4 / SUS304 FGSPM plate considered for analysis are listed in section 4.3 and Table 4.1.

8.3.1. Convergence and comparison study

The robustness of the proposed nonlinear finite element model enables the parametric analyses to be carried out by validating and comparing obtained results with solutions available in the open literature.

Table 8.1: Comparison of the flutter bounds of the square FG plate with different temperature gradients.

m	Sources	ω_1	ω_2	ω_{cr}	λ_{cr}
T_c = 300 K, *h* = 0.05					
0	Present [2 × 2]	46.6896	205.11	-	-
	Present [4 × 4]	45.2038	110.9326	-	-
	Present [6 × 6]	45.2288	111.4524	-	-
	Present [8 × 8]	45.2366	111.5802	98.2621	776
	Prakash et al. (2006)	45.258	112.009	98.292	775.78
	Zhou et al. (2018)	45.246	111.697	98.148	775.63
0.5	Present [8 × 8]	31.234	76.8942	67.6584	667
	Prakash et al. (2006)	31.244	77.152	67.639	666.01
	Zhou et al. (2018)	31.229	76.931	67.535	665.73
Tc = 600 K, h = 0.05					
1	Present [8 × 8]	18.2765	58.589	49.8206	493.64
	Prakash et al. (2006)	18.772	59.197	50.289	499.61
	Zhou et al. (2018)	18.326	58.734	49.892	495.27
2.5	Present [8 × 8]	14.7491	50.2064	42.4959	451.68
	Prakash et al. (2006)	15.286	50.846	43.004	458.59
	Zhou et al. (2018)	14.815	50.413	42.628	454.22

Example 1: The aero-thermo-elastic flutter characteristics of the FG plate are carried out for the convergence and validation of the proposed model. The geometrical and material parameters are identical to the reference literature (Prakash and Ganapathi 2006; Zhou et al. 2018). Further, to compare the current model's stability and effectiveness, various mesh sizes are explored for comparison, and the proposed model's responses converge at a mesh size of [8 × 8]. The validation is carried out for various VFGI and temperature gradients. It can be observed from Table 8.1 that the first two natural frequencies, critical frequency and critical aerodynamic pressure load at the point of coalescence of the proposed model, present an excellent agreement with the reference literature (Prakash and Ganapathi 2006; Zhou et al. 2018).

Example 2: The critical aerodynamic pressure of the simply supported FG porous plate for different porosity distributions and porosity volume index subjected to various thermal loads has been validated with the reference literature (Zhou et al. 2018). It can be found from Tables 8.2 & 8.4 that the obtained results from the proposed model agree very well with the reference (Zhou et al. 2018) for various porosity distributions, temperature rise, and VFGI.

Table 8.2: A comparison of the critical aerodynamic pressure of the simply supported square FG plate with different VFGI (m). (T_c = 300 K). [Ref: Zhou et al. (2018)].

Type	e_p	m= 0.2		m=1		m=5	
		λ_{cr}		λ_{cr}		λ_{cr}	
		Ref.	Present	Ref.	Present	Ref.	Present
	0	716.68	717.63	625.61	625.72	571	570.19
P_e	0.2	572.25	573.16	481.5	481.45	429.16	428.28
	0.4	438.35	439.03	345.8	345.35	295.35	294.12
	0	716.68	717.63	625.61	625.72	571	570.19
P_c	0.2	678.58	679.41	587.31	587.02	533.67	532.19
	0.4	641.53	642.25	549.82	548.99	497.1	494.63

Table 8.3: Comparison of the critical aerodynamic pressure of the square FG plate with different porosity distributions. (m = 1). [Ref: Zhou et al. (2018)].

Type	e_p	Tc = 300K		Tc = 450K		Tc = 600K	
		λ_{cr}		λ_{cr}		λ_{cr}	
		Ref.	Present	Ref.	Present	Ref.	Present
	0	625.61	625.72	561.86	561.13	495.27	493.64
P_e	0.2	481.5	481.45	443.6	442.69	404.24	402.38
	0.4	345.8	345.35	326.15	324.93	306.17	304.07
	0	625.61	625.72	561.86	561.13	495.27	493.64
P_c	0.2	587.31	587.02	536.86	535.52	483.23	481.51
	0.4	549.82	548.99	509.47	508.09	467	465.06

Further, validation studies are presented in sections 4.3.1 (except Examples 3 and 6) and 7.3.1 of Chapters 4 and 7, respectively. The same has been utilized for the present analysis also.

The examples above reveal that the proposed model is reliable, accurate, and efficient in investigating the nonlinear vibration and flutter behavior of the FGSPM plate in a thermal environment.

8.3.2. Effect of VFGI with different temperature gradients

The VFGI (m) is a crucial parameter for establishing the properties of the FGSPM plate, which determines the stiffness of a material. The fluctuations of the critical aerodynamic pressure (λ_{cr}) for various amplitude ratios (W_{max}/h) of the simply supported FGSPM plate with varying VFGI and temperature gradients are shown in Figure 8.1. The analysis is carried out for the perfect FG plate, i.e., e_p = B = 0. It can be observed from Figure 8.1 that the critical aerodynamic pressure increases with an increase in the amplitude ratio. It indicates that the hardening behavior of the FG plate increases with an increase in the amplitude ratio, leading to an increase in stiffness. Besides, the critical aerodynamic pressure decreases with an increase in temperature gradient and VFGI for a given amplitude ratio. This is because a drop in ceramic content with an increase in the VFGI decreases the plate's rigidity. In addition, the stiffness of the plate decreases with an increase in the temperature gradient.

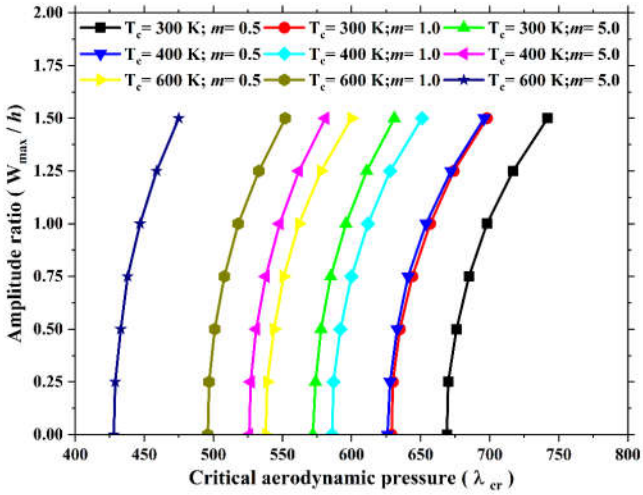

Figure 8.1: The variations of the λ_{cr} for various amplitude ratios (W_{max}/h) of the simply supported FGSPM plate having different VFGI and temperature gradients (a/b = 1, a/h = 20, e_p = 0, and B = 0).

8.3.3. Effect of fluid-free porosity and its porosity distributions

The porosity volume index significantly affects the critical aerodynamic pressure of the FGSPM plate. An increase in the porosity volume index reduces the stiffness and

weight of the FGSPM plate. The variations of the critical aerodynamic pressure (λ_{cr}) for various amplitude ratios (W_{max}/h) of the simply supported square FGSPM plate with different thermal loads and porosity distributions are illustrated in Figure 8.2. The parameters considered for the analysis are $a/h = 20$, $m = 1$, and B = 0. It can be noticed from Figure 8.2 that the critical aerodynamic pressure decreases with an increase in porosity volume index for a given porosity distribution, amplitude ratio, and temperature gradient. It is because the stiffness of the FGSPM plate decreases as the porosity volume index rises. In addition, it can be observed that the centrally distributed porosities have higher values of critical aerodynamic pressure than the evenly distributed porosities ($P_c > P_e$) for a given porosity volume index and temperature gradient. It is because the stiffness depends on the distribution of the porosities across the thickness of the plate. Hence, the FGSPM plate with P_c has greater stiffness than the FGSPM plate with P_e.

Furthermore, the vehicle structures are subjected to various thermal loadings during the voyage to simulate the flight. The variations of the nonlinear frequencies for various porosity distributions of the simply supported square FGSPM plate having different thermal loads with aerodynamic pressure (λ) are illustrated in Figure 8.3. T_0 is the reference temperature (300 K) exerted on the bottom surface of the FGSPM plate. Besides, it is presumed that the top surface is exposed to three different ambient temperatures. The results show that the nonlinear frequencies and critical aerodynamic pressure (λ_{cr}) of the FGSPM plate drop significantly with the rise in porosity volume index and temperature regardless of the type of porosity distribution. It is simple to comprehend that a rise in temperature and porosity volume index reduces the structural rigidity of the FGSPM plate. In addition, evenly distributed porosities significantly impact the critical aerodynamic pressure more than centrally distributed porosities. This is because the distribution of porosities across the plate's thickness affects the stiffness of the FGSPM plate. However, P_c has greater values of λ_{cr} than P_e for a given porosity volume index and temperature gradient.

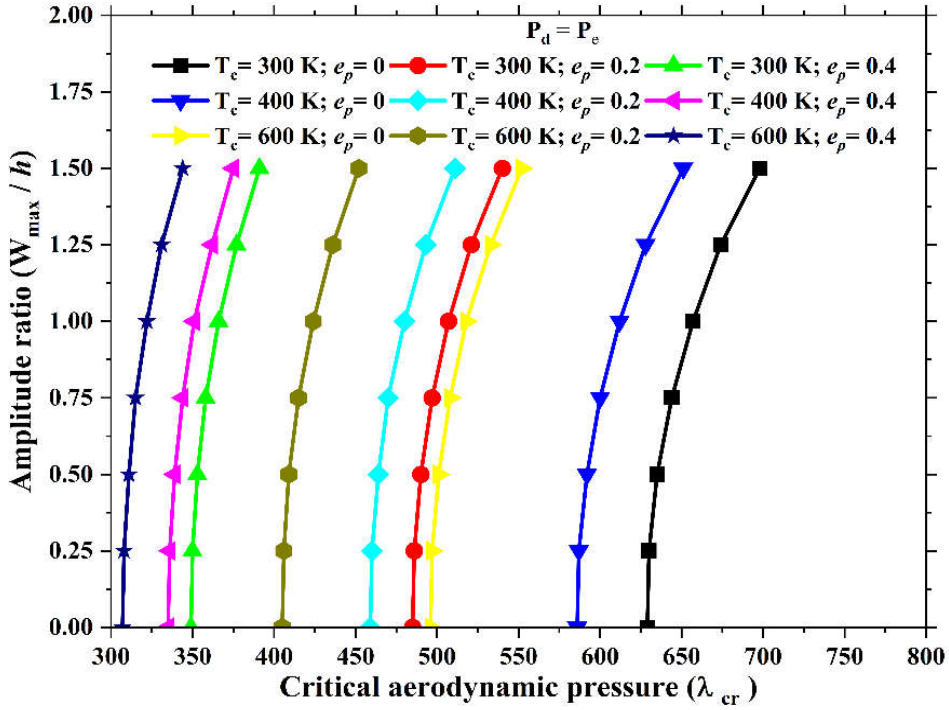

(a) P_e

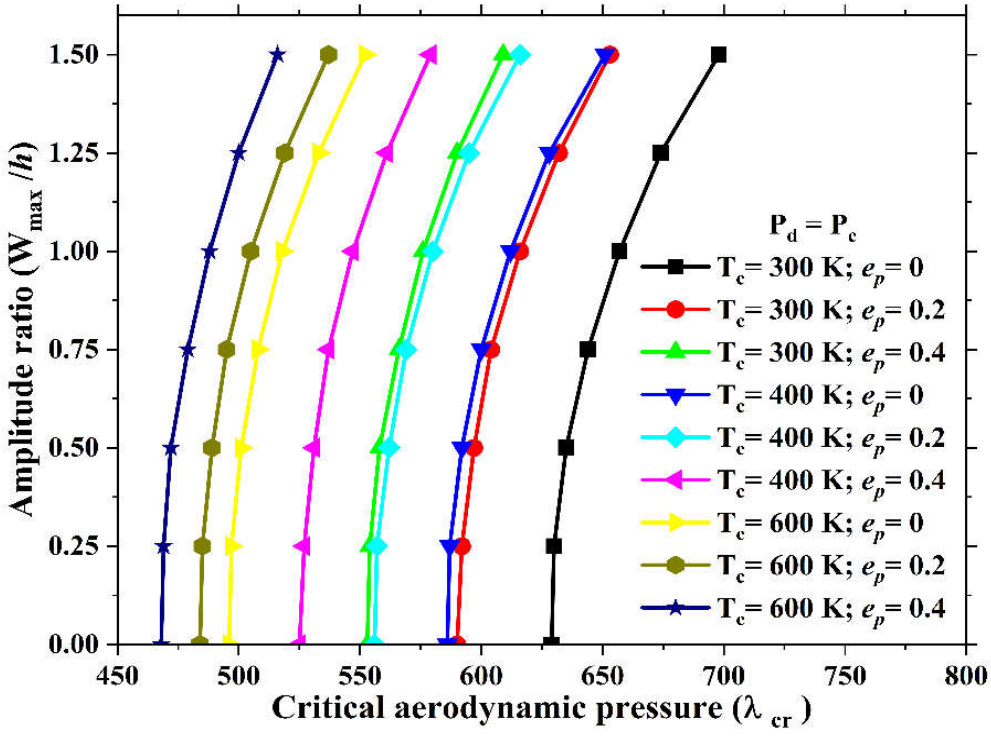

(b) P_c

Figure 8.2: The variations of the λ_{cr} for various amplitude ratios (W_{max}/h) of the simply supported square FGSPM plate with different thermal loads and porosity distributions (a/h = 20, m = 1, and B = 0). (a) P_e, and (b) P_c.

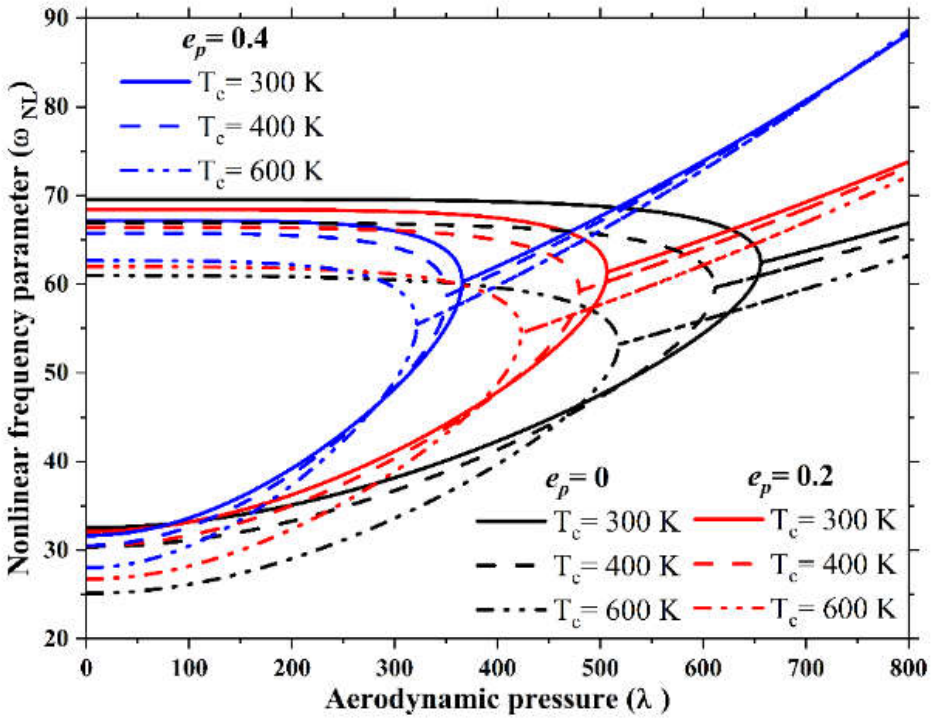

(a) P_e

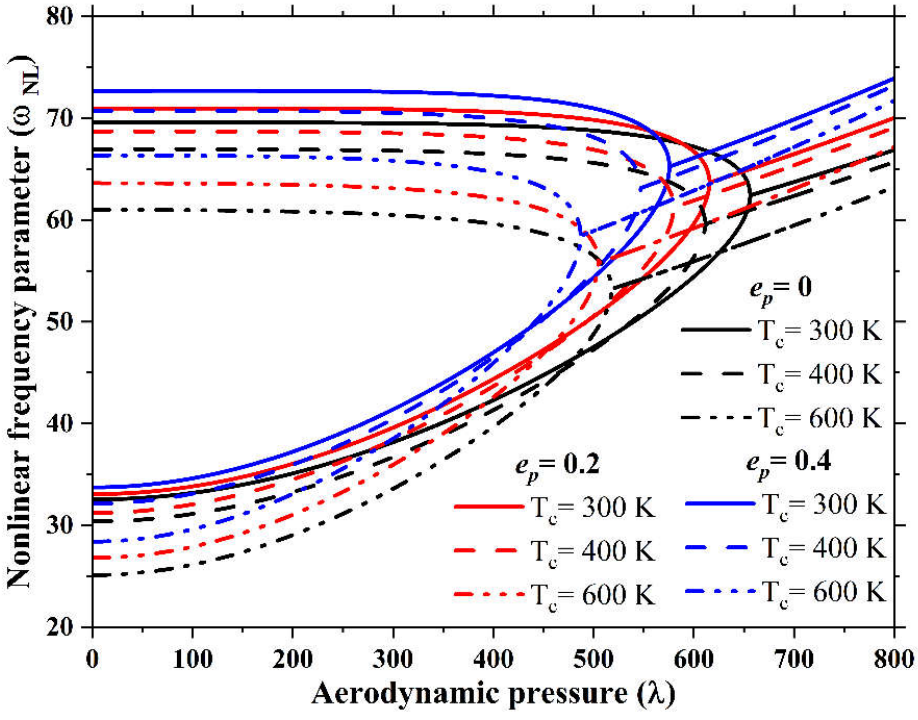

(b) P_c

Figure 8.3: The variations of the nonlinear frequencies for various porosity distributions of the simply supported square FGSPM plate having different thermal loads with aerodynamic pressure (λ) (a/h = 20, m = 1, W_{max}/h = 1, and B = 0). (a) P_e, and (b) P_c.

8.3.4. Effect of Skempton coefficient (saturated-fluid pressure)

The variations of the critical aerodynamic pressure (λ_{cr}) for various Skempton coefficients (B) of the simply supported square FGSPM plate with different saturated porosity distributions and thermal loads are depicted in Figure 8.4. It can be seen in Figure 8.4 that the critical aerodynamic pressure increases with an increase in the amplitude ratio for a given Skempton coefficient and temperature gradient. This trend indicates that the FGSPM plate's hardening response rises when the amplitude ratio grows in the presence of saturated fluids. Further, the critical aerodynamic pressure increases with an increase in the Skempton coefficient for a given amplitude ratio. It is because the rigidity of the FGSPM plate increases with pore fluid pressure (Skempton coefficient). Besides, the critical aerodynamic pressure decreases with the temperature rise irrespective of the Skempton coefficient and amplitude ratio. In addition, noticeable differences in λ_{cr} can be observed for both the types of porosity distributions ($P_c > P_e$) for a given Skempton coefficient and temperature gradient.

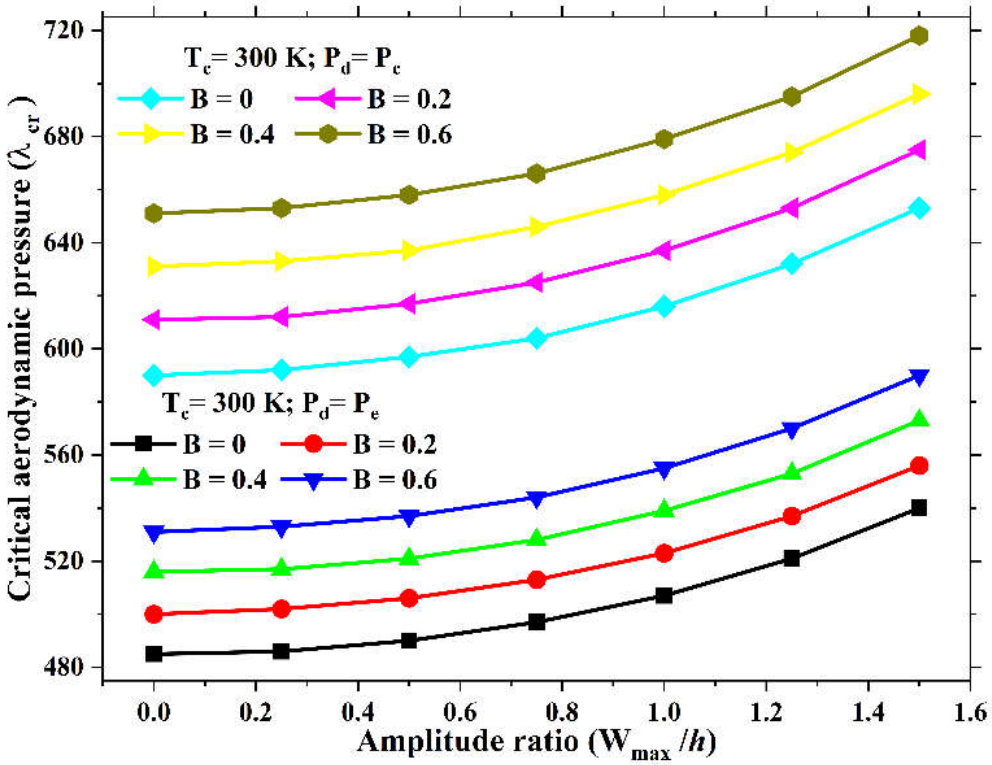

(a) T_c = 300 K

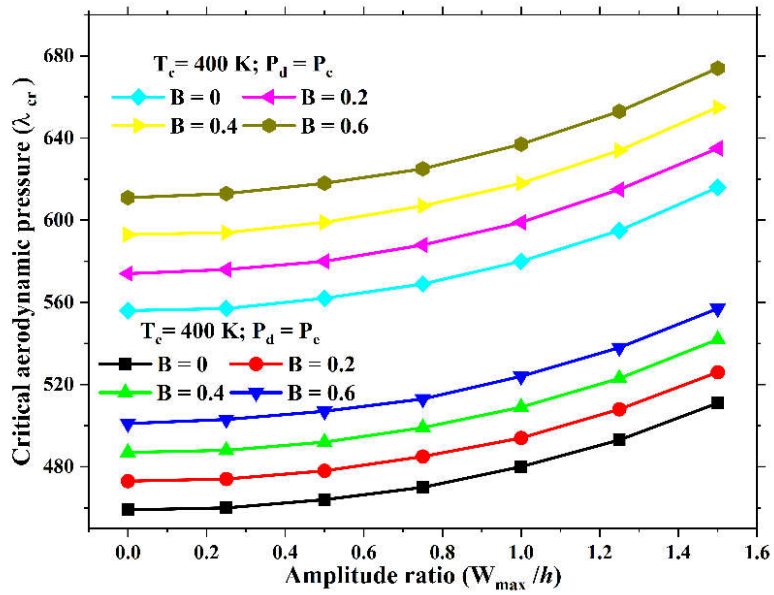

(b) T_c = 400 K

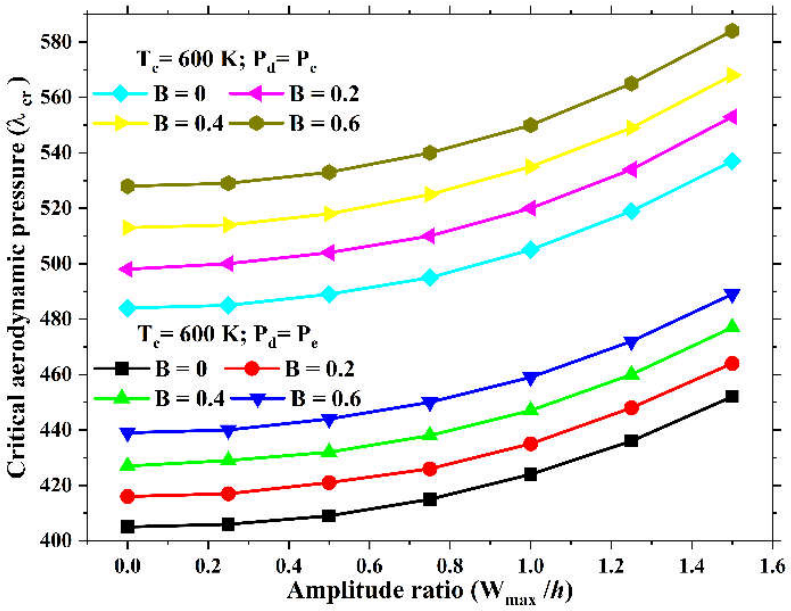

(c) T_c = 600 K

Figure 8.4: The variations of the λ_{cr} for various Skempton coefficients (B) of the simply supported square FGSPM plate with different porosity distributions and thermal loads (a/h = 20, m = 1, and e_p = 0.2). (a) T_c = 300 K , (b) T_c = 400 K, and (c) T_c = 600 K.

Further, the variations of the nonlinear frequencies for various Skempton coefficients (B) of the simply supported square FGSPM plate having different thermal loads and saturated porosity distributions with aerodynamic pressure (λ) are depicted in Figure 8.5. The results from Figure 8.5 show that the nonlinear frequency increases with the

Skempton coefficient for a given temperature gradient. The FGSPM plate exhibits the lowest nonlinear frequency and critical aerodynamic pressure load under a drained situation (no fluid; B = 0). It is due to the compressibility of the pores being high at this stage (no fluid in pores). Therefore, the behavior of the FGSPM plate replicates that of functionally graded porous plates without fluid when the compressibility of the fluid in pores is large (B = 0; drained state). In contrast, in undrained conditions, the compressibility of the fluid reduces with the Skempton coefficient. As a result, nonlinear frequencies and critical aerodynamic pressure increase. Moreover, in drained conditions, the FGSPM plate has the lowest stiffness; hence, the nonlinear frequencies and λ_{cr} are also at their lowest. In addition, the maximum critical nonlinear frequencies and λ_{cr} can be reached when the compressibility of the fluid in cavities (B > 0) is low. Consequently, the FGSPM plate behaves similarly to stiff plates.

Further, it can be observed from Figure 8.5 that the critical nonlinear frequencies and λ_{cr} decrease with an increase in the temperature gradient and porosity volume index for a given Skempton coefficient and porosity distribution. However, the evenly distributed porosities significantly impact the variation of critical nonlinear frequencies and λ_{cr} than the centrally distributed porosities ($P_e < P_c$) for a given Skempton coefficient, temperature gradient, and porosity volume index.

8.3.5. Effect of thickness ratio and aspect ratio

The effect of thickness ratio on the critical aerodynamic pressure for different Skempton coefficients (B) of simply supported FGSPM plates having different porosity distributions and thermal loads is presented in Figure 8.6. It is inferred from Figure 8.6 that the critical aerodynamic pressure reduces significantly as the thickness ratio increases from 10 to 20 for a given Skempton coefficient, porosity distribution, and temperature gradient. This is because the stiffness reduces as the plate transforms from a thick plate to a thin plate, which reduces the plate's stiffness. Further, the critical aerodynamic pressure decreases as the thickness ratio increases from 20 to 40. However, a noticeable difference is negligible. It indicates that the smaller thickness ratios result in increased rigidity.

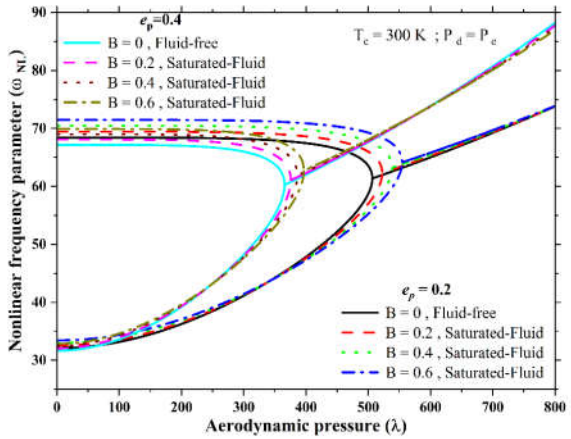

(a) P_e, and T_c = 300 K

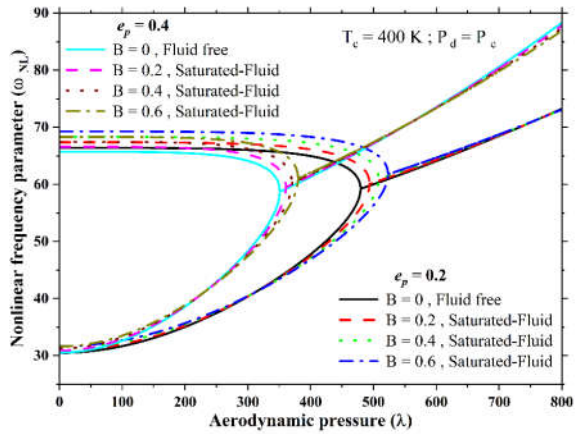

(b) P_e, and T_c = 400 K

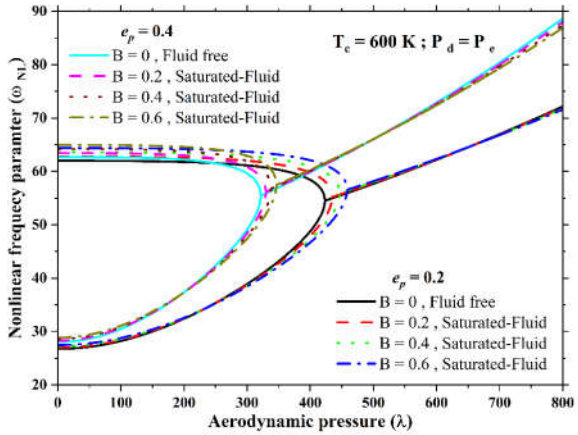

(c) P_e, and T_c = 600 K

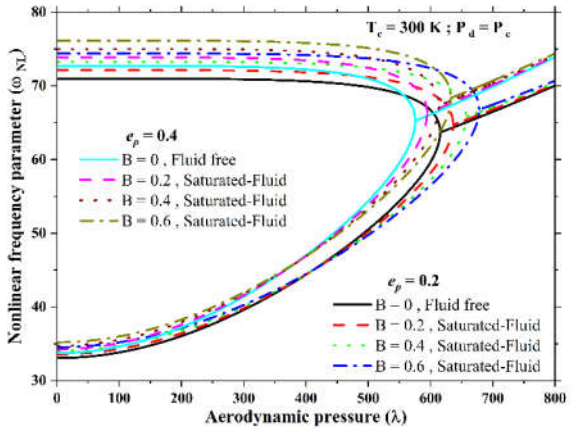

(d) P_c, and T_c = 300 K

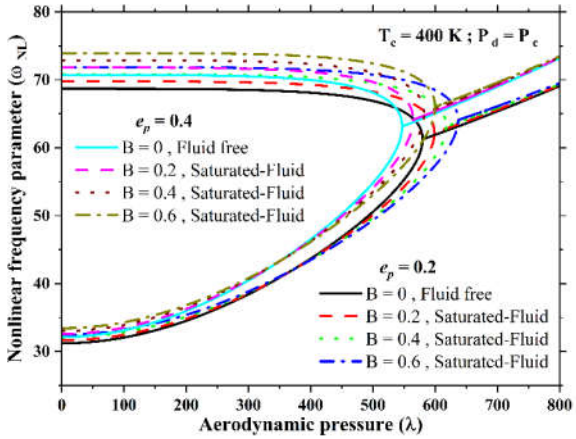

(e) P_c, and T_c = 400 K

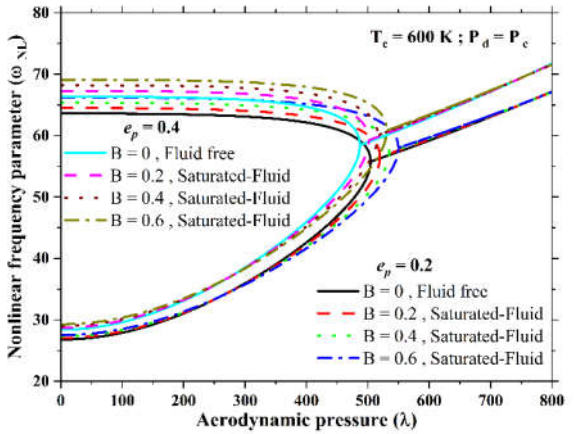

(f) P_c, and T_c = 600 K

Figure 8.5: The variations of the nonlinear frequencies for various Skempton coefficients (B) of the simply supported square FGSPM plate having different thermal loads and porosity distributions with aerodynamic pressure (λ) (a/h = 20, m = 1, and W_{max}/h = 1).

Additionally, it can be noticed that, for a given porosity distribution and temperature gradient, no substantial difference in the variation of λ_{cr} can be found for thinner plates with an increase in the Skempton coefficient and thickness ratio. As a result, the influence of pore fluid pressure is insignificant for thinner plates.

Moreover, in the case of thin plates, the aspect ratio could be regarded as a critical plate geometry element. The dynamic behavior of the plate is influenced by the increasing geometric instability as the structural components become thinner. The influence of aspect ratio on a thin rectangular plate (b/a = 0.5) with the shorter side aligned along the flow direction is presented in Figure 8.7. It may be concluded that the critical aerodynamic pressure is more significant for plates with b/a = 0.5 than for those with b/a = 1 or 2 for a given Skempton coefficient, porosity distribution, and temperature gradient.

Besides, the critical aerodynamic pressure increases with the Skempton coefficient for both thickness and aspect ratios. In contrast, λ_{cr} decreases as the temperature rises. This trend is observed for both types of porosity distribution. However, centrally distributed porosities have higher λ_{cr} values than evenly distributed porosities ($P_c > P_e$) for both thickness and aspect ratio.

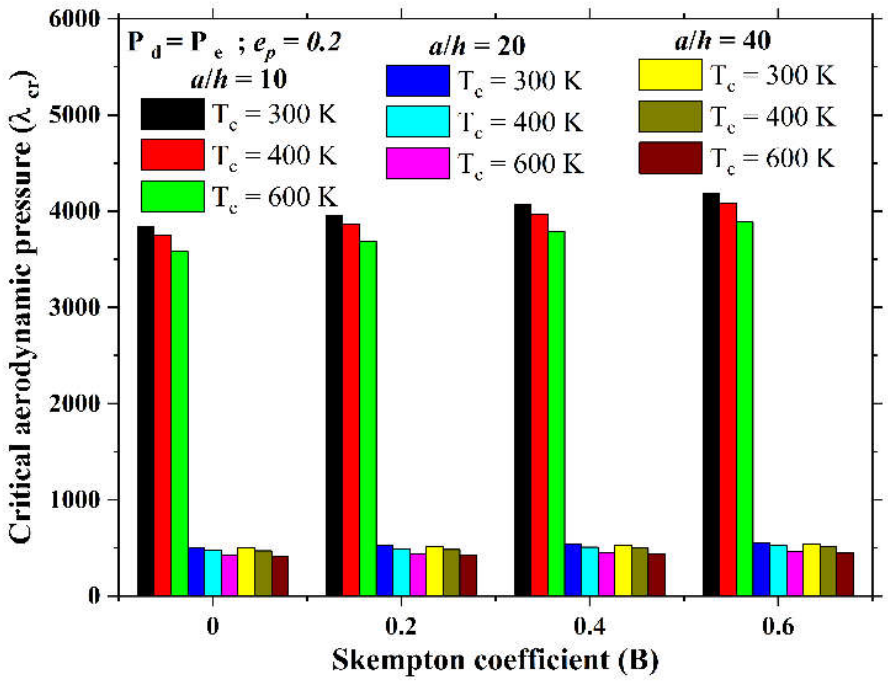

(a) P_e

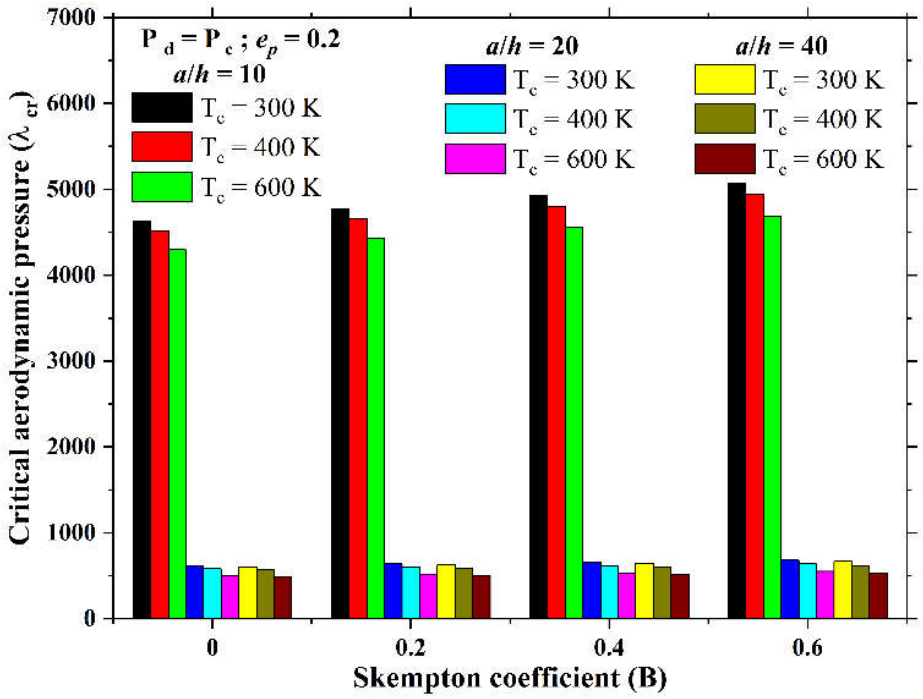

(b) P_c

Figure 8.6: Effect of thickness ratio on the critical aerodynamic pressure for different Skempton coefficients (B) of simply supported FGSPM plate having different porosity distributions and thermal loads (a/b = 1, W_{max}/h = 1, m = 1, and e_p = 0.2).

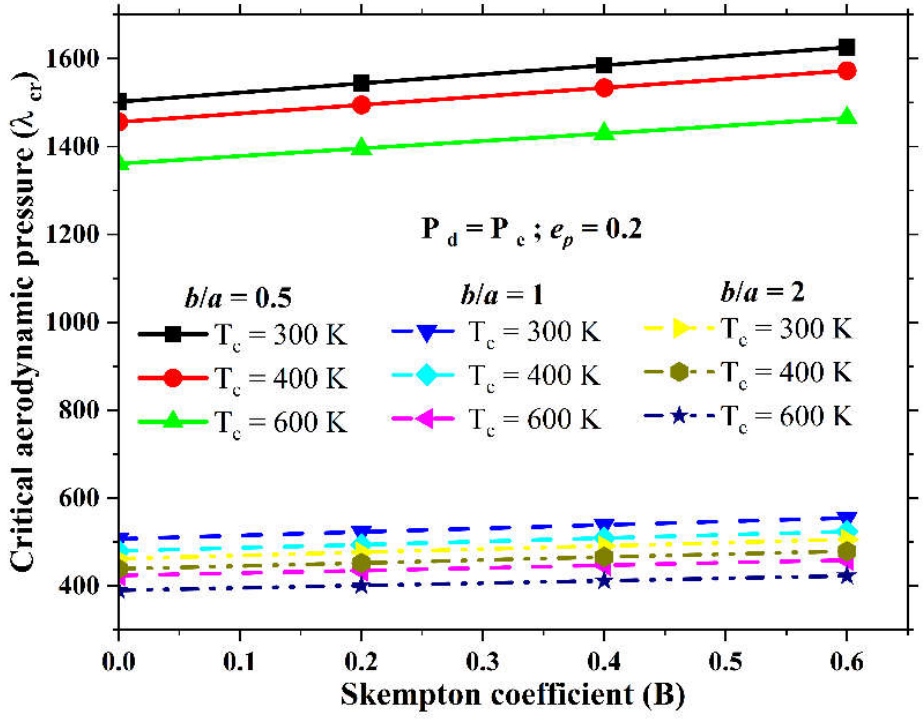

(a) P_e

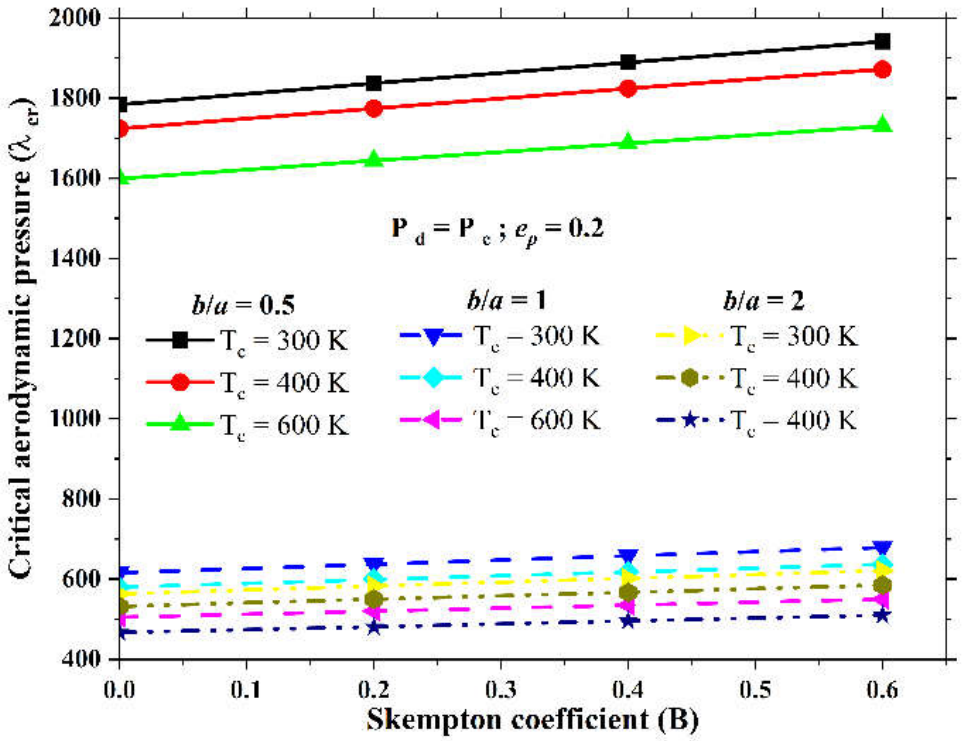

(b) P_c

Figure 8.7: Effect of aspect ratio on the critical aerodynamic pressure for different Skempton coefficients (B) of simply supported FGSPM plate having different porosity distributions and thermal loads (a/h = 20, W_{max}/h = 1, m = 1, and e_p = 0.2).

8.3.6. Effect of yawed flow angles

The effect of yawed flow angles on the critical aerodynamic pressure (λ_{cr}) of the square FGSPM plate having different VFGI, porosity volume index (e_p), and thermal loadings is depicted in Figure 8.8. It can be seen from Figure 8.8 that the highest critical aerodynamic pressure is attained at a yawed flow angle equal to 45º, and the lowest values appear at yawed angles equal to 0º and 90º. The curves of the variation of critical aerodynamic pressure (λ_{cr}) of the FGSPM plate are symmetric to the yawed flow angle of 45º. The trend is similar for a chosen VFGI, porosity volume index, porosity distributions, and temperature gradients. Consequently, it reveals that the critical aerodynamic pressure is dependent on the yawed flow angle. Besides, from Figure 8.8, it can be found that the λ_{cr} decreases with an increase in the VFGI, porosity volume index, and temperature gradient for a chosen yawed flow angle and porosity distribution. In addition, the evenly distributed porosities significantly impact the λ_{cr} of the FGSPM plate more than the P_c.

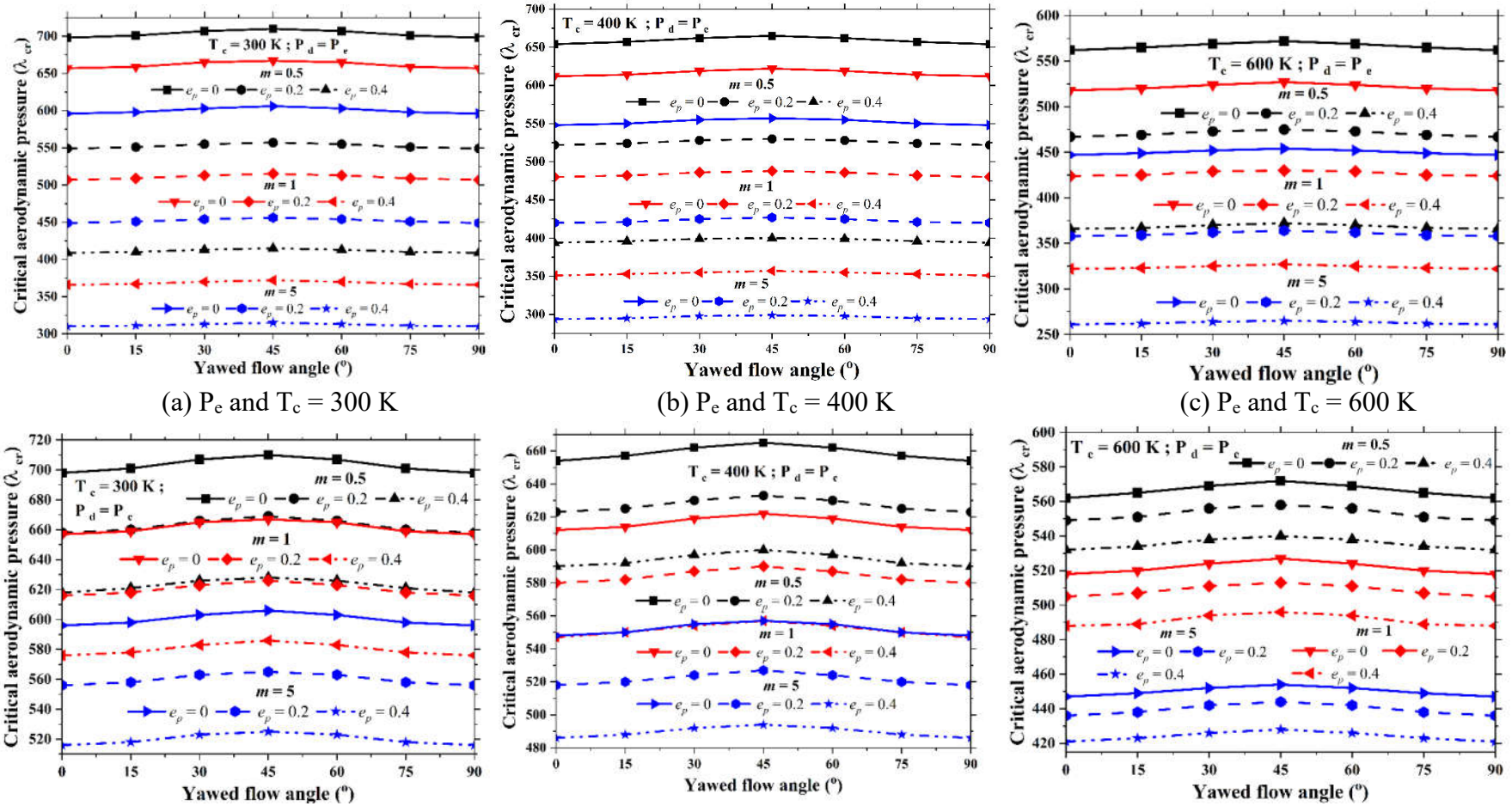

(a) P_e and T_c = 300 K (b) P_e and T_c = 400 K (c) P_e and T_c = 600 K

(d) P_c and T_c = 300 K (e) P_c and T_c = 400 K (f) P_c and T_c = 600

Figure 8.8: The variations of the critical aerodynamic pressure (λ_{cr}) of the square FGSPM plate having different VFGI, porosity volume index (e_p), and thermal loadings with yawed flow angles (a/h = 20, W_{max}/h = 1, and B = 0).

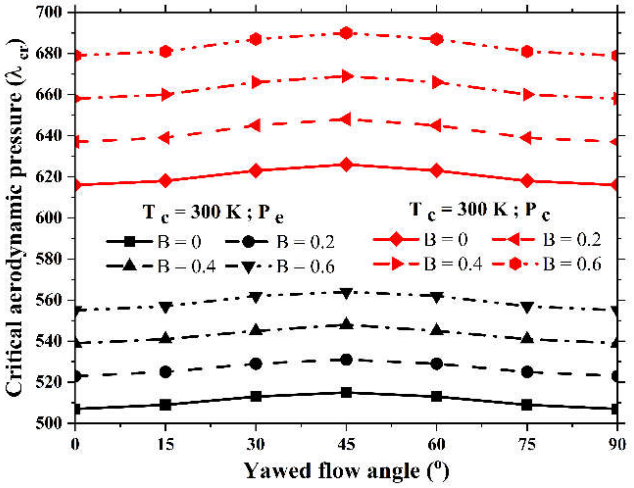

(a) T_c = 300 K

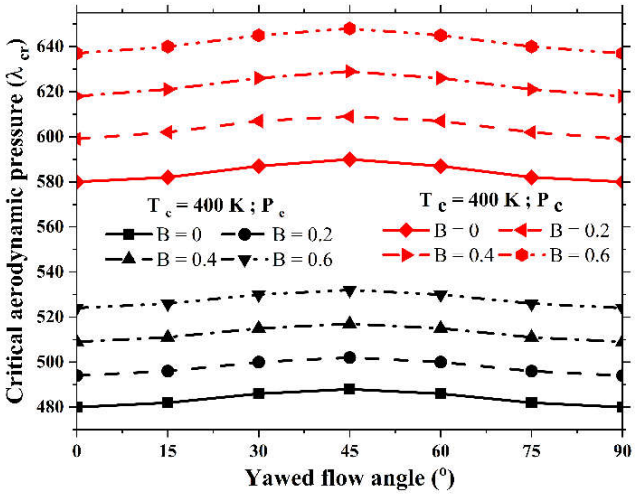

(b) T_c = 400 K

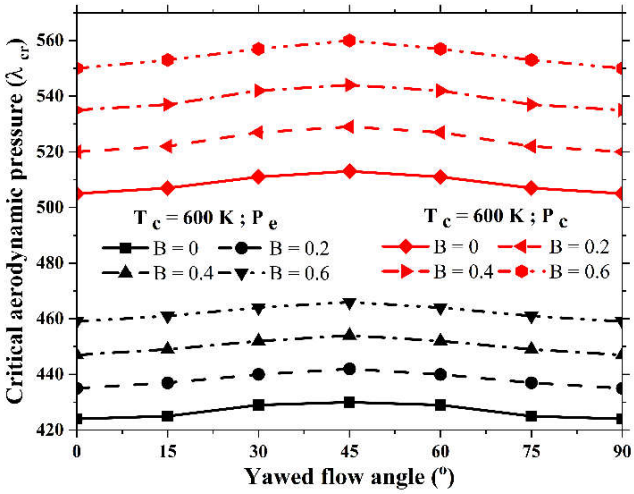

(c) T_c = 600 K

Figure 8.9: The variations of the critical aerodynamic pressure (λ_{cr}) of the square FGSPM plate having different Skempton coefficient (B), porosity distributions, and thermal loadings with yawed flow angles (a/h = 20, W_{max}/h = 1, m = 1, and e_p = 0.2).

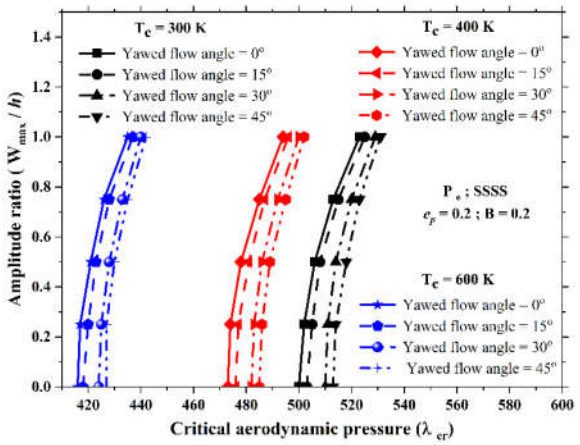

(a) P_e and SSSS

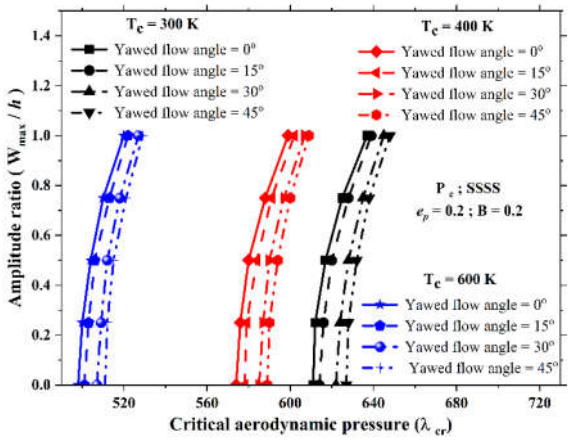

(b) P_c and SSSS

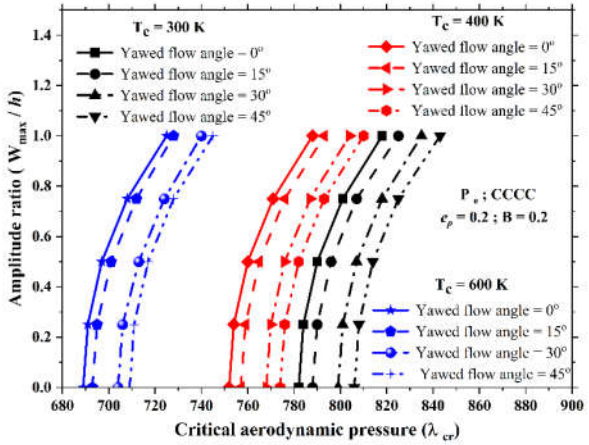

(c) P_e and CCCC

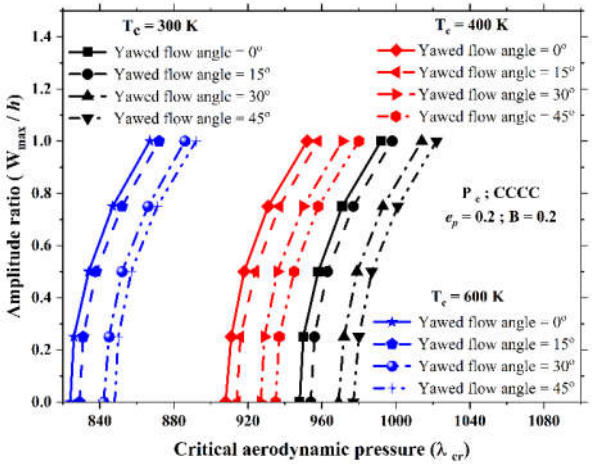

(d) P_c and CCCC

Figure 8.10: The variations of the λ_{cr} with amplitude ratio (W_{max}/h) of the square FGSPM plate having different yawed flow angles, porosity distributions, and thermal loadings with boundary conditions (a/h = 20, m = 1, B = 0.2, and e_p = 0.2).

However, P_c has higher values of λ_{cr} than P_e for a chosen yawed flow angle. Besides, regarding the yawed flow angle variation, the variation range of λ_{cr} is greater for P_c than for P_e.

Furthermore, the variations of the critical aerodynamic pressure (λ_{cr}) of the square FGSPM plate having different Skempton coefficients (B), porosity distributions, and thermal loadings with yawed flow angles are depicted in Figure 8.9. It can be observed from Figure 8.9 that the critical aerodynamic pressure increases with an increase in the Skempton coefficient for a chosen yawed flow angle. Further, the same trend is observed, as discussed in Figure 8.8.

8.3.7. Effect of boundary conditions

The influence of different boundary conditions on the critical aerodynamic pressure (λ_{cr}) with amplitude ratio (W_{max}/h) of the square FGSPM plate having different yawed flow angles is illustrated in Figure 8.10. It can be noticed from Figure 8.10 that the critical aerodynamic pressure (λ_{cr}) increases with an increase in the yawed flow angle for a given boundary condition and amplitude ratio. However, λ_{cr} decreases with an increase in the temperature gradient for simply supported and clamped boundary conditions. In addition, clamped boundary conditions have higher values of λ_{cr} for a chosen yawed flow angle. In the meantime, evenly distributed porosities and simply supported boundary conditions significantly affect λ_{cr} more than the clamped boundary condition and P_c for a given yawed flow angle.

8.4. CONCLUSIONS

This chapter presents the geometrically nonlinear vibration and flutter behavior of the supersonic FGSPM plate in a thermal environment. The IFSDT and von Karman's geometric nonlinearity with supersonic first-order piston theory are utilized to develop a nonlinear FE model. Meanwhile, the temperature-dependent effective material properties are obtained using a modified power-law series. The constitutive equations incorporate saturated fluids in the pores by employing the linear poroelasticity theory. Hamilton's principle and direct iterative methods are used to extract the solutions.

Numerous intriguing findings observed in numerical investigations can lead to the following conclusions: The effect of pore fluid pressure significantly influences the flutter bounds compared to the fluid-free FG porous plate by varying fluid compressibility within the pores. The FGSPM plates under undrained conditions have a more significant critical aerodynamic pressure (λ_{cr}) than the FG porous plate under drained conditions. The evenly distributed porosities are significantly more affected by pore fluid pressure on the flutter bounds than the centrally distributed porosities. The critical aerodynamic pressure decreases with an increase in the temperature gradient, porosity volume index, yawed flow angle, and VFGI for a given amplitude ratio and porosity distribution. However, critical aerodynamic pressure increases with the Skempton coefficient. Parametric studies on thickness and aspect ratios indicate that the influence of pore fluid pressure is insignificant for thinner plates. The critical aerodynamic pressure is dependent on the yawed flow angle on the supersonic FGSPM plate. The highest critical aerodynamic pressure is attained at a yawed flow angle of 45º, and the lowest values appear at yawed angles of 0º and 90º. In addition, the clamped boundary conditions have higher values of λ_{cr} for a chosen yawed flow angle than the simply supported boundary conditions.

CHAPTER 9

CONCLUSIONS AND FUTURE SCOPE

This chapter summarizes the significant outcomes of the present research work and the possible future improvements in the analysis of functionally graded porous structures.

9.1. MAJOR FINDINGS

This dissertation investigates the influence of porosity distributions, saturated porosities, two-directional gradation, temperature, and geometrical non-uniformities on the nonlinear vibration and flutter behavior of the porous FG plates and shells. The nonlinear finite element model has been derived using shear deformation theory and von Kármán's nonlinearity relations with the aid of the total potential energy principle to evaluate the structural behavior of the porous FG plates and shells. The constitutive equations of FG porous structures are developed by accounting for the coupling between elastic, porosity, two-directional gradation, saturated porosities, and thermal fields. Temperature distribution across the thickness of the FG porous plate has been considered for the analysis. The effective material properties have been determined using the modified power-law series. The numerical solutions are obtained by using the direct iterative method and Newmark's integration method. The numerical evaluation suggests that the porosity distributions, saturated porosity distributions, and two-directional gradation significantly influence the nonlinear responses of the FG porous plates and shells. Special attention has been devoted to evaluating the influence of saturated porosities on the flutter bounds of the FGSPM plates.

The numerical analysis is carried out to investigate the nonlinear free vibration and transient responses of the FG porous plates with geometrical non-uniformities with and without thermal loading. The significance of different porosity distributions and geometrical non-uniformities such as skewness, variable thicknesses (linearly, bi-linearly, and exponentially) along with various material and geometrical parameters on

the nonlinear free vibration and transient responses is well established. The different porosity distributions are emphasized to understand the behavior of the FG porous plates. It is observed that the geometrical nonuniformities and different porosity distributions significantly influence the nonlinear responses of the FG porous plates with and without thermal loading.

Besides, the nonlinear vibration and dynamic responses of the two-directional FG porous plates and shells are evaluated. The nonlinear finite element of the TDFGP plates/shells is derived by considering the effects of two-directional gradation with porosities in the constitutive equations. The comprehensive analysis reveals that the volume fraction grading profiles in different directions exhibit a predominant effect on the responses of the TDFGP plates and shells. In addition, the TDFGP shells exhibit higher values of nonlinear frequencies and deflections than the TDFGP plate.

Further investigation is devoted to revealing the influence of saturated porosities and their distributions on the nonlinear vibration and supersonic flutter characteristics of the FGSPM plate under thermal loading. Particular emphasis has been paid to considering the effect of various pore fluid pressures on the different saturated porosity distributions to characterize the flutter bounds under thermal loads. The linear poroelasticity theory incorporates saturated porosity into the constitutive equations. Besides, the quasi-steady piston theory has been used to consider the effects of aerodynamic pressure. The results reveal that the pore fluid pressure and distribution of porosities have noticeable effects on the nonlinear behavior of the FGSPM plate.

The major outcomes drawn from the above research work are outlined as follows:

1. The nonlinear frequency ratio (NLFR) (ω_{NL}/ω) and nonlinear frequency parameter (NLFP) (ω_{NL}) both increase as the amplitude ratio (W_{max}/h) increase in the presence of porosity and temperature.
2. The effect of geometrical non-uniformities on the NLFR and NLFP of porous FG plates is always more significant than those with uniform thickness.
3. The NLFR and NLFP are more sensitive to centrally distributed porosities (P_c) than evenly distributed porosities (P_e) in an elevated thermal environment.

4. The geometrically nonlinear transient deflection of the porous FG skew plate in a thermal environment increases as the volume fraction grading index and temperature increase. Furthermore, the transient deflection decreases as the skew angle increases. The P_e type has a minimal impact on geometrically nonlinear deflections compared to the P_c.
5. The linear frequency, nonlinear frequency, and nonlinear deformations can be changed significantly by altering the volume fraction gradation profiles in the required direction for each material with a suitable combination of materials.
6. For TDFG porous structures, centrally distributed porosities have the highest linear frequencies, while evenly distributed porosities exhibit the largest nonlinear frequencies and deflections. Porous FG plates have the lowest nonlinear to linear frequency ratio and deformations compared to various shell geometries.
7. The saturated fluid pressure in the pores significantly influences the linear, nonlinear frequencies and nonlinear deformations compared to the fluid-free FG porous plates by varying the fluid compressibility within the pores.
8. The FGSPM plate under undrained conditions has enhanced stiffness because of pore fluid pressure compared to the FGSPM plate in drained conditions.
9. Evenly distributed porosities in the FGSPM plate significantly impact the flutter behavior more than the centrally distributed porosities.
10. Flutter analysis reveals that the nonlinear frequency and critical aerodynamic pressure have greater values for FGSPM plates than FG porous plates in drained conditions. Hence, FGSPM plates are more suitable for flights at supersonic speed.

9.2. SCOPE FOR THE FUTURE RESEARCH

The elementary purpose of this thesis has been fulfilled by the contributions presented in the preceding chapters of this dissertation. However, there is still scope for further research to enhance FG porous structures' performance. Among them, a few possible future research scopes have been outlined as follows:

1. The nonlinear vibration analysis of multi-directional porous FG structures in thermal and hygrothermal environments is a challenging objective.
2. Analysis of FG saturated porous structures in a thermal environment using non-local theory is still an overlooked area.

3. Nonlinear analysis of the FG saturated porous structures with solid-fluid interactions under thermal loading is a challenging objective.
4. Experimental verification of the proposed nonlinear finite element model will be handy for future applications of FG porous structures in a thermal environment.

APPENDIX - I

The various nodal strain displacement matrices $[ß]$, elemental stiffness, rigidity matrices, and vectors used in Eq. (4.14) are given as follows:

The generalized nodal strain displacement matrix is explicitly written as follows:

$$[ß_{tb}] = [ß_{tb1}\ ß_{tb2}\ ß_{tb3} \ldots ß_{tb8}]\ ;$$

$$[ß_1][ß_2] = [ß_1][ß_{21}\ ß_{21}\ ß_{23} \ldots ß_{28}];$$

$$[ß_{rb}] = [ß_{rb1}\ ß_{rb2}\ ß_{rb3} \ldots ß_{rb8}]\ ;$$

$$[ß_{ts}] = [ß_{ts1}\ ß_{ts2}\ ß_{ts3} \ldots ß_{ts8}];$$

$$[ß_{rs}] = [ß_{rs1}\ ß_{rs2}\ ß_{rs3} \ldots ß_{rs8}];$$

$$[ß_{Temp-tb}] = [ß_{Temp-tb1}\ ß_{Temp-tb2}\ ß_{Temp-tb3} \ldots ß_{Temp-tb8}];$$

$$[ß_{Temp-ts}] = [ß_{Temp-ts1}\ ß_{Temp-ts2}\ ß_{Temp-ts3} \ldots ß_{Temp-ts8}];$$

where $[ß_{tbn}]$, $[ß_{1n}]$, $[ß_{2n}]$, $[ß_{rbn}]$, $[ß_{tsn}]$, $[ß_{rsn}]$, $[ß_{Temp-tb}]$, and $[ß_{Temp-ts}]$ are the sub-matrices, in which n =1,2,3, …, 8 and are given by,

$$[ß_{tbn}] = \begin{bmatrix} \frac{\partial n_n}{\partial x} & 0 & 0 \\ 0 & \frac{\partial n_n}{\partial y} & 0 \\ \frac{\partial n_n}{\partial y} & \frac{\partial n_n}{\partial x} & 0 \end{bmatrix};\quad [ß_1] = \begin{bmatrix} \frac{\partial w_1}{\partial x} & 0 & \frac{\partial w_1}{\partial y} \\ 0 & \frac{\partial w_1}{\partial y} & \frac{\partial w_1}{\partial x} \end{bmatrix}^T;\quad [ß_{2n}] = \begin{bmatrix} 0 & 0 & \frac{\partial n_n}{\partial x} \\ 0 & 0 & \frac{\partial n_n}{\partial y} \end{bmatrix};$$

$$[ß_{rbn}] = \begin{bmatrix} \frac{\partial n_n}{\partial x} & 0 \\ 0 & \frac{\partial n_n}{\partial y} \\ \frac{\partial n_n}{\partial y} & \frac{\partial n_n}{\partial x} \end{bmatrix};\quad [ß_{tsn}] = \begin{bmatrix} 0 & 0 & \frac{\partial n_n}{\partial x} \\ 0 & 0 & \frac{\partial n_n}{\partial y} \end{bmatrix};\quad [ß_{rsn}] = \begin{bmatrix} n_n & 0 \\ 0 & n_n \end{bmatrix};$$

$$[ß_{Temp-tb}] = \begin{bmatrix} \frac{\partial n_n}{\partial x} & 0 & 0 \\ \frac{\partial n_n}{\partial y} & 0 & 0 \end{bmatrix};\quad [ß_{Temp-tsn}] = \begin{bmatrix} 0 & \frac{\partial n_n}{\partial x} & 0 \\ 0 & \frac{\partial n_n}{\partial y} & 0 \end{bmatrix}$$

Elemental Stiffness matrices

The elements stiffness matrices for bending and stretching deformations, as well as transverse shear deformations, are given as follows:

$$\left[K_{tb}^{e}\right]=\int_0^a\int_0^b\left[ß_{tb}\right]^T\left[Ð_{tb}\right]\left[ß_{tb}\right]dxdy \; ; \; \left[K_{trb}^{e}\right]=\int_0^a\int_0^b\left[ß_{tb}\right]^T\left[Ð_{trb}\right]\left[ß_{rb}\right]dxdy$$

$$\left[K_{rrb}^{e}\right]=\int_0^a\int_0^b\left[ß_{rb}\right]^T\left[Ð_{rrb}\right]\left[ß_{rb}\right]dxdy$$

$$\left[K_{tbNL}^{e}\right]=\int_0^a\int_0^b\left(\frac{1}{2}\left[ß_{tb}\right]^T\left[Ð_{tb}\right]\left[ß_1\right]\left[ß_2\right]+\left[ß_2\right]^T\left[ß_1\right]^T\left[Ð_{tb}\right]\left[ß_{tb}\right]+\frac{1}{2}\left[ß_2\right]^T\left[ß_1\right]^T\left[Ð_{tb}\right]\left[ß_1\right]\left[ß_2\right]\right)dxdy$$

$$\left[K_{trbNL}^{e}\right]=\int_0^a\int_0^b\left(\left[ß_2\right]^T\left[ß_1\right]^T\left[Ð_{trb}\right]\left[ß_{rb}\right]\right)dxdy \; ; \; \left[K_{rtbNL}^{e}\right]=\frac{1}{2}\left[K_{trbNL}^{e}\right]^T$$

$$\left[M^{e}\right]=\int_0^a\int_0^b\left[N_t\right]^T\overline{m}\left[N_t\right]dxdy \qquad \text{where,} \quad \overline{m}=\int_{-h/2}^{h/2}\rho\,dz$$

$$\left[K_{ts}^{e}\right]=\int_0^a\int_0^b\left[ß_{ts}\right]^T\left[Ð_{ts}\right]\left[ß_{ts}\right]dxdy \; ; \; \left[K_{trs}^{e}\right]=\int_0^a\int_0^b\left[ß_{ts}\right]^T\left[Ð_{trs}\right]\left[ß_{rs}\right]dxdy$$

$$\left[K_{rrs}^{e}\right]=\int_0^a\int_0^b\left[ß_{rs}\right]^T\left[Ð_{rrs}\right]\left[ß_{rs}\right]dxdy \; ;$$

$$\left[K_{Temp-tb}^{e}\right]=\int_0^a\int_0^b\left[ß_{Temp-tb}\right]^T\left[Ð_{Temp-tb}\right]\left[ß_{Temp-tb}\right]dxdy$$

$$\left[K_{Temp-ts}^{e}\right]=\int_0^a\int_0^b\left[ß_{Temp-ts}\right]^T\left[Ð_{ts}\right]\left[ß_{Temp-ts}\right]dxdy \; ;$$

The rigidity matrices and vectors are given by

$$\left[Ð_{tb}\right]=\int_{-h/2}^{h/2}\left[Q_b\left(z,T\right)\right]dz \; ; \; \left[Ð_{trb}\right]=\int_{-h/2}^{h/2}\left[Q_b\left(z,T\right)\right]z\,dz \; ; \; \left[Ð_{rrb}\right]=\int_{-h/2}^{h/2}\left[Q_b\left(z,T\right)\right]z^2dz$$

$$\left[Ð_{ts}\right]=\int_{-h/2}^{h/2}\left[Q_s\left(z,T\right)\right]dz \; ; \; \left[Ð_{trs}\right]=\int_{-h/2}^{h/2}\left[Q_s\left(z,T\right)\right]dz \; ; \; \left[Ð_{rrs}\right]=\int_{-h/2}^{h/2}\left[Q_s\left(z,T\right)\right]dz \; ;$$

$$\left[Ð_{Temp-tb}\right]=\int_{-h/2}^{h/2}\left[Q_b\left(z,T\right)\left[1\quad 1\quad 0\right]^T\alpha_{fg}\,\Delta T\right]dz$$

APPENDIX - II

The generalized nodal strain displacement matrix for aerodynamic loading used in Eq. (8.12) is explicitly written as follows:

$$\left[A_{fe}\right]=\left[A_{fe1}\ A_{fe2}\ A_{fe3}\ldots\ A_{fe8}\right]$$

where $\left[\overline{A_{fe}}\right]$ is the sub-matrix, in which n =1,2,3, …, 8 and are given by

$$\left[\overline{A_{fe}}\right]=\begin{bmatrix}0 & 0 & 0\\ 0 & 0 & 0\\ 0 & 0 & \dfrac{\partial w_1}{\partial x}\cos\theta\end{bmatrix}$$

Elemental Stiffness matrices

The elements stiffness matrices for aerodynamic loading is given by

$$\left[K^{e}_{Afe}\right]=\int_0^a\int_0^b\left[\overline{A_{fe}}\right]^T\left[\overline{A_{fe}}\right]dxdy$$

REFERENCES

Adineh, M., and Kadkhodayan, M. (2017). "Three-dimensional thermo-elastic analysis and dynamic response of a multi-directional functionally graded skew plate on elastic foundation." *Compos. Part B Eng.*, 125, 227–240.

Ahlawat, N., and Lal, R. (2016). "Buckling and Vibrations of Multi-directional Functionally Graded Circular Plate Resting on Elastic Foundation." *Procedia Eng.*, 144, 85–93.

Akbari, H., Azadi, M., and Fahham, H. (2020). "Free vibration analysis of thick sandwich cylindrical panels with saturated FG-porous core." *Mech. Based Des. Struct. Mach.*, 0(0), 1–19.

Alhaifi, K., Arshid, E., and Khorshidvand, A. R. (2021). "Large deflection analysis of functionally graded saturated porous rectangular plates on nonlinear elastic foundation via GDQM." *Steel Compos. Struct.*, 39(6), 795–809.

Alijani, F., Bakhtiari-Nejad, F., and Amabili, M. (2011). "Nonlinear vibrations of FGM rectangular plates in thermal environments." *Nonlinear Dyn.*, 66(3), 251–270.

Alimirzaei, S., Mohammadimehr, M., and Tounsi, A. (2019). "Nonlinear analysis of viscoelastic micro-composite beam with geometrical imperfection using FEM: MSGT electro-magneto-elastic bending, buckling and vibration solutions." *Struct. Eng. Mech.*, 71(5), 485–502.

Alinaghizadeh, F., and Shariati, M. (2016). "Geometrically non-linear bending analysis of thick two-directional functionally graded annular sector and rectangular plates with variable thickness resting on non-linear elastic foundation." *Compos. Part B Eng.*, 86, 61–83.

Alipour, M. M., Shariyat, M., and Shaban, M. (2010). "A semi-analytical solution for free vibration of variable thickness two-directional-functionally graded plates on elastic foundations." *Int. J. Mech. Mater. Des.*, 6(4), 293–304.

Allahkarami, F., Ghassabzadeh Saryazdi, M., and Tohidi, H. (2020a). "Dynamic buckling analysis of bi-directional functionally graded porous truncated conical shell with different boundary conditions." *Compos. Struct.*, 252(November 2019), 112680.

Allahkarami, F., Tohidi, H., Dimitri, R., and Tornabene, F. (2020b). "Dynamic Stability of Bi-Directional Functionally Graded Porous Cylindrical Shells Embedded in an

Elastic Foundation." *Appl. Sci.*, 10(4), 1345.

Amir, M., and Talha, M. (2019). "Nonlinear vibration characteristics of shear deformable functionally graded curved panels with porosity including temperature effects." *Int. J. Press. Vessel. Pip.*, 172(February), 28–41.

Amir, S., Arshid, E., and Ghorbanpour Arani, M. R. (2019). "Size-dependent magneto-electro-elastic vibration analysis of FG saturated porous annular/ circular micro sandwich plates embedded with nano-composite face sheets subjected to multi-physical pre loads." *Smart Struct. Syst.*, 23(5), 429–447.

Arshid, E., and Amir, S. (2021). "Size-dependent vibration analysis of fluid-infiltrated porous curved microbeams integrated with reinforced functionally graded graphene platelets face sheets considering thickness stretching effect." *Proc. Inst. Mech. Eng. Part L J. Mater. Des. Appl.*, 235(5), 1077–1099.

Arshid, E., and Khorshidvand, A. R. (2018). "Free vibration analysis of saturated porous FG circular plates integrated with piezoelectric actuators via differential quadrature method." *Thin-Walled Struct.*, 125(November 2016), 220–233.

Arshid, E., Khorshidvand, A. R., and Khorsandijou, S. M. (2019). "The effect of porosity on free vibration of SPFG circular plates resting on visco-Pasternak elastic foundation based on CPT, FSDT and TSDT." *Struct. Eng. Mech.*, 70(1), 97–112.

Asemi, K., Salehi, M., and Akhlaghi, M. (2011). "Elastic solution of a two-dimensional functionally graded thick truncated cone with finite length under hydrostatic combined loads." *Acta Mech.*, 217(1–2), 119–134.

Asgari, M., and Akhlaghi, M. (2011). "Natural frequency analysis of 2D-FGM thick hollow cylinder based on three-dimensional elasticity equations." *Eur. J. Mech. - A/Solids*, 30(2), 72–81.

Asgari, M., Akhlaghi, M., and Hosseini, S. M. (2009). "Dynamic analysis of two-dimensional functionally graded thick hollow cylinder with finite length under impact loading." *Acta Mech.*, 208(3–4), 163–180.

Babaei, M., and Asemi, K. (2020). "Stress analysis of functionally graded saturated porous rotating thick truncated cone." *Mech. Based Des. Struct. Mach.*, 0(0), 1–28.

Babaei, M., Asemi, K., and Kiarasi, F. (2020a). "Static response and free-vibration analysis of a functionally graded annular elliptical sector plate made of saturated porous material based on 3D finite element method." *Mech. Based Des. Struct. Mach.*, 0(0), 1–

25.

Babaei, M., Asemi, K., and Kiarasi, F. (2021). “Dynamic analysis of functionally graded rotating thick truncated cone made of saturated porous materials.” *Thin-Walled Struct.*, 164(April), 107852.

Babaei, M., Hajmohammad, M. H., and Asemi, K. (2020b). “Natural frequency and dynamic analyses of functionally graded saturated porous annular sector plate and cylindrical panel based on 3D elasticity.” *Aerosp. Sci. Technol.*, 96, 105524.

Babaei, M., Hajmohammad, M. H., and Asemi, K. (2020c). “Natural frequency and dynamic analyses of functionally graded saturated porous annular sector plate and cylindrical panel based on 3D elasticity.” *Aerosp. Sci. Technol.*, 96, 105524.

Bahaadini, R., Saidi, A. R., and Majidi-Mozafari, K. (2019). “Aeroelastic Flutter Analysis of Thick Porous Plates in Supersonic Flow.” *Int. J. Appl. Mech.*, 11(10).

Barati, A., Hadi, A., Nejad, M. Z., and Noroozi, R. (2020). “On vibration of bi-directional functionally graded nanobeams under magnetic field.” *Mech. Based Des. Struct. Mach.*, 0(0), 1–18.

Barati, M. R., and Shahverdi, H. (2017). “Aero-hygro-thermal stability analysis of higher-order refined supersonic FGM panels with even and uneven porosity distributions.” *J. Fluids Struct.*, 73, 125–136.

Behravan Rad, A. (2018). “Static analysis of non-uniform 2D functionally graded auxetic-porous circular plates interacting with the gradient elastic foundations involving friction force.” *Aerosp. Sci. Technol.*, 76, 315–339.

Bergan, P. G., and Clough, R. W. (1972). “Convergence criteria for iterative processes.” *AIAA J.*

Boggarapu, V., Gujjala, R., Ojha, S., Acharya, S., Venkateswara babu, P., Chowdary, S., and kumar Gara, D. (2021). “State of the art in functionally graded materials.” *Compos. Struct.*, 262(November 2020), 113596.

Bouguenina, O., Belakhdar, K., Tounsi, A., and Adda Bedia, E. A. (2015). “Numerical analysis of FGM plates with variable thickness subjected to thermal buckling.” *Steel Compos. Struct.*, 19(3), 679–695.

Chen, C.-S. (2005). “Nonlinear vibration of a shear deformable functionally graded plate.” *Compos. Struct.*, 68(3), 295–302.

Chen, C.-S., Chen, T., and Chien, R.-D. (2006). “Nonlinear vibration of initially

stressed functionally graded plates." *Thin-Walled Struct.*, 44(8), 844–851.

Chen, J., Dawe, D. . J., and Wang, S. (2000). "Nonlinear transient analysis of rectangular composite laminated plates." *Compos. Struct.*, 49(2), 129–139.

Chen, M., Ye, T., Zhang, J., Jin, G., Zhang, Y., Xue, Y., Ma, X., and Liu, Z. (2020). "Isogeometric three-dimensional vibration of variable thickness parallelogram plates with in-plane functionally graded porous materials." *Int. J. Mech. Sci.*, 169(November 2019), 105304.

Chen, X., Chen, L., Huang, S., Li, M., and Li, X. (2021). "Nonlinear forced vibration of in-plane bi-directional functionally graded materials rectangular plate with global and localized geometrical imperfections." *Appl. Math. Model.*, 93, 443–466.

Chu, F., Wang, L., Zhong, Z., and He, J. (2014). "Hermite radial basis collocation method for vibration of functionally graded plates with in-plane material inhomogeneity." *Comput. Struct.*, 142, 79–89.

DETOURNAY, E., and CHENG, A. H.-D. (1993). "Fundamentals of Poroelasticity." *Anal. Des. Methods*, Elsevier, 113–171.

Do, D. T. T., Nguyen-Xuan, H., and Lee, J. (2020). "Material optimization of tri-directional functionally graded plates by using deep neural network and isogeometric multimesh design approach." *Appl. Math. Model.*, 87, 501–533.

Do, T. Van, Nguyen, D. K., Duc, N. D., Doan, D. H., and Bui, T. Q. (2017a). "Analysis of bi-directional functionally graded plates by FEM and a new third-order shear deformation plate theory." *Thin-Walled Struct.*, 119(July), 687–699.

Do, T. Van, Nguyen, D. K., Duc, N. D., Doan, D. H., and Bui, T. Q. (2017b). "Analysis of bi-directional functionally graded plates by FEM and a new third-order shear deformation plate theory." *Thin-Walled Struct.*, 119(May), 687–699.

DOWELL, E. H. (1966). "Nonlinear oscillations of a fluttering plate." *AIAA J.*, 4(7), 1267–1275.

DOWELL, E. H. (1970). "Panel flutter - A review of the aeroelastic stability of plates and shells." *AIAA J.*, 8(3), 385–399.

Ebrahimi, F., and Dabbagh, A. (2019). *Wave Propagation Analysis of Smart Nanostructures*. *Wave Propag. Anal. Smart Nanostructures*, CRC Press.

Ebrahimi, F., and Dabbagh, A. (2020). *Mechanics of Nanocomposites*. *Mech. Nanocomposites*, CRC Press.

Ebrahimi, F., and Dabbagh, A. (2021). “Magnetic field effects on thermally affected propagation of acoustical waves in rotary double-nanobeam systems.” *Waves in Random and Complex Media*, 31(1), 25–45.

Ebrahimi, F., and Habibi, S. (2016). “Deflection and vibration analysis of higher-order shear deformable compositionally graded porous plate.” *Steel Compos. Struct.*, 20(1), 205–225.

Ebrahimi, M. J., and Najafizadeh, M. M. (2014). “Free vibration analysis of two-dimensional functionally graded cylindrical shells.” *Appl. Math. Model.*, 38(1), 308–324.

Esmaeilzadeh, M., and Kadkhodayan, M. (2019). “Dynamic analysis of stiffened bi-directional functionally graded plates with porosities under a moving load by dynamic relaxation method with kinetic damping.” *Aerosp. Sci. Technol.*, 93, 105333.

Farsadi, T., Rahmanian, M., and Kurtaran, H. (2021). “Nonlinear analysis of functionally graded skewed and tapered wing-like plates including porosities: A bifurcation study.” *Thin-Walled Struct.*, 160(December 2020), 107341.

Feyzi, M. R., and Khorshidvand, A. R. (2017). “Axisymmetric post-buckling behavior of saturated porous circular plates.” *Thin-Walled Struct.*, 112(June 2016), 149–158.

Gao, Y., Xiao, W. S., and Zhu, H. (2019). “Nonlinear vibration of functionally graded nano-tubes using nonlocal strain gradient theory and a two-steps perturbation method.” *Struct. Eng. Mech.*, 69(2), 205–219.

Garg, A. K., Khare, R. K., and Kant, T. (2006). “Free vibration of skew fiber-reinforced composite and sandwich laminates using a shear deformable finite element model.” *J. Sandw. Struct. Mater.*, 8(1), 33–53.

Ghatage, P. S., Kar, V. R., and Sudhagar, P. E. (2020). “On the numerical modelling and analysis of multi-directional functionally graded composite structures: A review.” *Compos. Struct.*, 236(December 2019), 111837.

Grover, N., Singh, B. N., and Maiti, D. K. (2016). “An inverse trigonometric shear deformation theory for supersonic flutter characteristics of multilayered composite plates.” *Aerosp. Sci. Technol.*, 52, 41–51.

Gupta, A., and Talha, M. (2017). “Nonlinear flexural and vibration response of geometrically imperfect gradient plates using hyperbolic higher-order shear and normal deformation theory.” *Compos. Part B Eng.*, 123, 241–261.

Gupta, A., and Talha, M. (2018). “Influence of Porosity on the Flexural and Free Vibration Responses of Functionally Graded Plates in Thermal Environment.” *Int. J. Struct. Stab. Dyn.*, 18(01), 1850013.

Han, W., and Petyt, M. (1997). “Geometrically nonlinear vibration analysis of thin, rectangular plates using the hierarchical finite element method—I: The fundamental mode of isotropic plates.” *Comput. Struct.*, 63(2), 295–308.

Hong, N. T. (2020). “Nonlinear Static Bending and Free Vibration Analysis of Bidirectional Functionally Graded Material Plates.” *Int. J. Aerosp. Eng.*, (M. Pizzarelli, ed.), 2020, 1–16.

Hosseini-Hashemi, S., Fadaee, M., and Atashipour, S. R. (2011). “Study on the free vibration of thick functionally graded rectangular plates according to a new exact closed-form procedure.” *Compos. Struct.*, 93(2), 722–735.

Hosseini-Hashemi, S., Rokni Damavandi Taher, H., Akhavan, H., and Omidi, M. (2010). “Free vibration of functionally graded rectangular plates using first-order shear deformation plate theory.” *Appl. Math. Model.*, 34(5), 1276–1291.

Huang, X.-L., Dong, L., Wei, G.-Z., and Zhong, D.-Y. (2019). “Nonlinear free and forced vibrations of porous sigmoid functionally graded plates on nonlinear elastic foundations.” *Compos. Struct.*, 228(November 2018), 111326.

Huang, X.-L., and Shen, H.-S. (2004). “Nonlinear vibration and dynamic response of functionally graded plates in thermal environments.” *Int. J. Solids Struct.*, 41(9–10), 2403–2427.

Huang, X.-L., and Shen, H.-S. (2006). “Vibration and dynamic response of functionally graded plates with piezoelectric actuators in thermal environments.” *J. Sound Vib.*, 289(1–2), 25–53.

Ibrahim, H. H., Tawfik, M., and Al-Ajmi, M. (2007a). “Thermal buckling and nonlinear flutter behavior of functionally graded material panels.” *J. Aircr.*, 44(5), 1610–1618.

Ibrahim, H. H., Tawfik, M., and Al-Ajmi, M. (2007b). “Thermal Buckling and Nonlinear Flutter Behavior of Functionally Graded Material Panels.” *J. Aircr.*, 44(5), 1610–1618.

Ibrahim, H. H., Tawfik, M., and Al-Ajmi, M. (2008). “Non-linear panel flutter for temperature-dependent functionally graded material panels.” *Comput. Mech.*, 41(2), 325–334.

Ibrahim, H. H., Yoo, H. H., and Lee, K.-S. (2009). “Supersonic Flutter of Functionally Grated Panels Subject to Acoustic and Thermal Loads.” *J. Aircr.*, 46(2), 593–600.

Jabbari, M., Hashemitaheri, M., Mojahedin, A., and Eslami, M. R. (2014a). “Thermal Buckling Analysis of Functionally Graded Thin Circular Plate Made of Saturated Porous Materials.” *J. Therm. Stress.*, 37(2), 202–220.

Jabbari, M., Mojahedin, A., Khorshidvand, A. R., and Eslami, M. R. (2014b). “Buckling Analysis of a Functionally Graded Thin Circular Plate Made of Saturated Porous Materials.” *J. Eng. Mech.*, 140(2), 287–295.

Javaheri, R., and Eslami, M. R. (2002a). “Thermal buckling of functionally graded plates based on higher order theory.” *J. Therm. Stress.*, 25(7), 603–625.

Javaheri, R., and Eslami, M. R. (2002b). “Thermal Buckling of Functionally Graded Plates.” *AIAA J.*, 40(1), 162–169.

Jha, D. K., Kant, T., and Singh, R. K. (2013). “A critical review of recent research on functionally graded plates.” *Compos. Struct.*, 96, 833–849.

Kar, V. R., and Panda, S. K. (2016). “Nonlinear free vibration of functionally graded doubly curved shear deformable panels using finite element method.” *JVC/Journal Vib. Control*, 22(7), 1935–1949.

Karamanlı, A. (2018). “Free vibration analysis of two directional functionally graded beams using a third order shear deformation theory.” *Compos. Struct.*, 189(December 2017), 127–136.

Katiyar, V., and Gupta, A. (2021). “Vibration response of a geometrically discontinuous bi-directional functionally graded plate resting on elastic foundations in thermal environment with initial imperfections.” *Mech. Based Des. Struct. Mach.*, 0(0), 1–29.

Kattimani, S. C., and Ray, M. C. (2014). “Smart damping of geometrically nonlinear vibrations of magneto-electro-elastic plates.” *Compos. Struct.*, 114(1), 51–63.

Kattimani, S. C., and Ray, M. C. (2015). “Control of geometrically nonlinear vibrations of functionally graded magneto-electro-elastic plates.” *Int. J. Mech. Sci.*, 99, 154–167.

Kermani, I. D., Ghayour, M., and Mirdamadi, H. R. (2012). “Free vibration analysis of multi-directional functionally graded circular and annular plates.” *J. Mech. Sci. Technol.*, 26(11), 3399–3410.

Khalafi, V., and Fazilati, J. (2022). “Panel flutter analysis of cracked functionally

graded plates in yawed supersonic flow with thermal effects." *Appl. Math. Model.*, 101, 259–275.

Khorshidi, K., and Karimi, M. (2019). "Flutter analysis of sandwich plates with functionally graded face sheets in thermal environment." *Aerosp. Sci. Technol.*, 95, 105461.

Kiran, M. C., Kattimani, S. C., and Vinyas, M. (2018). "Porosity influence on structural behaviour of skew functionally graded magneto-electro-elastic plate." *Compos. Struct.*, 191(February), 36–77.

Koizumi, M. (1997). "FGM activities in Japan." *Compos. Part B Eng.*, 28(1–2), 1–4.

Kumar, V., Singh, S. J., Saran, V. H., and Harsha, S. P. (2021). "Vibration characteristics of porous FGM plate with variable thickness resting on Pasternak's foundation." *Eur. J. Mech. - A/Solids*, 85(July 2020), 104124.

Lal, R., and Ahlawat, N. (2017). "Buckling and vibrations of two-directional functionally graded circular plates subjected to hydrostatic in-plane force." *J. Vib. Control*, 23(13), 2111–2127.

Lei, Z. X., Zhang, L. W., and Liew, K. M. (2015). "Buckling of FG-CNT reinforced composite thick skew plates resting on Pasternak foundations based on an element-free approach." *Appl. Math. Comput.*, 266, 773–791.

Lezgy-Nazargah, M. (2015). "Fully coupled thermo-mechanical analysis of bi-directional FGM beams using NURBS isogeometric finite element approach." *Aerosp. Sci. Technol.*, 45, 154–164.

Li, F. M., and Song, Z. G. (2014). "Aeroelastic flutter analysis for 2D Kirchhoff and Mindlin panels with different boundary conditions in supersonic airflow." *Acta Mech.*, 225(12), 3339–3351.

Li, L., Li, X., and Hu, Y. (2018). "Nonlinear bending of a two-dimensionally functionally graded beam." *Compos. Struct.*, 184(February 2017), 1049–1061.

Lieu, Q. X., Lee, D., Kang, J., and Lee, J. (2019). "NURBS-based modeling and analysis for free vibration and buckling problems of in-plane bi-directional functionally graded plates." *Mech. Adv. Mater. Struct.*, 26(12), 1064–1080.

Lieu, Q. X., Lee, S., Kang, J., and Lee, J. (2018a). "Bending and free vibration analyses of in-plane bi-directional functionally graded plates with variable thickness using isogeometric analysis." *Compos. Struct.*, 192(August 2017), 434–451.

Lieu, Q. X., Lee, S., Kang, J., and Lee, J. (2018b). “Bending and free vibration analyses of in-plane bi-directional functionally graded plates with variable thickness using isogeometric analysis.” *Compos. Struct.*, 192(March), 434–451.

Liew, K. M., Xiang, Y., Kitipornchai, S., and Wang, C. M. (1993). “Vibration Of Thick Skew Plates Based On Mindlin Shear Deformation Plate Theory.” *J. Sound Vib.*, 168(1), 39–69.

Lü, C. F., Lim, C. W., and Chen, W. Q. (2009). “Semi-analytical analysis for multi-directional functionally graded plates: 3-D elasticity solutions.” *Int. J. Numer. Methods Eng.*, 79(1), 25–44.

Malekzadeh, P., and Alibeygi Beni, A. (2015). “Nonlinear Free Vibration of In-Plane Functionally Graded Rectangular Plates.” *Mech. Adv. Mater. Struct.*, 22(8), 633–640.

Manna, M. C. (2012). “Free vibration of tapered isotropic rectangular plates.” *J. Vib. Control*, 18(1), 76–91.

Marques, F. D., Natarajan, S., and Ferreira, A. J. M. (2017). “Evolutionary-based aeroelastic tailoring of stiffened laminate composite panels in supersonic flow regime.” *Compos. Struct.*, 167, 30–37.

Marzocca, P., Fazelzadeh, S. A., and Hosseini, M. (2011). “A review of nonlinear aero-thermo-elasticity of functionally graded panels.” *J. Therm. Stress.*, 34(5–6), 536–568.

Matsunaga, H. (2008). “Free vibration and stability of functionally graded plates according to a 2-D higher-order deformation theory.” *Compos. Struct.*, 82(4), 499–512.

Minh, P. P., and Duc, N. D. (2019). “The effect of cracks on the stability of the functionally graded plates with variable-thickness using HSDT and phase-field theory.” *Compos. Part B Eng.*, 175(May), 107086.

Mlzusawa, T. (1993). “Vibration of rectangular mindlin plates with tapered thickness by the spline strip method.” *Comput. Struct.*, 46(3), 451–463.

Mojahedin, A., Jabbari, M., Khorshidvand, A. R., and Eslami, M. R. (2016). “Buckling analysis of functionally graded circular plates made of saturated porous materials based on higher order shear deformation theory.” *Thin-Walled Struct.*, 99, 83–90.

Muc, A., and Flis, J. (2021). “Flutter characteristics and free vibrations of rectangular functionally graded porous plates.” *Compos. Struct.*, 261(October 2020), 113301.

Naebe, M., and Shirvanimoghaddam, K. (2016). “Functionally graded materials: A review of fabrication and properties.” *Appl. Mater. Today*, 5, 223–245.

Navazi, H. M., and Haddadpour, H. (2007). “Aero-thermoelastic stability of functionally graded plates.” *Compos. Struct.*, 80(4), 580–587.

Navazi, H. M., and Haddadpour, H. (2011). “Nonlinear aero-thermoelastic analysis of homogeneous and functionally graded plates in supersonic airflow using coupled models.” *Compos. Struct.*, 93(10), 2554–2565.

Nejad, M. Z., and Hadi, A. (2016). “Non-local analysis of free vibration of bi-directional functionally graded Euler–Bernoulli nano-beams.” *Int. J. Eng. Sci.*, 105, 1–11.

Nejad, M. Z., Hadi, A., and Rastgoo, A. (2016). “Buckling analysis of arbitrary two-directional functionally graded Euler–Bernoulli nano-beams based on nonlocal elasticity theory.” *Int. J. Eng. Sci.*, 103, 1–10.

Nemat-Alla, M. (2003). “Reduction of thermal stresses by developing two-dimensional functionally graded materials.” *Int. J. Solids Struct.*, 40(26), 7339–7356.

Nemat-Alla, M. (2009). “Reduction of thermal stresses by composition optimization of two-dimensional functionally graded materials.” *Acta Mech.*, 208(3–4), 147–161.

Nemat-Alla, M., Ahmed, K. I. E., and Hassab-Allah, I. (2009). “Elastic–plastic analysis of two-dimensional functionally graded materials under thermal loading.” *Int. J. Solids Struct.*, 46(14–15), 2774–2786.

Nguyen, D. K., Nguyen, Q. H., Tran, T. T., and Bui, V. T. (2017). “Vibration of bi-dimensional functionally graded Timoshenko beams excited by a moving load.” *Acta Mech.*, 228(1), 141–155.

Nie, G., and Zhong, Z. (2007). “Axisymmetric bending of two-directional functionally graded circular and annular plates.” *Acta Mech. Solida Sin.*, 20(4), 289–295.

Nie, G., and Zhong, Z. (2010). “Dynamic analysis of multi-directional functionally graded annular plates.” *Appl. Math. Model.*, 34(3), 608–616.

Panah, M., Khorshidvand, A. R., Khorsandijou, S. M., and Jabbari, M. (2019). “Pore pressure and porosity effects on bending and thermal postbuckling behavior of FG saturated porous circular plates.” *J. Therm. Stress.*, 42(9), 1083–1109.

Parida, S., and Mohanty, S. C. (2017). “Thermoelastic vibration analysis of functionally graded skew plate using nonlinear finite element method.” *J. Therm. Stress.*, 40(9), 1111–1133.

Parida, S., and Mohanty, S. C. (2018). “Nonlinear free vibration analysis of functionally

graded plate resting on elastic foundation in thermal environment using higher order shear deformation theory." *Sci. Iran.*, 26(2), 0–0.

Phung-Van, P., Ferreira, A. J. M., Nguyen-Xuan, H., and Abdel Wahab, M. (2017). "An isogeometric approach for size-dependent geometrically nonlinear transient analysis of functionally graded nanoplates." *Compos. Part B Eng.*, 118, 125–134.

Phung-Van, P., Thai, C. H., Ferreira, A. J. M., and Rabczuk, T. (2020). "Isogeometric nonlinear transient analysis of porous FGM plates subjected to hygro-thermo-mechanical loads." *Thin-Walled Struct.*, 148(September 2019), 106497.

Phung-Van, P., Thai, C. H., Nguyen-Xuan, H., and Abdel Wahab, M. (2019). "Porosity-dependent nonlinear transient responses of functionally graded nanoplates using isogeometric analysis." *Compos. Part B Eng.*, 164(August 2018), 215–225.

Pilafkan, R., Folkow, P. D., Darvizeh, M., and Darvizeh, A. (2013). "Three dimensional frequency analysis of bidirectional functionally graded thick cylindrical shells using a radial point interpolation method (RPIM)." *Eur. J. Mech. - A/Solids*, 39, 26–34.

Prakash, T., and Ganapathi, M. (2006). "Supersonic flutter characteristics of functionally graded flat panels including thermal effects." *Compos. Struct.*, 72(1), 10–18.

Prakash, T., Singha, M. K., and Ganapathi, M. (2008). "Thermal postbuckling analysis of FGM skew plates." *Eng. Struct.*, 30(1), 22–32.

Prakash, T., Singha, M. K., and Ganapathi, M. (2012). "A finite element study on the large amplitude flexural vibration characteristics of FGM plates under aerodynamic load." *Int. J. Non. Linear. Mech.*, 47(5), 439–447.

Praveen, G. N., and Reddy, J. N. (1998). "Nonlinear transient thermoelastic analysis of functionally graded ceramic-metal plates." *Int. J. Solids Struct.*, 35(33), 4457–4476.

Rad, A. B., and Shariyat, M. (2013). "A three-dimensional elasticity solution for two-directional FGM annular plates with non-uniform elastic foundations subjected to normal and shear tractions." *Acta Mech. Solida Sin.*, 26(6), 671–690.

Ramteke, P. M., and Panda, S. K. (2021). "Free Vibrational Behaviour of Multi-Directional Porous Functionally Graded Structures." *Arab. J. Sci. Eng.*, 46(8), 7741–7756.

Reddy, J. N. (2000). "Analysis of functionally graded plates." *Int. J. Numer. Methods Eng.*, 47(1–3), 663–684.

Reddy, J. N., and Chin, C. D. (1998). “Thermomechanical analysis of functionally graded cylinders and plates.” *J. Therm. Stress.*, 21(6), 593–626.

Rezaei, A. S., Saidi, A. R., Abrishamdari, M., and Mohammadi, M. H. P. (2017). “Natural frequencies of functionally graded plates with porosities via a simple four variable plate theory: An analytical approach.” *Thin-Walled Struct.*, 120(September), 366–377.

Saleh, B., Jiang, J., Fathi, R., Al-hababi, T., Xu, Q., Wang, L., Song, D., and Ma, A. (2020). “30 Years of functionally graded materials: An overview of manufacturing methods, Applications and Future Challenges.” *Compos. Part B Eng.*, 201(January), 108376.

Satouri, S., Kargarnovin, M. H., Allahkarami, F., and Asanjarani, A. (2015). “Application of third order shear deformation theory in buckling analysis of 2D-functionally graded cylindrical shell reinforced by axial stiffeners.” *Compos. Part B Eng.*, 79, 236–253.

Shariyat, M., and Alipour, M. M. (2011). “Differential transform vibration and modal stress analyses of circular plates made of two-directional functionally graded materials resting on elastic foundations.” *Arch. Appl. Mech.*, 81(9), 1289–1306.

Shariyat, M., and Mohammadjani, R. (2014). “Three-dimensional stress field analysis of rotating thick bidirectional functionally graded axisymmetric annular plates with nonuniform loads and elastic foundations.” *J. Compos. Mater.*, 48(23), 2879–2904.

Şimşek, M. (2016). “Buckling of Timoshenko beams composed of two-dimensional functionally graded material (2D-FGM) having different boundary conditions.” *Compos. Struct.*, 149, 304–314.

Sobhani Aragh, B., and Hedayati, H. (2012). “Static response and free vibration of two-dimensional functionally graded metal/ceramic open cylindrical shells under various boundary conditions.” *Acta Mech.*, 223(2), 309–330.

Sohn, K.-J., and Kim, J.-H. (2009). “Nonlinear thermal flutter of functionally graded panels under a supersonic flow.” *Compos. Struct.*, 88(3), 380–387.

Sohn, K. J., and Kim, J. H. (2008). “Structural stability of functionally graded panels subjected to aero-thermal loads.” *Compos. Struct.*, 82(3), 317–325.

Soleimani-Javid, Z., Arshid, E., Amir, S., and Bodaghi, M. (2021). “On the higher-order thermal vibrations of FG saturated porous cylindrical micro-shells integrated with

nanocomposite skins in viscoelastic medium." *Def. Technol.*, (xxxx).

Srividhya, S., Basant, K., Gupta, R. K., Rajagopal, A., and Reddy, J. N. (2018). "Influence of the homogenization scheme on the bending response of functionally graded plates." *Acta Mech.*, 229(10), 4071–4089.

Su, Z., Wang, L., Sun, K., and Wang, D. (2019). "Vibration characteristic and flutter analysis of elastically restrained stiffened functionally graded plates in thermal environment." *Int. J. Mech. Sci.*, 157–158(May), 872–884.

Sundararajan, N., Prakash, T., and Ganapathi, M. (2005). "Nonlinear free flexural vibrations of functionally graded rectangular and skew plates under thermal environments." *Finite Elem. Anal. Des.*, 42(2), 152–168.

Swaminathan, K., and Sangeetha, D. M. (2017). "Thermal analysis of FGM plates – A critical review of various modeling techniques and solution methods." *Compos. Struct.*, 160, 43–60.

Talha, M., and Singh, B. N. (2011). "Large amplitude free flexural vibration analysis of shear deformable FGM plates using nonlinear finite element method." *Finite Elem. Anal. Des.*, 47(4), 394–401.

Tang, Y., and Ding, Q. (2019). "Nonlinear vibration analysis of a bi-directional functionally graded beam under hygro-thermal loads." *Compos. Struct.*, 225(June), 111076.

Tang, Y., Lv, X., and Yang, T. (2019). "Bi-directional functionally graded beams: asymmetric modes and nonlinear free vibration." *Compos. Part B Eng.*, 156(August 2018), 319–331.

Tanov, R., and Tabiei, A. (2000). "Simple correction to the first-order shear deformation shell finite element formulations." *Finite Elem. Anal. Des.*, 35(2), 189–197.

Thang, P.-T., Nguyen-Thoi, T., and Lee, J. (2016). "Closed-form expression for nonlinear analysis of imperfect sigmoid-FGM plates with variable thickness resting on elastic medium." *Compos. Struct.*, 143, 143–150.

Tomar, S. S., and Talha, M. (2019). "Large amplitude vibration analysis of functionally graded laminated skew plates in thermal environment." *Mech. Adv. Mater. Struct.*, 26(5), 451–464.

Torabi, K., and Afshari, H. (2019). "Optimization of flutter boundaries of cantilevered

trapezoidal functionally graded sandwich plates." *J. Sandw. Struct. Mater.*, 21(2), 503–531.

Tran, T. T., Pham, Q.-H., and Nguyen-Thoi, T. (2020). "Static and free vibration analyses of functionally graded porous variable-thickness plates using an edge-based smoothed finite element method." *Def. Technol.*, (xxxx), 1–16.

Truong, T. T., Nguyen-Thoi, T., and Lee, J. (2019). "Isogeometric size optimization of bi-directional functionally graded beams under static loads." *Compos. Struct.*, 227(January), 111259.

Upadhyay, A. K., and Shukla, K. K. (2013). "Geometrically nonlinear static and dynamic analysis of functionally graded skew plates." *Commun. Nonlinear Sci. Numer. Simul.*, 18(8), 2252–2279.

Vinyas, M., Harursampath, D., and Nguyen-Thoi, T. (2020). "Influence of active constrained layer damping on the coupled vibration response of functionally graded magneto-electro-elastic plates with skewed edges." *Def. Technol.*, 16(5), 1019–1038.

Vinyas, M., Nischith, G., Loja, M. A. R. A. R., Ebrahimi, F., and Duc, N. D. D. (2019). "Numerical analysis of the vibration response of skew magneto-electro-elastic plates based on the higher-order shear deformation theory." *Compos. Struct.*, 214(December 2018), 132–142.

Wang, Y. Q., and Zu, J. W. (2017a). "Large-amplitude vibration of sigmoid functionally graded thin plates with porosities." *Thin-Walled Struct.*, 119(June), 911–924.

Wang, Y. Q., and Zu, J. W. (2017b). "Nonlinear dynamic thermoelastic response of rectangular FGM plates with longitudinal velocity." *Compos. Part B Eng.*, 117, 74–88.

Wang, Y. Q., and Zu, J. W. (2017c). "Vibration behaviors of functionally graded rectangular plates with porosities and moving in thermal environment." *Aerosp. Sci. Technol.*, 69, 550–562.

Wang, Y., and Zu, J. W. (2017d). "Nonlinear oscillations of sigmoid functionally graded material plates moving in longitudinal direction." *Appl. Math. Mech. (English Ed.*, 38(11), 1533–1550.

Wattanasakulpong, N., Gangadhara Prusty, B., Kelly, D. W., and Hoffman, M. (2012). "Free vibration analysis of layered functionally graded beams with experimental validation." *Mater. Des.*, 36, 182–190.

Woo, J., Meguid, S. A., and Ong, L. S. (2006). “Nonlinear free vibration behavior of functionally graded plates.” *J. Sound Vib.*, 289(3), 595–611.

Xie, K., Wang, Y., Niu, H., and Chen, H. (2020). “Large-amplitude nonlinear free vibrations of functionally graded plates with porous imperfection: A novel approach based on energy balance method.” *Compos. Struct.*, 246(January), 112367.

Xu, Y., and Zhou, D. (2009). “Three-dimensional elasticity solution of functionally graded rectangular plates with variable thickness.” *Compos. Struct.*, 91(1), 56–65.

Yang, J., Hao, Y. X., Zhang, W., and Kitipornchai, S. (2010). “Nonlinear dynamic response of a functionally graded plate with a through-width surface crack.” *Nonlinear Dyn.*, 59(1–2), 207–219.

Yang, J., and Huang, X.-L. (2007). “Nonlinear transient response of functionally graded plates with general imperfections in thermal environments.” *Comput. Methods Appl. Mech. Eng.*, 196(25–28), 2619–2630.

YANG, J., and SHEN, H.-S. (2002). “VIBRATION CHARACTERISTICS AND TRANSIENT RESPONSE OF SHEAR-DEFORMABLE FUNCTIONALLY GRADED PLATES IN THERMAL ENVIRONMENTS.” *J. Sound Vib.*, 255(3), 579–602.

Yanga, J., and Shen, H.-S. (2003). “Non-linear analysis of functionally graded plates under transverse and in-plane loads.” *Int. J. Non. Linear. Mech.*, 38(4), 467–482.

Yazdi, A. A. (2019). “Large amplitude flutter analysis of functionally graded carbon nanotube reinforced composite plates with piezoelectric layers on nonlinear elastic foundation.” *Proc. Inst. Mech. Eng. Part G J. Aerosp. Eng.*, 233(2), 533–544.

Yu, T., Bui, T. Q., Yin, S., Doan, D. H., Wu, C. T., Do, T. Van, and Tanaka, S. (2016). “On the thermal buckling analysis of functionally graded plates with internal defects using extended isogeometric analysis.” *Compos. Struct.*, 136, 684–695.

Zafarmand, H., and Kadkhodayan, M. (2015). “Three dimensional elasticity solution for static and dynamic analysis of multi-directional functionally graded thick sector plates with general boundary conditions.” *Compos. Part B Eng.*, 69, 592–602.

Zare Jouneghani, F., Dimitri, R., Bacciocchi, M., and Tornabene, F. (2017). “Free Vibration Analysis of Functionally Graded Porous Doubly-Curved Shells Based on the First-Order Shear Deformation Theory.” *Appl. Sci.*, 7(12), 1252.

Zhang, L. W., and Liew, K. M. (2015). “Large deflection analysis of FG-CNT

reinforced composite skew plates resting on Pasternak foundations using an element-free approach.” *Compos. Struct.*, 132, 974–983.

Zhao, X., Lee, Y. Y., and Liew, K. M. (2009). “Free vibration analysis of functionally graded plates using the element-free kp-Ritz method.” *J. Sound Vib.*, 319(3–5), 918–939.

Zhou, K., Huang, X., Tian, J., and Hua, H. (2018). “Vibration and flutter analysis of supersonic porous functionally graded material plates with temperature gradient and resting on elastic foundation.” *Compos. Struct.*, 204(July), 63–79.

Zhu, J., Lai, Z., Yin, Z., Jeon, J., and Lee, S. (2001). “Fabrication of ZrO2-NiCr functionally graded material by powder metallurgy.” *Mater. Chem. Phys.*, 68(1–3), 130–135.

List of publications based on Ph.D. work

Sl no	Title of paper	Authors	Journal Name, Year, Volume Number, Issue, Pages)	Month, year of publication	Category*
1	Influence of porosity distribution on nonlinear free vibration and transient responses of porous functionally graded skew plates. https://doi.org/10.1016/j.dt.2021.02.003	**NaveenKumar H S**, Subhaschandra Kattimani, and T. Nguyen-Thoi	Defence Technology, Volume 17(6), 2021, 1918-1935. **IF – 4.035**	December, 2021	1
2	Effect of different geometrical non-uniformities on nonlinear vibration of porous functionally graded skew plates: a finite element study. https://doi.org/10.1016/j.dt.2021.05.002	**H S Naveen Kumar**, and Subhaschandra Kattimani	Defence Technology, 2021, 18(6), 2022, 918-936. **IF – 4.035**	June, 2022	1
3	Nonlinear analysis of two-directional functionally graded doubly curved panels with porosities. https://doi.org/10.12989/sem.2022.82.4.477	**H. S. Naveen Kumar** and Subhaschandra Kattimani	Structural Engineering and Mechanics, 2022, 82 (4), 477-490. **IF – 2.998**	May, 2022	1
4	Geometrically nonlinear behavior of two-directional functionally graded porous plates with four different materials. https://doi.org/10.1177/09544062221111038	**Naveen Kumar Hosur Shivaramaiah**, Subhaschandra Kattimani, T. Nguyen-Thoi, Mahdi Shariati.	Part C: Journal of Mechanical Engineering Science, **IF – 1.758**	June, 2022	1

5	Geometrically nonlinear study of functionally graded saturated porous plates based on refined shear deformation plate theory and Biot's theory. https://doi.org/10.1142/S021945542350013X	**H S Naveen Kumar**, Subhaschandra Kattimani, Flavio D Marques, T. Nguyen-Thoi, Mehdi Shariati.	International Journal of Structural Stability and Dynamics, (Accepted and In press) **IF – 2.957**	--	1
6	Geometrically nonlinear study of functionally graded saturated porous plates under thermal environment based on refined shear deformation plate theory and Biot's theory	**Naveen Kumar H S**, Subhaschandra Kattimani, Flavio D Marques	25th International Conference on Composite Structures. (ICCS-25), Portugal	--	4

Category* 1: Journal paper,full paper reviewed 2: Journal paper, Abstract reviews

3: Conference /Symposium paper, full paper reviewed 4: Conference /Symposium paper, Abstract reviewed

5: Others (including paper in workshop, NITK Bulletin, short notes etc.)

30/09/2022.

Naveen Kumar H S
Research Scholar

30/09/2022

Dr. Subhaschandra Kattimani
Research Guide

BIO-DATA

Name	Naveen Kumar H S
Father's Name	Shivaramaiah
Date of Birth	May 05, 1988
Nationality	Indian
Permanent Address	# 23, s/o Shivaramaiah, Hosur, Kathrigatta Post, Huthridurga Hobli, Kunigal Taluk, Tumkur – 572126, Karnataka, India.
Mobile Number	+91-9538326373
Email Id	naveenhsk@gmail.com

Educational Qualification:

Qualification	University	College	Period	Performance
Ph.D	National Institute of Technology Karnataka	National Institute of Technology Karnataka, Surathkal	2019-2022	8.50
M.Tech, Machine Design	Visvesvaraiah Technological University	R V College of Engineering, Bangalore	2010-2012	78.70%
B.E, Mechanical Engineering	Bangalore University	University Visvesvaraya College of Engineering, Bangalore	2005-2009	75.28%

I declare that the above information is true and correct to the best of my knowledge.

(Naveen Kumar H S)

BIO-DATA

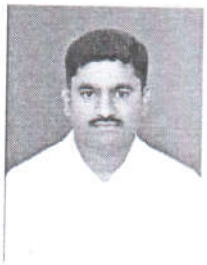

Name	Naveen Kumar H S
Father's Name	Shivaramaiah
Date of Birth	May 05, 1988
Nationality	Indian
Permanent Address	# 23, s/o Shivaramaiah, Hosur, Kathrigatta Post, Huthridurga Hobli, Kunigal Taluk, Tumkur – 572126, Karnataka, India.
Mobile Number	+91-9538326373
Email Id	naveenhsk@gmail.com

Educational Qualification:

Qualification	University	College	Period	Performance
Ph.D	National Institute of Technology Karnataka	National Institute of Technology Karnataka, Surathkal	2019-2022	8.50
M.Tech, Machine Design	Visvesvaraiah Technological University	R V College of Engineering, Bangalore	2010-2012	78.70%
B.E, Mechanical Engineering	Bangalore University	University Visvesvaraya College of Engineering, Bangalore	2005-2009	75.28%

I declare that the above information is true and correct to the best of my knowledge.

30/09/2022.

(Naveen Kumar H S)